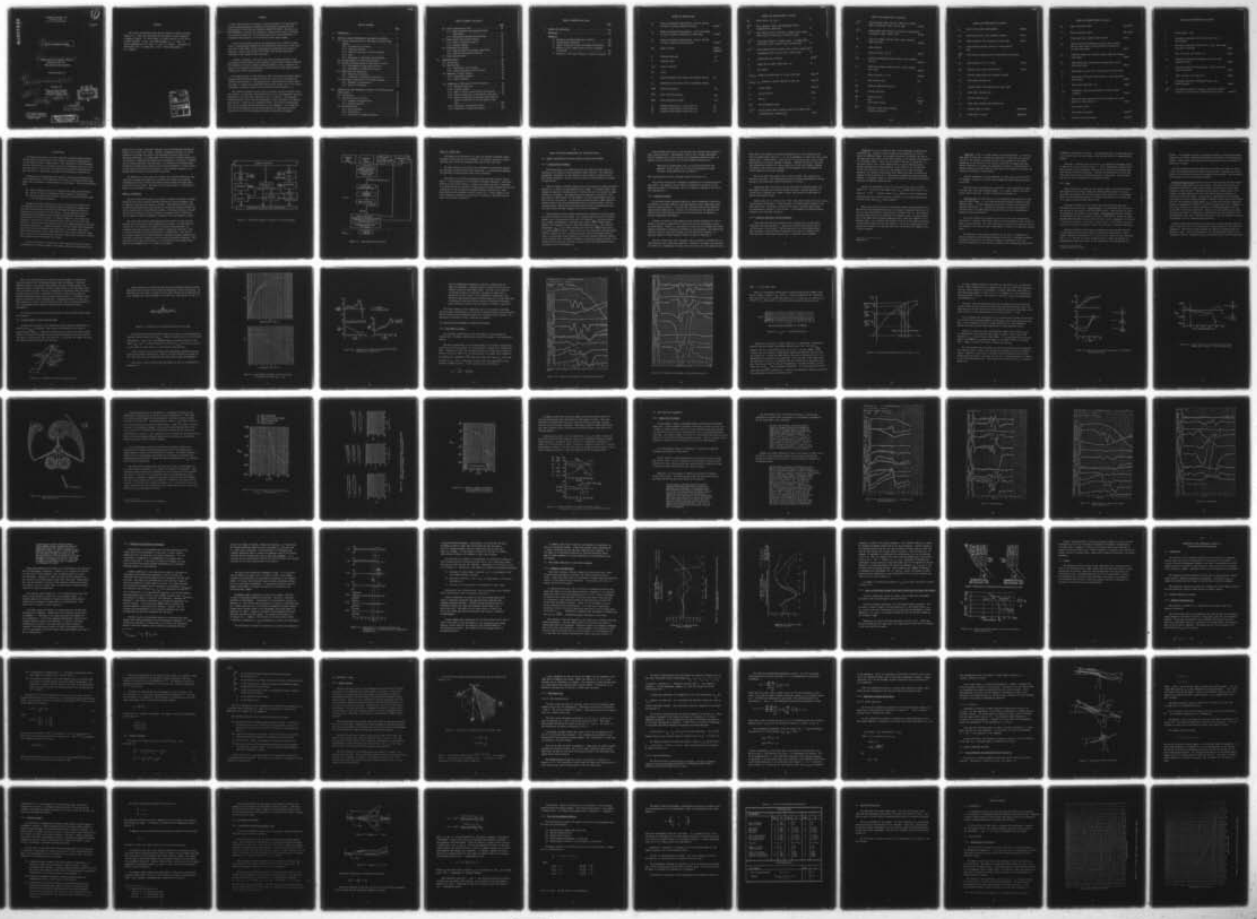
AD-A033 940 SYSTEMS CONTROL INC PALO ALTO CALIF F/G 1/2
IDENTIFICATION OF AIRCRAFT STABILITY DERIVATIVES FOR THE HIGH A--ETC(U)
1972 W E HALL N00014-72-C-0328
UNCLASSIFIED TR-1 NL

1 OF 3
AD A033940



ADA033940

(1)

SYSTEMS CONTROL, INC.
260 SHERIDAN AVENUE
PALO ALTO, CALIFORNIA 94306

TELEPHONE (415)
327-9333

(9) INTERIM ENGINEERING REPORT.

(6) IDENTIFICATION OF AIRCRAFT STABILITY DERIVATIVES FOR THE HIGH ANGLE-OF-ATTACK REGIME.

Technical Report #1

(15) N0014-72-C-0328

Prepared for

(11) 1972

Office of Naval Research
800 North Quincy Road
Arlington, Virginia 22217

(14) TR-1

(12) 209 p.

DDC
RECEIVED
NOV 11 1976
B

Approved by:

J. S. Tyler, Director
Aeronautical and Marine
Systems Branch

Prepared by

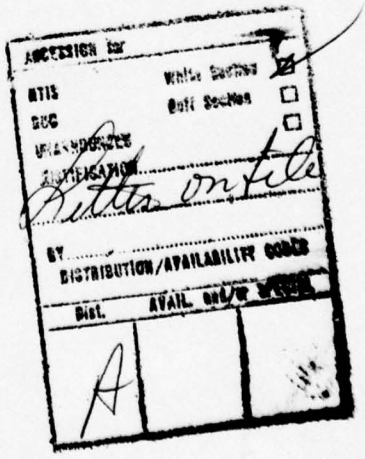
(10) W. E. Hall, Jr

DISTRIBUTION STATEMENT A
Approved for public release;
Distribution Unlimited

LB
389333

FOREWORD

This report was prepared under Contract N00014-72-C-0328 by Systems Control, Inc., Palo Alto, California for the Office of Naval Research, Arlington, Virginia. Mr. David Siegel is project monitor for the Office of Naval Research. At SCI, the project manager is J. S. Tyler, Jr. Project engineers are W. E. Hall, Jr. and D. E. Stepner. Consultants for this project are R. K. Mehra and J. Bull. Project programmer is M. V. Bullock.



ABSTRACT

This report presents the results of the initial phase of a high angle-of-attack integrated parameter identification development program sponsored by the Office of Naval Research (Contract N00014-72-C-0328). The purpose of this program is to develop the simulations, identification models, and flight test procedures which will offer improved accuracy in the determination of aerodynamic characteristics in the stall/post-stall flight regime.

A review of high angle-of-attack aerodynamics is first presented in this report to summarize the complicated flow interactions which occur in the stall/post-stall flight regime and to isolate important phenomena that should be simulated. Motions such as "pitch up", "wing rock" and "yaw departure" characterize such incipient spin conditions.

A summary of analysis, wind tunnel and flight testing experience in the high angle-of-attack regime is also presented. These results clearly illustrate the importance of accurate flight testing procedures in order to achieve the goal of better modeling, understanding, and predicting of high angle-of-attack stability and control characteristics.

The major sections of this report describe a six-degree-of-freedom computer program which has been developed by SCI as the first step in the integrated identification procedure. This program will be used by SCI to simulate flight test data, to compare with simplified identification models, and for the overall development of the high angle-of-attack identification procedures.

The simulation program has been used to reproduce typical stall/post-stall/spin motions. In particular "wing rock", "pitch up" and "yaw departure" have been reproduced using a "1g" stall maneuver for the F-4 aircraft. The simulation includes nonlinear "table look-up" aerodynamics, and an "autopilot" to reproduce pilot motions. Buffet and air turbulence effects, and effects of measurement noise on the recorded response histories are also simulated. It is shown that this simulation generates the data characteristics of high angle-of-attack responses for use with the integrated parameter identification program.

TABLE OF CONTENTS

		PAGE
I.	INTRODUCTION	1
II.	SURVEY OF PREVIOUS EXPERIMENTAL AND ANALYTICAL RESULTS	1
	2.1 General Characteristics of High Angle-of-Attack Flight Regimes	6
	2.1.1 Introduction and Summary	6
	2.1.2 Analytical Aspects	7
	2.1.3 Pitch-Up, Wing Drop, and Yaw Divergence	8
	2.1.4 Spin	11
	2.1.5 Discussion of Simplified Spin Mechanism	13
	2.2 Pitching Moments at High Angle-of-Attack	15
	2.3 Rolling and Yawing Moments at High Angle of Attack	19
	2.3.1 Roll Moments at High Angle-of-Attack	19
	2.3.2 Yaw Moments at High Angle-of-Attack	27
	2.4 "Wing Rock" and "Departure"	35
	2.4.1 Flight Test Occurrence	35
	2.4.2 Prediction of Wing Rock and Departure	44
	2.5 Wind Tunnel Prediction of Free Flight Responses	48
	2.5.1 Examples of Inconsistency	48
	2.5.2 Basis of Differences	51
III.	SIMULATION OF HIGH PERFORMANCE AIRCRAFT IN THE HIGH ANGLE-OF-ATTACK REGIME	54
	3.1 Introduction	54
	3.2 Aircraft Equations of Motion	54
	3.2.1 Kinematic Representations	54
	3.2.2 Dynamic Equations	58
	3.3 Aerodynamic Model	60
	3.3.1 Model Selection	60
	3.3.2 Wind Tunnel	62
	3.3.3 Simulation of Random Disturbances	65

TABLE OF CONTENTS (Continued)

		PAGE
3.4	Initial Conditions and Trim.	66
3.4.1	Input Parameters and Longitudinal Trim Calculation.	66
3.4.2	Differential Equation Initialization.	69
3.5	Control Inputs and Autopilot Design.	70
3.5.1	Types of Simulated Controls.	70
3.5.2	Autopilot Design.	71
3.6	Instrumentation Modeling.	73
3.6.1	Angle-of-Attack and Sideslip Angle Vanes.	73
3.6.2	Gyro and Accelerometer Modeling.	76
3.7	Output Specifications.	79
IV.	SIMULATION RESULTS.	80
4.1	Introduction.	80
4.2	Trim Solutions.	80
4.2.1	Longitudinal Trim Solutions.	80
4.2.2	Lateral-Directional Trim Solutions.	83
4.3	Responses in Linear Regions.	83
4.3.1	Longitudinal Response.	83
4.3.2	Lateral Response.	86
4.4	Simulation of High Angle-of-Attack Responses.	92
4.4.1	Simulation Objective.	92
4.4.2	Autopilot Design.	92
4.4.3	Types of Control Specification for Wing Rock. . .	94
4.4.4	Computer Simulation of Pre-Departure Wing Rock. .	95
4.4.5	Effect of Individual Aerodynamic Coefficients in Computer Simulation of the Pre-Departure Wing Rock.	106
4.4.6	Simulation of Measurement System.	115
4.4.7	Simulation of Random Disturbances	121

TABLE OF CONTENTS (Continued)

PAGE

V. SUMMARY AND CONCLUSIONS. 132

REFERENCES. 136

APPENDICES

A. Six-Degree-of-Freedom Equations of Motion. 141

B. Instrumentation Equations. 153

C. Typical Variations of Force and Moment Coefficients. . 158

D. Review of Actual Flight Traces of the F-4 Airplane at High AOA. 175

E. Discussion of the Phasor Diagram in Stability Analysis 194

SYMBOLS AND ABBREVIATIONS

a_x	linear acceleration along positive x axis of aircraft at center of gravity (positive forward)	ft/sec^2
a_y	linear acceleration along positive y axis of aircraft at center of gravity (positive out right wing)	ft/sec^2
a_z	linear acceleration along positive z axis of aircraft at center of gravity (positive down)	ft/sec^2
AOA	angle of attack	(units) (degrees)
b	reference wing span	ft.
$\bar{c}$	reference chord	ft.
c.g.	center of gravity	
CR	cruise	
D	drag (aerodynamic force along total velocity vector)	lb
K_σ	generalized scale factor error in instrument reading	
KTAS	knots true airspeed	kts
KIAS	knots indicated airspeed	kts
KCAS	knots calibrated airspeed	kts
ℓ_x	distance along aircraft x axis from c.g.	ft.
ℓ_y	distance along aircraft y axis from c.g.	ft.
ℓ_z	distance along aircraft z axis from c.g.	ft.

SYMBOLS AND ABBREVIATIONS (Continued)

$\bar{\ell}_V$	vector sum of ℓ_x, ℓ_y, ℓ_z	ft.
F^{ext}_B	sum of gravity, thrust, and aerodynamic forces, coordinatized in body frame	lb
$F_x^{(\cdot)}$	force along positive x axis due to engine (F_x^e), aerodynamics (F_x^a), inertial (F_x^I) and gravity (F_x^s)	lb
$F_y^{(\cdot)}$	force along positive aircraft z axis to engine (F_y^e), aerodynamics (F_y^a), inertial (F_y^I), gravity (F_y^g)	lb
$F_z^{(\cdot)}$	force along position aircraft z axis is due to engine (F_z^e), aerodynamics (F_z^a), inertia (F_z^I), gravity (F_z^g)	lb
g	acceleration due to gravity	ft/sec^2
h	moment arm of engine thrust about c.g.	ft
I	unit matrix	
I_x, I_y, I_z	moments of inertia about x, y, and z body axes	slug ft^2
I_{xz}, I_{yz}, I_{xy}	products of inertia referred to body axes	slug ft^2
$\bar{\bar{I}}$	inertia tensor	slug ft^2
m	mass of aircraft	slug
M	Mach No.	----
MAC	mean aerodynamic chord	----
$M_x^{(\cdot)}$	rolling moment about aircraft x axis due to engine (M_x^e), aerodynamics M_x^a, inertia (M_x^I)	ft-lb

$M_y^{(\cdot)}$	pitching moment about aircraft y axis due to engine (M_y^e), aerodynamics (M_y^a), inertia (M_y^I)	ft-lbs
$M_z^{(\cdot)}$	yawing moment about aircraft z axis due to engine (M_z^e), aerodynamics (M_z^a), inertia (M_z^I)	ft-lbs
P,p	roll rate (angular velocity about x axis, positive right wing down)	rad/sec
PA	power approach	
q	dynamic pressure, $\frac{1}{2}\ \rho V^2$	lb/ft^2
Q,q	pitching rate(angular velocity about y axis, positive nose up)	rad/sec
R,r	yawing rate (angular velocity about z axis, positive nose right)	rad/sec
s	Laplace operator, $\sigma + j\omega$	rad/sec
S	wing reference area	ft^2
SAS	stability augmentation system	-
TED	trailing edge down	----
TEU	trailing edge up	----
t	time	seconds
T	total engine thrust	lbs
T^{B-I}	direction cosine matrix defining aircraft orientation	----

SYMBOLS AND ABBREVIATIONS (Continued)

T_m	matrix of instrument misalignments	degrees
U,u	velocity along the x axis (positive forward)	ft/sec
V,v	velocity along y axis (positive out right wing)	ft/sec
V_T	total aircraft velocity relative to fixed inertial axes	
V_T^{B-I} B	total aircraft velocity vector coordinatized in body axes	
V_V	total velocity of α or β vane	ft/sec
W,w	velocity along z axis (positive down)	ft/sec
x	aircraft longitudinal axis (positive forward)	
X_e	earth frame reference axis	
y	aircraft lateral axis (positive out right wing)	
Y_e	earth frame reference axis	
z	aircraft vertical axis	
Z_e	earth frame reference axis (positive up)	
α	aircraft angle of attack	(degs)(rad)
α_s	stall angle of attack	(degs)(rad)

α_w	angle of attack of wing	(degs)(rad)
β	aircraft sideslip angle	(degs)(rad)
γ	flight path angle, positive above horizon	(degs)
δ_a	aileron and spoiler deflection, positive when trailing edge of right aileron is down and when left spoiler is up (left stick input)	(degs)
δ_s	stabilator deflection, positive trailing edge down (forward stick input)	(degs)
δ_r	rudder deflection, positive when trailing edge is left (left pedal input)	(degs)
ε_o	generalized rms error due to white noise on an instrument	
θ	pitch angle (right hand rotation about y axis, hence nose up positive)	(degs)
Θ	Euler pitch angle (fig. 3.2)	(degs)
θ_m	measurement instrument misalignment in pitch (random variable)	(degs)
λ	angle in xz plane between thrust line of engine and x axis, positive in same sense as θ	(degs)
λ	taper ratio of wing	
ρ	air density at altitude	$slug/ft^3$
ρ_o	reference sea level density	$slug/ft^3$

σ	density ratio, ρ/ρ_o	
σ	generalized instrument error (in position, rate, or acceleration)	
ϕ	bank angle (right hand rotation about x axis, hence right wing down is positive)	(degs)
Φ	Euler roll angle (see figure 3.2)	(degs)
ϕ_m	measurement instrument misalignment about roll axis (random variable)	(degs)
ψ	yaw angle (right hand rotation about z axis) hence nose right is positive)	(degs)
Ψ	Euler yaw angle (see figure 3.2)	(degs)
Ψ_m	measurement instrument misalignment about z axis (random variable)	(degs)
Ω_B^{B-I}	total angular velocity of aircraft relative to inertial relative to inertial axes, coordinatized in body axes	(rad/sec)

Nondimensional Force and Moment Coefficients

a) Longitudinal

$$C_N = \frac{-F_z^{aero}}{qS} \quad \text{(positive up)}$$

$$C_z = -C_N$$

$$C_x = \frac{F_x^{aero}}{qS}$$

$$C_m = \frac{M_x^{aero}}{qS\bar{c}}$$

$$C_L = \frac{L}{qS}$$

$$C_D = \frac{D}{qS}$$

$$C_{m_\alpha} = \frac{\partial C_m}{\partial \alpha} \qquad C_{z_\alpha} = \frac{\partial C_z}{\partial \alpha} \qquad C_{x_\alpha} = \frac{\partial C_x}{\partial \alpha}$$

$$C_{m_{\dot\alpha}} = \frac{\partial C_m}{\partial\left(\frac{\dot\alpha \bar{c}}{2V_T}\right)} \qquad C_{z_{\dot\alpha}} = \frac{\partial C_z}{\partial\left(\frac{\dot\alpha \bar{c}}{2V_T}\right)} \qquad C_{x_{\dot\alpha}} = \frac{\partial C_x}{\partial\left(\frac{\dot\alpha\, \bar{c}}{2V_T}\right)}$$

$$C_{m_q} = \frac{\partial C_m}{\partial\left(\frac{q\bar{c}}{2\bar{V}}\right)} \qquad C_{z_q} = \frac{\partial C_z}{\partial\left(\frac{q\bar{c}}{2\bar{V}}\right)} \qquad C_{x_q} = \frac{\partial C_x}{\partial\left(\frac{q\bar{c}}{2V_T}\right)}$$

$$C_{m_{\delta_s}} = \frac{\partial C_m}{\partial \delta_s} \qquad C_{z_{\delta_s}} = \frac{\partial C_z}{\partial \delta_s} \qquad C_{x_{\delta_s}} = \frac{\partial C_x}{\partial \delta_s}$$

(b) Lateral Body Axis

$$C_y = \frac{F_y^{aero}}{qS}$$

$$C_\ell = \frac{M_x^{aero}}{qSb}$$

$$C_n = \frac{M_z^{aero}}{qSb}$$

$$C_{y_\beta} = \frac{\partial C_y}{\partial \beta} \qquad C_{\ell_\beta} = \frac{\partial C_\ell}{\partial \beta} \qquad C_{n_\beta} = \partial C_n / \partial \beta$$

$$C_{y_{\delta a}} = \frac{\partial C_y}{\partial \delta_a} \qquad C_{\ell_p} = \frac{\partial C_\ell}{\partial (pb/2V_T)} \qquad C_{n_p} = \partial C_n / \partial (pb/2V_T)$$

$$C_{y_{\delta r}} = \frac{\partial C_y}{\partial \delta_r} \qquad C_{\ell_r} = \frac{\partial C_\ell}{\partial (rb/2V_T)} \qquad \partial C_{nr} = \partial C_n / \partial (rb/2V_T)$$

$$C_{\ell_{\delta a}} = \frac{\partial C_\ell}{\partial \delta_a} \qquad \partial C_{n_{\delta a}} = \frac{\partial C_n}{\partial \delta_a}$$

$$C_{\ell_{\delta r}} = \frac{\partial C_\ell}{\partial \delta_r} \qquad \partial C_{n_{\delta r}} = \frac{\partial C_n}{\partial \delta_r}$$

$$C_{\ell_{\delta_s}} = \frac{\partial C_\ell}{\partial \delta_s} \qquad \partial C_{A_{\delta s}} = \frac{\partial C_n}{\partial \delta_s}$$

Subscripts and Superscripts

$(\ )_{max}$ maximum value

$(\hat{})$ estimated value

$(\ )_I$ inertial reference

I INTRODUCTION

The mission requirements of present and future high-performance military aircraft demand an improvement in the stability and control characteristics in high angle-of-attack flight regimes. Past experience has well documented the poor characteristics of aircraft such as the F-4 during stall, post stall, and spin regimes. It has been estimated that out-of-control aircraft losses have cost the U. S. government an average of $40 million/year (Reference 1).

A prerequisite to developing better stability and control characteristics is the understanding of basic phenomena that occur in stall/post stall flight regime and the relation of these phenomena to spin entry. Such an understanding would

(1) enable existing aircraft to be employed more safely and effectively
(2) provide the basis for designing control systems to prevent spin
(3) improve the high angle-of-attack stability and control characteristics of future military aircraft.

Although stall/spin phenomena have been a safety hazard for many years, the introduction of thin swept wings and axially-concentrated fuselage mass in modern high performance aircraft has compounded the danger and focused attention on the seriousness of the problem. Several approaches have been developed for understanding and predicting stall/post-stall/spin flight characteristics of these aircraft. As shown in Figure 1.1 the three basic elements: theoretical calculations, wind tunnel tests, and full scale tests all play an essential but often limited role in this understanding and prediction. These three approaches are highly interactive; what is learned from one approach may often be used to strengthen other approaches. For example, where aerodynamic characteristics can be predicted on the basis of theory and wind tunnel tests, such as for the design phase, full scale flight tests are used to validate these predictions and substantiate the design.

It is often found that deficiencies in wind tunnel predictions resulting from differences in Reynolds number, Mach number, and pilot actions cause these

flight tests to assume a much more important role in understanding aerodynamic behavior of the full scale design. However, determining stability and control parameters from flight test data in the high angle-of-attack region is an ambitious undertaking. The large number of parameters and nonlinear models that are necessary to describe high angle-of-attack phenomena, the presence of dynamic noise resulting from buffet and turbulence, the difficulty of obtaining angle-of-attack and sideslip measurements, and the strong dependence on control inputs, require rigorous data reduction techniques. Such techniques represent, at a minimum, state-of-the-art identification technology.

The objective of this project is to develop the required simulations, identification programs, and flight test procedures and to apply the resulting methodology to extract stability and control characteristics from high angle-of-attack flight test data. The scope of the overall project is illustrated in Figure 1.2 and outlined as follows:

Phase I - Simulation

The first task in this phase is to develop a complete six degree of freedom simulation that will accurately describe high angle-of-attack responses, such as wing rock, roll and yaw departure, and spin. This simulation will be used to generate simulated flight test data and to corraborate simplified models that will be required for the identification process. This phase includes a development of the equations of motion, a nonlinear aerodynamic model, selection of control inputs and initial conditions and modeling the instrumentation system.

The second task includes developing simplified models for identification purposes and simulating the entire identification process. The main objective of this task is to simplify the complete six-degree-of-freedom model to a realistic model with a greatly reduced number of parameters that will be used to extract stability and control parameters from flight data. This task is an iterative process between model selection, simulated parameter identification and model verification (comparing to the six-degree-of-freedom responses). This task would also include specifications for instrumentation and flight control inputs, and recommendations for a flight test program.

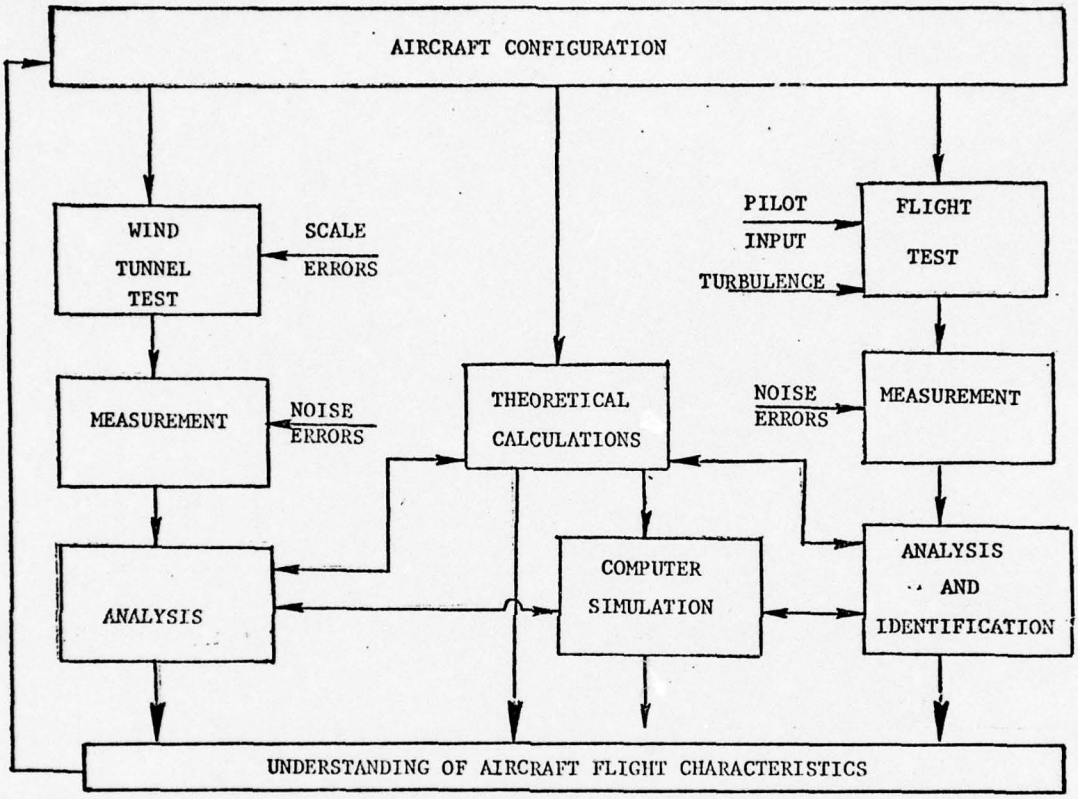


Figure 1.1 Conceptual Diagram of Analysis of Aircraft Dynamics

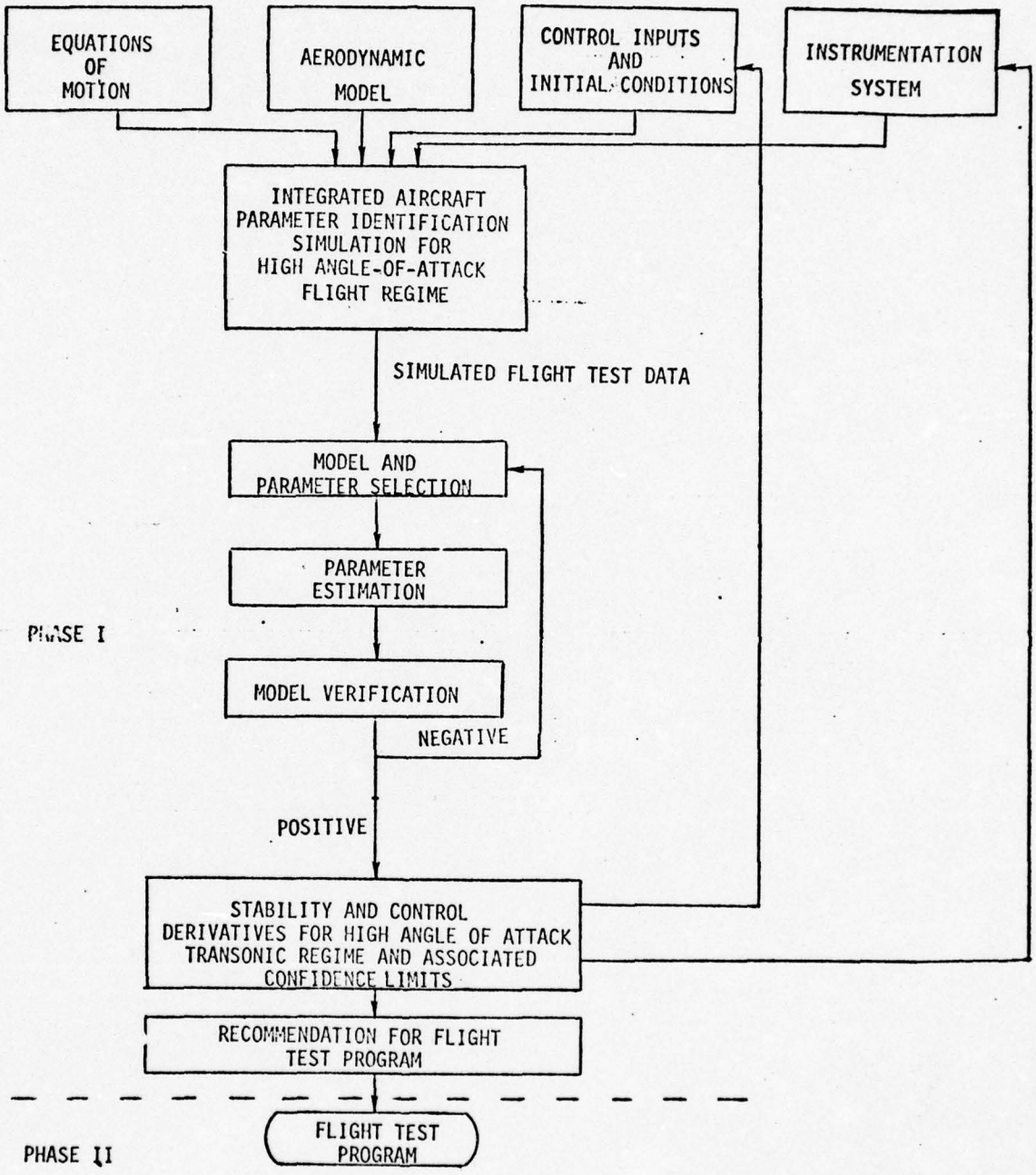


Figure 1.2. Generalized Work Flow Chart

Phase II - Flight Test

The objective of this phase is to apply the analysis techniques, understanding of high angle-of-attack phenomena, and computer programs to extract stability and control characteristics from actual flight test data.

The above program is believed to be a methodical and systematic approach for extending existing identification technology, to a successful methodology for high-angle-of-attack flight test and data reduction.

This report is an interim engineering report covering the first task of phase I - the development of the six-degree-of-freedom simulation. Succeeding sections of this report include: a review of previous work that is pertinent to an understanding and simulation of high angle-of-attack responses (Section II), a discussion of the six degree-of-freedom simulation (Section III), and a presentation of the simulation results (Section IV). A brief summary of the work accomplished during this period and the conclusions resulting from this study are presented in Section V.

II

SURVEY OF PREVIOUS EXPERIMENTAL AND ANALYTICAL RESULTS

2.1 GENERAL CHARACTERISTICS OF HIGH ANGLE-OF-ATTACK FLIGHT REGIMES

2.1.1 Introduction and Summary

An understanding of the stall/post-stall high angle-of-attack regime is essential to the design of high performance fighter aircraft. The complicated aerodynamic interactions of this regime have been studied by theoretical and wind tunnel techniques. The most relevant results of these efforts are reviewed in this section.

There are abrupt, nonlinear changes in force and moments on a high performance aircraft as it enters the high angle-of-attack regime. In subsonic flight, these changes are caused by increasing areas of stalled flow over the aircraft as angle-of-attack is increased. Some separation may be expected as low as 10° or 12°. Such stall not only affects the wing moments, but also causes changes in the air flow over the tail surfaces. As the angle-of-attack increases, these combine to produce nonlinear and often destabilizing effects on vehicle motion. With increasing speeds, compressibility effects complicate the flow significantly and can cause further nonlinear changes in the forces and moments.

These nonlinear effects produce characteristic responses of aircraft which are used to define the stall regime. For nonswept-wing aircraft at low subsonic speeds, stall, flow separation over much of the wing, $C_{L_{max}}$, and drag increase occur nearly simultaneously. On highly swept wings at high subsonic speeds, however, flow separation occurs at lower incidences than $C_{L_{max}}$. For some configurations, $C_{L_{max}}$ is not easily defined since there is no significant loss in C_L at high angles of attack. It may even be that C_L continues to increase beyond "stall". Because of this, it is more practical, from an operational point of view, to define stall by the occurrence of aircraft responses which are peculiar to the nonlinear force and moment variations of post-stall angles-of-attack. For example, buffet intensity, pitch-up, and wing rock are defining characteristics for stall in the F-4 (Reference 2).

These phenomena also serve to cue the pilot that incipient spin conditions exist during a maneuver. Unfortunately, there is not a unique relationship between responses such as wing rock and the instantaneous angle-of-attack. An example of this is discussed in the F-4 pilot handbook (Reference 2):

> "Wing rock is unpredictable (e.g., in an accelerated stall) but generally starts at about 22 to 25 units and progresses to high frequency, large amplitude roll oscillation."

This unpredictability will be discussed further in Section 2.3.1.

This section discusses the aerodynamic environment of the stall/post-stall/spin regime. The important area of inertial coupling and its effect on roll departure and spin is not reviewed, due to its extensive coverage in the literature (References 3).

2.1.2 Analytical Aspects

As with many extreme operating conditions, purely mathematical predictions of behavior of aircraft response in the high angle-of-attack, high-speed region have not proven successful. It is true that developed spin has been mathematically analyzed (Reference 3). However, the flow fields for the transient conditions of post-stall gyrations and of recovery have proven too complex for accurate mathematical description.

Instead, the basis for high angle-of-attack response simulation has come to depend on wind tunnel measurements of the aircraft forces and moments, usually on scaled models. These forces and moments are then used in six-degree-of-freedom computer simulations to describe the behavior by time histories. Such simulations have been used for many years by NASA, and more recently by industry. An excellent summary of these simulation efforts is given in Reference 4.

The use of wind tunnel force and moment data is subject to uncertainties for high angle-of-attack, high-speed conditions. Reference 5 discusses the properties of lateral and longitudinal stability derivatives below the stall angle-of-attack.

Above stall, the concept of a stability derivative (i.e., first partial of the force or moments with respect to α or β) is meaningful, at best, only over a small region, due to nonlinearities. Hence the use of wind tunnel data to give linear approximations to aircraft response is dubious. Chambers (Reference 6) has used this approximation procedure to obtain quantitative stability results, although he emphasizes the need for the computer set of nonlinear forces and moments for actual simulation of aircraft response.

The rotary forces and moments (due to rates of pitch, roll, and yaw) are difficult to measure. The interpretation and use of these measurements is obscure because of the nonlinearity and nonstationarity of the flow.

Compounding these difficulties are the differences in Reynolds numbers and Mach numbers between tunnel and free flight conditions. Hancock (Reference 7) reviews these conditions with respect to swept wing aircraft at high angle-of-attack and transonic speeds.

Clearly then, it is the full scale flight tests which finally define the adequacy of wind tunnel measurements, or more correctly, the modifications required to the wind tunnel data. The degree to which the two sources correlate may be based on characteristic responses of the aircraft. Such responses are discussed qualitatively in the following subsection.

2.1.3 Pitch-Up, Wing Drop, and Yaw Divergence

Three important phenomena associated with separated flow are "pitch-up", "wing drop" and "yaw divergence". These terms describe motions about each of the three axes of the aircraft. The driving moments for these motions arise from aerodynamic flow disturbances associated with regions of separated flow. There may also be interference effects due to asymmetric vortex shedding.

"Pitch-up" is due to a change in sign of the aerodynamic pitching moment derivative, C_{m_α}. Commonly, this is caused by flow separation in the tip region of swept-back wings. As the angle-of-attack is increased, the tips of the swept-back wings tend to stall first (because of the spanwise flow component of the boundary layer). Since the tip region of the wing is behind the c.g., the sudden loss in lift in that region creates a nose-up pitching moment. Another mechanism which creates pitch-up is the effect of the wing and body on the flow conditions at the tail. For example, as the wing tip region separates, the trailing vortex system moves inboard and tends to increase the downwash on the horizontal tail. This creates an additional nose-up pitching movement. In addition, there is a pitch-up contribution from inertial coupling discussed in Blakelock (Reference 35).

Pitch-up is predictable for the F-4 from static wind tunnel tests* (see Figure 2.5). The slope of the moment curve, C_{m_α}, changes sign locally in the region of $\alpha = 15°$. Positive values of C_{m_α} indicate a static longitudinal instability and the aircraft will tend to pitch up to a new equilibrium point (if such exists) where C_{m_α} is again negative.

Pitch-up may also be caused in the transonic regime by shock-induced stall. The aircraft will experience pitch-up if the region of separated flow is aft of the c.g., and "tuck-under" if this region is forward of the c.g. The mechanism of shock-induced stall is an inability of the boundary layer to remain attached due to the added adverse pressure gradient across a shock wave adjacent to the boundary layer. On an airfoil, the chordwise position of the shock is important in determining whether the flow will separate. One of the design goals of the supercritical airfoil is to position the shock forward where the boundary layer is still energetic.

---

*Reference 8

"Wing drop" is due to a sudden change in the rolling moment. It occurs at high angle of attack due to asymmetric progression of stall over the aircraft. Because of the nonlinear and abrupt nature of flow separation, only slight asymmetries in the aircraft or air flow are sufficient to trigger wing drop. Hancock (Reference 7) stresses that wing drop is sensitive to small details in aircraft geometry and states that its exact nature "is impossible to predict and difficult to produce in a wind tunnel".

Aircraft asymmetries have been measured in a wind tunnel (see Reference 8 for example), of course, but these slight asymmetries would vary from aircraft to aircraft.

Wing drop may be associated with "wing rock", a roll oscillation of dutch-roll mode with only slight sideslip angles. It is clear, however, that other factors affect wing rock - as will be discussed in Section 2.4.

"Yaw departure" (or nose slice) is a now well-known characteristic of high angle-of-attack flight. It is a rapid directional divergence leading to large sideslip angles. It arises primarily from negative values of the directional-stability derivative, C_{n_β}. Although not necessarily a high-speed problem, it has been found to be aggravated by high velocities and by the configuration designs of high-speed aircraft.

The yawing (weathercock stability) is the sum of two large contributions, specifically a normally stable moment from the vertical stabilizer and an unstable moment from the fuselage. The wind contribution is small for low angles-of-attack, but asymmetric flow from the wing at high angles of attack is an important consideration.

The mechanism of directional divergence for the F-4 is a combination of adverse sidewash and reduced dynamic pressure at the tail. According to Chambers and Anglin (Reference 6), "The adverse sidewash was generated by the wing-fuselage combination and was related to stalling of the leading-wing panel during

a sideslip at high angles of attack." . An additional factor at high speed would be the reduction in lift-curve-slope of the vertical fin due to compressibility effects.

Reference 9 indicates that for the A-7, a yaw departure mechanism similar to that of the F-4 is believed to exist: "...VAC* investigations indicated that early boundary [layer] separation occurs on the A-7 wing near the leading edge just inboard of the chord extension. Continued inboard expansion of this separated flow region occurs with increased angle of attack until, near the stall, the vertical tail is subjected to a strong vortex flow".

2.1.4 Spin

When an airplane is stalled and the controls fixed, the craft will perform some combination of rolling, yawing, and pitching motion, which, if left uncontrolled, may develop into a characteristic motion called spin. In developed spin, the airplane decends rapidly in a helical movement about a vertical axis at an angle of attack between stall and 90°.

Spin may be divided into three phases (Reference 10)--incipient spin, developed spin, and recovery. Incipient spin is the non-steady state portion of the spin and is also known as the post-stall gyration. Wing rock and nose slice (yaw departure) are observed in this regime. Developed spin involves a balance of aerodynamic and inertial moments and forces. This phase is capable of being analyzed mathematically and correlated with flight tests. Recovery is the response of the spinning aircraft to the proper control inputs. Both incipient spin and recovery are transient conditions, and are more difficult to define analytically.

Extensive analytical effort has been generated on spin and spin.recovery. A recent general spin/recovery analysis is discussed in Reference 11. This analysis minimizes a function of α, β, v, p, q, and r subject to the constraints that $\alpha > \alpha_s$, and that the motion is purely helical. Hence the analysis, by minimizing the functional, solves for the equilibrium, or developed spin con-

*Vought Aeronautics Company

ditions. To investigate recovery, the analysis includes a six-degree-of-freedom simulation with initial conditions determined by the solution of the minimization problem. Several spins and recoveries are demonstrated, but no correlation with flight test is given.

The full six-degree-of-freedom simulation has proved most useful for analyzing and correlating mathematical models to predict spin. Although a brute force method, it has been used extensively by industry and government. Some documented spin programs are from the following companies.

McDonnell-Douglas Company (Reference 12) has done extensive stall/post-stall/spin analysis, principally on the F-4 aircraft. More wind tunnel testing and documented high angle-of-attack flight testing has been done on the F-4 than perhaps any other aircraft. McDonnell has been able to simulate spins and recoveries, although modifications to the wind tunnel data were necessary to simulate the erect spin modes. C_m, C_{ℓ_p}, and C_n were modified by corrections from flight test and by changes necessary to simulate certain spin effects (Reference 14). The resulting pitching moment, C_m, to match spin rates and angles-of-attack was significantly different from the wind tunnel predictions. Damping in roll, C_{ℓ_p}, was found to be highly significant in influencing spin of the F-4, as are all of the rotary derivatives. Reference 14 is an extensive spin study, the purpose of which is to determine a configuration and entry conditions for a non-recoverable flat spin. Many characteristics of spin are simulated, although the emphasis is not on stall/post-stall gyrations.

Northrop Corporation (Reference 13) claims that the spin-resistant characteristic of the F-5 is due to an integration of design, analytical, and tunnel-test approaches. This reference also discusses the effects of Reynolds number and geometry on spin. Again, the gyrations of the stall/post-stall regime are not considered; however, simplified criteria for predicting spin entry are discussed.

Vought Aeronautics Company's experience with the high-wing, low-tailed A-7 and F-8 has been directed to freedom from pitch-up and transonic trim changes (Reference 9). Such a configuration however, produces a large destabilizing directional stability gradient with angle of attack. The Vought A-7 can enter two modes of erect spin. Proper recovery technique requires one-half to two turns. "The airplane will then recover in a steep dive requiring 6,000 to 8,000 feet to achieve level flight." (Reference 9)

In summary, the six-degree-of-freedom simulation, with wind tunnel measurements, has proved useful in analyzing spin and recovery. There has been less attention toward the stall/post-stall region, and less correlation documented in that regime. Developed spin, on the other hand, is simulated and correlated reasonably well.

2.1.5 Discussion of Simplified Spin Mechanism

For a conventional aircraft with unswept wings, the primary aerodynamic driving mechanism of spin is a positive contribution to C_{ℓ_p} from the rolling, stalled wing ("auto-rotation"). This may be seen by examing the lift curve in the stalled region Figure 2.1.

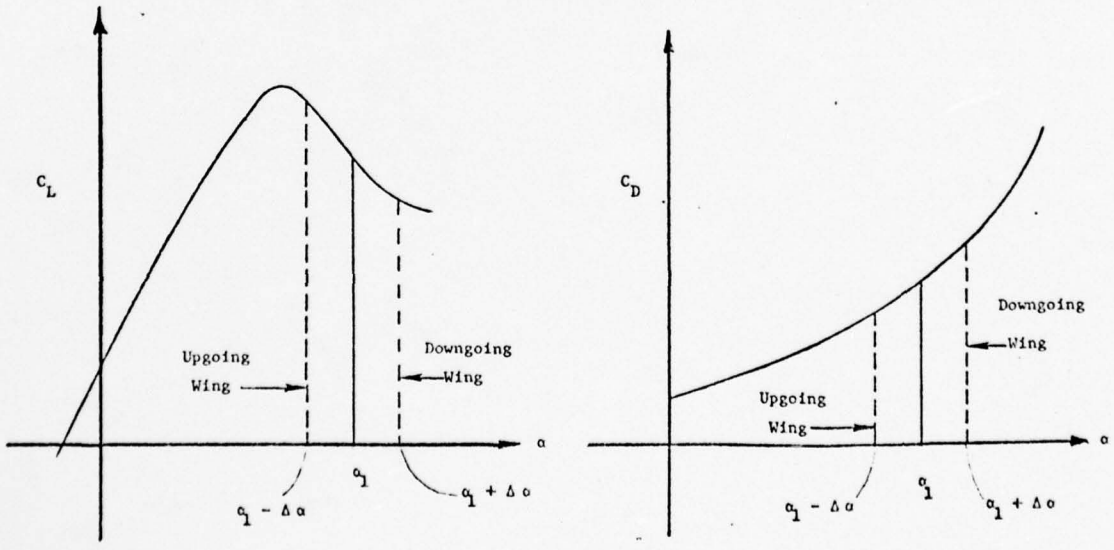


Figure 2.1 Typical Unswept Wing Lift and Drag Characteristics

Suppose the aircraft has an angle-of-attack, α_1. If a roll motion is superimposed, the downgoing wing will see an increased angle-of-attack, $\alpha_1 + \Delta\alpha$, while the upgoing wing will experience a reduced angle-of-attack, $\alpha_1 - \Delta\alpha$. Below stall this would result in greater lift on the downgoing wing (stable), but above stall, it yields less lift. This, coupled with increased lift on the upgoing wing, propels the aircraft to continuous rolling motion. The angle-of-attack difference between the two wings also creates a yawing moment due to drag (see the drag curve, Figure 2.1). The result of these moments is a continuous rolling, yawing motion called spin.

For modern fighter aircraft with swept wings, the mechanism of spin depends less on wing autorotation and more on yawing moments from the wing and fuselage(Figure 2.2). This effect is exagerated if the vertical tail becomes ineffective due to separated flow. The lift and drag curves of a swept-wing aircraft exhibit less change in lift and more in drag at high angles-of-attack:

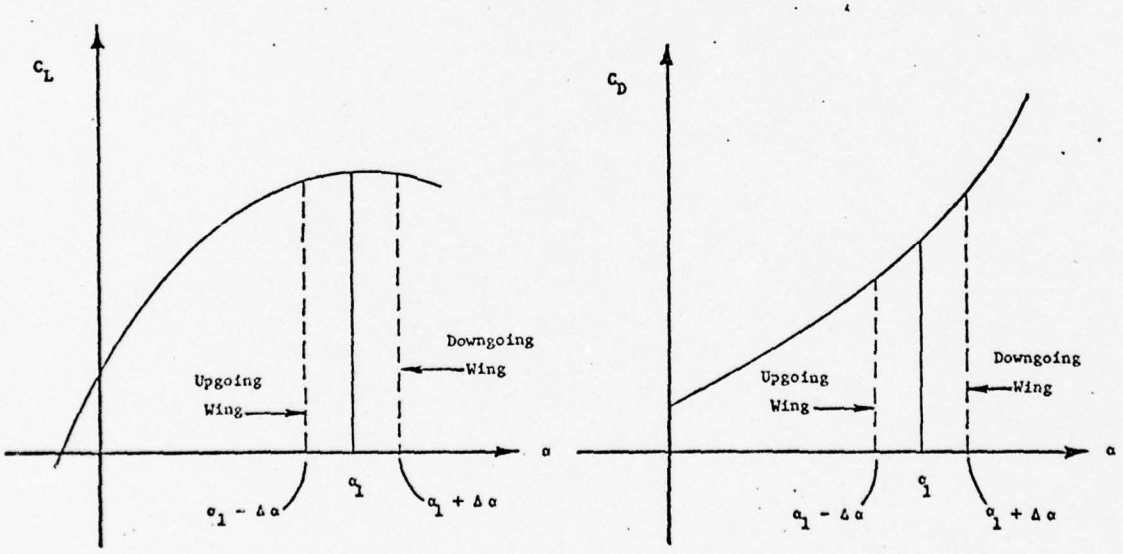


Figure 2.2 Typical Lift and Drag Coefficients for a Swept Wing Aircraft

Thus, for swept-wing aircraft, the basic pro-spin moment is differential wing drag coupled with a destabilizing moment from the fuselage. Increased dynamic pressure on the outside wing creates a pro-spin rolling moment. The mass distribution in high-speed aircraft designs creates an inertia moment which tends to flatten the spin. There is no known way of recovering from a flat spin in some types of aircraft. (Reference 11 presents a spin recovery method of pulsating stabilator inputs which excites an oscillation in α, eventually breaking the aircraft out of the extremely high α [approximately 80°] of flat spin. This technique is shown to yield recovery from flat spin in a computer simulation for a configuration which cannot be recovered using conventional control techniques.)

In the next three sections, the major factors of the stall/post-stall regime are discussed.

2.2 PITCHING MOMENTS AT HIGH ANGLE-OF-ATTACK

As discussed in Section 2.1.3, swept-wing aircraft typically experience tip stall before $C_{L_{MAX}}$ is obtained. This creates a nonlinearity in the curve of pitching moment versus α, which may be described as a reduction in static margin. Figure 2.3 illustrates the shift of the aircraft aerodynamic center, AC1, with no tip stall, to the position, AC2, with tip stall. In general, the larger the sweep, the larger the pitch-up tendency of the wing.

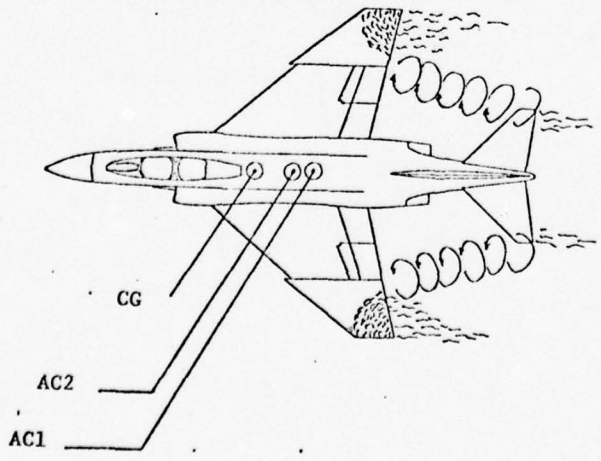


Figure 2.3. Schematic of Effects of Wing Tip Stall

Abzug (Reference 15) points out that the wing contribution may be of lesser importance than the effect of the wing flow separation on the tail surfaces. If the wing tips stall first, the wing vortices shift inboard and increase the tail local downwash for a given airplane lift coefficient. (See Figures 2.3 and 2.4).

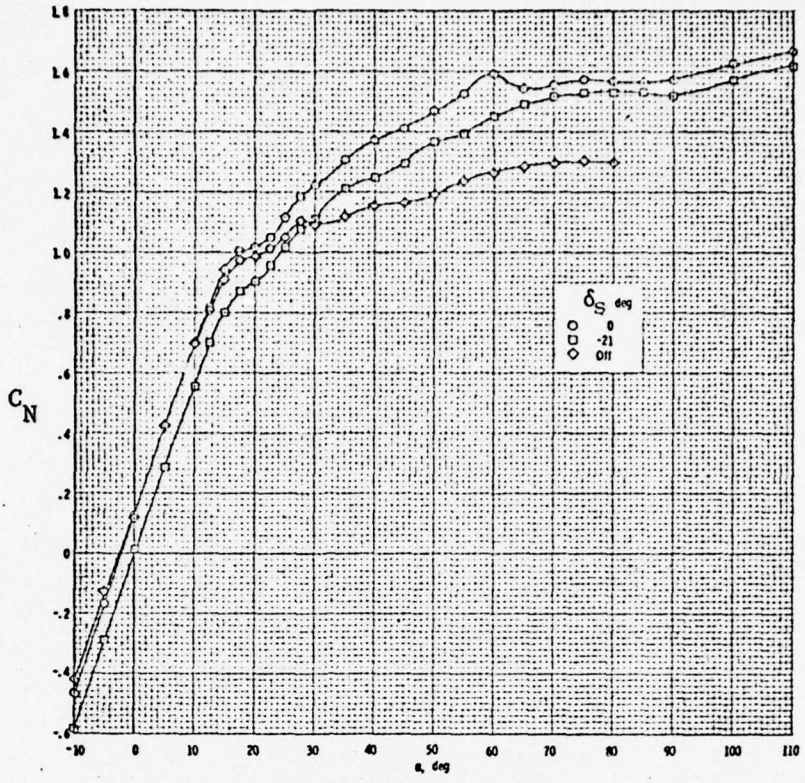


Figure 2.4 Schematic of Flow Redistribution with Tip Stall

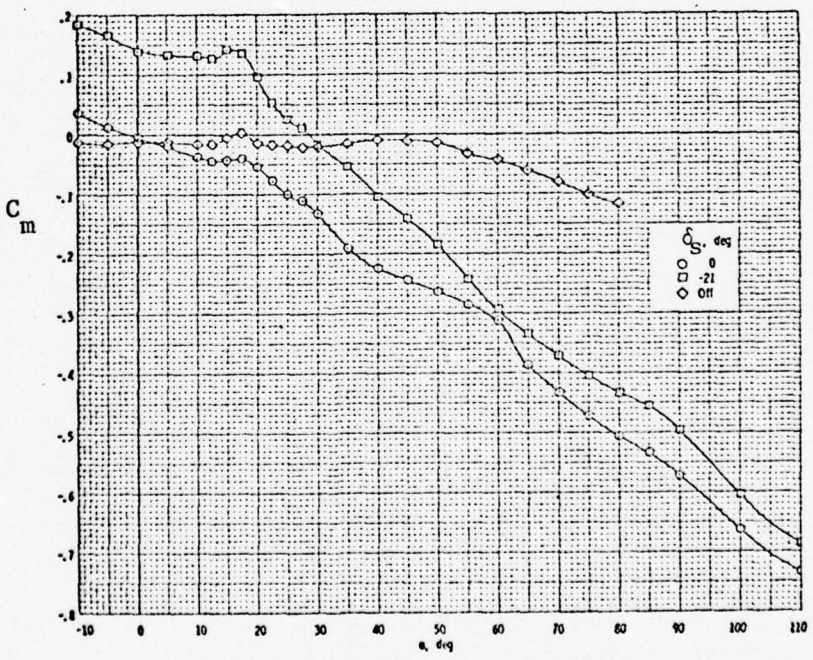
The sum of these effects produces nonlinear C_m versus $-\alpha$ curve in which the nonlinear effects appear before $C_{L_{MAX}}$. Figure 2.5 shows this for an F-4 aircraft (Reference 8). Hence, for an instantaneous angle of attack of about 15°, the slope, C_{m_α}, is zero or slightly positive even though $C_{L_{MAX}}$ has not yet occurred. At this angle of attack there is a destabilizing pitch-up moment.

Stone (Reference 16) has calculated the longitudinal responses caused by this pitching moment nonlinearity. Based on the data reproduced in Figure 2.6 for a 60° swept wing, the calculated and flight motions show good agreement.

The effect of these nonlinear pitching moments on the F-4 is described in Reference 17:



(a) Variation of C_N with α.



(c) Variation of C_m with α.

Figure 2.5 Wind Tunnel Variations of C_N and C_m with α (Reference 8) (Note: $C_N = - C_Z$)

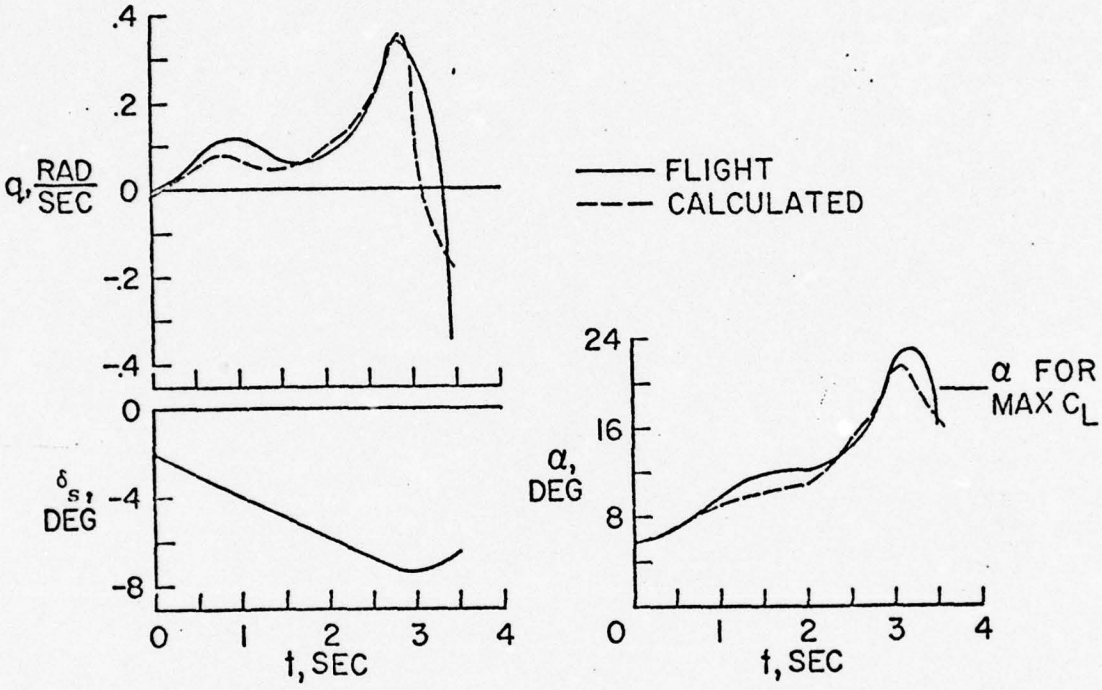


Figure 2.6. Comparison of Flight and Calculated Pitching Motion (from Reference 16)

"The F-4 longitudinal instability condition is demonstrated in Figure 53, Appendix I, (reproduced here as Figure 2.7) for the test aircraft during low Mach number flight. The nose rise is shown by the unstable gradient of stabilator and angle of attack near 8 seconds on the time history. This longitudinal instability, combined with deteriorating control effectiveness near the stall AOA's, led to inadvertent excursions into the region of directional divergence when attempts were made to roll with aileron or rudder at high AOA."

The latter comment is very significant, and is the reason for including the pitch moment characteristic in any study of lateral-direction flying qualities. Before considering this inadvertent entry into stall/post-stall conditions, the aerodynamic environment of these conditions is reviewed.

2.3 ROLLING AND YAWING MOMENTS AT HIGH ANGLE-OF-ATTACK

2.3.1 Roll Moments at High α

The principal contributions to the roll moments are the wing and the vertical tail. Secondary contributions are made by fuselage - wing interference effects.

The basic consideration for the understanding of roll moment at high angle of attack is the wing C_L-versus - α, as introduced in Section 2.1.5. Ellison and Hoak (Reference 5) state that, for wings of moderate-to-high aspect ratios and moderate sweep, the value of C_{ℓ_p} in the nonlinear lift ranges may be estimated by assuming that variations in the lift-curve slope will affect C_{ℓ_p} in the same portions as C_{L_α}. Such a conclusion is based on the large moment arm of wing sections in promoting roll. In fact, one may write (Reference 18)

$$C_{\ell_p} = \frac{- C_{L_\alpha}}{12} \left(\frac{1 + 3\lambda}{1 + \lambda}\right)$$

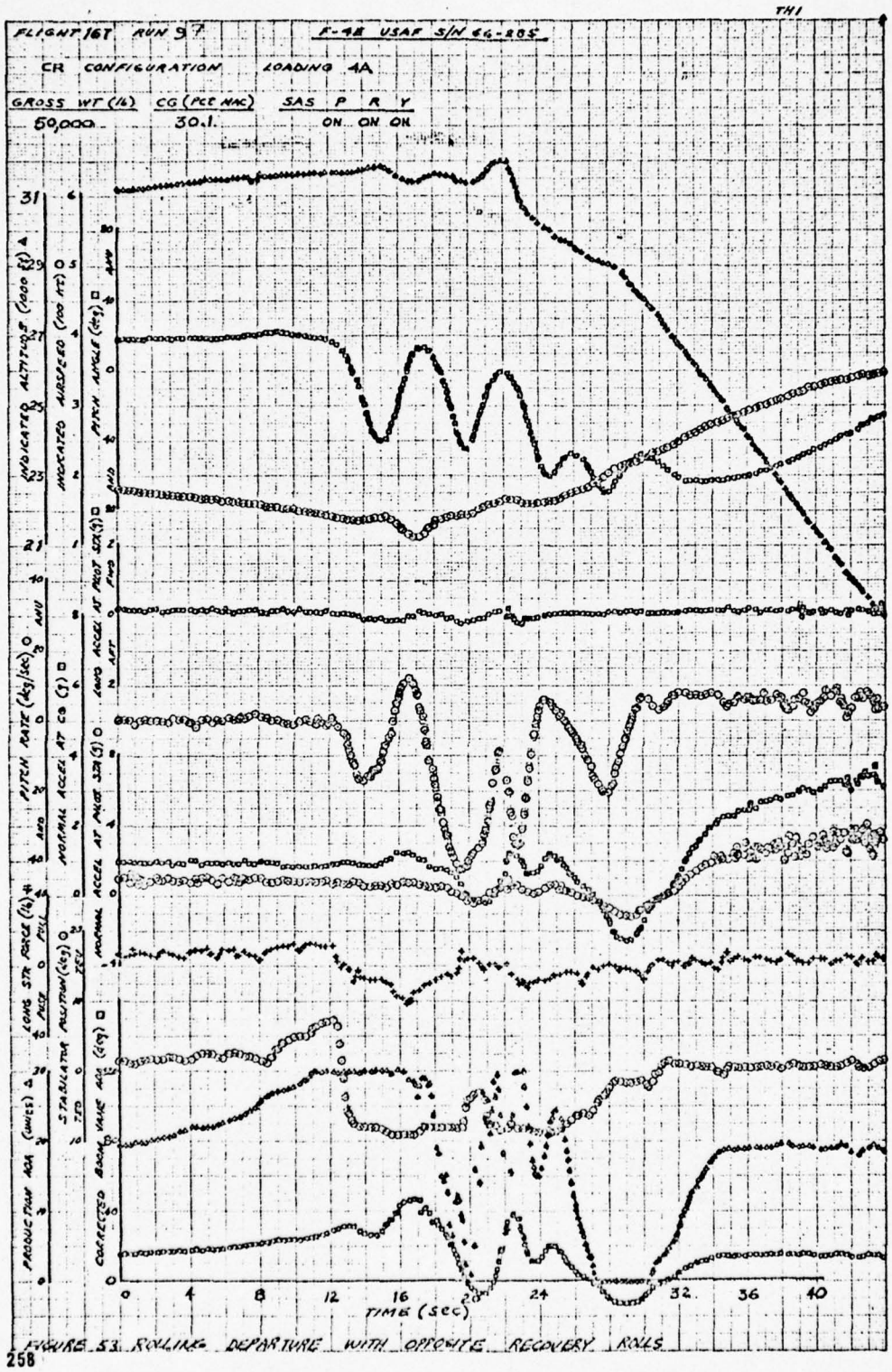


Figure 2.7a Flight Test Recording of Pitch-Up (Reference 17)

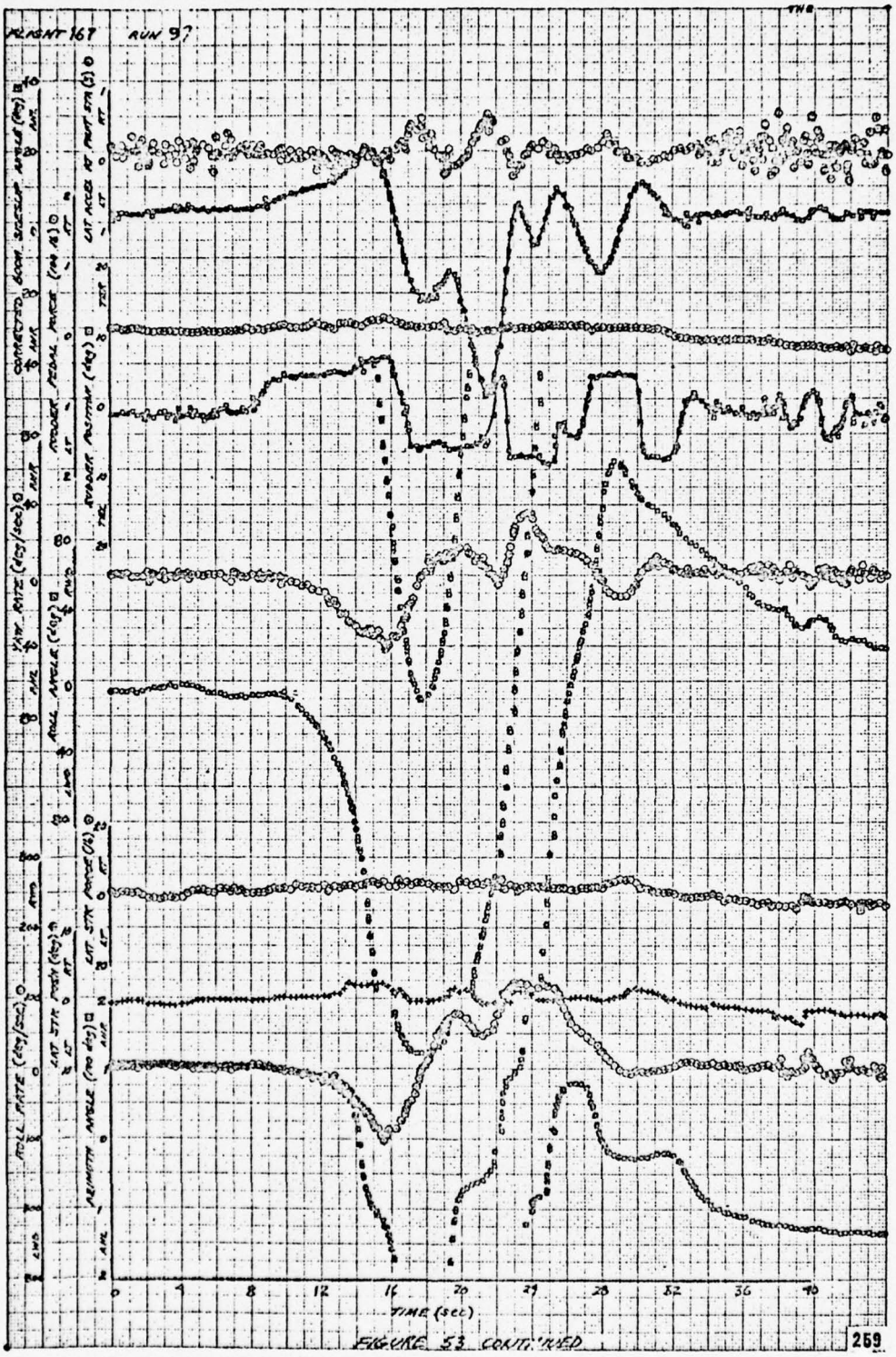
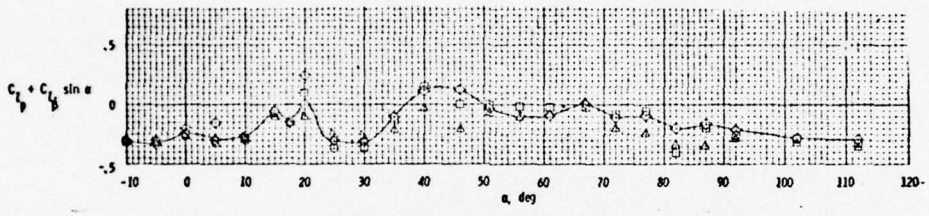


Figure 2.7b Flight Test Recording of Pitch-Up (Reference 17)

where λ is the taper ratio.

There is a correlation between onset of pitch-up and the roll moment instability. Figure 2.8 shows a C_{ℓ_p}, versus α curve from Reference 19. Comparing these with the C_m and C_z curves from Figure 2.5, it is seen that the destabilizing increase in C_{ℓ_p} begins when the C_m and C_z curves indicate inception of stall.



Roll Oscillation Amplitude = $\pm$ 5.0 Degrees

Figure 2.8 C_{ℓ_p} vs α (from Reference 19)

Figure 2.9 is a sketch of typical wing C_L vs α relationship. Depending on geometry, Reynolds number, Mach number, spanwise flow, etc., the post $C_{L_{max}}$ behavior may vary, as indicated by lines A, B, or C. If, for example, a disturbance sets up a positive rolling moment (right wing down), then the left wing C_L decreases to d while the right wing C_L increases or decreases to a, b, or c depending on the particular wing condition. It is seen that if the slope of the pre-stall part of the curve is greater than the negative of the post-stall curve, then the net C_{ℓ_p} across the span is destabilizing. Of course, had the α_o been below that for $C_{L_{max}}$, the C_{ℓ_p} would be stabilizing. It is also seen that a limit cycle type behavior is possible if α lies in the post-stall "bucket" of curve (B). This phenomenon is discussed in Reference 20.

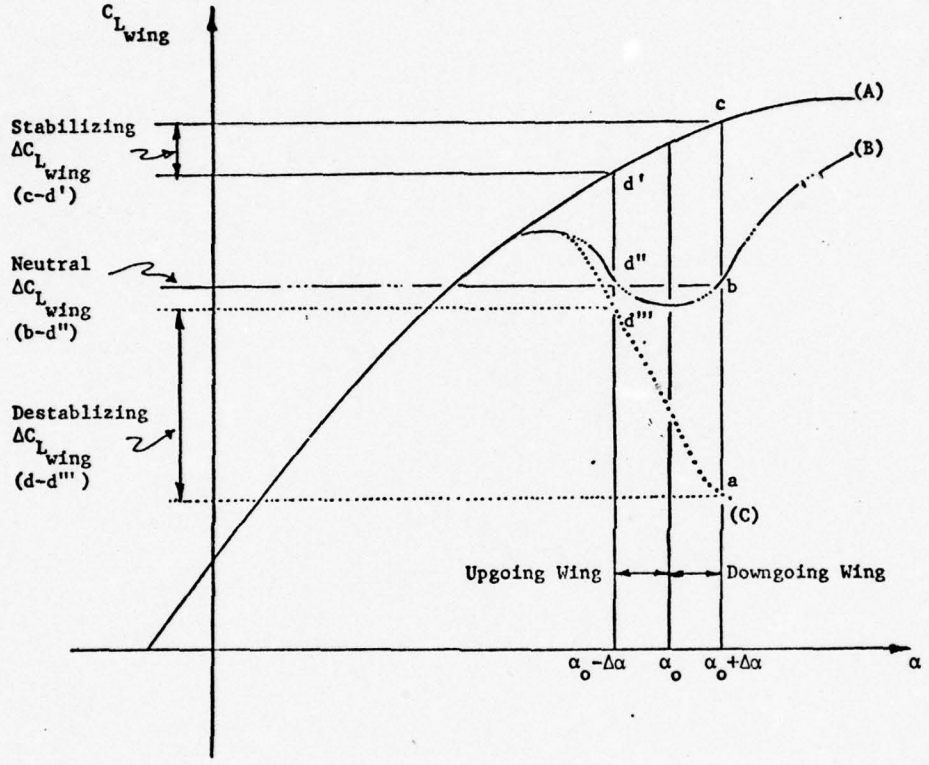


Figure 2.9 Typical Post-Stall Variations of Wing C_L vs α.

A similar argument applies to the effect of wing stall on C_{ℓ_β}, the dihedral effect. Pilots normally rely on a negative value of C_{ℓ_β} to lift the wing moving into the sideslip. However, at high angles of attack, conditions could exist on the leading wing similar to that of A, B, or C of Figure 2.9. The trailing wing would correspond to point 0. The result is a positive C_{ℓ_β} for the leading wing corresponding to A.

Of course, other mechanisms are producing roll moments such as side-forces on the fuselage and tail from the vortices being shed off the stalled wing. The important point is that these vortices are primarily dependent on the stall of the wing and hence on the characteristics of the wing C_L-versus-α curve.

It is concluded that differences in C_L-α characteristics between the two wings are the basis for the unpredictability of asymmetric roll moments leading to wing drop. These differences are due to slight geometrical or flow asymmetries between the wings and only become significant as local separation occurs.

Reference 21 points out that increasing Mach number tends to cause C_{ℓ_p} to be destabilizing at successively lower angles of attack. This is due to the decrease in $C_{L_{max}}$ with increase in Mach number. It is also shown that hysteresis effects are present in C_{ℓ_p} when sweep angle is very small (3.6°) or very large (60°). Figure 2.10 shows the effect of sweep on C_L and C_{ℓ_p}.

The rolling moment due to sideslip is discussed in Reference 22 for subsonic and transonic speeds. However, the results are applicable only for low angles of attack. Chambers, in Reference 6, concludes from tuft studies on the F-4 that leading edge panel stall is the cause for the loss of effective dihedral at angles of attack of approximately 15°. The effect of lift coefficient on C_{ℓ_p} is shown in Figure 2.11.

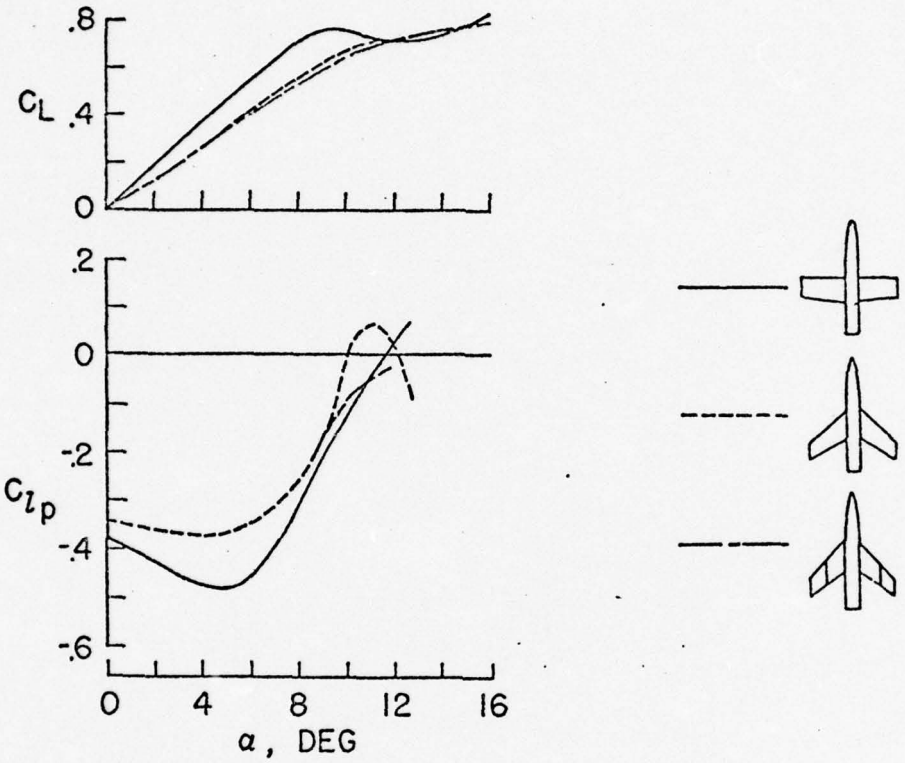


Figure 2.10 Effects of Sweep and Wing Fences on Roll Damping. (From Reference 16)

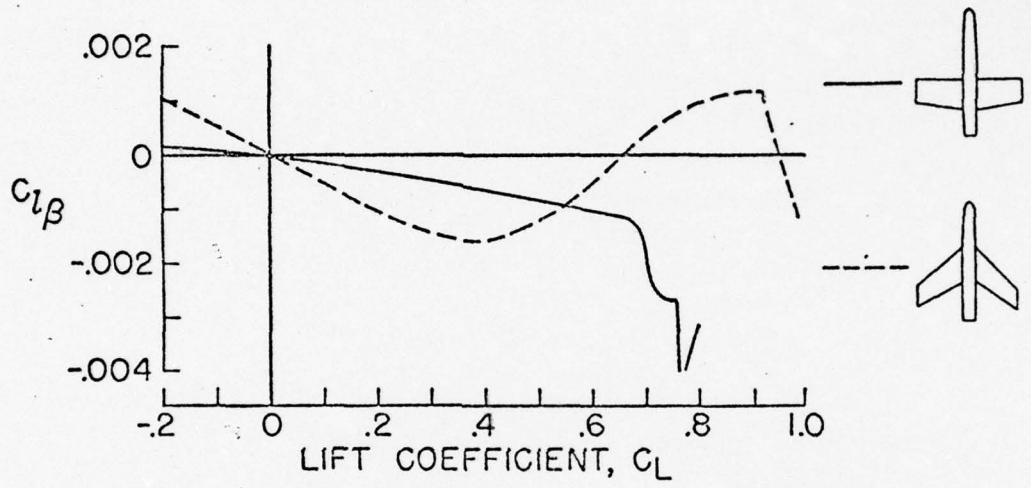


Figure 2.11 Typical Effects of Wing Sweep on the Rolling Moment Due to Sideslip. (From Reference 16)

2.3.2 Yaw Moments at High Angles-of-Attack

Yaw moments have been extensively studied at high angles of attack. Such moments are known to be a primary cause for yaw departure and entry into flat spins.

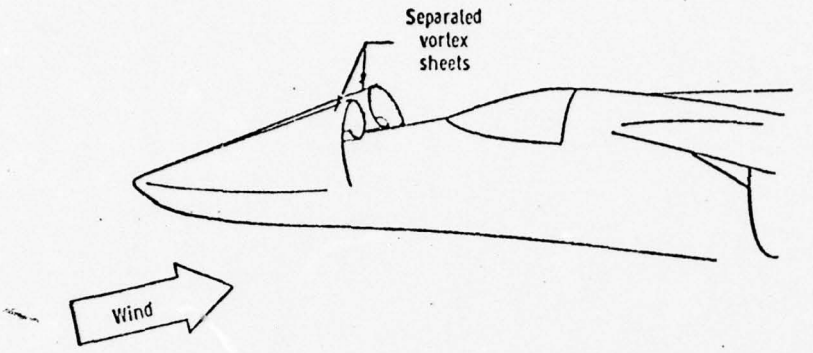
Both sweepback and the decreased aspect ratio of modern designs, have resulted in a decrease in lift-curve slope and an increase in the stall angle-of-attack. Thus the vertical tail must maintain stability through a large range of angle of attack. The disturbed flow from the wing and fuselage at the larger angles of attack, is, however, generally such as to reduce the vertical tail effectiveness, and hence the directional stability.

Some factors responsible for the loss of high angle-of-attack directional stability are:

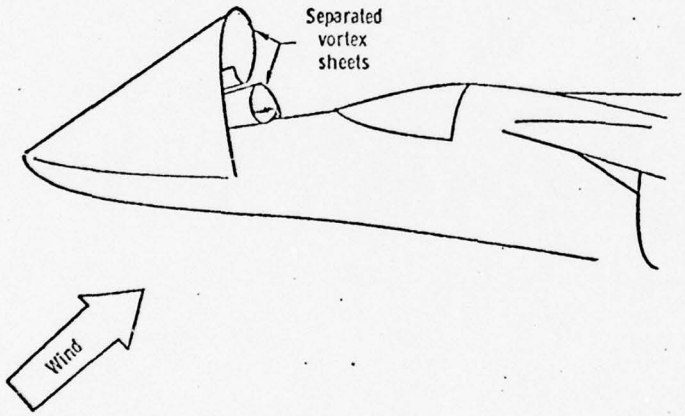
(a) Strong vortex shedding from sharp nosed fuselages (References 23 and 24). Figure 2.12 shows this effect for an F-111-type nose. Reference 17 attributes the differences in spin characteristics of the F-4E from those of the F-4C or F-4D to the increased length and different shape of the F-4E nose.

(b) Adverse sidewash interference on fuselage afterbodies and vertical tails associated with swept-wing fuselage combination in yaw (References 6 and 25). Figure 2.13 is an example of the effect of stabilator flow separation on the vertical fin for the F-4 (Reference 12). C_{n_β} is further degraded by blanketing of the vertical tail by the wake (reduced dynamic pressure) of the fuselage and the wing.

Aeroelastic effects on the lateral moments become significant only at supersonic speeds (Reference 15).



(a) Low angles of attack.



(b) High angles of attack.

Figure 2.12 Sketches of Separated Vortex Sheets on Fuselage Forebody (from Reference 24)

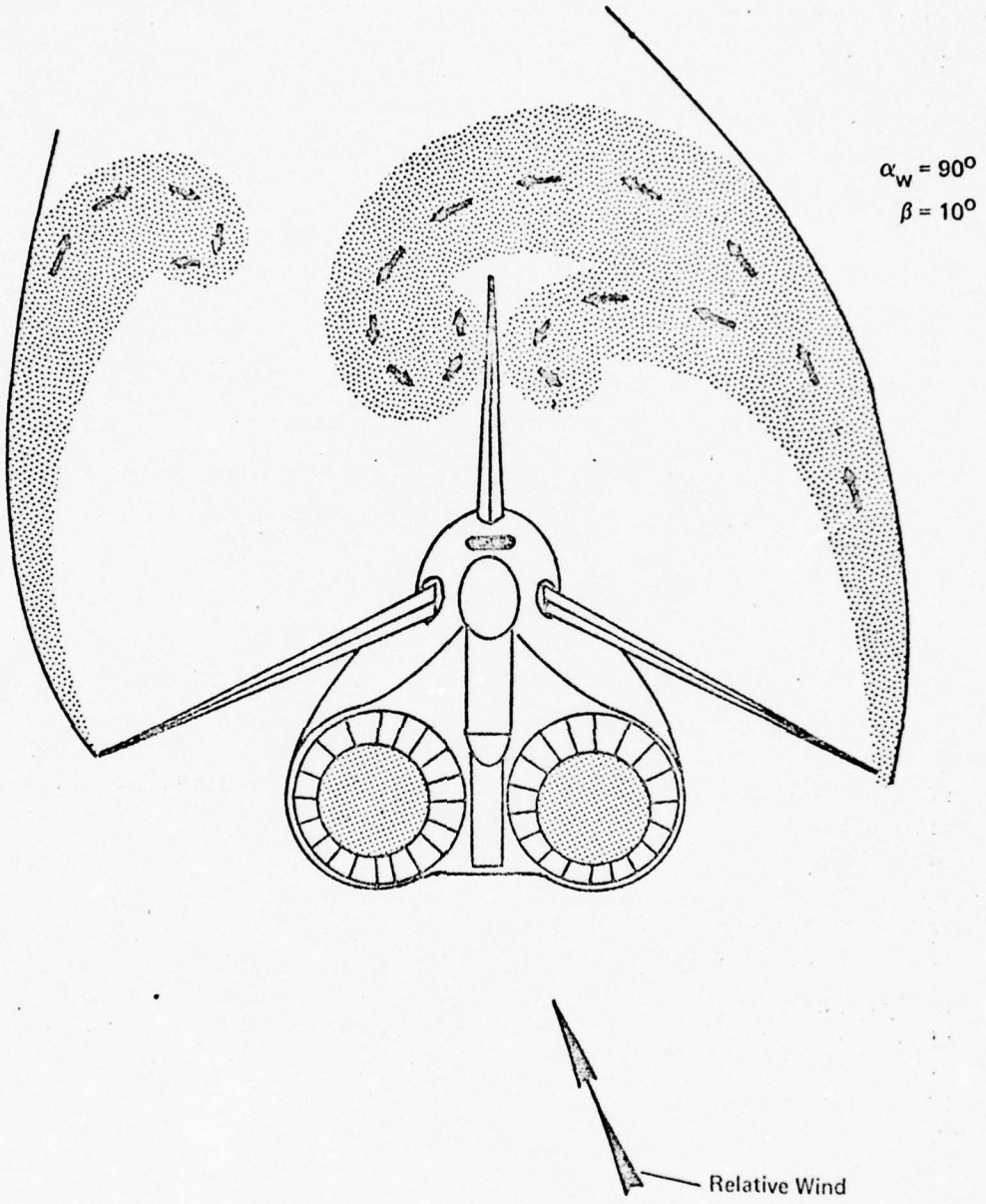


Figure 2.13 Asymmetric Vortex Pattern About Vertical Tail. (from Reference 12)

A well-documented study of the effects of configuration elements on the yawing moment coefficient C_n for the F-4 is given in Reference 6. Wind tunnel tests show an abrupt change in the yawing moment coefficient between an angle of attack of 20° and 25°*. The abrupt nonlinear change in C_{n_β} is shown in Figure 2.14 for various vertical tail size modifications. Figure 2.15 shows the effects of other F-4 configuration changes. It is seen that the wing has little effect on C_{n_β} and that it is primarily the wing-fuselage combination that causes the large nonlinear variations. Tuft studies are used to verify that the destabilizing effect of the wing-fuselage-induced sidewash over the fuselage is increased by leading wing panel stall in aircraft sideslip.

It is concluded that the loss of directional stability results from a combination of an adverse sidewash region at the rear of the airplane and a reduced dynamic pressure at the vertical tail location. The adverse sidewash is generated by the wing-fuselage combination and is related to stalling of the leading wing during sideslip. Figure 2.16 shows the improvement in C_{n_β} resulting from a drooped leading edge.

The sharp-nosed fuselage effect has been seen on the F-111 (Reference 24) as a nonrepeatable variation in C_n at angles of attack of 30° and higher. This seemingly random variation was confirmed to be due to asymmetric flow separation off the nose. The sense of the asymmetric moment was established by slight geometric or aerodynamic asymmetries and could be controlled by nose strakes. The time-varying randomness of the C_n moments is similar to that experienced in missiles, as discussed most recently in Reference 26. The effects of such yaw moment sensitivities tends to make wind tunnel correlation with free flight tests difficult at very high angles of attack.

---

* See also figures C.25 and C.26 of Appendix C.

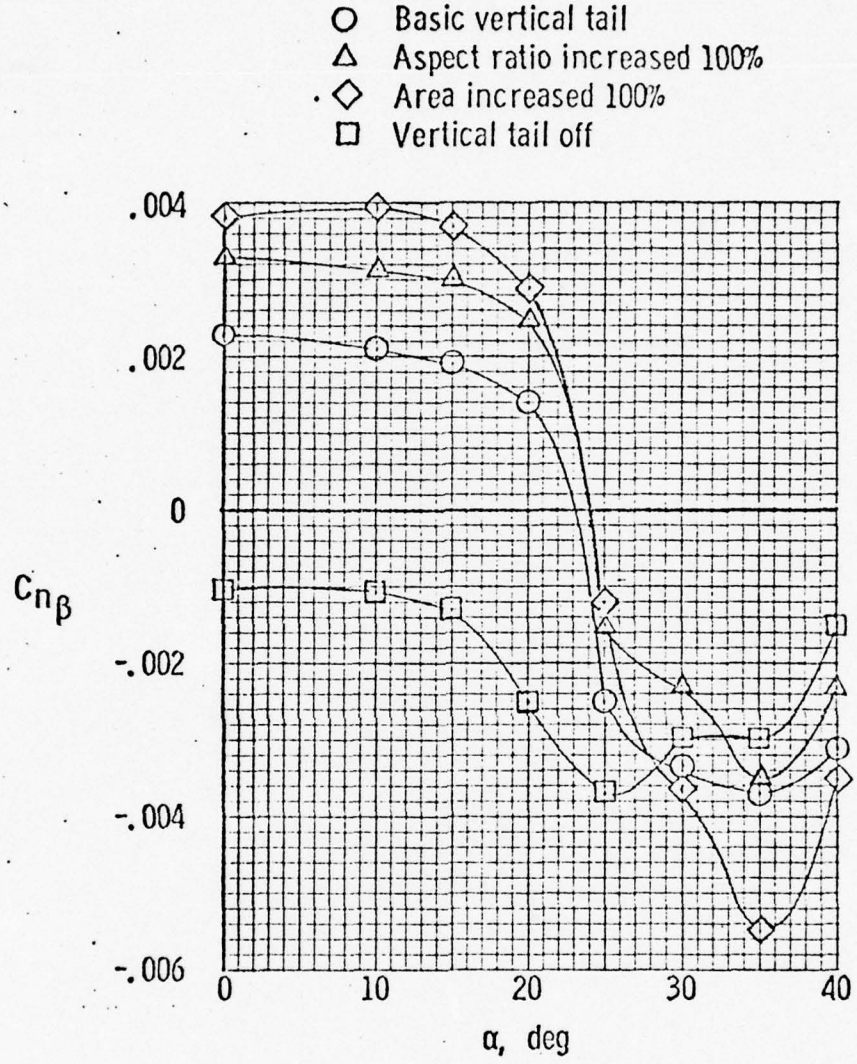


Figure 2.14 Effect of Vertical Tail Modifications on C_{n_β}. (from Reference 6)

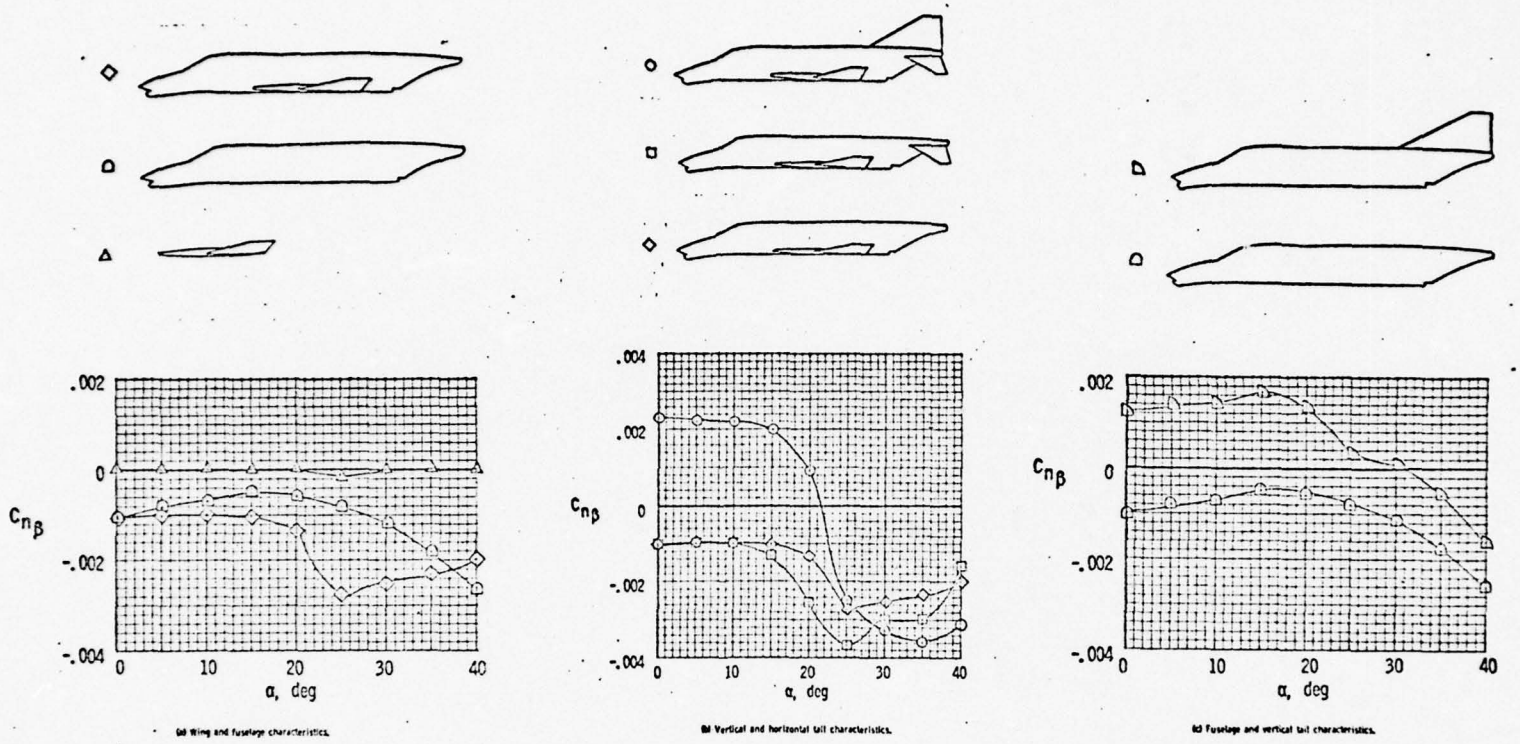


Figure 2.15. Effect of Configuration Changes on F-4 Yawing Moment With Respect to Sideslip (from Reference 6)

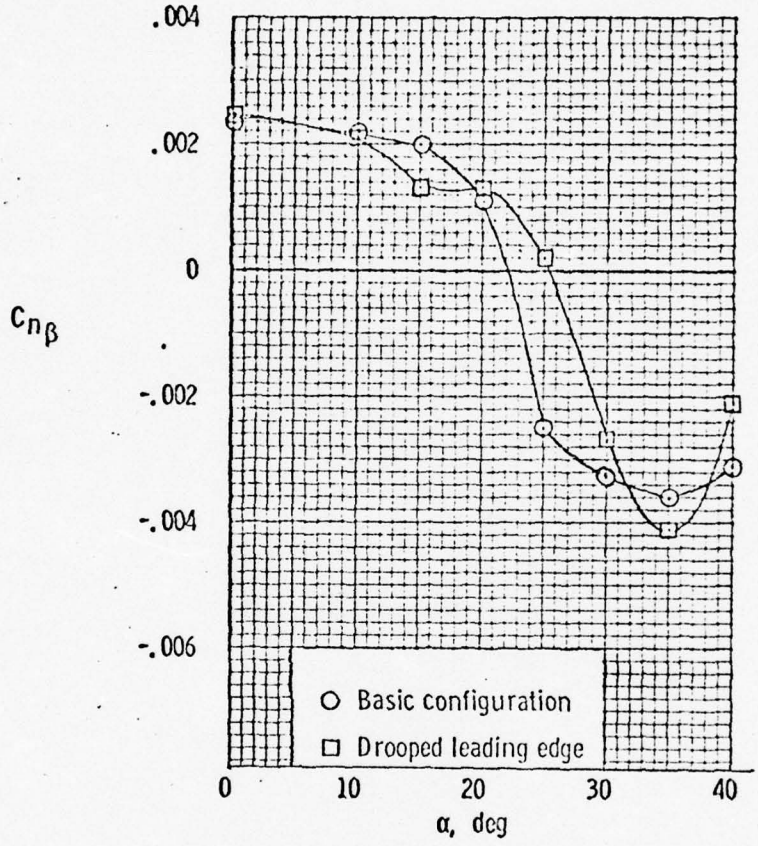


Figure 2.16. Effect of Drooped Leading Edge on Yawing Moment With Respect to Sideslip (from Reference 6)

In summary, wind tunnel tests have demonstrated the nonlinear behavior of critical lateral-directional derivatives at high angles of attack. These nonlinearities originate with wing stall, and interactions of fuselage and wing vortices with the airframe components. Wind-tunnel evidence further demonstrates that these nonlinear effects are sensitive to Reynolds number, Mach number, and airframe geometry.

As discussed in Section 2.2, the nonlinearity in C_{m_α} can lead to inadvertent entry into stall/post-stall angles of attack, where the lateral direction moments become nonlinear. An example of this for the F-4 is described in Section 2.2. Figure 2.17 from Reference 16 shows a calculated, inadvertent entry into a critical yawing moment condition. Once the stall angle of attack has been exceeded, several types of behavior may occur. These are discussed in the following section.

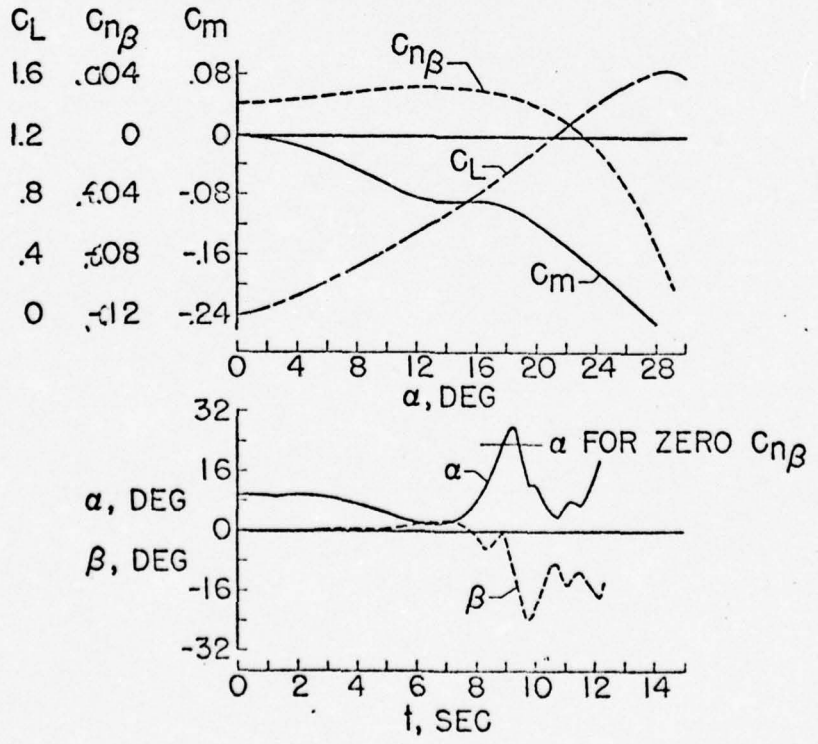


Figure 2.17 Combined Effects of Pitch-Up and Directional Divergence at Large Angles-of-Attack. (From Reference 16)

2.4 "WING ROCK" AND "DEPARTURE"

2.4.1 Flight Test Occurrence

At high angles of attack, swept-wing fighter aircraft have experienced "wing rock," a lightly damped or unstable oscillation, primarily in roll, with a period of several seconds. There is no well formulated physical mechanism for this motion; however, most sources describe it as a lightly-damped Dutch-roll mode. For subsonic speeds, it occurs at a sufficiently high angle-of-attack that much of the aircraft experiences separated flow. Thus the classical linear analysis of Dutch-roll must be modified to account for nonlinearities.

Of a more dangerous nature is "departure," a term used to describe the abrupt yawing motion of spin entry.

Several studies of these phenomena have been performed, both in flight and in model tests. The F-4 is again the most thoroughly studied aircraft. Excerpts from these various studies are included below to indicate the type of aircraft motions experienced at high angles-of-attack.

Reference 27 is the Category II stability and control evaluation of the F-4E aircraft. The following quote (page 28) describes wing rock and indicates that SAS had little effect on this motion:

> At high angles of attack (outside the normal operational envelope) the Dutch roll mode was undamped and/or divergent. The undamped data... were obtained during what is commonly referred to as wing rock which generally occurred at AOA's between 24 and 30 units. The wing rock was encountered with SAS either on or off and maximum bank angle excursions were as high as ±40 degrees. The roll SAS had little or no effect on reducing these oscillations and increased the AOA at which wing rock became divergent. The ratio of bank to yaw (approximately 3) remained unchanged with SAS engagement.

Air Force flight tests of the F-4E, Reference 17, present both qualitative and quantitative descriptions of pre-departure phenomena in the low Mach number cruise condition:

> For the clean loading, lateral-directional stability breakdown was usually observed to begin near 22-24 units (AOA) in the form of wing rock, an unstable dutch-roll oscillation. Examples of wing rock are presented in figures 16 and 36, Appendix I [Figures 2.18, 2.19 in this report]. As AOA was further increased, the oscillations, as viewed by the pilot, progressed from a primarily roll motion to excursions in yaw (nose slice) ....For an angle-of-attack range from 20° to 35°, directional instability increased, and the nose slice became the indication of impending departure.

Chambers and Anglin (Reference 6) report the results of flight tests for the F-4 as an introductory section to their work on lateral and directional stability characteristics. This discussion of flight data is reproduced here:

> The directional divergence exhibited by the airplane at high angles of attack is illustrated by the time histories presented in Figure 2 [Figure 2.20 in this report]. Shown in Figure 2 are flight recorder traces of the major flight variables and control-surface deflections during an accelerated stall at 25,000 feet (7620 m.) with the airplane configured for cruise (M = .4). Unfortunately, there is no record of yaw angle or yaw rate. The maneuver was initiated by rolling to a 60° banked turn to the left. Angle of attack was then increased at an approximately constant rate. The normal acceleration trace indicates airframe buffet occurred at angles of attack as low as 10°. At about 38 seconds the magnitude of the normal acceleration trace starts to decrease, even though angle of attack is increasing, thereby indicating major stall. The angle-of-attack at this time was about 18°; this value should be remembered when analyzing the force test results presented subsequently.

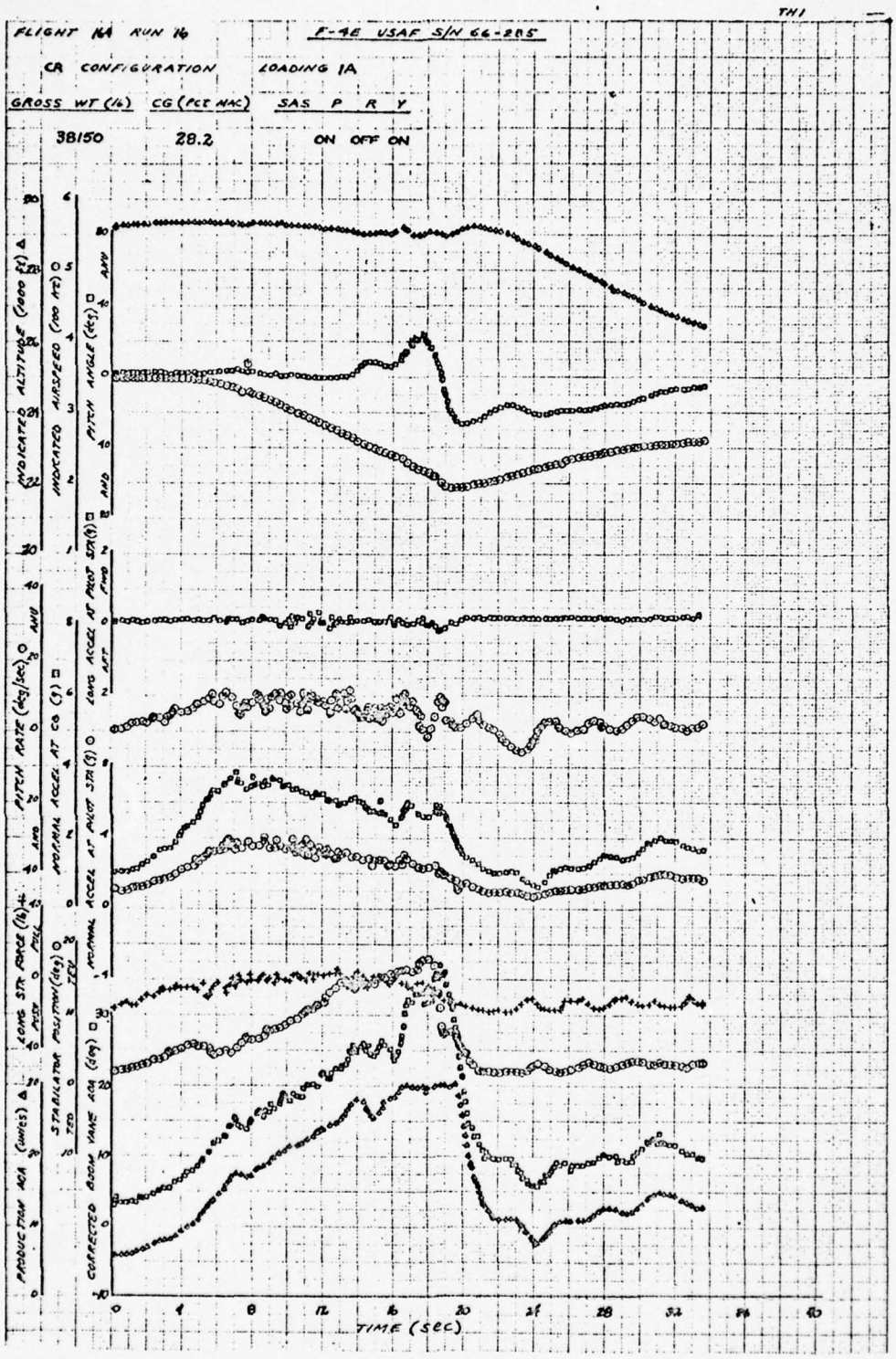


Figure 2.18 Rolling Departure from a 4g Right Turn (from Reference 17)

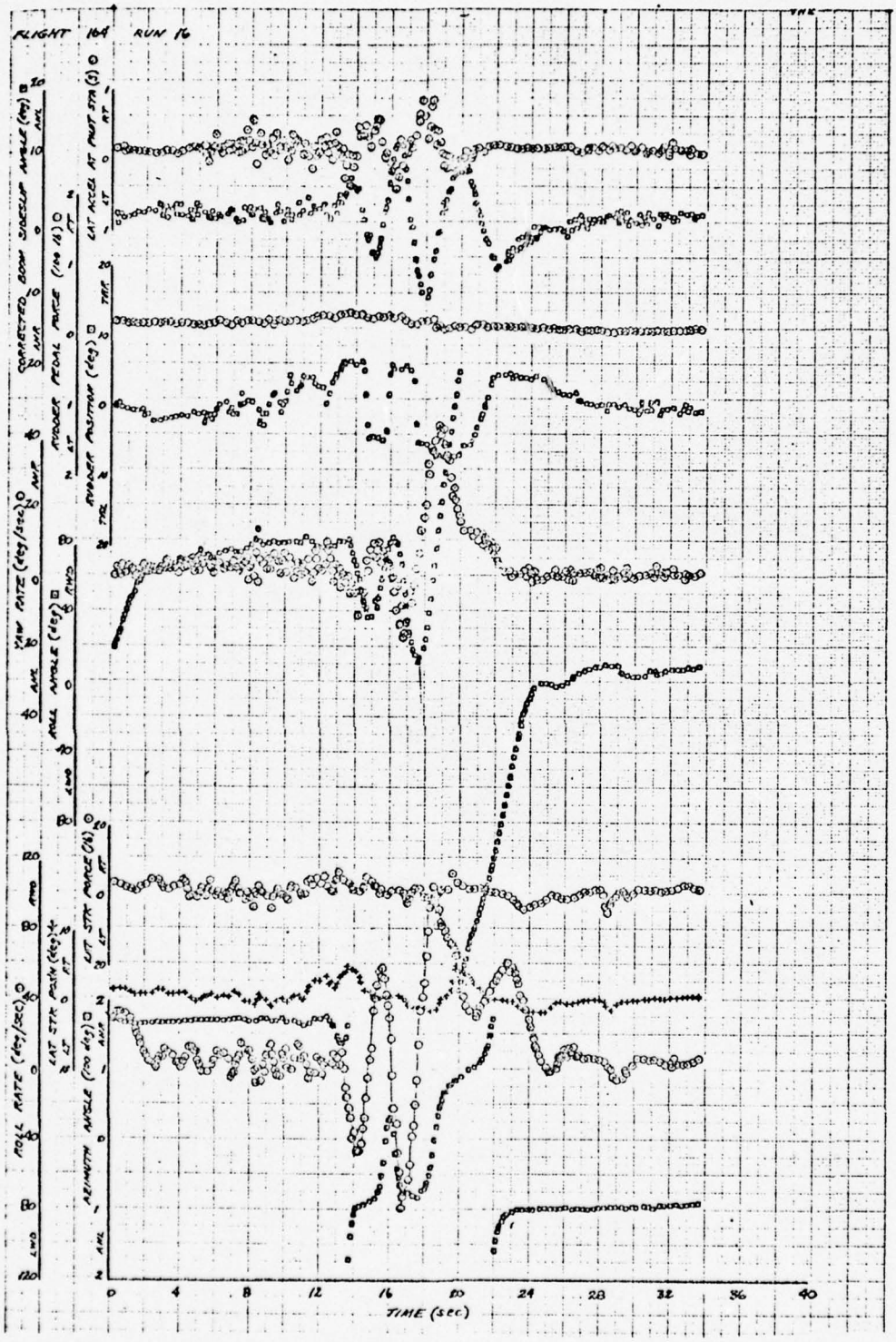


Figure 2.18 (continued)

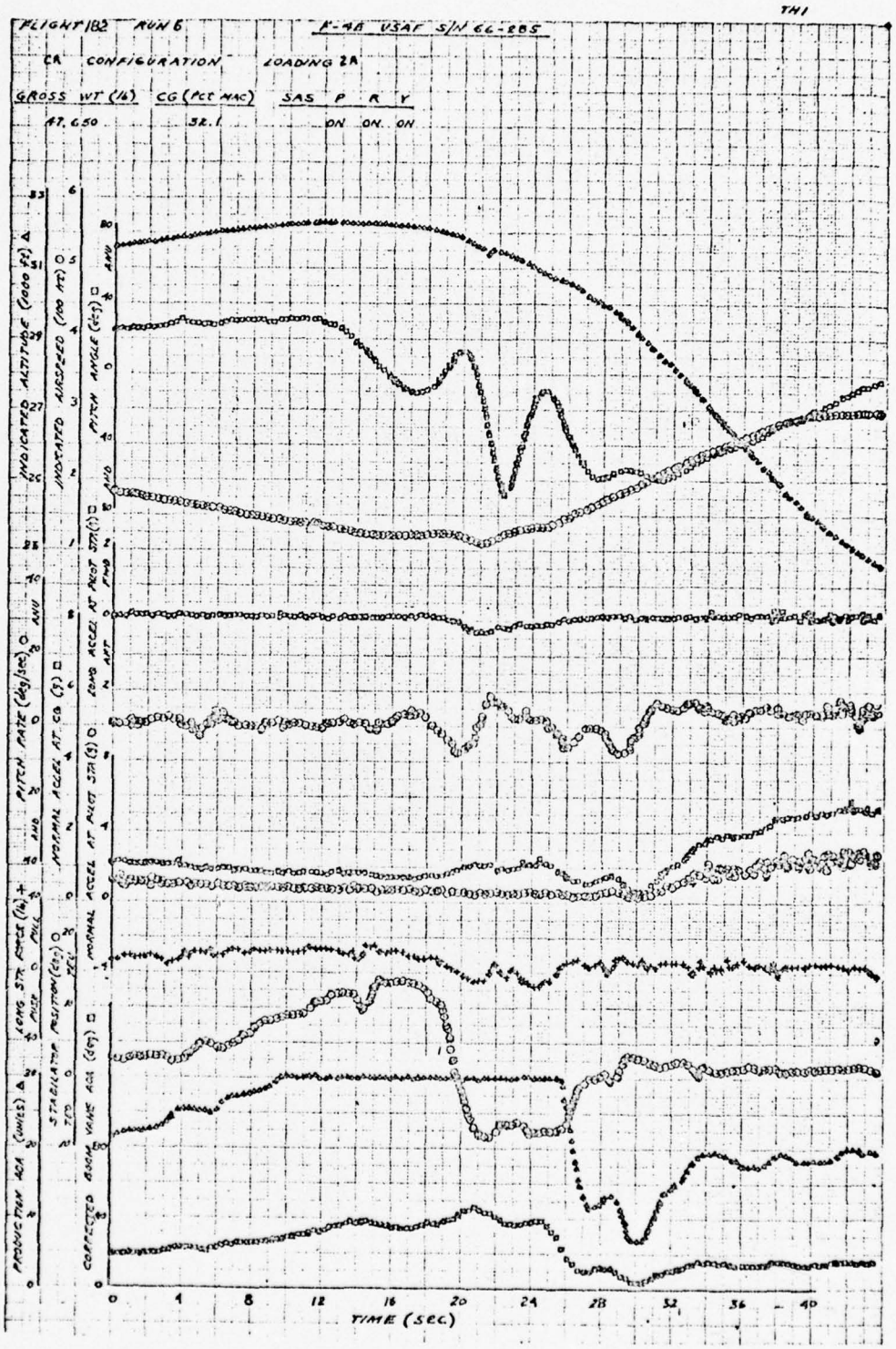


Figure 2.19 Rolling Departure and Recovery Rolls
(from Reference 17)

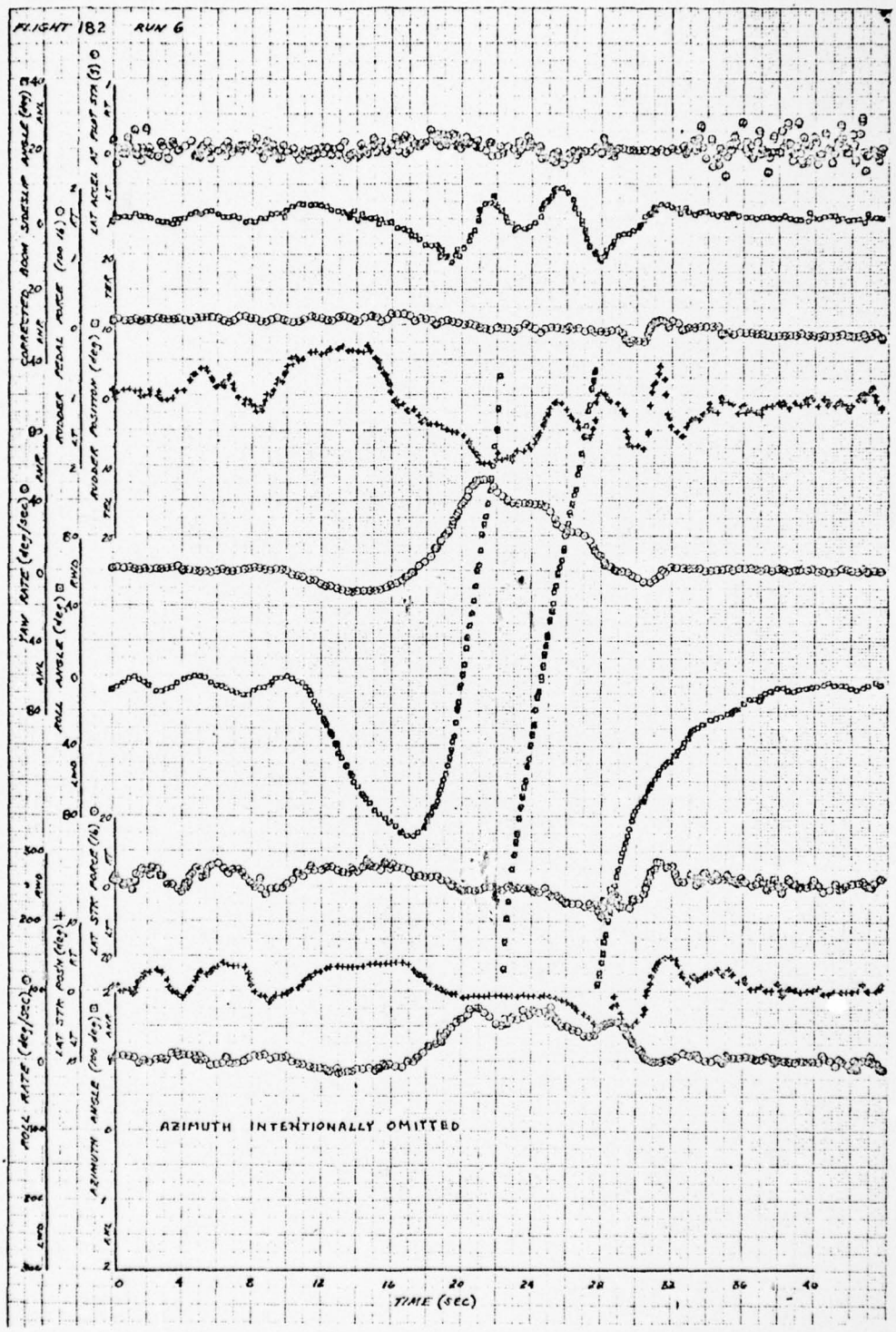
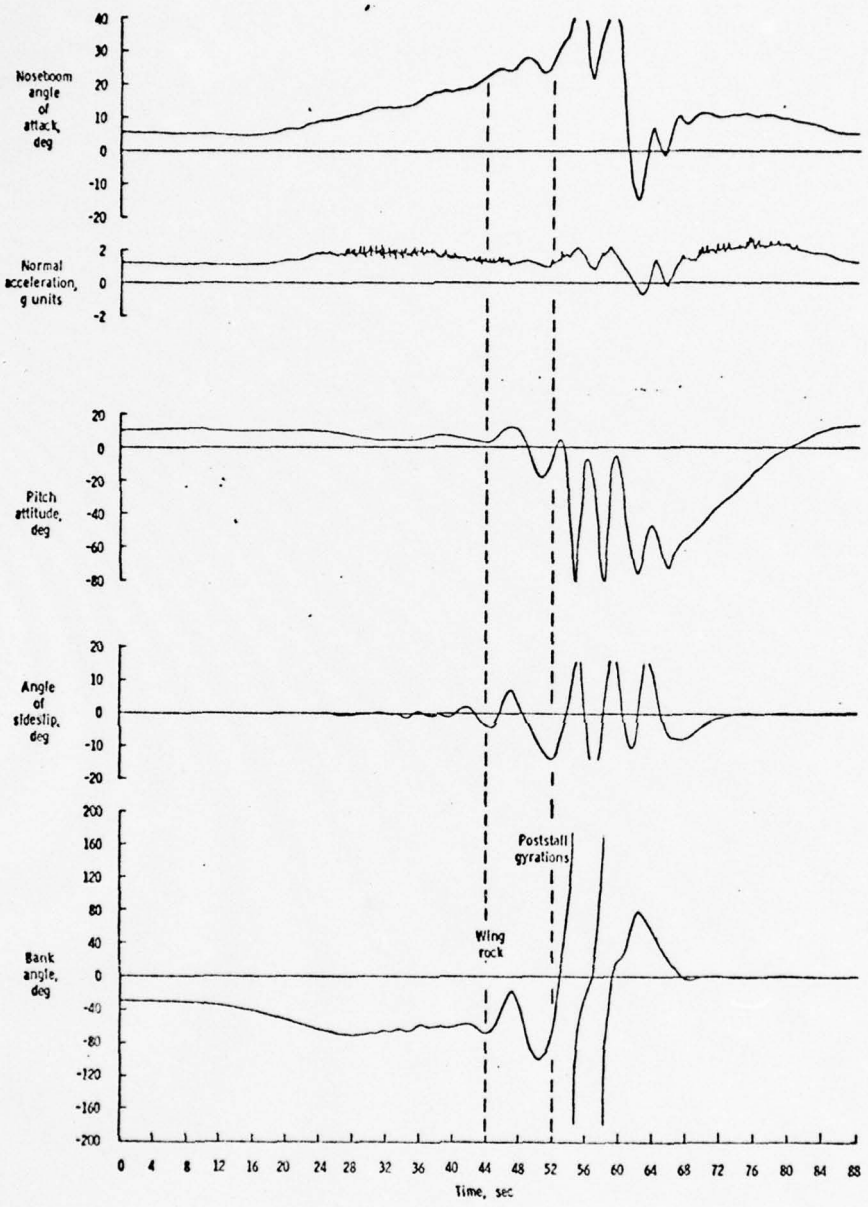
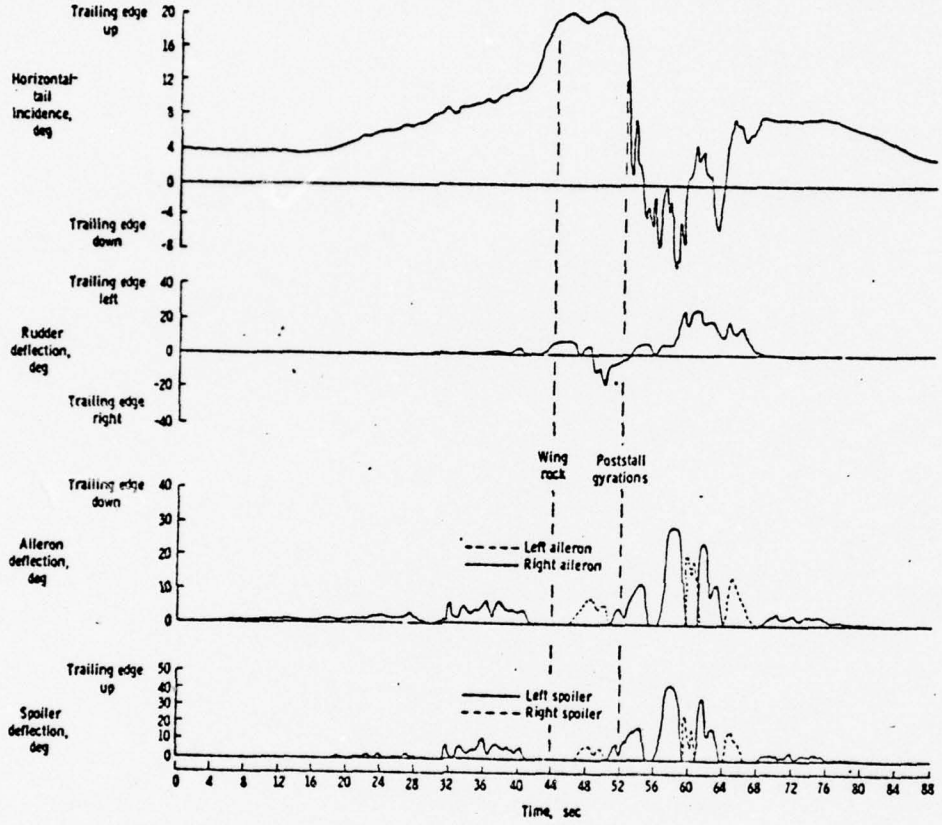


Figure 2.19 (Continued)



(a) Flight variables.

Figure 2.20 Time Histories of Directional Divergence Encountered in Actual Flight. (Reference 29)



(b) Control-surface deflections.

Figure 2.20 --Concluded.

> As the angle of attack increased further, lightly damped lateral oscillations about the longitudinal body axis (termed "wing rock") became noticeable. At about 44 seconds severe wing rock was experienced; at about 50 seconds the oscillation diverged violently and the aircraft entered a 2-1/2-turn spin to the right... The angle of attack at the time of directional divergence was between 20° and 25°; this range of angle of attack should also be remembered for subsequent reference."

These three references are typical of the descriptions of "wing rock" and its relationship to departure. However, it is recalled from Section 2.1 that the F-4J pilot handbook cites the unpredictability of wing rock occurrence. Reference 17 found that wing rock was repeatable for one aircraft in the Power Approach (gear down, flaps down) Configuration. Note that the extension of flaps in Power Approach Configuration allows the aircraft to go to a higher angle of attack before incurring instabilities due to wing flow separation.

The transonic flight regime ($M > .8$) is characterized by wing rock onset at lower angles of attack than in the subsonic regime. At transonic speeds, the intensity of wing rock increases with angle of attack and the frequency is higher than in low speed flight. Such effects may be related to shock separation.

The flight traces of Reference 17 display wing rock and show its relationship to departure. These results are discussed in more detail in Appendix D . Basically it was found that wing rock depended on the configuration. In the Power Approach Configuration, wing rock was slightly unstable (Figure 12 of Reference 17), while in the Cruise Configuration, only one or two cycles were seen before departure occurred. The latter type of motion is called "pre-departure wing rock" to distinguish it from the slower, more highly damped wing rock of the PA Configuration.

2.4.2 Prediction of Wing Rock and Departure

Qualitatively, it is concluded from the cited references and the flight tests that the phenomena of "wing rock" is like a lightly-damped Dutch roll in which the roll motion predominates. This roll oscillation is triggered by the asymmetrical roll moments which produce "wing drop." As the angle of attack is increased, the same basic Dutch-roll-like motion becomes predominantly yaw, eventually becoming unstable as a yaw departure.

Chambers (Reference 6) has explored this aspect by analyzing the linearized lateral-directional equations of the F-4 and has substantiated that wing rock and departure may be associated with the Dutch roll mode - with wing rock predominating at lower pre-stall angles of attack and departure at higher angles of attack. He further concludes that directional divergence can be predicted by the parameter $(C_{n_\beta})_{\text{dynamic}}$. This quantity, which involves* C_{n_β}, C_{ℓ_β} and α, determines the sign of the s^2 coefficient in the characteristic equation of the lateral dynamics. Although usually used to predict spin, Chambers concludes that $(C_{n_\beta})_{\text{dynamic}}$ also predicts the angle of attack for yaw divergence. Weissman, in Reference 27, has recently correlated C_{n_β} with spin susceptibility for several aircraft. Such criteria are indeed useful for predicting critical regions of stall/post-stall responses. However, they are obtained from approximations to very nonlinear phenomena and cannot be classified as sufficient conditions for spin entry.

Criteria based on the nonlinear aspects of stall/post-stall aerodynamics have been investigated by Ross and Beecham in Reference 28. These criteria are developed by a modification to the Krylov and Bogoliuboff method in which the assumption that frequency and amplitude during a

---

* $(C_{n_\beta})_{\text{dynamic}} = C_{n_\beta} - \frac{I_z}{I_x} C_{\ell_\beta} \sin \alpha$

cycle do not change is removed. Using this technique, it is found that the lateral-directional equations with a nonlinear C_{n_β} will give rise to a limit-cycle oscillation. This oscillation was correlated with a digital simulation known to predict the behavior of an HP 115 aircraft (British), and the criterion was found to give good agreement. It is concluded that the nonlinearity prevents the Dutch-roll mode from becoming divergent as the linear approximation would predict.

The value of such analytical treatments is high. It is true that they do simplify the model, but it is useful to know if such simplifications give qualitative or quantitative predictions of the complete system. Of course, these analyses require accurate aerodynamic models just as do the digital simulations. As discussed previously, the aerodynamic coefficients of interest are difficult to specify for the stall/post-stall regime.

Documented digital simulation of wing rock is sparse. Reference 36 shows a calculated predeparture wing rock. This used a fixed-base simulator at NASA/Langley. A description of this simulator is given in Reference 29. The control inputs are made by a pilot in a fixed-base cockpit. These inputs are fed to a nonlinear, six-degree-of-freedom computer program which includes tables of the aerodynamic forces and moments as functions of α and β. Figure 2.21 presents the pre-departure wing rock which was achieved with this system. It correlates with Figure 2.20 of Section 2.4.1. However, modification to the data tables (notably a reduction in magnitude of C_{ℓ_p}) was necessary to obtain this correlation.

The time history of Figure 2.21 points out a problem with simulation

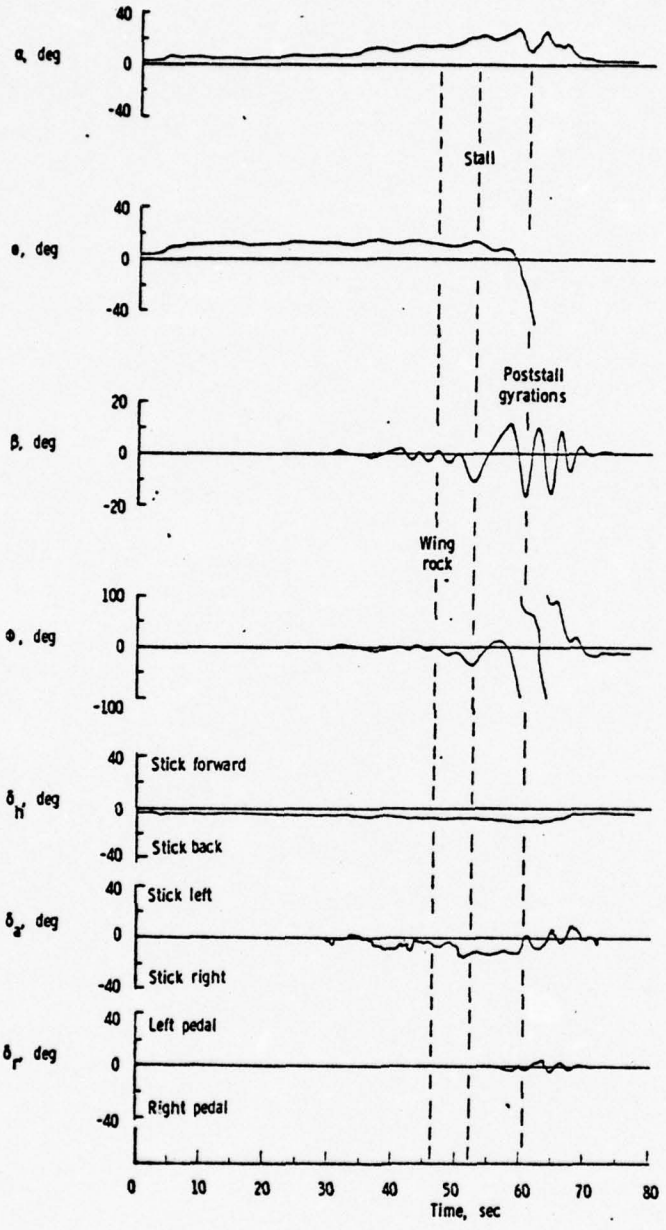


Figure 2.21 Time History of a Simulated 1g Stall for Configuration A with Rate Stability Augmentation. (Reference 30)

of stall/post-stall phenomena. Specifically, it is seen that the pilot is making corrective inputs with the ailerons as wing rock starts. This is a natural reaction, since the pilot would tend to raise the wing if it dropped. At high angles of attack, the aircraft is unstable and continual correction is necessary to keep from diverging.

The time history of Figure 2.19 illustrates the relationship between aircraft response and pilot reaction with the SAS on. This time history shows pitch-up into wing rock and roll departure. Examination of the traces of roll (ϕ), sideslip (β), aileron (δ_a), and rudder (δ_r) yields the following conclusions.

(1) The phase of rudder angle to sideslip ($\delta_{r/\beta}$) is approximately +165° (the rudder opposing sideslip)

(2) The phase of aileron to roll ($\delta_{a/\phi}$) is approximately -135° (aileron opposing roll)

(3) The ratio of roll amplitude to yaw amplitude is about three.

The period of the oscillations in ϕ and β vary between 4 and 6 seconds. These characteristics will be recalled in Section IV.

Stone, in Reference 16, points out that this problem makes correlation of digitally calculated high angle-of-attack responses with airplane responses difficult. A purely digital simulation would not ordinarily simulate the rapid and continual control inputs that a pilot would make. The same is true of model tests, of course, and this is one reason that piloted stall/spin model tests are conducted by NASA/Langley.

In most digital spin simulations, off-on control inputs can be used to cause the aircraft to spin (Reference 14). The stall/post-stall regime, however, is more sensitive and requires a more detailed manner of controlling the aircraft. This subject will be discussed further in succeeding sections.

In summary, the nature of wing rock and departure is understood, at least in a qualitative sense. Closed form analyses yield approximations to these occurrences and they have been simulated with computers. In all cases, it is found that prediction of the stall/post-stall phenomena is highly dependent on accurate knowledge of the aerodynamic forces and moments.

2.5 WIND TUNNEL PREDICTION OF FREE FLIGHT RESPONSES

2.5.1 Examples of Inconsistency

Wind tunnel testing of aircraft models has historically been a basis for predicting performances, stability, and control characteristics in flight. These predictions tend to be erroneous at extreme operating conditions, such as in high angles-of-attack maneuvers. In particular, the rotary or dynamic derivatives are suspect.

As mentioned previously, the F-4 aircraft has undergone extensive wind tunnel and flight test at high angles-of-attack. Reference 14 is a detailed analytical study of the spin characteristics of the F-4. These calculations are based on wind tunnel data and it was found that some of these data had to be modified to more closely simulate the characteristics of spin (such as spin rate and angles-of-attack). Figure 2.22 is an example of one of the more important static modifications. It is seen that a significant correction is made to the wind tunnel model prediction of the pitching moment coefficient, $C_{m_{.33\bar{c}}}$. Reference 14 attributes this discrepancy to engine inlet ducts and jet effects. The Reynolds number difference is also cited.

Rate dependent forces and moments are very difficult to determine from wind tunnel measurements. The most common method is to oscillate the model at varying amplitudes and frequencies. Amplitude changes are achieved by changing cams in the model drive mechanism. A typical example of the results of using different amplitude driving cams is shown in Figure 2.23 (from Reference 14). It is seen that this testing technique gives results which are difficult to

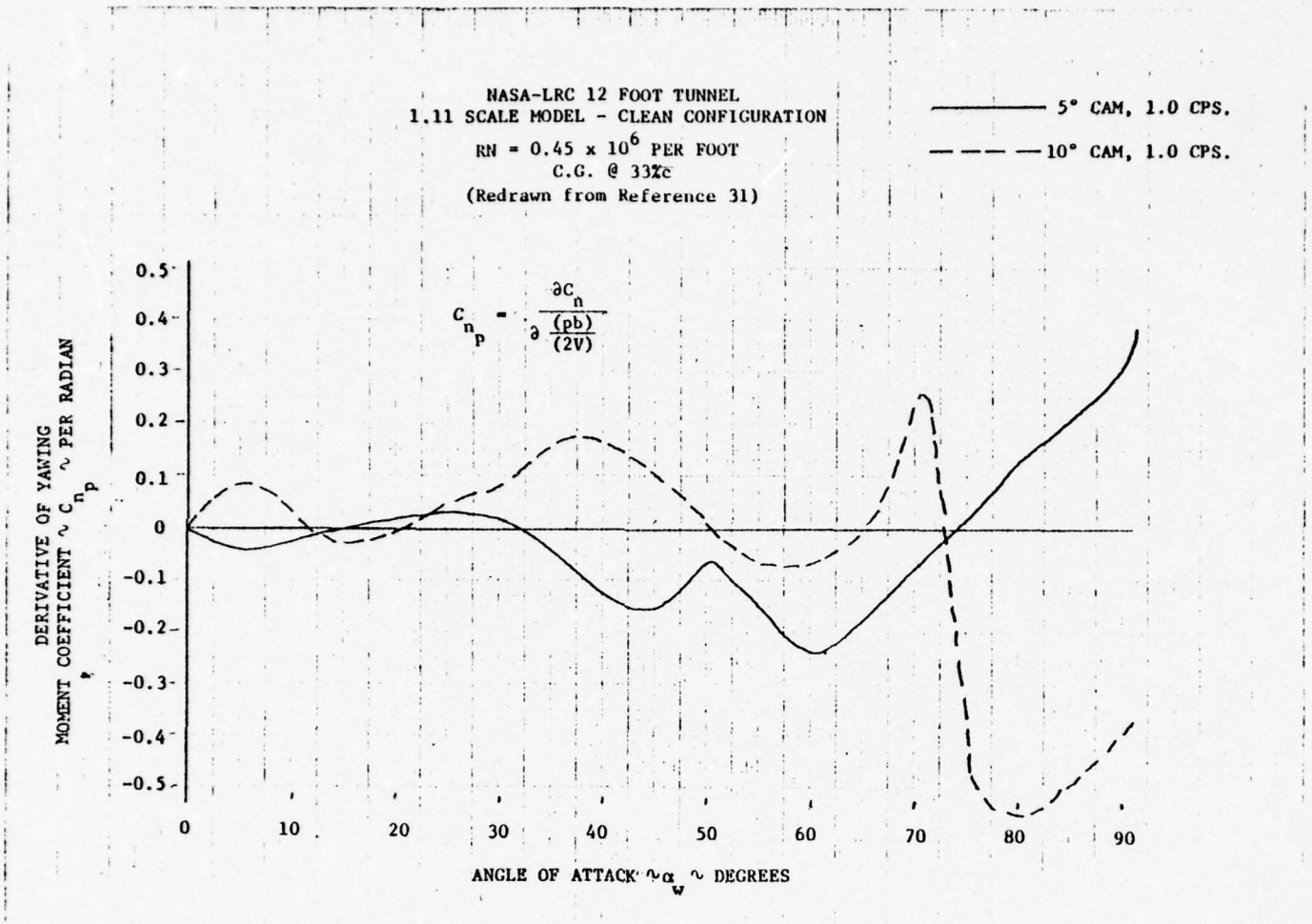


Figure 2.22. Model F-4 Yawing Moment Due to Rolling Velocity (LRC Test) (from Reference 14)

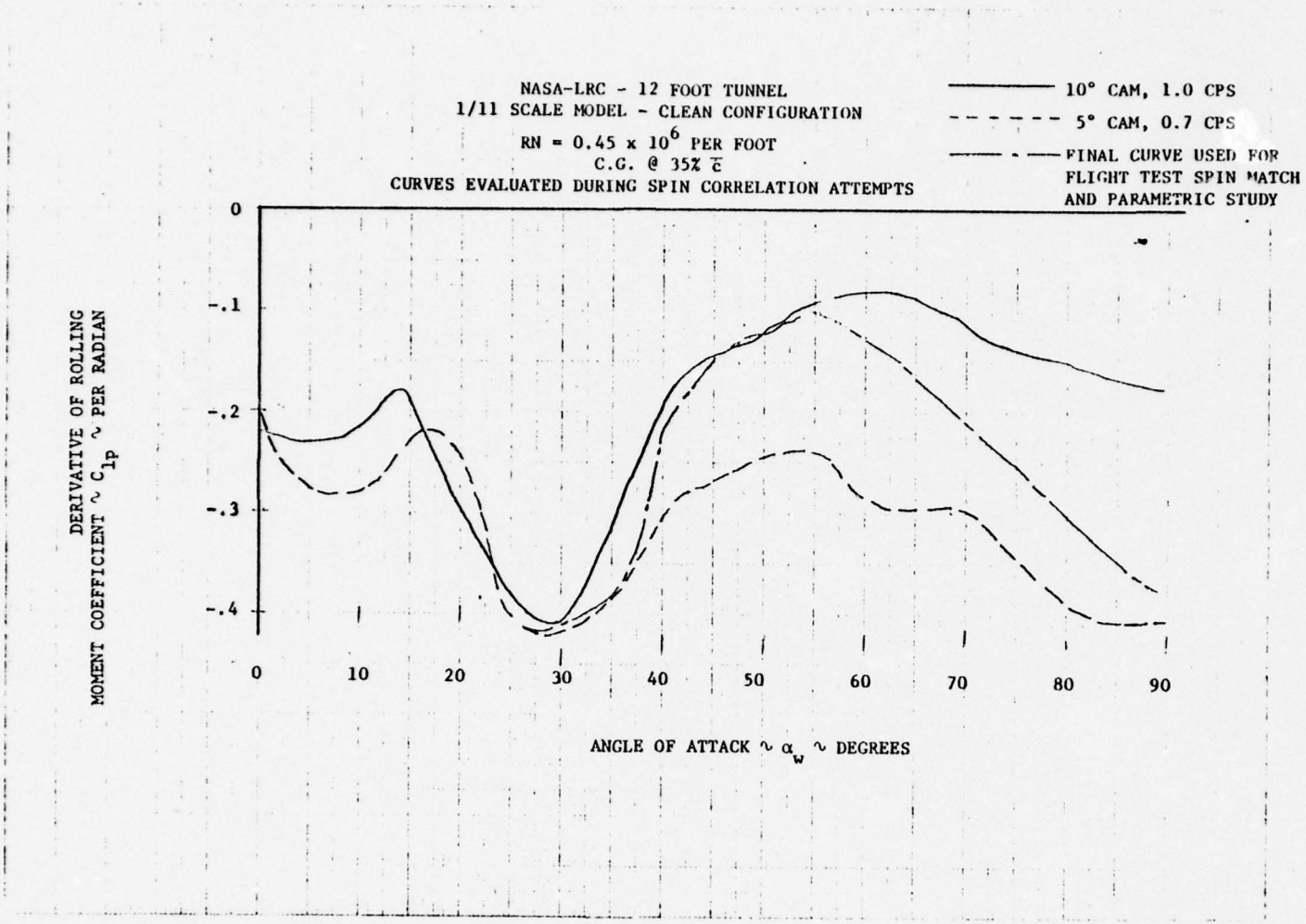


Figure 2.23. Model F-4 Rolling Moment Due to Rolling Velocity (LRC Test) (from Reference 14)

interpret in terms of free flight responses. Such nonlinear behavior is caused by unsteady aerodynamic effects and is not well understood. Another problem of the technique arises from the fact that the model oscillates about an axis that does not pass through the aircraft center of gravity. Thus pitching rate, for example, is simulated by a combination of pitching about the c.g. and heaving of the c.g. Thus, for example, wind tunnel rate measurements pair the contributions of the q and α effects, i.e., $C_q + C_{\dot{\alpha}}$. Reference 30 discusses the limitations of this pairing in using wind tunnel data in the equations of motion. Similarly, a rolling oscillatory test gives the component $C_{n_p} + C_{n_{\dot{\beta}}} \sin \alpha$ out of phase with the driving function. More elaborate test rigging is necessary to decompose this measurement into C_{n_p} and $C_{n_{\dot{\beta}}}$. Hence, the problem of determining the rate coefficients is more a question of how to use and interpret the data, as well as how to measure it.

An example of corrections necessary to C_{ℓ_p} for the spin correlation is given in Figure 2.23.

2.5.2 Basis of Differences Between Wind Tunnel Predictions and Flight Test Results

The basic differences between the tunnel and the flight test aerodynamic environment have been discussed in previous sections.

The most consistent difference is is the Reynolds number variation. Such an effect is shown in Figure 2.24 from Reference 13. Mach number affects C_D, C_{L_α} and also the stall characteristics by introducing the phenomenon of shock separation. Of course, the pressure distribution over the aircraft changes in the transonic regime.

Engine and jet effects have been discussed in Section 2.5.1. Slight geometrical differences have been shown to be significant in some forces and moments in the stall/post-stall regime.

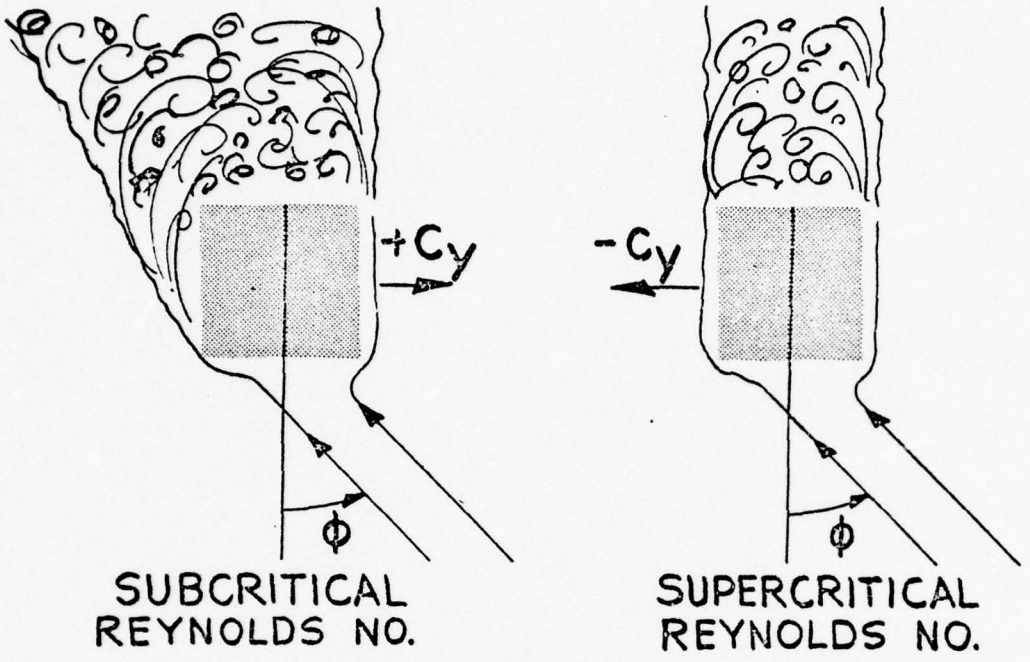


FIGURE 2. CROSSFLOW AS A FUNCTION OF REYNOLDS NUMBER (NACA TN 4176)

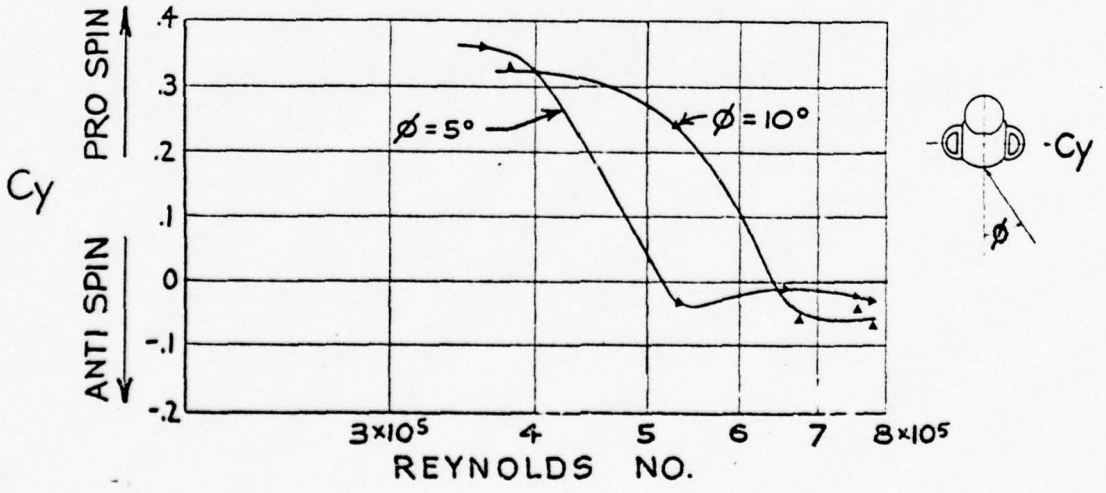


Figure 2.24. Effect of Reynolds Number on Side Force Coeffient (from Reference 13)

Finally, the introduction of the most nonlinear element, the pilot, has been discussed as a factor in obscuring the fundamental aerodynamic characteristics in flight tests. Attempts to account for such pilot effects have been made in remote control scale model tests. However inability to simulate "cues" and control delays, as well as scaling effects, again prevent complete simulation of full-scale phenomena.

2.6 SUMMARY

The foregoing review has shown how the complicated flow interactions which occur in the stall/post-stall flight regime cause nonlinear and unstable aircraft motions such as pitch-up, wing rock, and yaw departure, which may produce uncontrollable spins. Although significant effort has been expended to predict and understand this stall/post-stall aerodynamic environment, the complexity of the problem and the lack of sufficient powerful analytical techniques have precluded accurate prediction and understanding.

III

SIMULATION OF HIGH PERFORMANCE AIRCRAFT IN THE HIGH-ANGLE-OF-ATTACK REGIME

3.1 INTRODUCTION

The objective of the simulation discussed in this section is to generate typical flight data which is characteristic of stall/post-stall maneuvers. Prediction of aircraft performance, stability, and control characteristics at high angle-of-attack is requisite to this objective. This section gives an overview of the simulation program. Appendices A and B list the equations of the program.

The simulation has been developed with the goal of high flexibility toward model aircraft, operating conditions, and maneuvers. Provision is also included for studying the basic causes of certain types of aircraft responses.

The simulation presently calculates the responses for an F-4 fighter aircraft. The wind tunnel data restricts these results to subsonic speeds.

3.2 AIRCRAFT EQUATIONS OF MOTIONS

3.2.1 Kinematic Representations

The aircraft is assumed to be a rigid body and no elastic effects are presently considered.

The aircraft body axes are an orthogonal right hand set with the coordinate origin located at the center of gravity. The x_B and z_B axes lie in the plane of symmetry. The x_B axis is parallel to any convenient fore and aft line (e.g., water line, wing chord line, etc.), positive in the forward sense. The positive sense of the z_B axis is downward. The angular velocity of the aircraft is resolved about the x_B, y_B, and z_B axes as

$$\underset{B}{\Omega}^{B-I} \triangleq (p \quad q \quad r)^T \tag{3.1}$$

with the positive sense defined by the conventional right hand rule. The aircraft linear velocity is defined as

$$V_B^{B-I} \triangleq (u \quad v \quad w)^T. \qquad 3.2$$

Figure 3.1 illustrates these conventions.

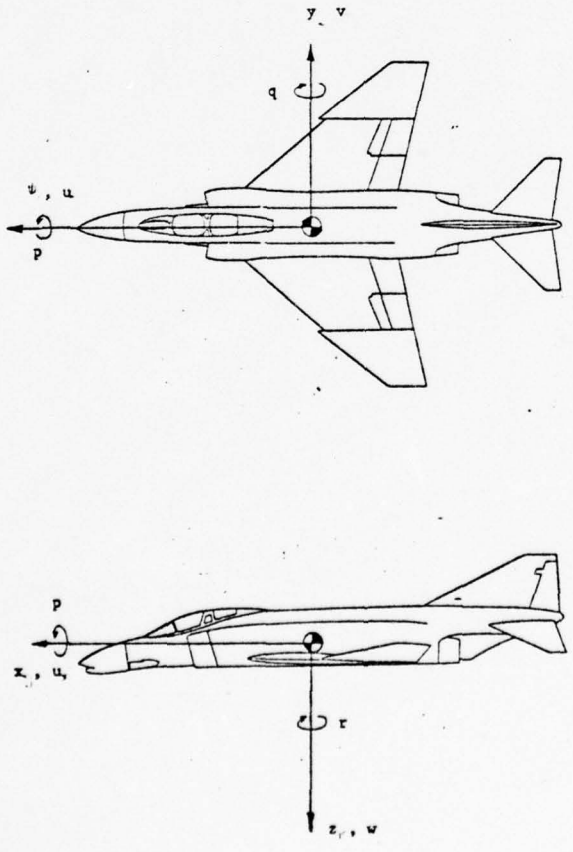


Figure 3.1 Body Axes and Sign Conventions

The orientation of the aircraft axes relative to the inertial, or earth axes, (X_e, Y_e, Z_e) is specified by the Euler angles pitch (Θ), roll (Φ), and yaw (Ψ). The sequence of rotations is Ψ, then θ, then ϕ , as shown in Figure 3.2. The corresponding direction cosine matrix is

$$T^{B-I} = \begin{bmatrix} \cos\Theta\cos\Psi & \cos\Theta\sin\Psi & -\sin\Theta \\ \sin\Phi\sin\Theta\cos\Psi - \cos\Phi\sin\Psi & \sin\Phi\sin\Theta\sin\Psi + \cos\Phi\cos\Psi & \sin\Phi\cos\Theta \\ \cos\Phi\sin\Theta\cos\Psi + \sin\Phi\sin\Psi & \cos\Phi\sin\Theta\sin\Psi - \sin\Phi\cos\Psi & \cos\Phi\cos\Theta \end{bmatrix} \qquad 3.3$$

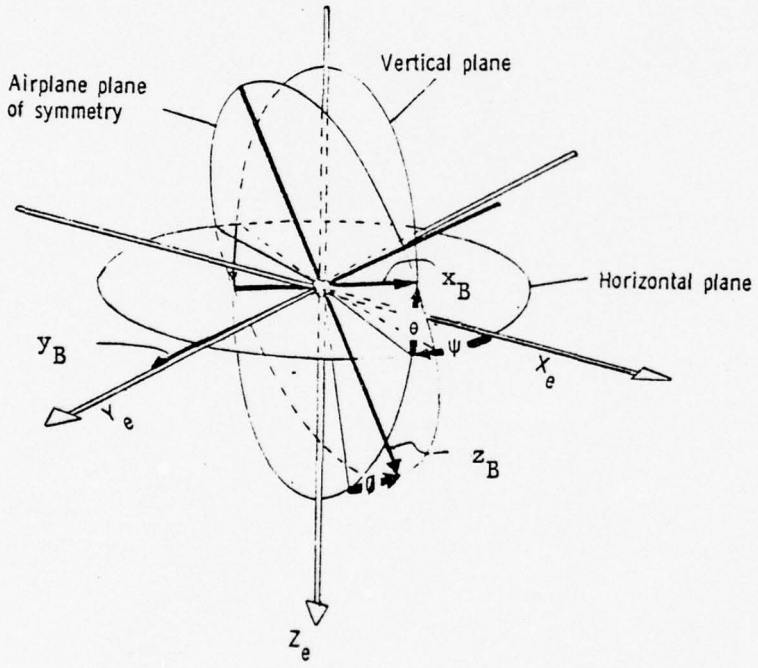


Figure 3.2 - Body system of axes and related angles.
Arrows indicate positive directions.

For small attitudes, Ψ is called the heading, Θ the attitude, and Φ the bank angle. For large Θ , however, this nomenclature is ambiguous. For example, at $\Theta = \pi/2$, Φ is heading and Ψ is roll. This ambiguity is a consequence of the fact that the large-angle Euler rotations do not constitute a sequence of orthogonal rotations. There are two important consequences of the non-orthogonality and the large angles involved.

(1) A singularity is encountered at $\Theta = \pi/2$ when integrating the three Euler angle rate equations (i.e. "gimbal lock".)

(2) The inertial orientation is not the algebraic sum of the steady state (or trim) and perturbed angles, except for small perturbations. The components p, q, and r are the time rate of change of the perturbation angles θ_B, ϕ_B, and ψ_B about the body axes and are not the derivatives of Φ, Ψ, and Θ.

The matrix T^{B-I}, and its differential equation, does not suffer from this orthogonality problem, and the elements of T uniquely define the aircraft orientation. At any instant of time, the direction cosine matrix T^{B-I} is the solution of the differential equations

$$\dot{T}^{B-I} = -\underset{B}{\Omega}^{B-I}{}_x T^{B-I} \qquad 3.4$$

where

$$\Omega^{B-I}{}_x \triangleq \begin{bmatrix} 0 & -r & q \\ r & 0 & -p \\ -q & p & 0 \end{bmatrix}. \qquad 3.5$$

Only three of the elements of T^{B-I} are independent, so it is not necessary to solve the nine differential equations of equation 3.4. Since T^{B-I} is orthogonal, nine algebraic equations result from

$$T^{B-I}(T^{B-I})^T = I. \qquad 3.6$$

Further, other algebraic equations may be obtained based on the representations of a given vector in the rotated and non-rotated frames.

Since the simulation was to be valid for large angles, the direction cosine integration was adopted with the integration of six differential and three algebraic equations for the nine elements of T^{B-I}. The addition of the three differential equations was desired to have an option in checking orthogonality of T^{B-I} at each step.

The direction cosine matrix is used frequently in the simulation. The inertial angles Θ, Φ, and Ψ are determined from the elements of T as shown in equations A.5.3 of Appendix A. The velocities and accelerations in the body frame yield those of the inertial frame directly through

$$\underset{I}{V} = (T^{B-I})^{T} \underset{B}{V}.$$

Accelerations are similarly transformed. For example, the gravity acceleration in body axes is

$$g \begin{pmatrix} -\sin\Theta \\ \sin\Phi \cos\Theta \\ \cos\Phi \cos\Theta \end{pmatrix}$$

3.2.2 Dynamic Equations

The equations of motion are written in the body frame. These equations are

$$\underset{B}{\dot{\Omega}}^{B-I} = \bar{\bar{I}}^{-1}\{(+\underset{B}{\Omega}^{B-I} x \bar{\bar{I}} \cdot \underset{B}{\Omega}^{B-I}) + \underset{B}{M}^{ext}\} \qquad 3.7$$

$$\underset{B}{\dot{V}}^{B-I} = +\underset{B}{\Omega}^{B-I} x \underset{B}{V}^{B-I} + \frac{1}{m} \underset{B}{F}^{ext} \qquad 3.8$$

where

Ω_B^{B-I} is the aircraft angular velocity resolved in body axes (cf. section 3.2.1)

V_B^{B-I} is the aircraft c.g. linear velocity in body axes (cf. Section 3.2.1)

M_B^{ext} is the sum of thrust, engine gyroscopic and aerodynamic moments, coordinatized in the body frame

F_B^{ext} is the sum of gravity, thrust, and aerodynamic forces, coordinatized in the body frame.

$\bar{\bar{I}}$ is the aircraft inertia tensor

m is the aircraft mass.

The scalar expansions of these equations may be found in most advanced texts, for example, Etkin (reference 18). These scalar expansions are presented in equations A.3.1 through A.3.2 of Appendix A.

The following characteristics of these equations will be noted:

(1) All nonlinear state coupling terms have been retained. In particular, nonlinear dynamic terms involving products and squares of aircraft states have been kept because of their importance in predicting roll departure.

(2) Engine gyro moments are retained. Reference 16 points out that these moments may affect the direction of departure in some maneuvers.

(3) No aeroelastic effects are included as mentioned in Section 3.2.1.

(4) There are a total of 15 differential equations which are integrated to predict the aircraft motion. Of these, nine are simply kinematic and six are equations of motion.

A fixed step size of .1 second is used for the fourth order Runge-Kutta integration of these equations. This step size was chosen as a compromise between accuracy and running time.

3.3 AERODYNAMIC MODEL

3.3.1 Model Selection

The most important aspects of the simulation are involved with the representation of the aerodynamic forces and moments in body axes. As discussed in Section II. the high angle-of-attack regime is not amenable to accurate mathematical modeling of the flow fields, even though such modeling provides useful insight. Because of this, six-degree-of-freedom simulations must rely on detailed wind tunnel measurements to most accurately model the effects of the flow on the forces and moments. Unfortunately, such tests are restricted with respect to the type and number of independent variable. Usually, only a limited number of Mach number, Reynolds number, and model configurations may be investigated. Extension of the results so obtained must be made by extrapolation.

These limitations being realized, wind tunnel data are used in this simulation as the model basis. Extensive use of the technique by previous workers in the field, the excellent data available from tests such as those at NASA/Langley, and the availability of high speed computers justify this approach.

Although extensive data do exist, there are many ways to use them. The reference axis system (body, wind, or stability) must be selected. The type of data interpretation (Taylor series expansion, polynominal fit, straight line approximation, or table look-up) must be established. The use of the rotary derivative data must be specified (the frequency and amplitude).

For this simulation, the aircraft forces and moments are assumed to be resolved into body axes. (It is noted that relatively simple transformations can be made to use stability axis data.) It is further assumed that this data specifies implicitly the x_B axis, and that collateral inertias about the concommitant body axes are given.

The instantaneous angle-of-attack and sideslip angle are defined from Figure 3.3 as

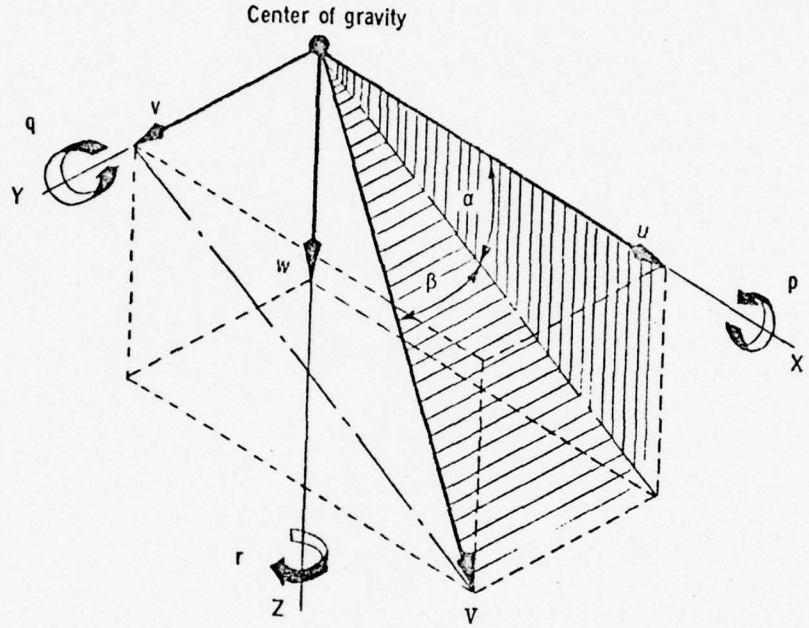


Figure 3.3 Definitions of Angle-of-Attack and Sideslip Angle

$$\alpha = \tan^{-1} \frac{u}{w}$$

$$\beta = \sin^{-1} \frac{v}{V}$$

where V is the total relative wind, $\sqrt{u^2 + v^2 + w^2}$. α is positive when w is positive and β is positive when v is positive. α and β completely fix the relative wind in body axes.

A basic assumption is that the forces and moments are not dependent on the time rates of change of the states. Hence, the effects of $\dot{q}$, $\dot{p}$, $\dot{r}$, in the airloads are not considered, for example. This assumption is made because there is no wind tunnel data isolating these unsteady effects. Furthermore, it is generally concluded that the effects of these terms are small.

3.3.2 Wind Tunnel Data

3.3.2.1 Data Characteristics

The wind tunnel data which is currently used is that of the extensive NASA/Langley tests of the F-4 configuration. These data are reported in References 8 and 19. The form of the data is tabular. NASA/Langley supplied the computer cards in a readily usable form.

The static force and moment coefficients, C_x, C_z, C_m, C_ℓ, C_n and C_y are given as functions of α and β ($-10 \leq \alpha \leq 110°$ and $-40 \leq \beta \leq 40°$). The control effectiveness derivatives are given as functions of α and β. The rotary, or rate derivatives are given as functions of only α.

The largest increment between data points is 10° and the smallest is 2.5°, with 5° being the most used increment. This increment was determined by the nonlinearity of the coefficient being measured. The interpolation of these data is discussed in the next section.

Plots of the data are given in Appendix C. These plots are useful in understanding the simulation results, and, in some cases, predicting those results. These plots are made for $\beta=0$ since the incipient motions in the stall/post-stall regime involve little sideslip.

The characteristics of $C_m(\alpha,o)$, $C_Z(\alpha,o)$, and $C_X(\alpha,o)$ are depicted in Figures C.1-C.3. The variations of these forces and moment are characteristic of swept wing aircraft and the significance of stall is easily seen.

The control effectiveness forces and moments are plotted in Figures C.4-C.15. Note that the lateral control effectiveness ($C_{y_{\delta_r}}$, $C_{\ell_{\delta_r}}$, $C_{n_{\delta_r}}$, $C_{y_{\delta_a}}$, $C_{\ell_{\delta_a}}$, $C_{n_{\delta_a}}$) is given as a function of α instead of the more usual β. The purpose of choosing α as the independent argument is to see the decrease of control effectiveness with α.

Of particular importance is the magnitude of the cross derivatives, $C_{\ell_{\delta_s}}$ and $C_{n_{\delta_s}}$, Figures C.13 and C.15. It is indicated that stabilator inputs give rise to lateral-directional moments. This observation should be remembered for reference from Section IV.

The rotary or rate derivatives are shown in Figures C.16 through C.24. These derivatives correspond to the rotary data taken at a frequency of .7 cps and amplitude ± 5 degrees. It is recalled that the effect of frequency and amplitude on the rotary derivatives is nonlinear. These data use the values corresponding to the lowest excitation frequency and smallest excitation amplitude.

The derivatives C_{ℓ_p}, C_{n_p}, and C_{n_r} are of primary importance. All of these damping effects obtain critical values of destabilization at an α of about 20°.

The remaining figures illustrate the dramatic change in C_{n_β} characteristics as α varies from $\alpha = 20°$ to $\alpha = 22.5°$. These characteristics were discussed in detail in Section II.

3.3.2.2 Data Interpretation

The data are stored in tables called by program. In order to determine values of the force and moment coefficients at intermediate data points, Lagrange interpolating polynominals are used.

Two types of interpolating polynominals are used. For force and moment coefficients which are only functions of α, a one-dimensional interpolating polynominal,

$$P_n(\alpha) = \sum_{i=0}^{3} \prod_{\substack{j=0 \\ j\neq i}}^{3} \frac{\alpha - \alpha_j}{\alpha_i - \alpha_j} C(\alpha_i)$$

which uses four points (two on either side of α) for the polynominal of order three. $C(\alpha_i)$ are the force or moment coefficient values at α_i, (the given values of α for which the coefficient is specified). For coefficients which are functions of α and β, a two-dimensional interpolating polynominal is found

$$P_{3,3}(\alpha, \beta) = \sum_{i=0}^{3} \sum_{i=0}^{3} \prod_{\substack{k=0 \\ k\neq i}} \frac{\alpha - \alpha_K}{\alpha_i - \alpha_K} \prod_{\substack{k=0 \\ k\neq j}} \frac{\beta - \beta_k}{\beta_j - \beta_k} C(\alpha, \beta_i)$$

which uses a total of sixteen points (i.e., on a four-by-four grid over the intermediate point). $C(\alpha_i,\beta_i)$ are the coefficient values at the given α_i and β_i.

The interpolation polynomial, using the values $C(\alpha_o) \ldots C(\alpha_3)$ approximates the function $C(\alpha)$ in the interval $(\alpha_{max}, \alpha_{min})$, where

$$\alpha_{max} = \max(\alpha_o \ldots \alpha_3)$$

$$\alpha_{min} = \min(\alpha_o \ldots \alpha_3)$$

A Taylor's polynomial, on the other hand, uses values of the coefficient $C(\alpha_o)$ and its first n derivatives at the point α_o to approximate the function $C(\alpha)$ in the neighborhood of α. The third-order Lagrangian interpolating polynomial is equivalent to a third-order Taylor series polynomial with remainder proportional to the fourth derivative of the coefficient with respect to α or β. Since the data is smooth, it is seen that at least coupling terms such as $C_{\alpha\beta}$ are contained

in the simulation. Use of the Lagrangian interpolating polynomials gives flexibility for handing different types of data (more independent variables, variable step sizes, etc.) and an extremely accurate routine was already available for this simulation.

Since the integration routine is a fourth-order Runge-Kutta scheme, these tables and the interpolation are used four times per integration step.

3.3.3 Simulation of Random Disturbances

3.3.3.1 Buffet Simulation

One of the most significant indicators of the stall/post-stall regime is the buffet due to flow separation (References 37 through 41). There are several possible ways to simulate this effect.

For this simulation the buffet is simulated as a random component in lift. This random component is represented as a white noise disturbance added to C_z, i.e.,

$$(C_z)\ \text{random} = (C_z)\ \text{deterministic} + (\delta C_{z_o})$$

where δC_z is evaluated at trim and

$$E(\delta C_z) = 0$$

$$E(\delta C_z^2) = \left(\frac{m\Delta g}{q_B S}\right)^2$$

and

$$\Delta g_v = .02g$$

This representation thus corresponds to a mean buffet intensity with variance .02g (and zero mean)

Such a buffet model is certainly oversimplified. However, a general analytical treatment of buffet is not available. The objective of this buffet model is to generate more realistic random data from the aircraft sensors. Other representations of buffet could be obtained by increasing the order of the simulation with shaping filters for the white noise, although this would increase the order of the system of differential equations.

3.3.3.4 Turbulence

Atmospheric turbulence is another important random force acting on the aircraft. For this simulation, the turbulence is simulated as a random variation in angle-of-attack. The random process is modeled as a white noise disturbance with zero mean and RMS value of .01α. The subsequent random component of α is added to the state dependent α (Section 3.3.1) and used in the aerodynamic tables for determination of corresponding C_Z, C_m, and C_X.

Note that this turbulence model is severe, and would correspond to a "worse case" calculation in the simulation. In particular, the vanes for measurement of α and β are sensitive to this component.

As with the buffet, other methods of simulation could be used for turbulence at the cost of an increased number of differential equations.

3.4 INITIAL CONDITIONS AND TRIM

3.4.1 Input Parameters and Longitudinal Trim Calculation

The basic set of input parameters specify the initial steady state flight condition. The geometric conditions are that (see Figure 3.4):

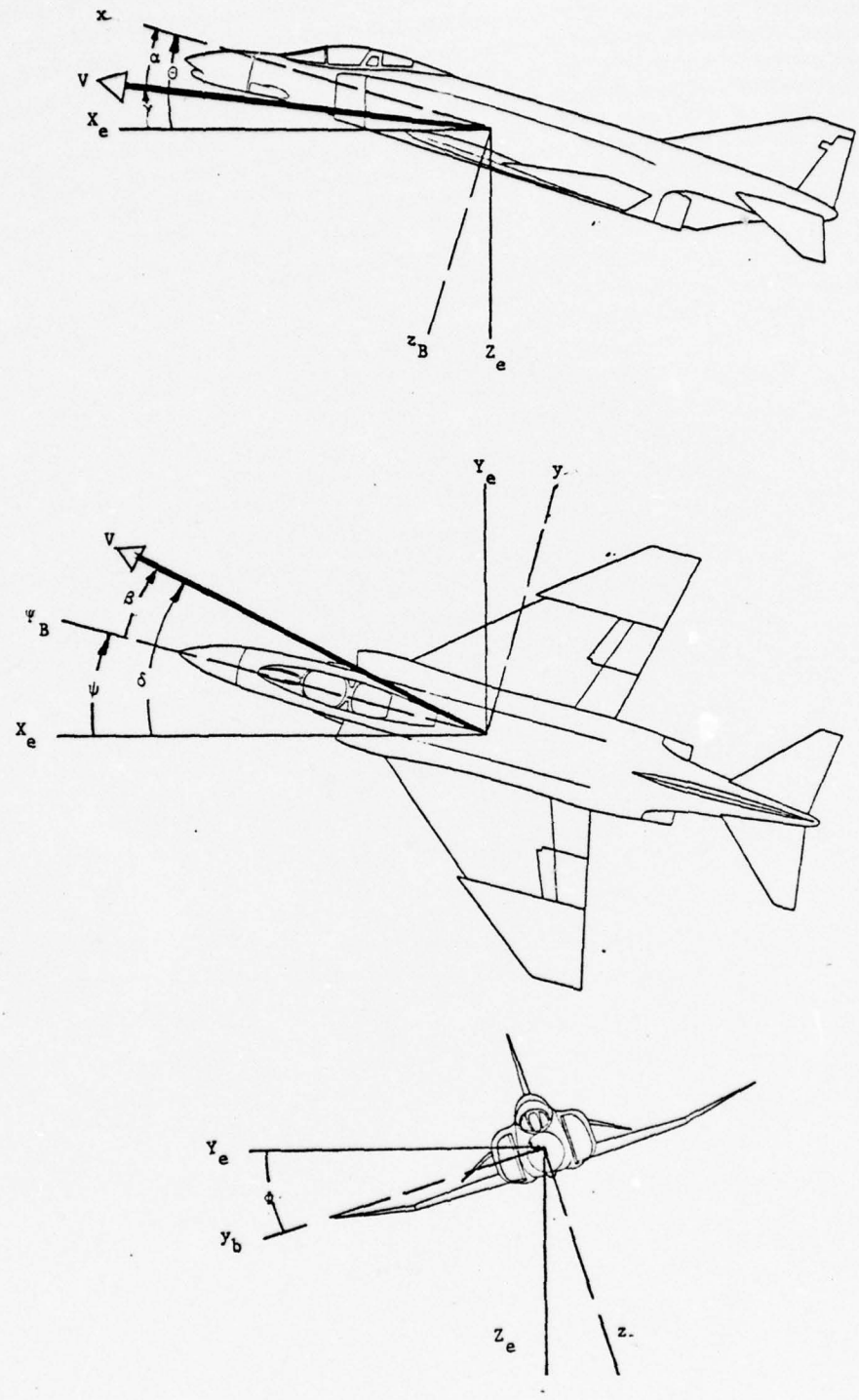


Figure 3.4 Trajectory States Definitions

$$\Theta_o = \gamma_o + \alpha_o$$

$$\Psi_o = \delta_o - \beta_o$$

where α_o and β_o are the initial angle-of-attack and sideslip angles. γ_o is the flight path angle and δ_o is the corresponding lateral equivalent. Θ and Ψ are the initial pitch and yaw angles. Input to the simulation consists of the four angles on the right hand side of these equations. Φ_o is usually taken to be zero initially.

Additional parameters which are inputed are the density ratio and speed of sound ratio at a preselected altitude.

With the values of the initial angles, the initial direction cosine matrix T_o^{B-I} is calculated, (equations A.1.1.2, Appendix A).

The initial α_o and β_o will yield the trim force and moment coefficients. The initial T_o^{B-I} will yield the components of gravity in the body axes. It is then necessary to solve for the trim velocity, thrust, and stabilator angle.

For straight and level flight,

$$\dot{u} = \dot{v} = \dot{w} = \dot{p} = \dot{q} = \dot{r} = 0$$

and the six equations of motion reduce to six nonlinear algebraic equations. To solve these equations it is assumed that a first approximation to the trim conditions may be obtained by neglecting cross axes coupling and solving only the three longitudinal equations. The resulting equations have three unknown engine moments as well as unknown stabilator angle and velocity. The number of unknown engine moments may be reduced by assuming that the geometry of the engine is known.

For example, the following equations approximate the thrust geometry of the F-4 aircraft.*

$$\left(\hat{F}_{T_x}\right)_o = T \cos \lambda$$

$$\left(\hat{F}_{T_z}\right)_o -T \sin \lambda$$

$$\left(\hat{M}_{T_y}\right)_o - Th \cos \lambda$$

where T is the engine thrust, λ is the angle of the thrust line to the x_B axis, and h is the moment arm of the thrust about the aircraft c.g. (Reference 13). Note that λ and h are, in general, dependent on flight condition. For the F-4, nominal values are $\lambda = 5.25°$ and h = .5 ft. (Reference 32).

With these approximations, the equations A.2.1.1 results. These equations are solved for thrust, velocity, and stabilator angle required for longitudinal trim.

The lateral trim is simpler because wings-level flight is assumed. This leads to equations A.2.4.2.

It is seen from equations A.2.1.1 that the trim velocity depends on the density altitude, which is an input to the program.

3.4.2 Differential Equation Initialization

The initial conditions for the differential equations of motion are specified by (T_o^{B-I}) , $(\delta_s)_o$, V_o , α_o, β_o .

The complete equations are coupled and nonlinear. It is necessary to recompute the exact engine forces and moments for the controls and velocity calculated from the linear approximation (equations A.2.2). The initial velocity

* It is assumed that the small engine cant in the xy plane may be neglected.

components in body axes are then found (equations A.2.3). The direction cosine equations are initialized by (T_o^{B-I}) .

The complete equations of motion are then integrated.

These trim procedures may be replaced by others, depending on the simulation objectives. For example, the trim calculation of the previous section may be by-passed and the initial velocity, and control angles used instead. Alternately, other types of trim calculations may be implemented. For example, controls for a steady climb or steady sideslip may be used. The simulation is written to be flexible with respect to initial flight condition.

3.5 CONTROL INPUTS AND AUTOPILOT DESIGN

3.5.1 Types of Simulated Controls

The simulation uses two types of control laws. Open loop control sequences for the stabilator, aileron, and rudder controls may be read in as functions of time. Closed loop, or feedback controls may also be specified to meet various requirements.

Open loop control sequencing is used whenever a particular type of test input (doublet, pulse, etc.) or a particular pilot input from flight is to be simulated. The pilot input simulation is usually difficult unless punched cards for the control history are available. Otherwise, only an approximation to the given control history is used. These control histories must also be given for the actual stabilator, aileron, or rudder deflections since the control system itself is not modeled.

The closed loop controls are added to whatever open loop controls are used. For the F-4 simulation, a stability augmentation system is modeled based on data

from Reference 33. The equations for this three axis damper are given in equations A.3.5 and A.4.1. Washout circuits are used in the pitch and yaw channels, requiring differential equations for δ_s and δ_r inputs of the SAS. All three axes are amplitude limited.

3.5.2 Autopilot Design

The difficulty of simulating the flight of high angle-of-attack regimes is discussed in Section II. Small perturbations from the steady flight condition produces large excursions in the aircraft motion if no control is exerted. In actual flight, of course, the pilot is able to control most of these instabilities. Such control is evident in the time histories of Section II. Hybrid simulations also retain this pilot controllability feature. Nonlinear six-degree-of-freedom simulations, however, require some autopilot to simulate the effect of pilot control, particularly in extreme operating conditions.

For the basic F-4 upon which this work has concentrated, such an autopilot is necessary at high angles of attack, particularly for the lateral-directional mode. The determination of such an autopilot is an iterative task. The steps involved in its determination are as follows:

(1) A detailed study was made of the time histories of Reference 17 to analyze the pilot control response to aircraft motions. Several discussions with John Bull, consulting engineer with the project were held. Mr. Bull's many flight test hours in the F-4 and analytical capabilities helped evolve an autopilot structure (see Appendix D).

(2) Using pole placement techniques, a linear autopilot design was completed and used as a first guess on the autopilot.

(3) Iteration on the autopilot structure was performed until one was found which stabilized lower angles-of-attack in stall/post-stall regions without completely masking some of the known phenomenon. In addition, this autopilot was selected on the closeness with which the phase and amplitudes of the simulated response matched those of flight test.

One lateral directional autopilot* which is used is

$$\delta_a^a = .3\,\phi$$

$$\delta_r^a = 7r + \phi$$

This autopilot reflects the pilot's tendency to lift the wings of the aircraft with aileron and rudder. The autopilot iteration will be summarized further in Section IV.

In addition to this lateral-directional autopilot, simplified altitude hold,

$$\delta_s^a = +\gamma$$

was used to reflect the pilot's reaction to altitude perturbations.

It should be noted that in the computer simulation, the autopilot controls the actual control surface deflections and not cockpit stick and rudder positions. Thus, any effects of the artificial feel system (bellows, spings, and weights) plus any lags in the system between pilot and control surfaces, is not present in the computer simulation. However, these effects on the purpose of the computer simulation are extremely minimal, if present at all, and are not considered to detract from the simulation.

The nominal flight condition was considered to include the stability augmentation system (SAS) to be on, as this is how the aircraft is operationally flown. Thus, autopilot development was conducted with the SAS on.

---

* The sign convention used here is:

positive δ_a is right aileron down

positive δ_r is trailing-edge left

positive δ_s is trailing-edge down

The principal concern for this autopilot was whether it distorted the frequencies and dampings of the high-angle-of-attack responses. This aspect is discussed on the next chapter. Note that the same question must be asked for the time histories of reference 18; i.e., how much of the aircraft response is affected by the pilot?

3.6 INSTRUMENTATION MODELING

3.6.1 Angle-of-Attack and Sideslip Angle Vanes

Of all the measurements required for this simulation, angle-of-attack and sideslip angle are the most important.

There are two basic methods for measuring angle-of-attack and sideslip angle. Vanes attached to a noseboom are the most prevalent methods for flight test (Figures 3.5 and 3.6). Pitot tubes are also used, but mainly in production aircraft as opposed to flight test vehicles. This simulation uses the former because most flight test data uses the vane approach. A basic reference for this type of instrument, as well as general flight test instrumentation is Sorensen (Reference 34). Other references are (30, 35, and 36).

For high angle-of-attack conditions, existing analytical models of vane measurements did not reflect nonlinear effects due to the large angles. The following development summarizes the necessary modifications.

The total velocity along the noseboom is given by equations A.2.3. It is assumed that the noseboom is parallel to the fuselage x_B axis. The vanes are assumed located relative to the aircraft c.g. by the body axis components $\overline{\ell}_v = (\ell_x, \ell_y, \ell_z)$. where $\ell_x >> \ell_y, \ell_z$. The lengths ℓ_x, ℓ_y, ℓ_z are are represented as random variables. The mean value of these variables are the nominal lengths while the variances model the uncertainty associated with location of the aircraft center-of-gravity.

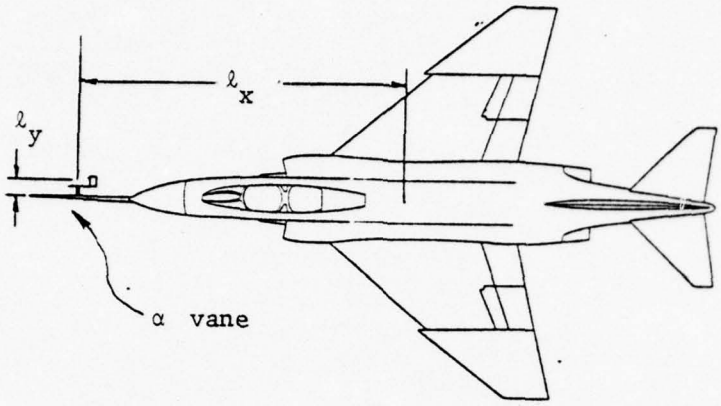


Figure 3.5 Geometry of α Vane

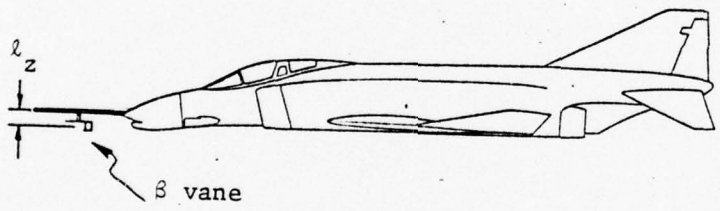


Figure 3.6 Geometry of β Vane

The linear velocity due to aircraft rates is then

$$V_V^{B-I} = \Omega_B^{B-I} \times \bar{\ell}_V \quad .$$

The total velocities at the vane are the sum of the velocity components of the aircraft and the rotational components, yielding

$$\alpha_V = \tan^{-1} \frac{V \sin \alpha \cos \beta + p_{\ell_y} - q_{\ell_x}}{V \cos \alpha \cos \beta + q_{\ell_z} - r_{\ell_y}}$$

$$\beta_V = \tan^{-1} \frac{V \sin \beta + r_{\ell_x} - p_{\ell_z}}{V \cos \alpha \cos \beta + q_{\ell_z} - r_{\ell_y}}$$

where α_V and β_V are the deterministic vane angles assuming no disturbances. Disturbances to these values arise from fuselage induced upwash, turbulence, vane dynamics, and boom bending. These are modeled by adding a white noise and a random bias to the α_v and β_v. The bias approximates the effect of fuselage induced upwash, and the white noise the effect of higher frequency errors due to vane dynamics boom bending, and turbulence. In addition, random scale factor errors due to miscalculation for Mach number and density effects are included. The resultant model for the α measurement is thus

$$\alpha_i = (1 + K_\alpha)\alpha_V + b_\alpha + \varepsilon_\alpha$$

where K_α is the scale factor (random), β_α is the random bias, and ε_α is the white noise. The β measurement is similarly modeled.

These indicated values for α and β are usually corrected for aircraft rotation rate and flight path curvature. Such corrections were discussed in References 30 and 34. Equations B-5 and B-6 of Appendix B give the complete α and β measurement models.

The indicated velocity is required for the correction to the individual angle-of-attack and sideslip angles. This velocity measurement is also subject to random errors. The velocity measurement model is equation B.4 , Appendix B.

3.6.2 Gyro and Accelerometer Modeling

The following error sources are assumed for the inertial measurements from the gyros and accelerometers.

(1) multiplicative random scale factors (K)
(2) additive random bias (b)
(3) additive white noise (ε)
(4) random angular misalignment of input axes
(5) random position errors of the instruments in the aircraft

The general equation for the measured value of an aircraft state, σ,(angle, rate, or acceleration) is

$$\sigma_m = (1 + K_\sigma)\,\sigma + b_\sigma + \varepsilon_\sigma ,$$

where

$$E\{K_\sigma\} = 0 \qquad E\{K_\sigma K_\sigma^T\} = K_\sigma^2$$

$$E\{b_\sigma\} = 0 \qquad E\{b_\sigma b_\sigma^T\} = b_\sigma^2$$

$$E\{\varepsilon_\sigma\} = 0 \qquad E\{\varepsilon_\sigma \varepsilon_\sigma^T\} = \varepsilon^2$$

and K_o, β_σ, and ε are RMS values of the dispersion.

The general angular misalignment transformation multiplies the angular rates and accelerations prior to the measurement, where the transformation (for small angles) is

$$T_m = \begin{pmatrix} 1 & \psi & -\theta_m \\ -\psi_m & 1 & \phi_m \\ \theta_m & -\phi_m & 1 \end{pmatrix}$$

where each misalignment angle has a zero mean. It is assumed that all of the rate gyros are misaligned with the same random distribution as would be the case if the gyros are mounted exactly on a misaligned platform. A similar assumption holds for all the angular gyros and accelerometers.

Equations B.1 through B.3 of Appendix B are the resulting models for the angular position, rate, and acceleration gyros.

Two sets of accelerometers are modeled. One set is nominally located at the aircraft c.g. while the other is located at the pilot seat.

The accelerometer readings are corrupted by errors in position, by misalignment, and by random biases, scale factors, and white noise. All of these effects are shown in the models of equations B-7 of Appendix B.

The statistical properties of these measurements are presented in Table 3.2.

Table 3.2 Gyro and Accelerometers Measurements

INSTRUMENT DATA						
MEASUREMENT	K		b		w	
	Mean	SD	Mean	SD	Mean	SD
Pitch Attitude		.005	0	.15	0	.15
Roll Attitude	0	.005	0	.5°	0	.5°
Pitch Rate	0	.005	0	.1°/sec	0	.1°/sec
Roll Rate	0	.005	0	.1°/sec	0	.1°/sec
Yaw Rate	0	.005	0	.1°/sec	0	.1°/sec
Pitch Acceleration	0	.005	0	.1°/sec^2	0	.1°/sec^2
Roll Acceleration	0	.005	0	.1°/sec^2	0	.1°/sec^2
Yaw Acceleration	0	.005	0	.1°/sec^2	0	.1°/sec^2
Velocity	0	.01	0	5 ft^2/sec^2	0	5 ft^2/sec^2
Angle of Attack	0	.02	0	.05°	0	.05°
Sideslip Angle	0	.02	0	.05°	0	.05°
Axial Acceleration	0	.005	0	.005g	0	.005g
Lateral Acceleration	0	.005	0	.005g	0	.001g
Vertical Acceleration	0	.005	0	.005g	0	.005g

MISALIGNMENT DATA			
MISALIGNMENT		Mean	SD
Gyro & Accelerometers	$(\psi = \Theta = \phi)$	0	.6°
Lengths	$(\ell_x, x_{c_g}, y_{c_g}, z_{c_g}$, etc.)	0	.5 ft

3.7 OUTPUT SPECIFICATIONS

The simulation has several output types. All runs yield tables of the state and the aerodynamic coefficients of interest as a function of time. Such data is used to clearly define the mechanisms procuring the simulation response.

Plots are available in two formats. For rapid evaluation of a calculation, printer plots give time histories of the responses. These plots, though useful for overall response examination, are not accurate enough for detailed analysis. To meet this latter requirement, line plots are available with an increased turn-around time.

All three types of output are used in the presentation of the results in the next section.

IV

SIMULATION RESULTS

4.1 INTRODUCTION

As reviewed in Section II, there has been much previous effort devoted to the simulation of high angle-of-attack responses, particularly spin. Generally, it has not been possible to match flight test results exactly with simulation results, although qualitative correlation has been good.

In this section, two main types of response are investigated. Response for low angle-of-attack test inputs, stabilator pulse and aileron doublet, are calculated. Then, a " 1 g" stall is simulated with the program.

4.2 TRIM SOLUTIONS

4.2.1 Longitudinal Trim Solutions

The trim solution technique is given in Section 3.3.1 and the equations are summarized in Appendix A. It is noted that this is an approximate solution technique consistent with the aircraft data available during this initial simulation effort.

The angle of attack and the aircraft parameters are the only inputs to this calculation. The output is a stabilator angle required to trim, a trim velocity, and the engine thrust. These quantities are only approximate because of the assumptions used to obtain them. The stabilator angle and velocity are then used to calculate the engine thrust required to trim the complete non-linear equations of motion.

The results of this calculation, for two values of c.g. location relative to the wing chord, are shown in the following figures. The trim velocity corresponding to the given angle-of-attack is plotted in Figure 4.1. The corresponding stabilator angles required to trim are shown in Figure 4.2.

The trim angle-of-attack increases as the dynamic pressure (velocity)

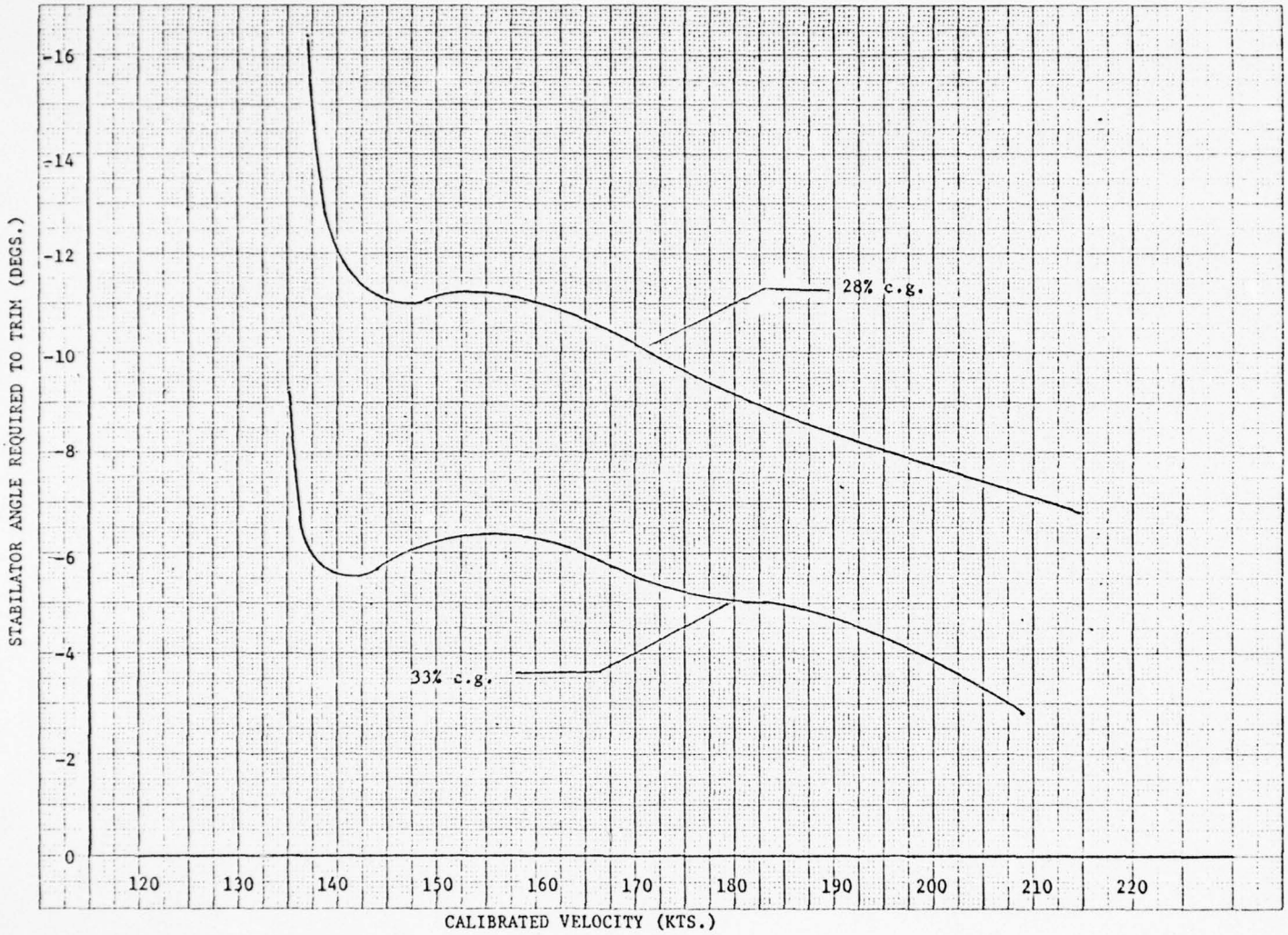


Figure 4.1. Stabilator Angle Required to Trim at Subsonic Speeds

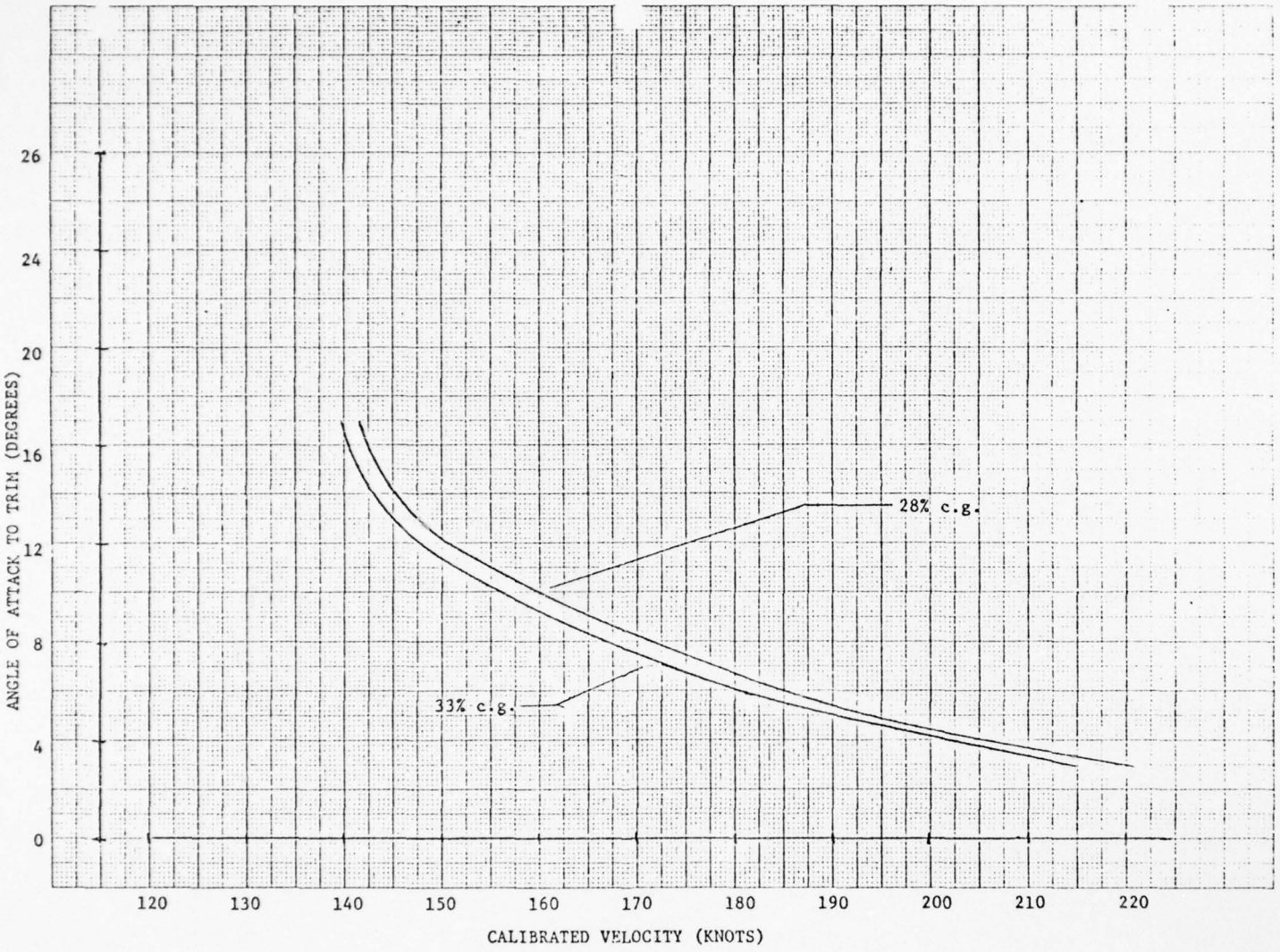
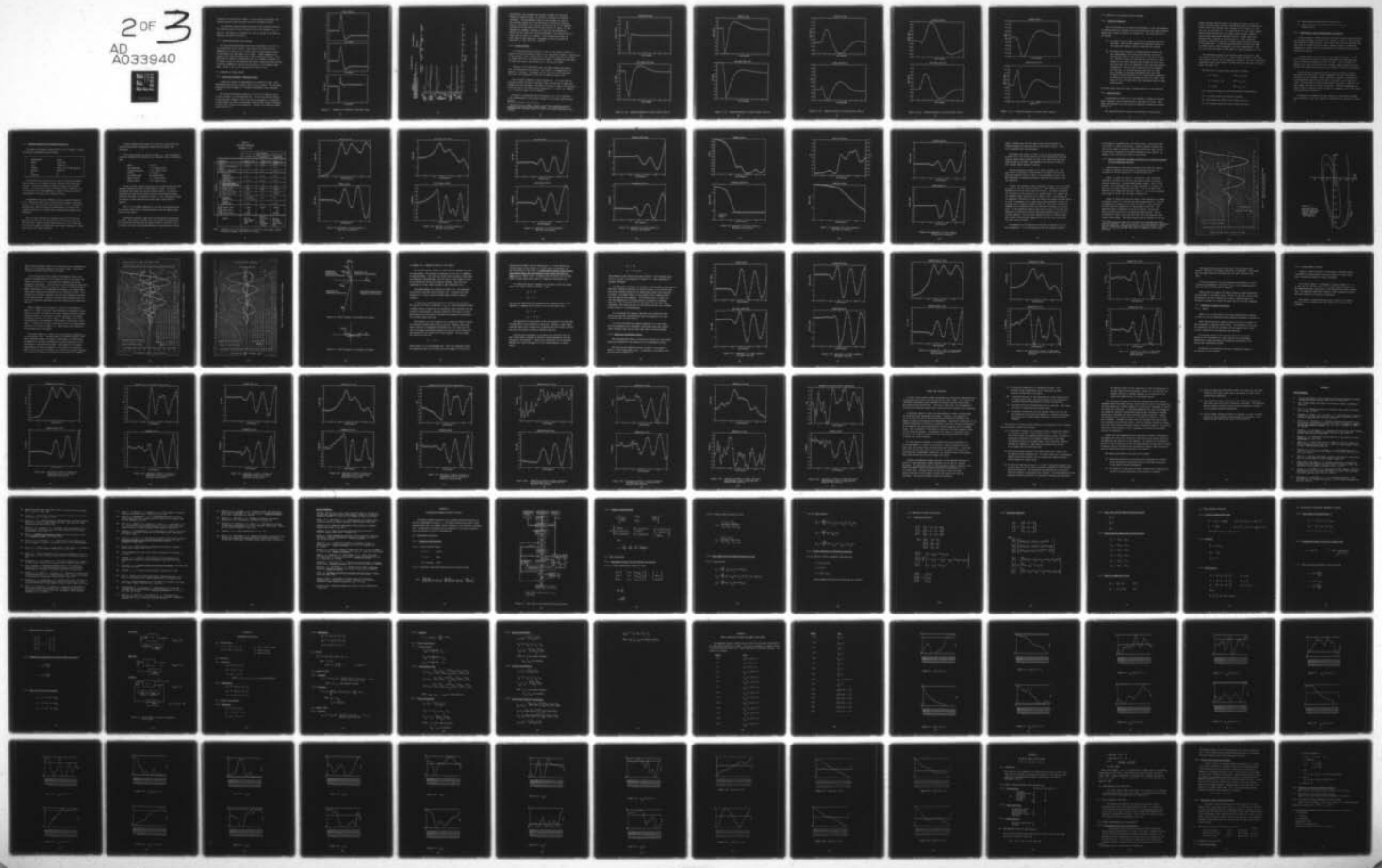


Figure 4.2. Angle of Attack Required to Trim at Subsonic Speeds

AD-A033 940 SYSTEMS CONTROL INC PALO ALTO CALIF F/G 1/2
IDENTIFICATION OF AIRCRAFT STABILITY DERIVATIVES FOR THE HIGH A--ETC(U)
1972 W E HALL N00014-72-C-0328
UNCLASSIFIED TR-1 NL

2 OF 3
AD
A033940



decreases for fixed aircraft weight. As stall speed is approached, the required angle-of-attack increases faster with decreased velocity.

The stabilator angle increases nonlinearly with decreasing velocity. The inflection point at about 160 knots is due to the change in C_{m_α} at about 11° (of Figure 2.5 of Section II). This is related to the pitch-up phenomenon discussed in Section II.

4.2.2 Lateral-Directional Trim Solutions

The trim lateral-directional controls are constrained to be zero for the calculations of this section. The original wind tunnel data has asymmetries in C_ℓ and C_n at $\beta = 0$ which result in large required values of trim aileron (δ_a) and rudder (δ_r) at high α. These asymmetries are removed in the trim calculations and in the differential equations. This modification is based on conversations with J. R. Chambers (reference 43) of Langley in which it was concluded that initial simulations should be made without the asymmetries, based on the uncertainty of the asymmetry magnitudes. Hence, δ_a and δ_r are calculated to be zero in trim.

4.3 RESPONSES IN LINEAR REGIONS

4.3.1 Longitudinal Response - Stabilator Doublet

A stabilator doublet was approximated by a sequence of ramps. This approximation was used as a control input in the δ_s control. The calculated response is shown in Figure 4.3 The SAS is operating in this calculated response.

The recorded longitudinal response of an F-4C to a stabilator input is shown in Figure 4.4 (from Reference 42). This run was selected because it met particular criteria. First, the test was performed at a relatively low Mach number, and thus its aerodynamic condition more closely corresponds to that of the F-4 data of the simulation. Secondly, the three-axis damper system (SAS) was on.

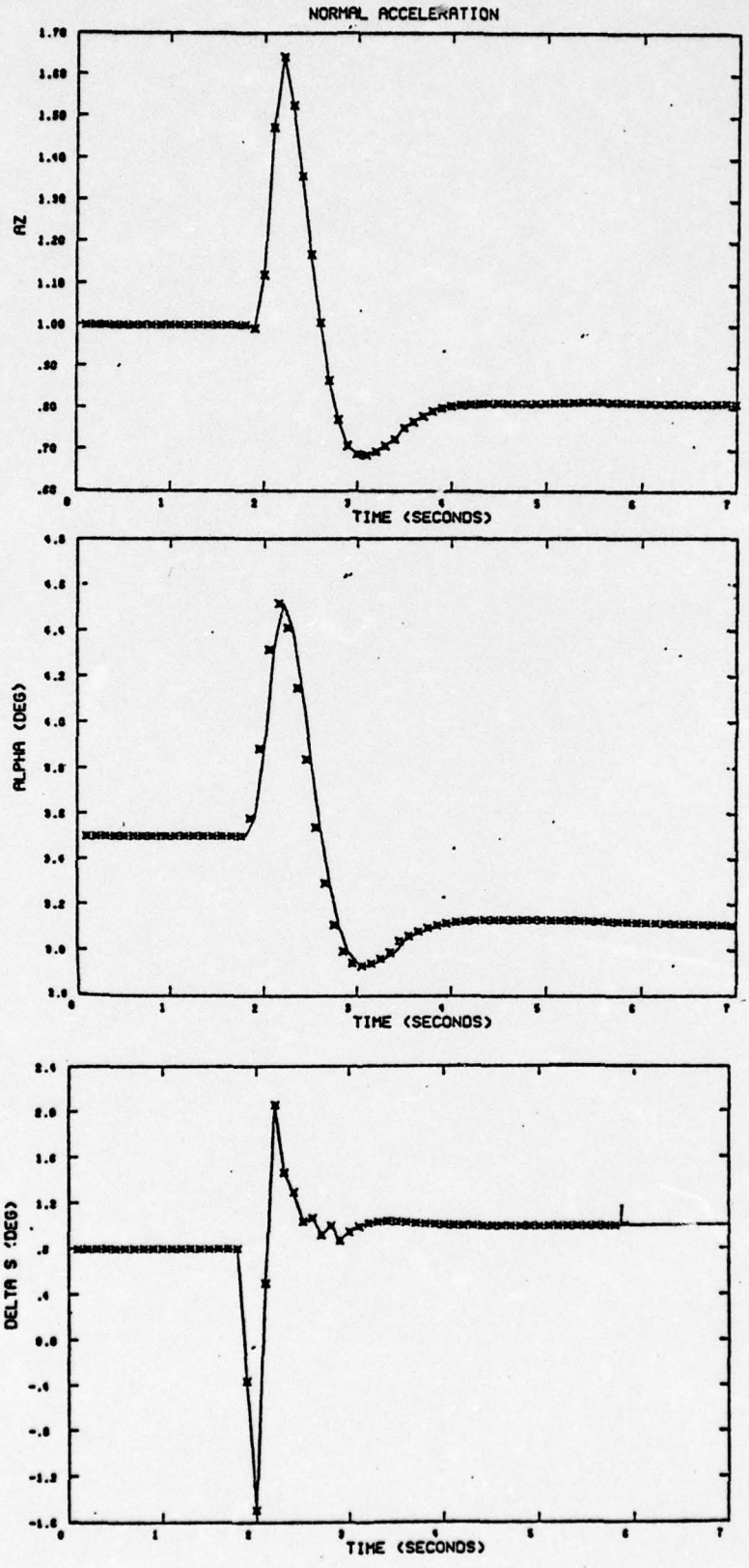


Figure 4.3. Simulated F-4 Response to Stabilator Input

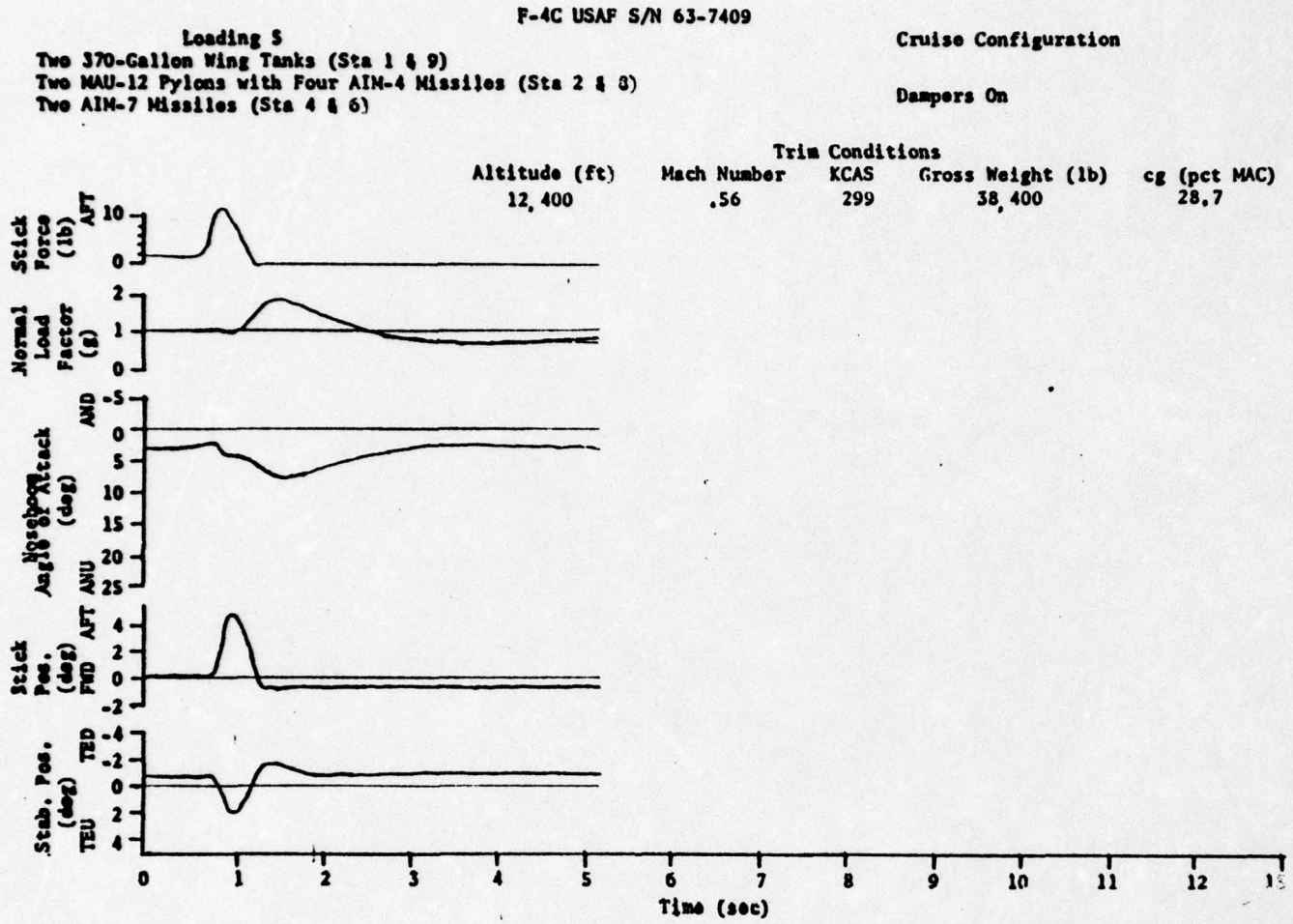


Figure 4.4. Typical F-4 Response to Stabilator Input (Reference 42)

Qualitatively, the responses are the same, although the calculated response is slightly faster. The overall correlation is considered acceptable. The approximated control is not precisely the same as that recorded, simply due to the difficulty of reading the stabilator history. Furthermore, the inertias, altitude and c.g. of the simulated airplane are not the same as for the test aircraft of Figure 4.3.* Both responses are deadbeat, although it is seen that the approximated control does not return the calculated response to the original angle of attack and that there is a residual. This residual would cause the pitch angle to keep increasing. Presumably, the pilot returned the stabilator to a zero pitch rate condition.

4.3.2 Lateral Response

No lateral-directional responses for the F-4 were found with which to perform a correlation similar to that of the longitudinal response. Specifically, it was desired to find a time history of the aircraft response to an aileron or rudder "kick" for a low angle-of-attack region. Although much high angle-of-attack data exists, such desired low α data was not formed.

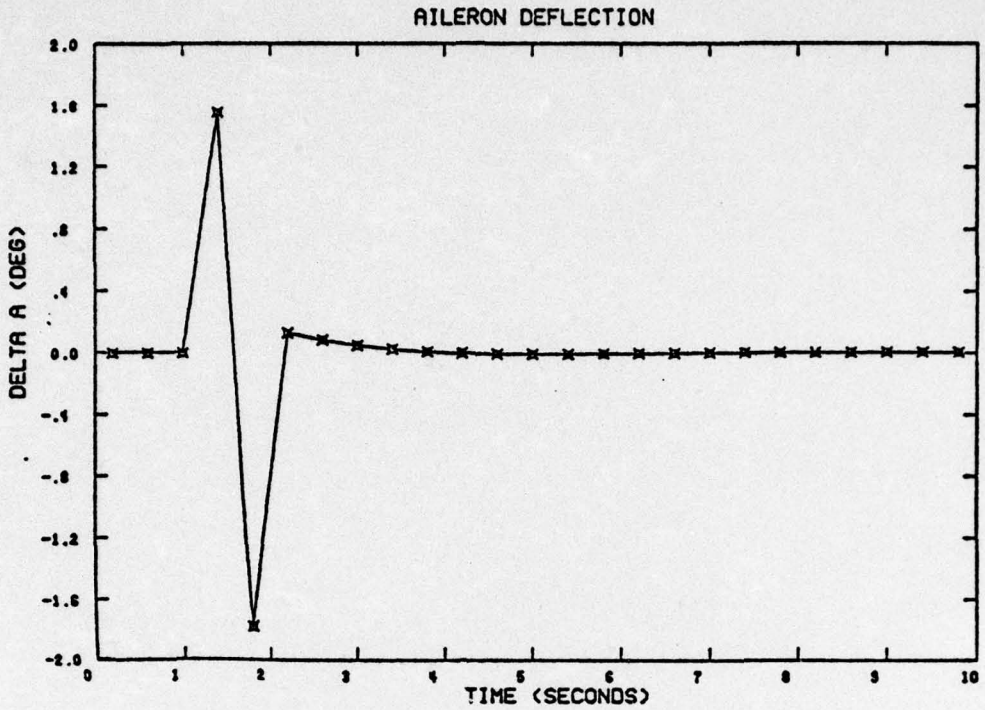
Analogous to the longitudinal case, an aileron doublet was chosen to test the lateral-direction response. The doublet is of magnitude $\pm$ 1.8° applied in .8 seconds. The dampers are on, just as for the longitudinal test case. The calculation is done for an angle-of-attack of 10°.

The calculated response is shown in Figure 4.5. It is seen that the response is stable and that the doublet returns the aircraft to almost the original bank and yaw angles. The effect of the SAS is seen in the reduction of the yaw rate to zero and the slow reduction of ψ as the a_y feedback (i.e. β feedback) washes out the sideslip.

Although no corroborative data was available, this run is considered to be representative of the aircraft response for the lower angle-of-attack regimes.

---

* Specific aircraft weight, inertias, and operating conditions were not available during this initial contract phase. This deficiency must be remembered when comparing simulation results with typical responses of the aircraft.



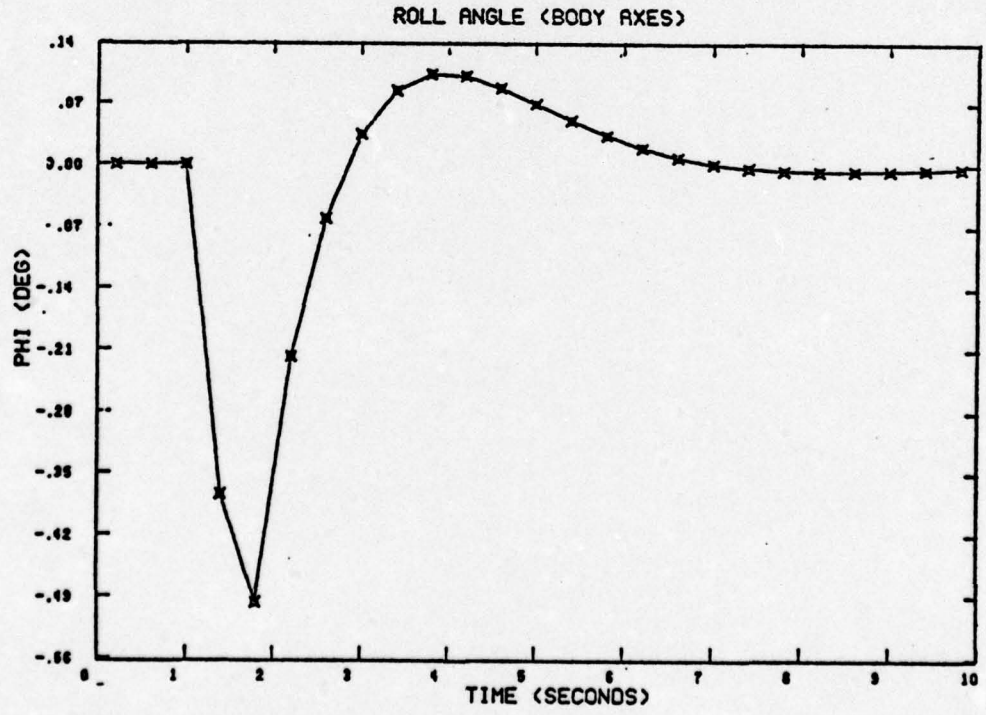
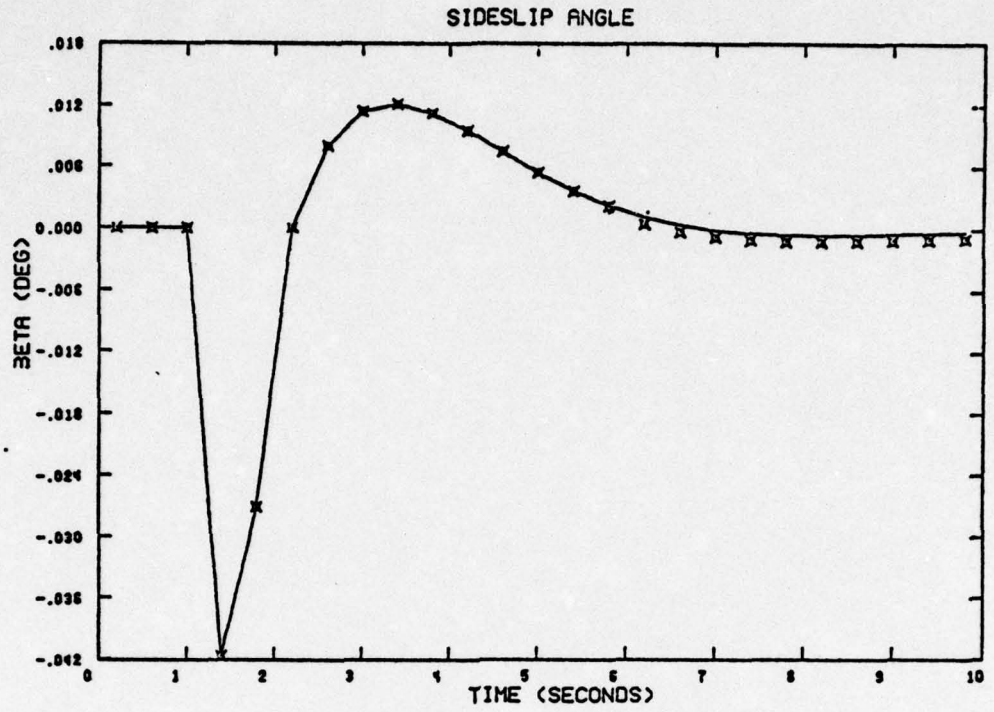


Figure 4.5 a,b. Simulated Response to Aileron Doublet (SAS on)



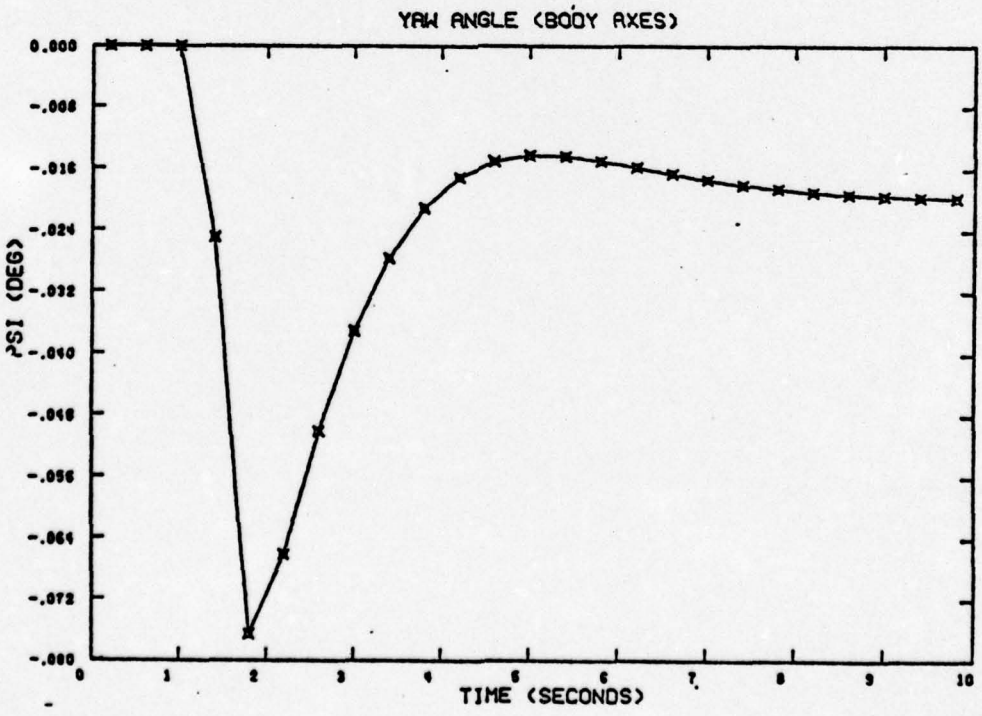
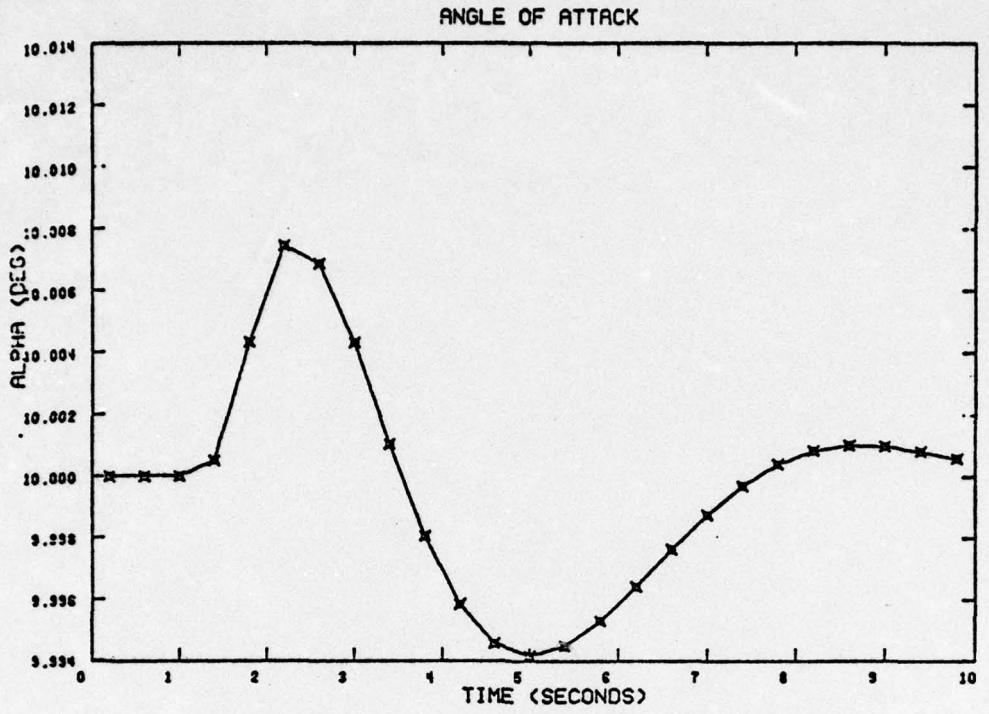


Figure 4.5 c,d. Simulated Response to Aileron Doublet (SAS on)



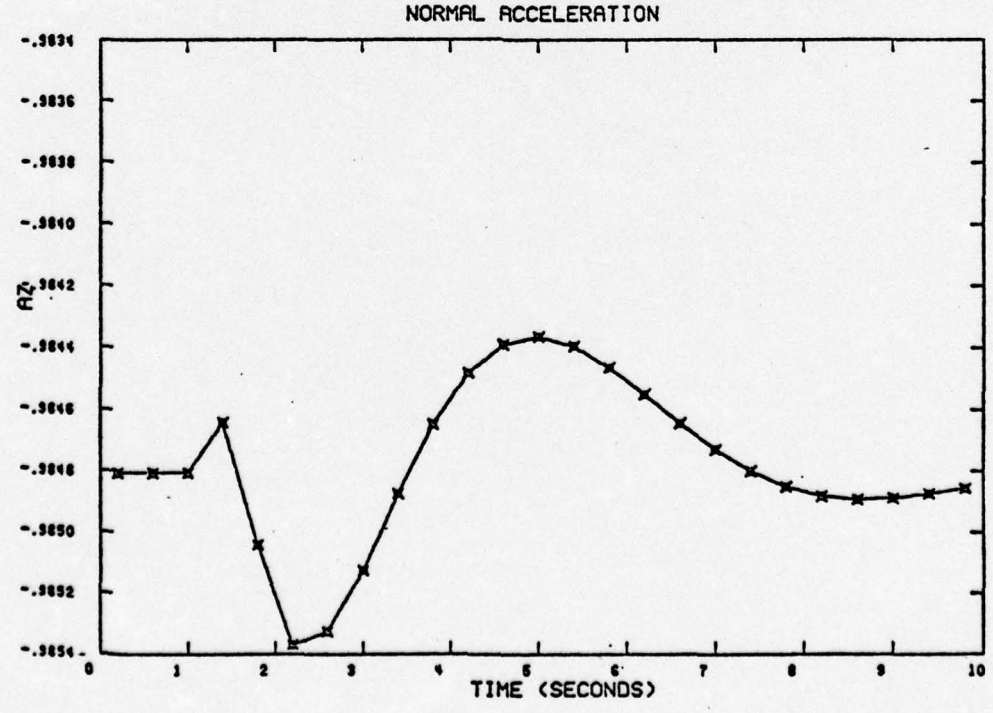
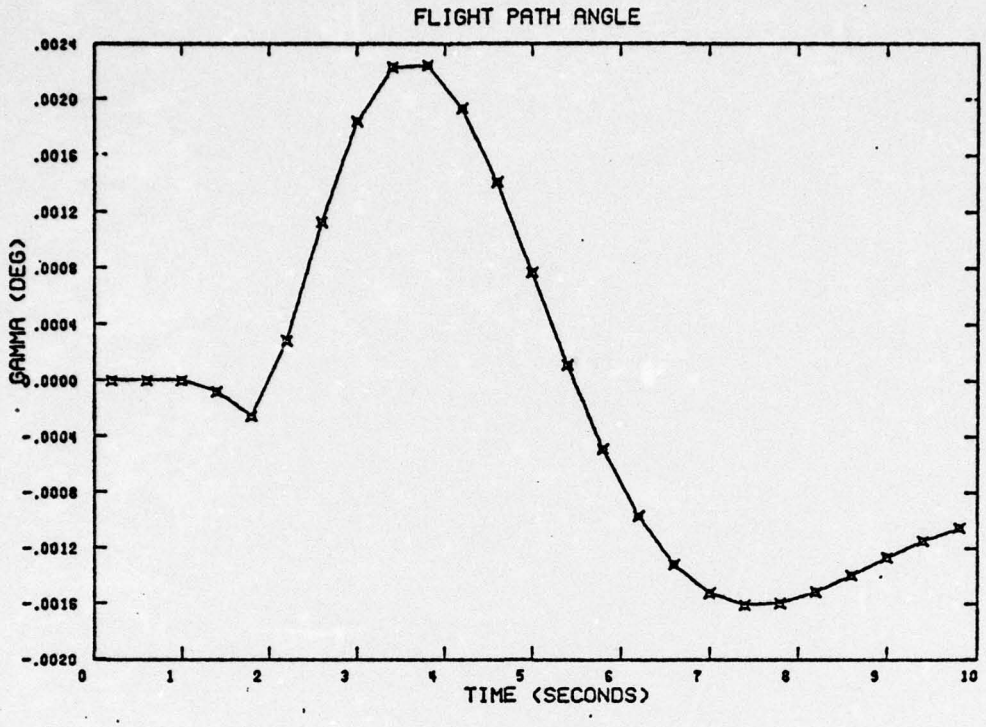


Figure 4.5 e,f. Simulated Response to Aileron Doublet (SAS on)



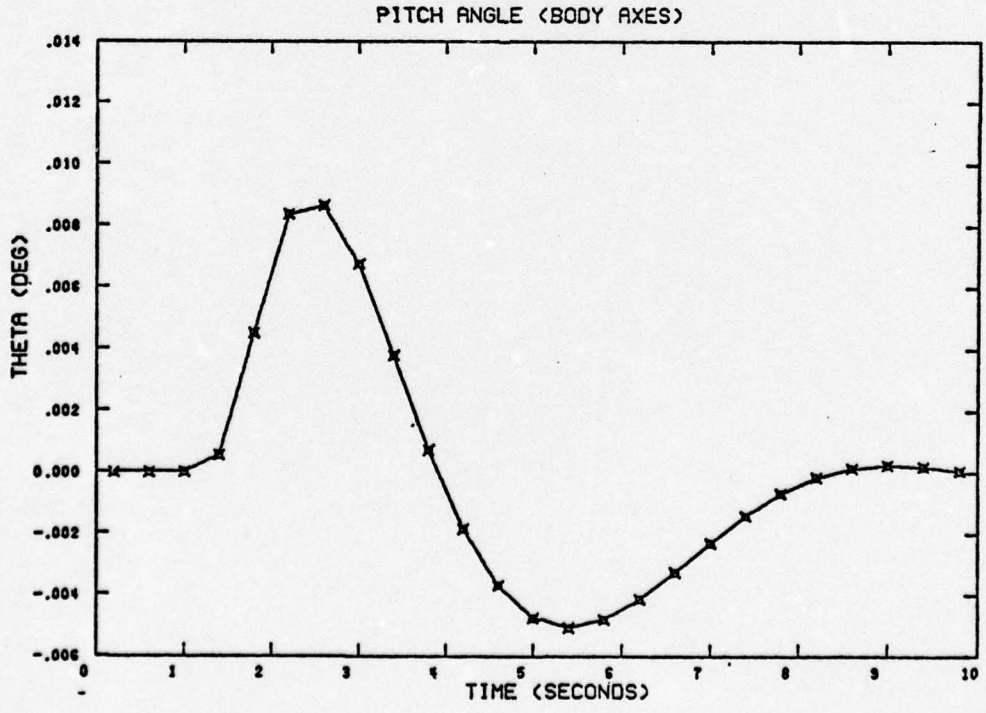
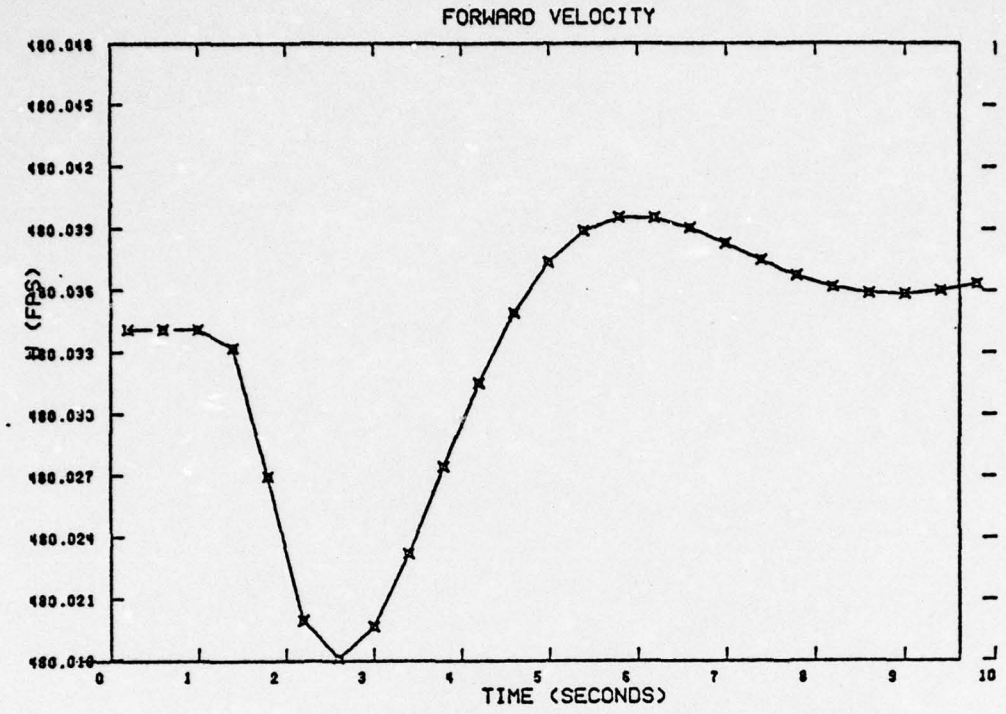


Figure 4.5 g,h. Simulated Response to Aileron Doublet (SAS on)



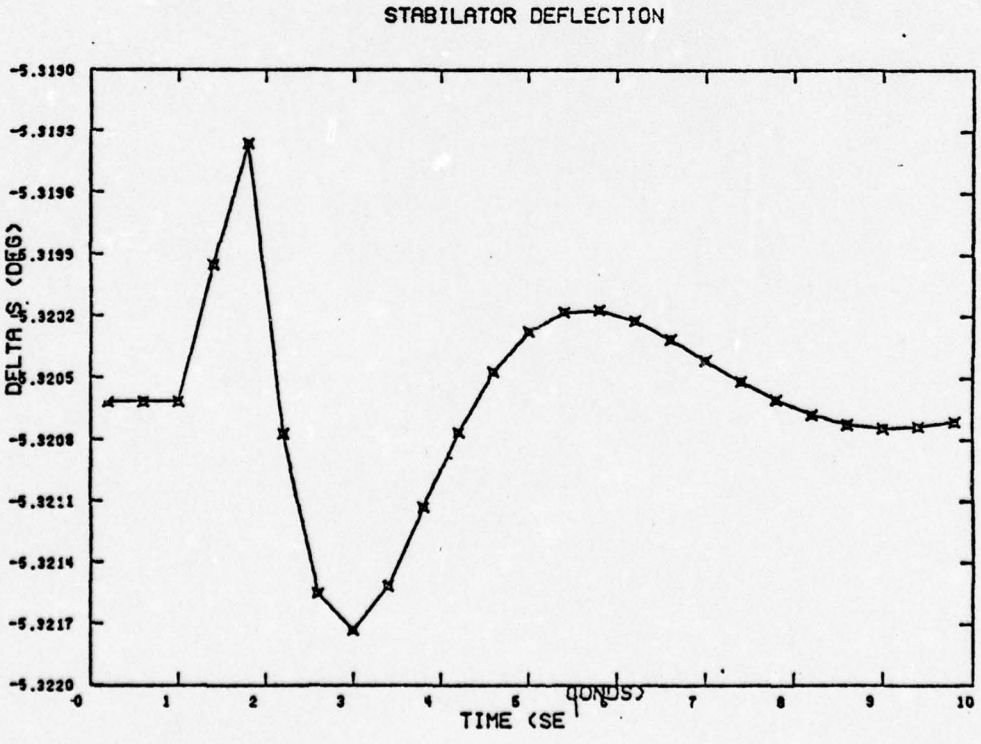


Figure 4.5 i,j. Simulated Response to Aileron Doublet (SAS on)

4.4 SIMULATION OF HIGH ANGLE-OF-ATTACK RESPONSES

4.4.1 Simulation Objective

From the initiation of the simulation development, it was felt necessary to simulate particular responses of the stall/post-stall high angle-of-attack regime such as shown in Figures 2.18 through 2.20. This goal was set for two reasons.

(1) This angle-of-attack range is critical for analyzing spin entry conditions. Wing rock and departure are responses peculiar to this region and therefore should be simulated and analyzed.

(2) Discussions with personnel at McDonnell-Douglas Aircraft Company, NASA/Langley, and Patuxent River Naval Air Test Center indicated that there is some question as to the nature of wing rock. Section II points out that wing rock occurrence is unpredictable in the cruise configuration, although Air Force tests have found wing rock to be repeatable in the flaps-down approach configuration. Air Force motion pictures have even suggested that wing rock, in the power approach mode, may be a limit cycle, although no confirming measurements have been found. The effect of pilot reactions to roll oscillations may aggravate the severity of wing rock, although not affect its onset. Simulation of this roll oscillation would help explain some of these characteristics.

For these reasons wing rock became a primary objective of the simulation.

4.4.2 Autopilot Design

As mentioned in Section III, it was necessary to design an autopilot which "simulated" pilot characteristics at high angle of attack. Phase angles and amplitude ratio were chosen as important correlation indicators (Appendix D).

The lateral/directional autopilot was developed by starting with a

simple linearized aircraft model at low angles of attack to arrive at initial gain amplitudes, and then iterating gains after each computer run. Aileron control was initially made a function of roll angle (ϕ), roll rate (p), and yaw angle (ψ). The rationale was that roll angle feedback should provide short-period roll control, while yaw angle feedback should provide long period directional control. Rudder control was initially made a function of only yaw rate (r). After iterations including a longitudinal autopilot, aileron control was made a function of roll angle only, It was also found desirable to include roll angle in rudder control, which corresponds to the pilot requirement to "pick up" a low wing with rudder at high angles of attack (Reference 2, p. 41).

The longitudinal autopilot was initially made a function of flight path angle (γ) and pitch rate (q). After several iterations it was found that sufficient natural and SAS damping was present so that very satisfactory longitudinal control was obtained by making stabilator position a function of flight path angle only.

The final set of autopilot gains used were as follows:

$$\delta_a = 0.3\,\phi_B \qquad -30^\circ \leq \delta_a \leq 30^\circ$$

$$\delta_r = 1.0\,\phi_B + 7.0r \qquad -30^\circ \leq \delta_r \leq 30^\circ$$

$$\delta_s = +1.0\gamma \qquad -21^\circ \leq \delta_s \leq 9^\circ$$

This autopilot provides the following desirable characteristics:

(1) true pilot response as closely as possible,

(2) good wings-level control at low angles of attack,

(3) an "average" wings-level control during wing rock,

(4) smooth angle-of-attack and pitch control, and

(5) control that does not significantly distort wing rock characteristics.

4.4.3 Characteristic Control Specification for Wing Rock

Initial attempts to obtain wing rock were based on simple aileron doublets such as those discussed in section 4.2.2. Angles of attack of 20° and higher were selected for these doublets. It was found that wing rock, departure, and spin could be obtained with such inputs. However, because no documented responses for similar doublets were available from flight test data, another approach was required.

A common maneuver for test pilots is the decelerating stall. A good aircraft maneuver with which to conduct simulations of pre-departure wing rock is a wings-level approach to a one "g" stall. This is because the maneuver very slowly puts the aircraft through a range of angles of attack in which the flight characteristics can be studied in detail as they develop.

A pilot performs an approach to one "g" stall by initially trimming the aircraft at some angle of attack, reasonably well below the range of interest, and then decreases throttle setting to commence a deceleration as he simultaneously pulls back on the stick to maintain a zero flight path angle. The deceleration should be sufficiently slow (about 1 KIAS/sec) that rapid energy loss does not effect the maneuver. Autopilot development was based as much as possible on what the pilot is attempting to do in the cockpit while performing the maneuver.

In addition, this maneuver has many features in common with the banked turn simulation of wing rock reported in reference 28 and discussed in Section II.

4.4.4 Computer Simulation of Pre-Departure Wing Rock

The flight test maneuver simulated was a one "g" approach to stall. The aircraft configuration was as follows:

Configuration	Cruise
Weight	39,000 lbs
c.g.	33.8% m.a.c.
Loading	clean (I_x = 27,500 slug-ft^2)
Altitude	30,000 ft.
SAS	On
Autopilot	On

The aircraft was initially put in a one "g" wings-level trimmed flight condition at 18° angle of attack (233 Knots) and 30,000 feet altitude. Thrust was decreased 3% below trim thrust and then held constant. As the aircraft slowly decelerated (about 1 KIAS/sec), the stick was pulled aft (corresponding to autopilot stabilator control) simultaneously to maintain zero flight path angle.

Pre-departure wing rock commenced at about an angle-of-attack of 21.5°. During the second cycle, wing rock had increased in amplitude to about ± 12° while sideslip angle reached about ± 3.5°. Between two and three full cycles of wing rock occurred prior to the end of the computer simulation run at which time it appeared that departure was commencing.

Full aft stick occurred at an angle of attack of 25° after one half cycle of wing rock, and was held aft by the autopilot until the end of the run. Angle of attack varied from 24.5° to 27.3° once full-aft stick was reached, and flight path angle began decreasing to a final value of about 10° below horizontal.

Aircraft heading slowly veered off to the left through wing rock. Pitch attitude motion was generally smooth with no abrupt, large excursions.

All of these motions are plotted in Figure 4.6. The pre-departure wing rock characteristics observed in the simulated flight test maneuver were:

Onset:	$\alpha = 21.5°$
Roll amplitude:	$\pm$ 12° (second cycle)
Sideslip amplitude:	$\pm$ 3.5° (second cycle)
Period:	7.5 seconds
ϕ_B-β phase angle	60° approximately
Aileron motion	$\pm$ 4° (second cycle)
Rudder motion	$\pm$ 19° (second cycle)

The goal of this computer simulation was to qualitatively match the phenomena observed in flight at high angles of attack. It was not anticipated that flight data could be matched exactly. The computer simulation was based on wind-tunnel data and as discussed previously, these data are known to be inexact at high α. Thus, differences between the results of this simulation and actual flight traces should be expected.

Table 4.1 is a summary comparison of the wing rock characteristics of an actual flight test, a piloted simulation, and the computer simulation of this report.

As observed previously, wing rock is not necessarily reproducible in flight. Many factors evidently enter the problem including geometry of the particular aircraft and the control forces of the pilot. Thus, one should not expect exact matching between a simulation and an actual

TABLE 4.1

WING-ROCK COMPARISON

(AIRCRAFT = F-4)

Parameter			Data Source: A.F. Flight Test	Data Source: NASA Fixed-Base Simulation	Data Source: SCI Digital Simulation
		Reference	Figure 2.19	Figure 2.21	Figure 4.6
		Onset α	$\sim$ 22°	$\sim$ 18°	21.5°
		Period of Oscillation (secs.)	$\sim$ 4.5	$\sim$ 3	$\sim$7.5
		Cycles to Departure	$\sim$ 3	$\sim$ 4	$\sim$ 2.5
	(During Second Cycle)	Roll (ϕ) Amplitude	± 7°	± 6°	± 11°
		Sideslip (β) Amplitude	± 2.1°	± 2.3°	± 3.1°
		$\left(\frac{\text{Roll Amplitude}}{\text{Sideslip Amplitude}}\right)$	3.3	2.6	3.5
		Phase (ϕ/β)	$\sim$ 60°	$\sim$ 0°	$\sim$ 60°
		Phase (δ_a/ϕ)	- 135°	$\sim$ 80°	- 150°
		Phase ($\delta_r/(-\beta)$)	+ 165°	---	+ 150°
		Aileron Deflection	± 5° (rt.) ± 2.5° (lt.)	± 3°	± 4°
		Rudder Deflection	± 3.5°	---	± 19°
	Aircraft Condition	Weight (lbs.)	47,650	36,187	39,000
		Speed (kts.)	290	?	233
		Altitude (ft.)	32,000	?	30,000
		Notes:	SAS on; Full Center-line Fuel Tank	SAS on; Pilot-In-Loop; Traces Difficult To Read	SAS on; Autopilot on; Used Wind Tunnel Data

NOTE: A subsequent run of the simulation at a 47,650 lb. gross weight yielded a slightly convergent "wing rock" at 263 knots.

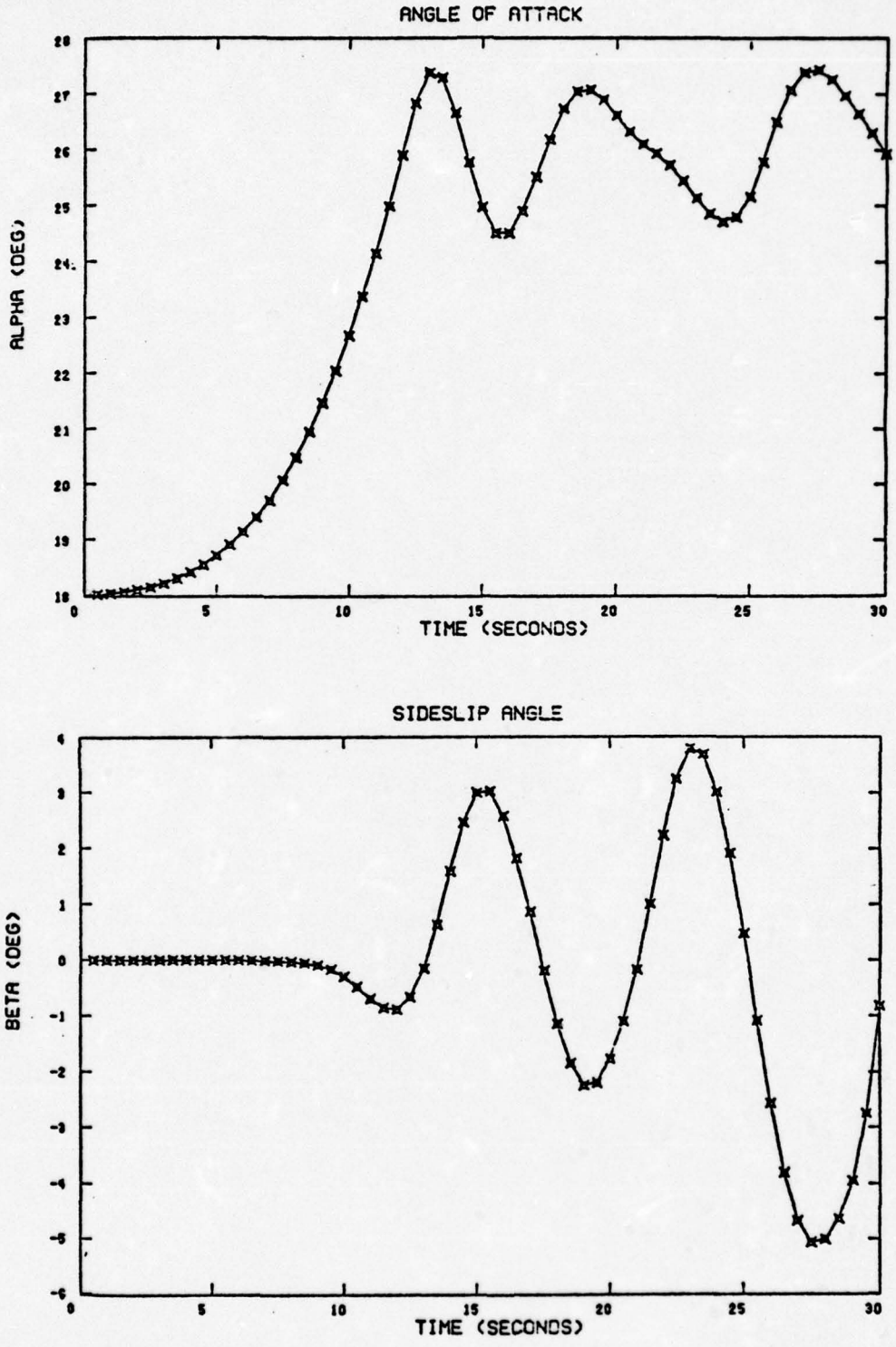
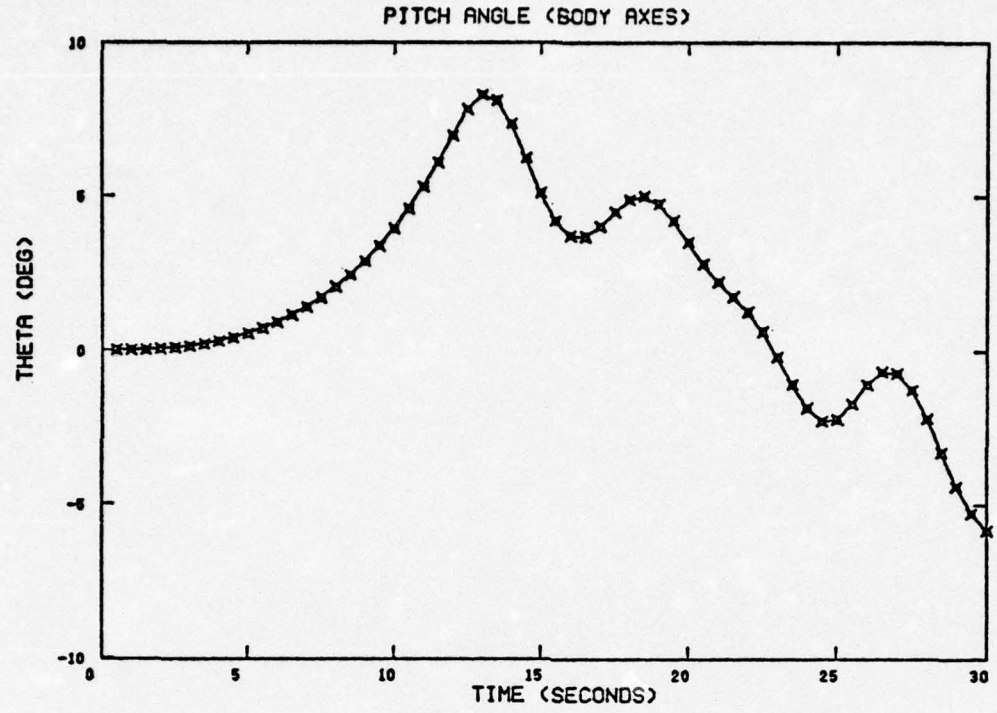


Figure 4.6a Simulated "1 g" Stall leading to Wing Rock and Departure



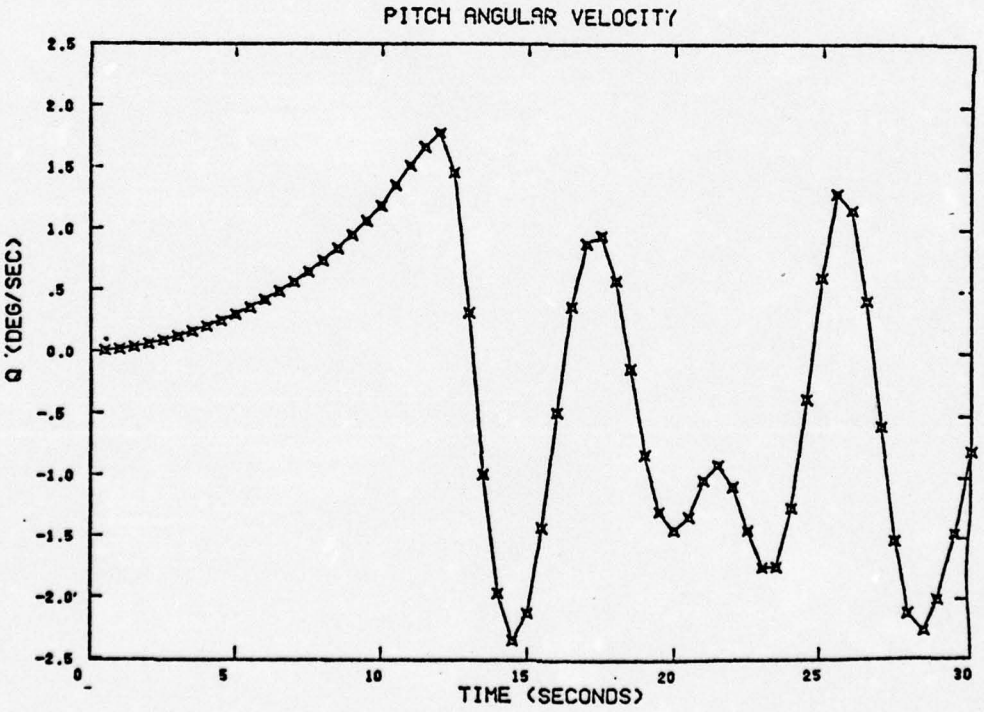


Figure 4.6b Simulated "1 g" Stall leading to Wing Rock and Departure

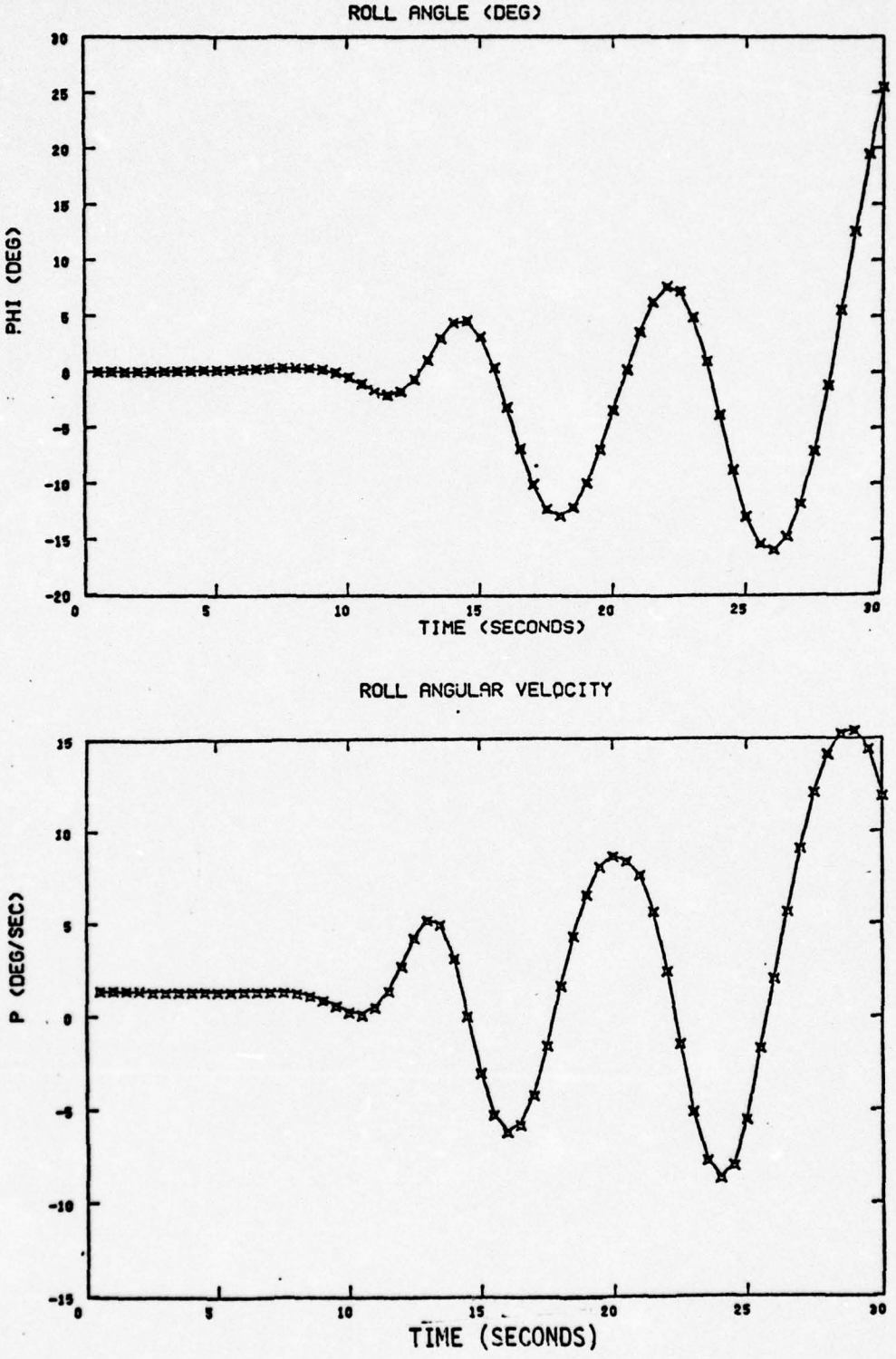
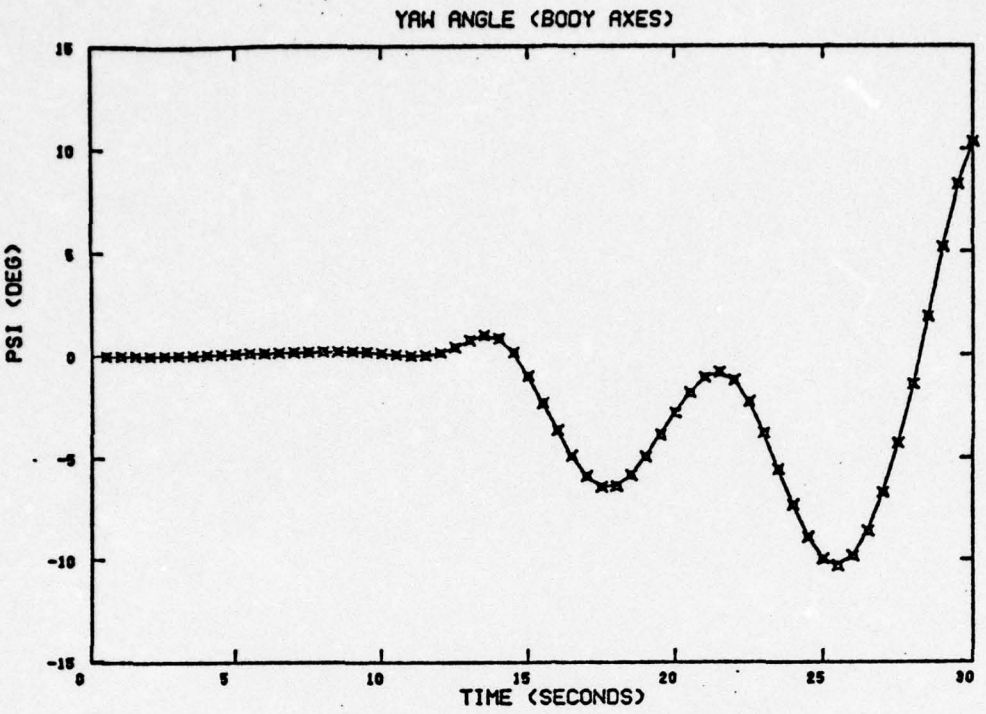


Figure 4.6c Simulated "1 g" Stall leading to Wing Rock and Departure



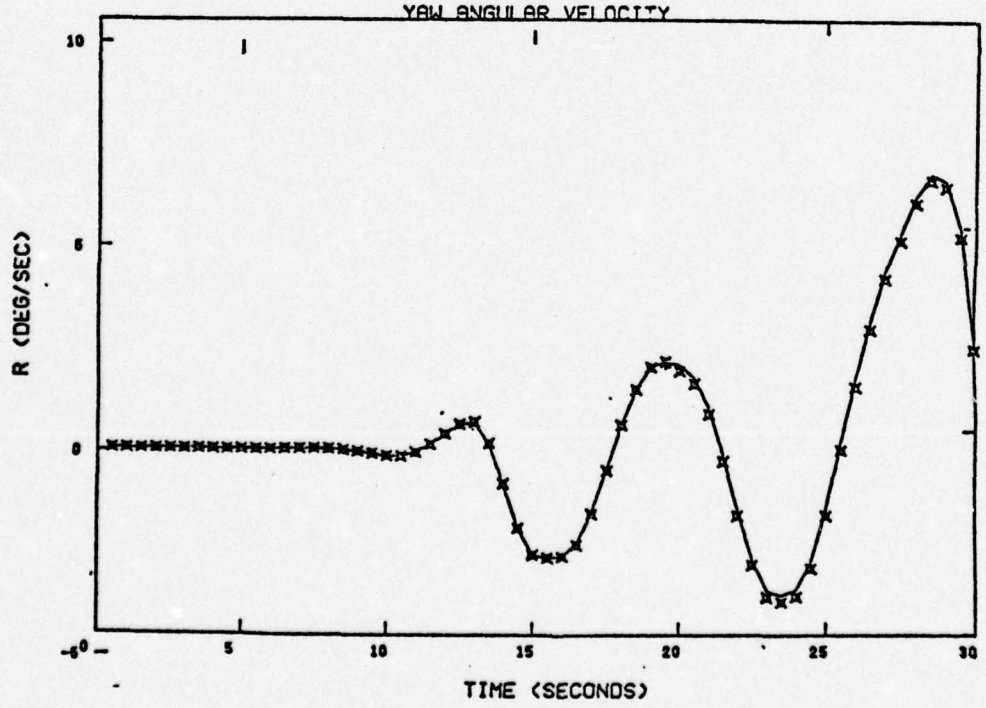


Figure 4.6d Simulated "1 g" Stall leading to Wing Rock and Departure

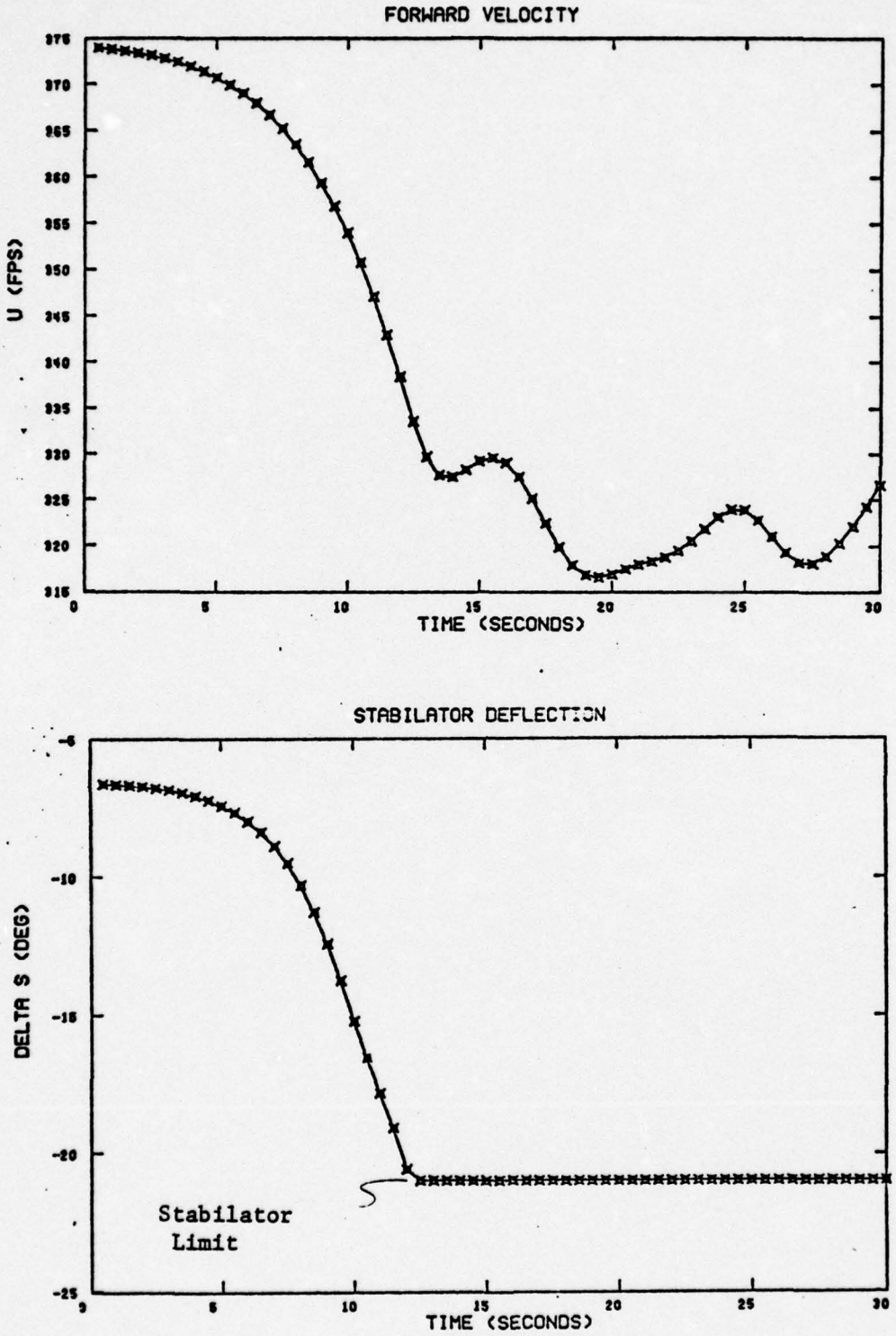
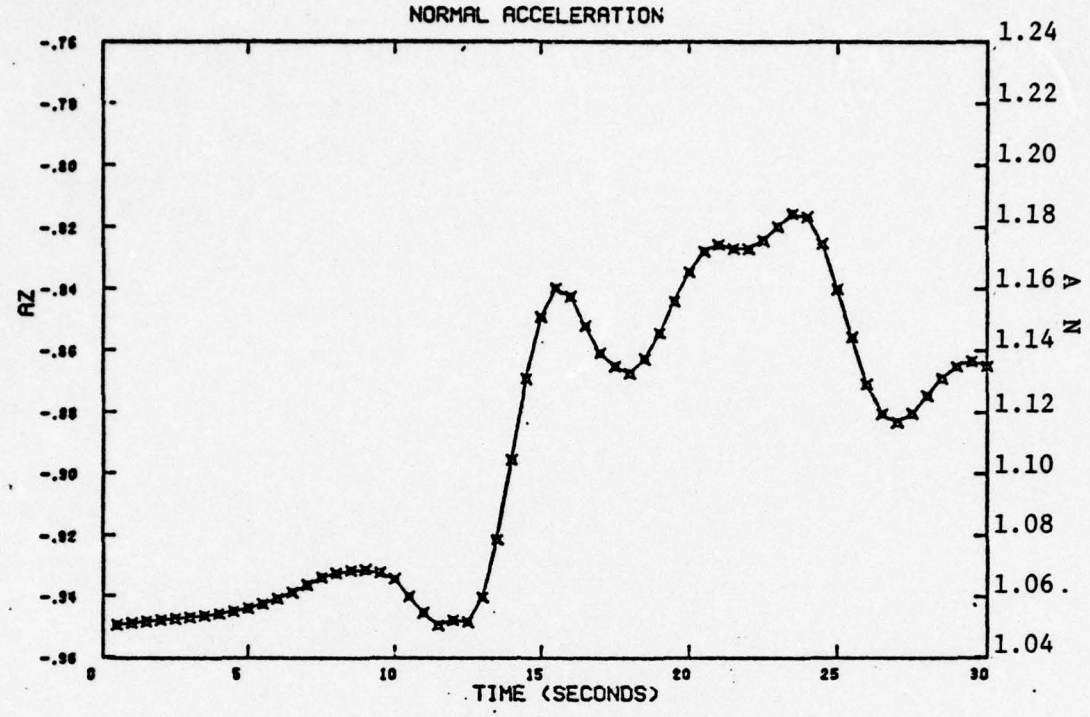


Figure 4.6 e Simulated "1 g" Stall leading to Wing Rock and Departure



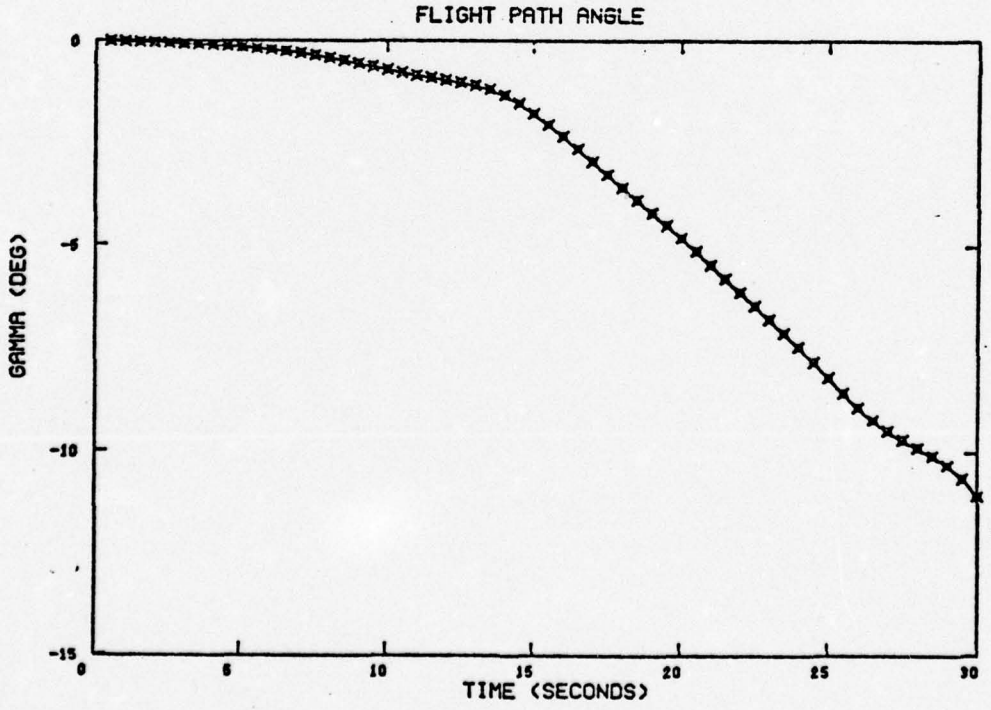
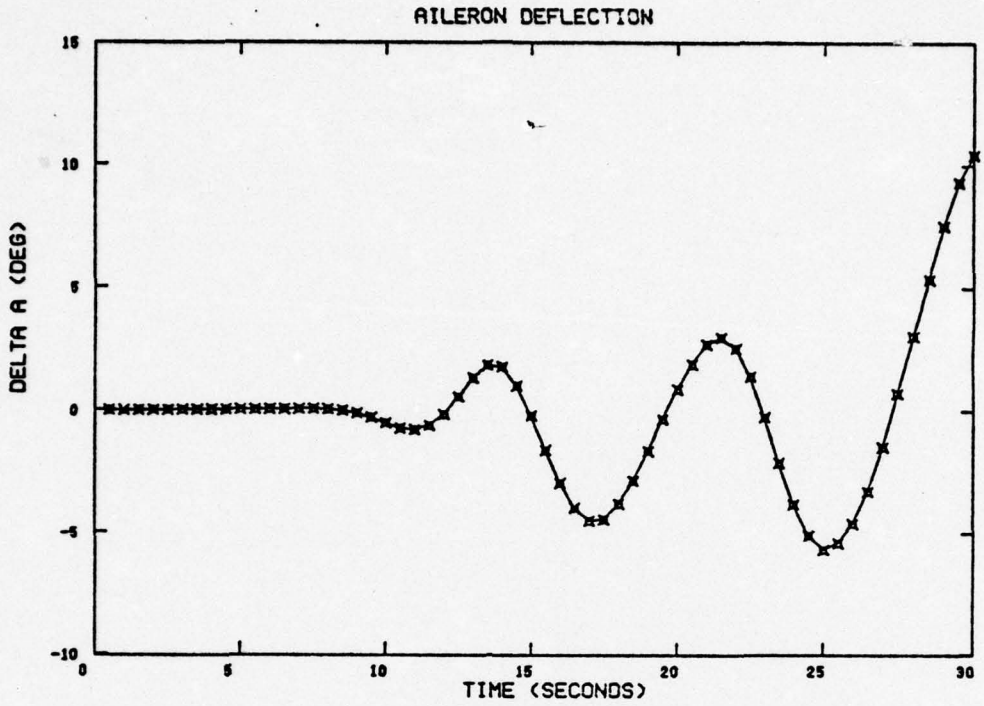


Figure 4.6f Simulated "1 g" Stall leading to Wing Rock and Departure



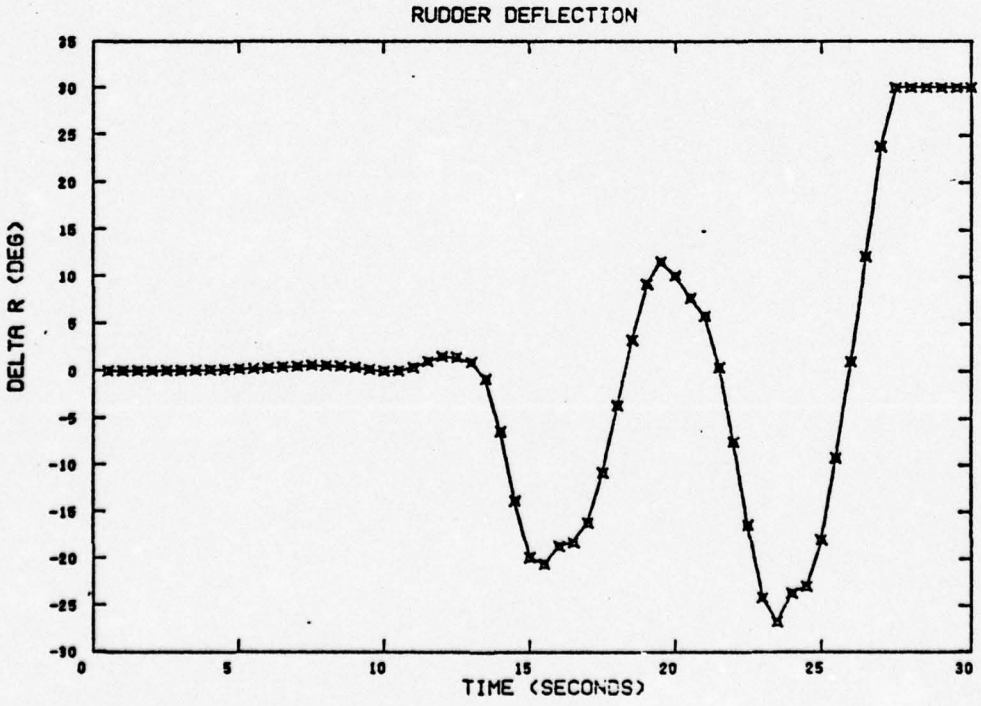


Figure 4.6 g Simulated "1 g" Stall Leading to Wing Rock and Departure

flight - anymore than one could expect exact matching between two different examples of wing rock with the same model aircraft. Table 4.1 is presented with this philosophy.

The flight test results in Table 4.1 are for the responses shown in Figure 2.19. The aircraft was in the cruise configuration (gear and flaps up, speed brake retracted) and had a full center-line fuel tank slung beneath the fuselage. Approximately three cycles of wing rock were obtained before departure occurred.

The NASA simulation in Table 4.1 is shown in Figure 2.20. This time history is difficult to read because of its small scale and the resulting numerical values in Table 4.1 are approximate at best. The NASA simulation is interesting because a human pilot was used to "fly" the simulation.

Finally, the simulation results presented in Figure 4.6 of this report are listed in the last column of Table 4.1. These results are in general agreement with the Air Force flight test results. The major differences are the period of the oscillation (7.5 seconds versus ~ 4.5 seconds) and the commanded rudder deflection ($\pm$ 19° versus $\pm$ 3.5°). The airspeed of the simulation (233 knots) is lower than that of the flight test (290 knots). As noted, a subsequent run at higher gross weight produced a velocity of 263 knots with a slightly convergent wing rock. The control deflections commanded in the simulation arise from the nature and gains of the autopilot. It was necessary to employ some form of control in the wing rock simulation to prevent the aircraft from departing before wing rock could be fully observed. Thus all three examples in Table 4.1 employ a feedback control on the aircraft dynamics; the first two use a pilot while the third uses an autopilot.

The selection of the autopilot is discussed in Sections 3.5, 4.2.2, and in Appendix D. It is reiterated here that the autopilot selected

was designed to reasonably model the control inputs a pilot might make in an effort to control the aircraft. However, numerous computer runs with various types of autopilot control-laws proved that wing rock can be made either convergent or divergent depending on the autopilot. An example of this will be given later in this section.

4.4.5 Effect of Individual Aerodynamic Coefficients in Computer Simulation of the Pre-Departure Wing Rock

Having achieved a qualitative correlation with wing rock observed in flight, an analysis was performed on the simulation results to determine the driving mechanisms of (simulated) wing rock.

Figure 4.7 shows roll angle (ϕ , positive for right wing down), sideslip (β, positive for nose left) and angle of attack (α, positive nose-up) versus time. The phase relationship between ϕ and β is also plotted. In the developed region of wing rock (after $\sim$ 1 cycle), it is seen that roll leads sideslip by about 60°. This is the phase value observed in the flight test results of Table 4.1. It is not an atypical phase angle for Dutch roll (see Etkin, Reference 18).

Figure 4.7 shows that wing rock starts* rather abruptly at an angle-of-attack of about 21.5° with the left wing dropping about 2°. This is accompanied by a sideslip to the right of about 1°. After initiation the roll leads the sideslip up to a phase angle of about 60°. The amplitude builds to departure at the end of the run. During this motion the wing tips trace out elliptically-shaped spirals. This is illustrated in Figure 4.8 for the left wing tip by plotting roll angle versus sideslip angle. The sideslip angle scale is reversed so that the

---

* For this simulation, wing rock is initiated by an asymmetrical moment from the stabilator. This is the only way - other than numerical instability - that this simulation (straight-ahead one-g pull-up) could start a lateral motion. For the real aircraft, any source of asymmetry could initiate wing rock.

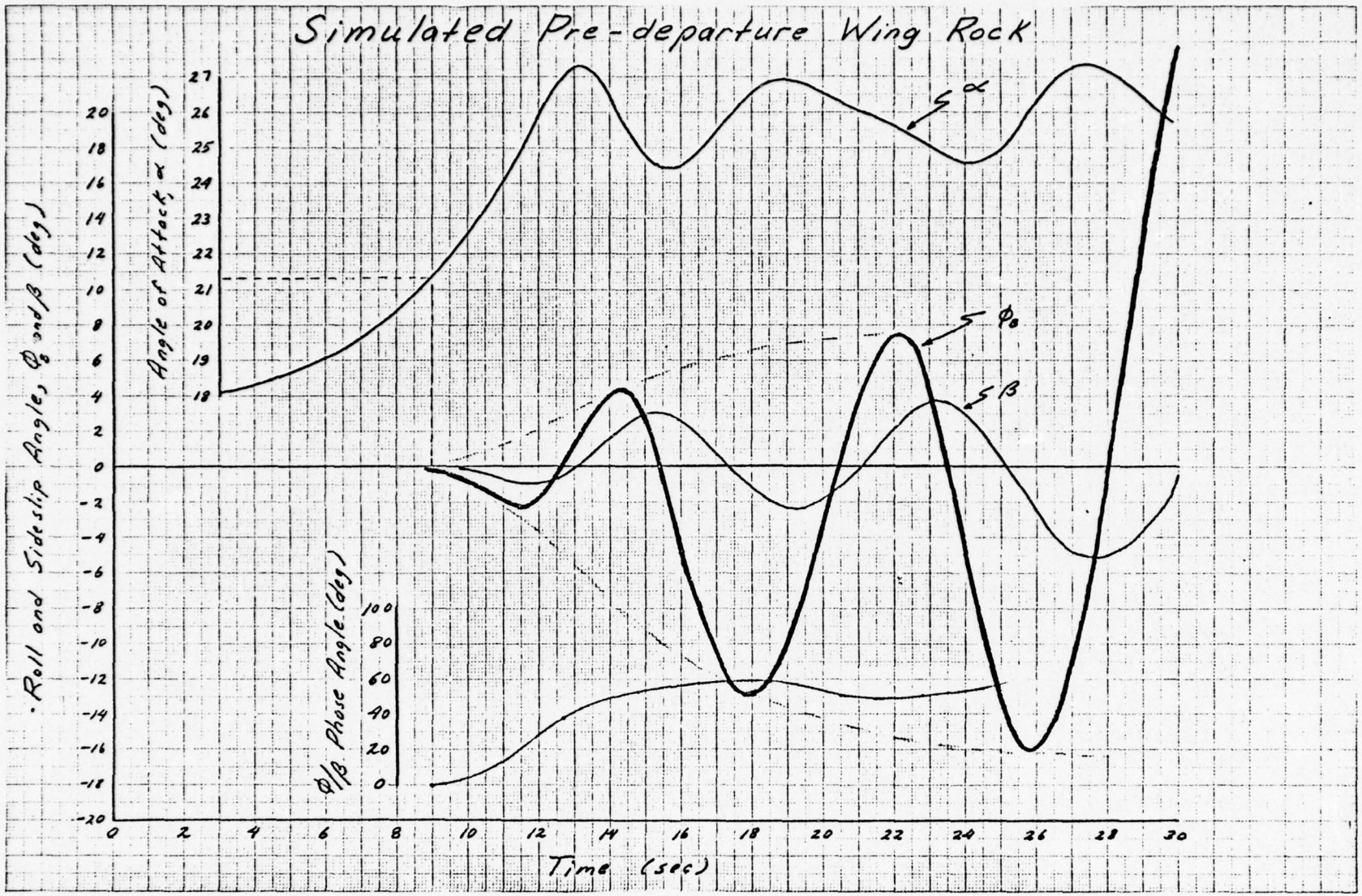


Figure 4.7 Time History of Roll/Sideslip Phase Angle of Simulated Wing Rock

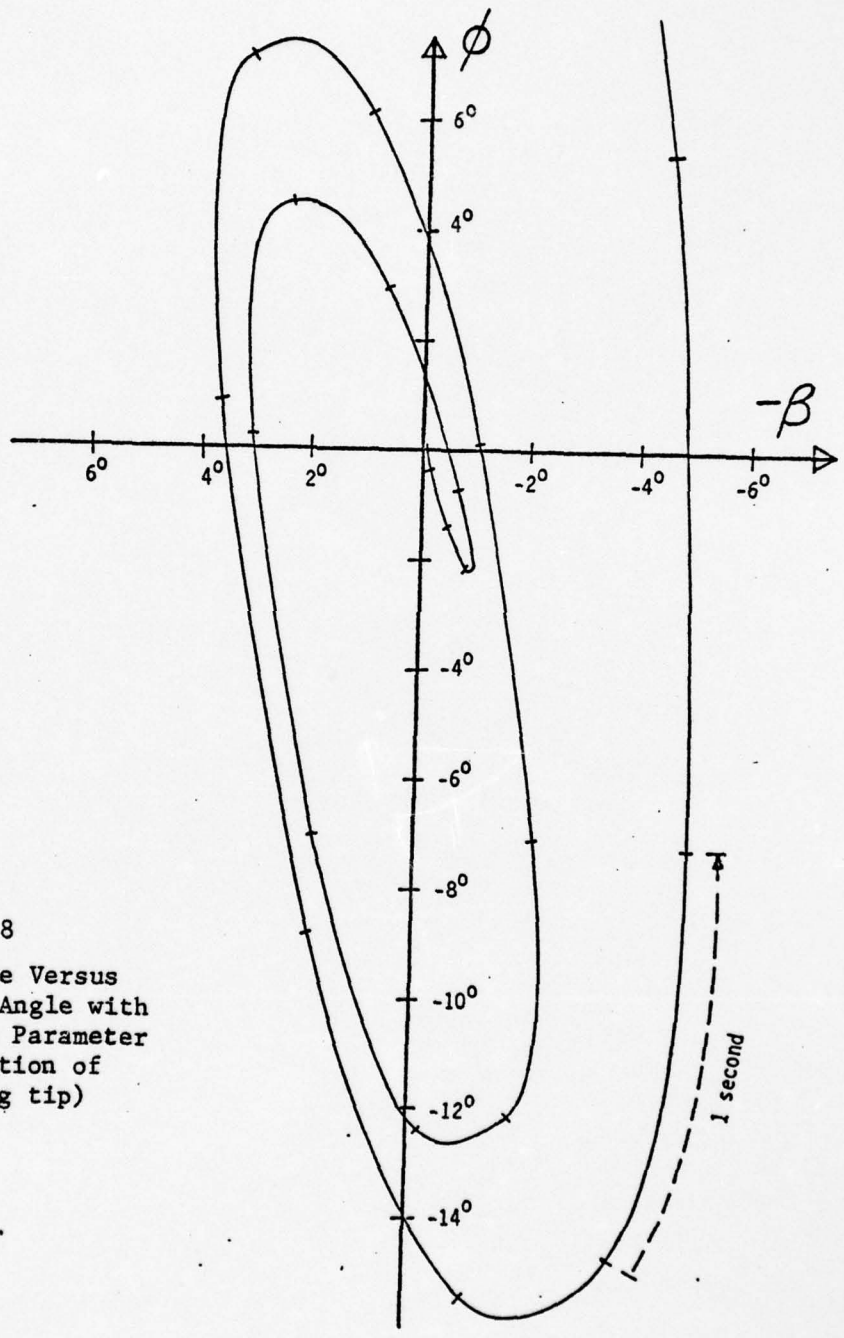


Figure 4.8

Roll Angle Versus Sideslip Angle with Time as a Parameter (shows motion of left wing tip)

proper counter-clockwise sense of left wing-tip motion is displayed (as viewed by a non-rotating observer in the pilot's seat). One-second intervals are marked on the trace by tic marks.

It is obvious that the net result of the moments acting on the aircraft is destabilizing for this simulation (and for the flight test results, see Table 4.1). It was desired to determine the driving mechanism of this motion. This was done by first plotting the individual aerodynamic moment components versus time. Figure 4.9 shows the aerodynamic contributions to rolling moment and Figure 4.10, yawing moment. These traces contain much information but are difficult to read. It is observed that the moment components have the same fundamental frequency as the angular motions. Moreover, the phase relationships between the traces are essentially maintained after the initiation phase and before departure.

Phasor diagrams for both Figures 4.9 and 4.10 are presented in Figure 4.11. Figure 4.11a plots each aerodynamic rolling-moment contribution as a vector. The angle of the vector (measured positive counter-clockwise) relative to the vector, ϕ, gives the phase of that moment contribution relative to the roll angle, ϕ. The length of the vector is proportional to the amplitude of the envelope of that moment contribution. A similar plot is made to the same scale for the yawing moments relative to $-\beta$ (+ yaw) in Figure 4.12. These phasors were obtained at the recording time of 20 seconds.

The phasor diagram is a useful tool in resolving the complexity of the time-history charts. The phase angle of the moment relative to the motion determines whether the moment is stabilizing or destabilizing. The magnitude of the phasor determines the relative importance of the contribution of that particular moment. These aspects of the phasor representation are shown in Appendix E. The phasor for a particular moment, such as $C_n(\alpha,\beta)$ is plotted in one of the four quadrants depending on its positive or negative contribution to the static (i.e., spring)

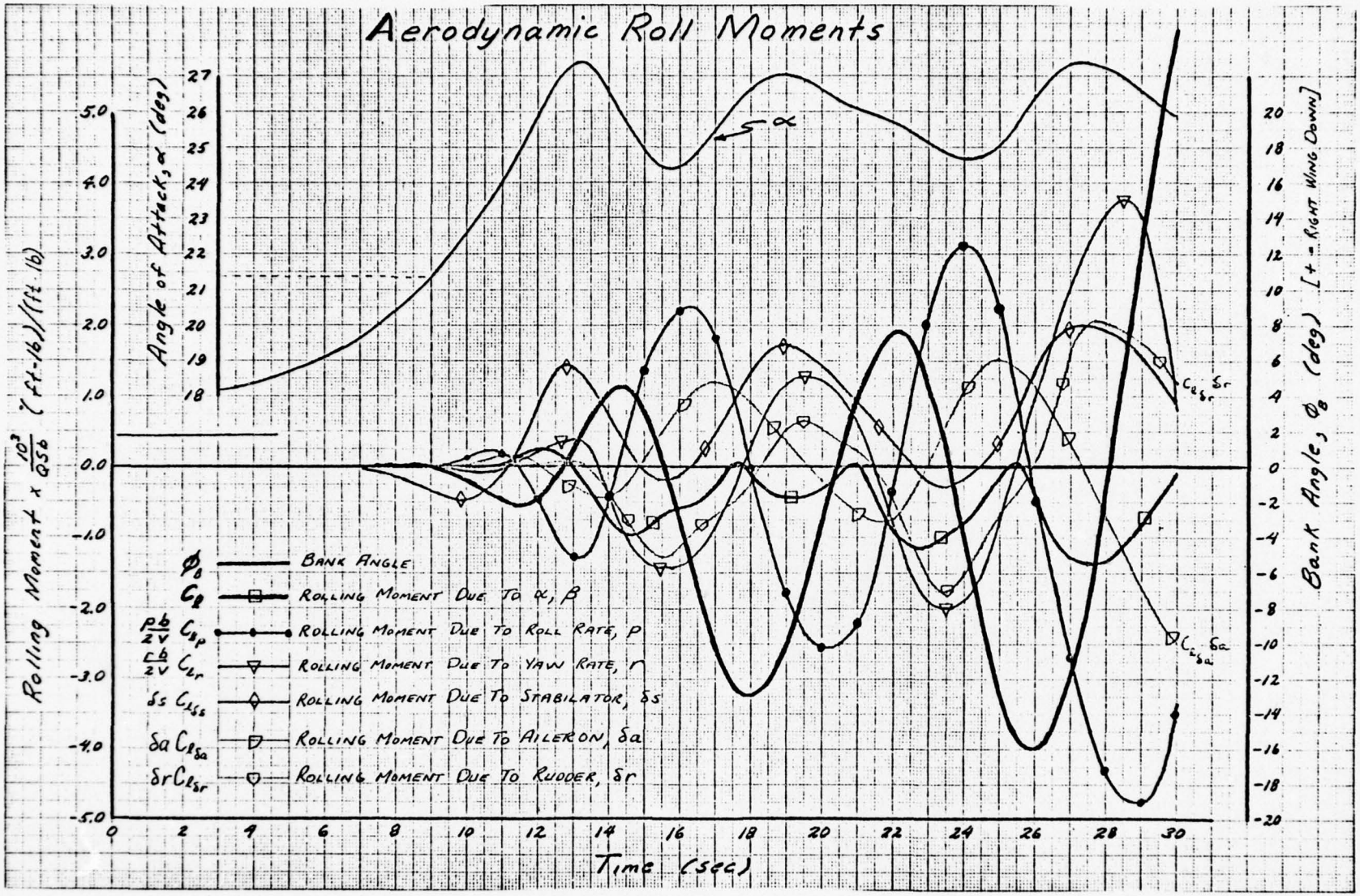


Figure 4.9 Time History of Aerodynamic Roll Moments

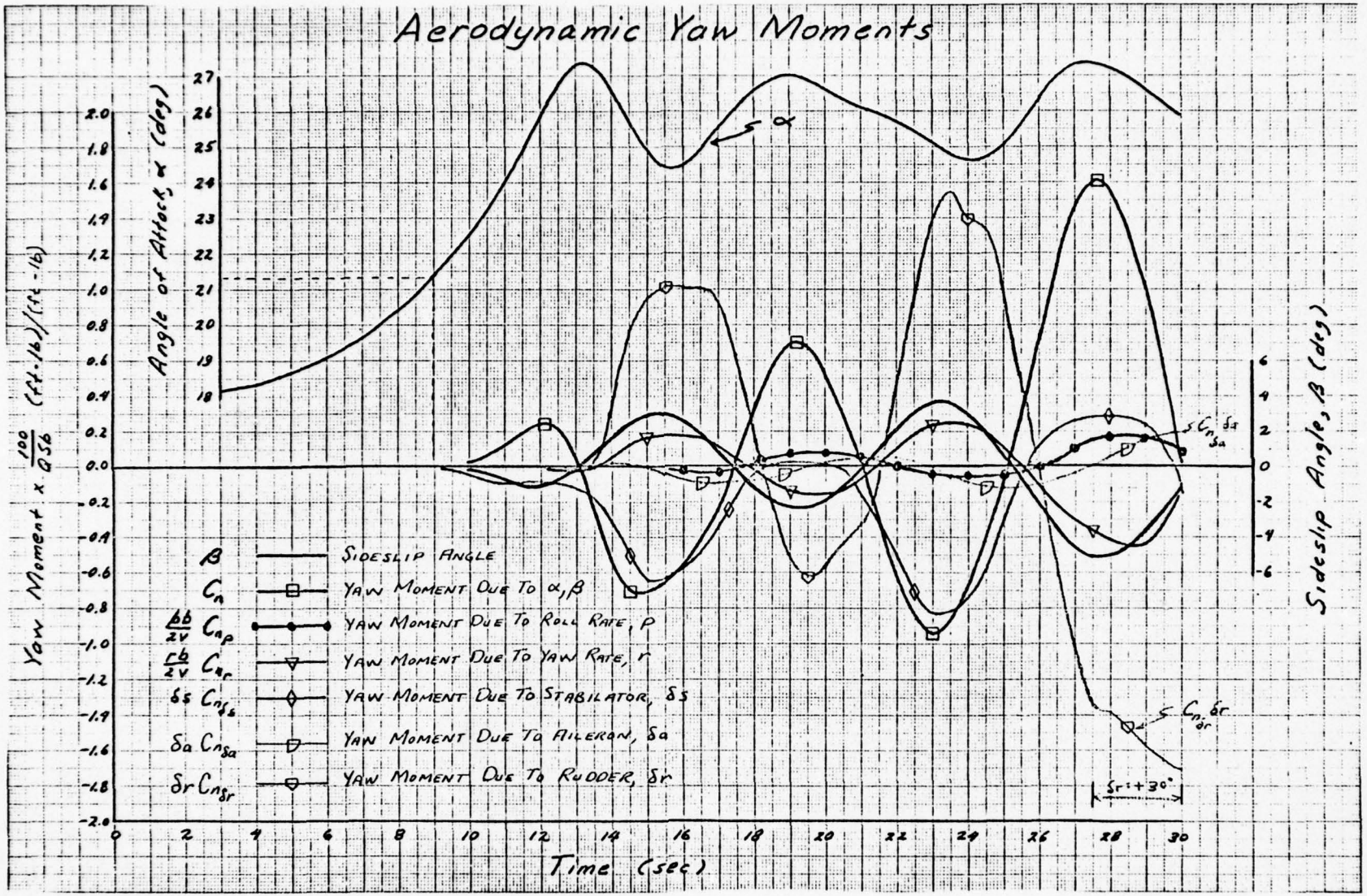


Figure 4.10 Time History of Aerodynamic Yaw Moments

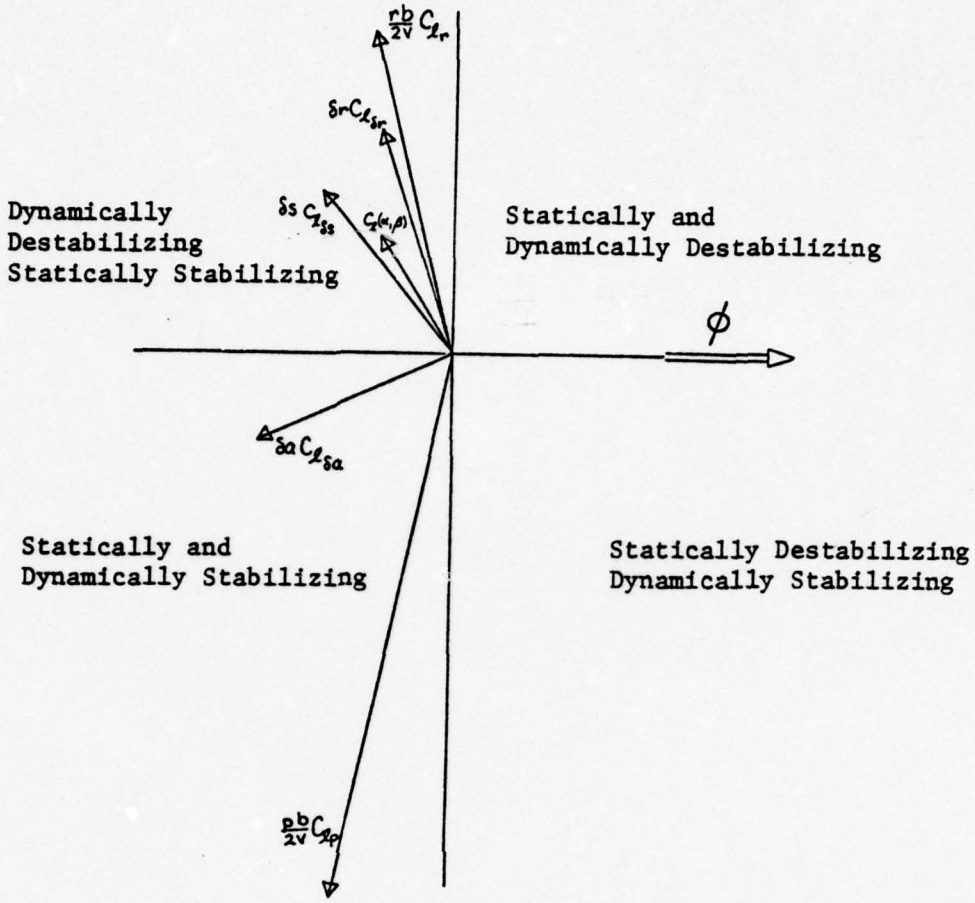


Figure 4.11 Phasor Diagram of Aerodynamic Roll Moments

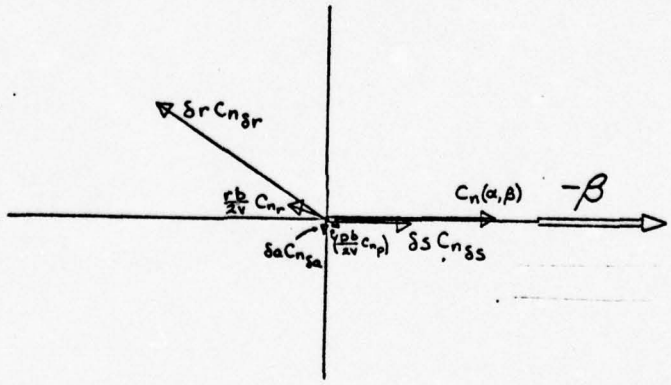


Figure 4.12 Phasor Diagram of Aerodynamic Yaw Moments

or dynamic (i.e., damping) stability of the motion.

For the roll motion, aileron (δ_a term) and roll damping (C_{ℓ_p} term) are stabilizing. The autopilot is opposing the roll and is attempting to damp the motion. The other four terms, while statically stabilizing, are dynamically destabilizing, The net result is that energy is added to the system and the motion eventually diverges. Note that both stabilator and rudder couple through to help destabilize roll.

The yawing moments are displayed in Figure 4.12. The magnitudes are plotted to the same scale as Figure 4.11. The phases are shown relative to $-\beta$, since a positive yawing moment creates a negative sideslip.

No significant stabilizing moments are found for the yaw motion. The $C_n(\alpha,\beta)$ term (which corresponds to C_{n_β} of a linear aerodynamic model) is almost exactly in phase with the yaw motion, which indicates that the aircraft is directionally statically unstable at this angle of attack. This reflects the fact that the aircraft would experience yaw departure if no control inputs were made.

The autopilot for this simulation acts through the rudder to oppose the statically destabilizing effect of $C_n(\alpha,\beta)$. However, this rudder motion also acts to dynamically destabilize yaw. The reason for this lies in the phase relationship between roll and yaw of this Dutch-roll-like mode and in the control law of this autopilot. For the rudder, the control law used was

$$\delta_r = 7r + \phi$$

where positive δ_r is trailing-edge left. This very reasonable control law opposes yaw rate with the first term and attempts to "pick up the

down-wing with rudder" with the second term. It is this second term, acting through the lead from β to ϕ, which tends to destabilize the yaw contribution of the rudder. A quantitatively similar phase relationship between rudder and β was observed in the flight test result of Table 4.1 (cf. Figure 2.19). It appears that the pilot's use of rudder came at a phase angle which tended to dynamically destabilize yaw.

To confirm this point, a computer run was made in which the second term of the rudder control was dropped. Thus:

$$\delta_a = .3\phi$$

$$\delta_r = 7r \quad .$$

The wing rock experienced was convergent with a damping ratio of 0.172 compared to a damping ratio of about -0.05 for the control law,

$$\delta_a = .3\phi$$

$$\delta_r = 7r + \phi \quad .$$

The implication of this result is that the actions of the pilot have a strong effect on the stability of wing rock. Moreover, a very simple, uncoupled control law in which roll is opposed only with aileron, and yaw rate only with rudder is found to stabilize wing rock.

From the above discussion, it is obvious that simulated wing rock may be made stable, unstable or neutrally stable depending on the form and gains of the autopilot. Based on an interpolation of the resulting damping ratio versus the gain on ϕ in the rudder equation, a control law of:

$$\delta_a = .3\phi$$

$$\delta_r = 7r + 0.74\phi$$

was estimated to give neutral wing rock stability. The resulting traces for β, ϕ, δ_a and δ_r are presented in Figure 4.13. These responses are slightly convergent.

One significant conclusion is the effect of the autopilot on the onset of wing rock. During the iteration of autopilot gains, it was observed that the lateral autopilot gains did not significantly affect wing rock onset or period. The primary effect of the autopilot was in damping present once the wing rock had commenced. The autopilot gains in rudder control were significant in producing either a divergent or convergent wing rock. This correlates with the conclusion, obtained from other researchers, that wing rock onset is not affected by the pilot, although he may control it to varying degrees.

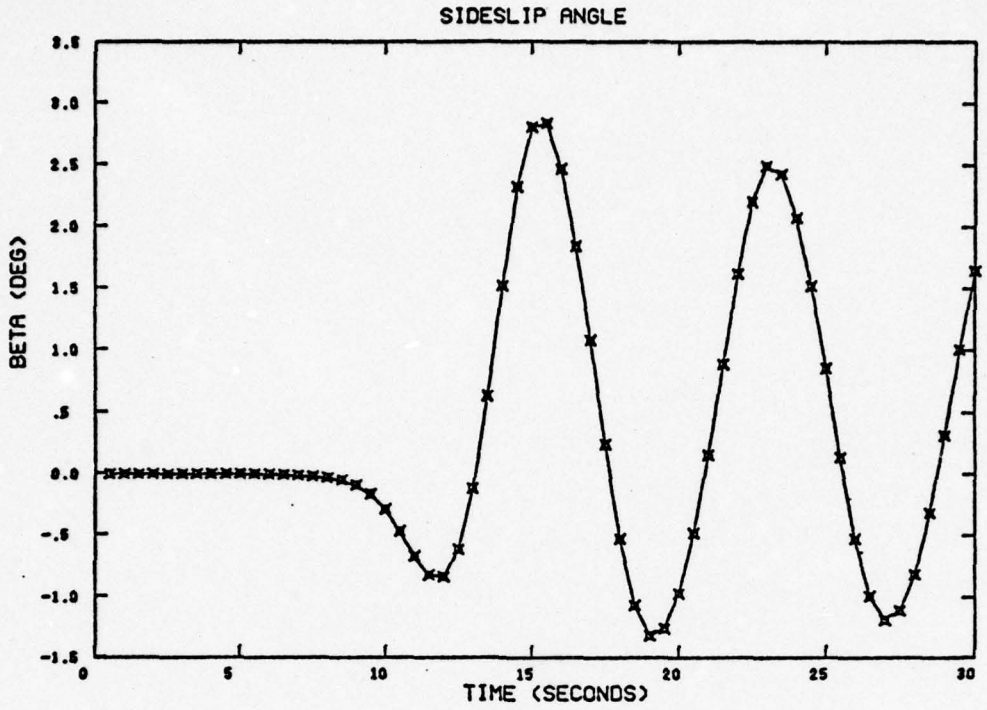
It is concluded that computer simulation can successfully demonstrate wing rock with characteristics which are generally very close to those of real aircraft dynamics.

It is also concluded that computer simulation is a very useful tool in investigating the aerodynamic coefficients which most significantly influence wing rock and other high angle of attack phenomena.

4.4.6 Simulation of Measurement System

The instrumentation system is discussed in Section III, and assumed values are presented for the statistics of the measurement process.

The wing rock and departure plotted in Figure 4.6 are shown in Figure 4.14 with measurement errors. In addition to the angles, rates are also shown in Figure 4.14.



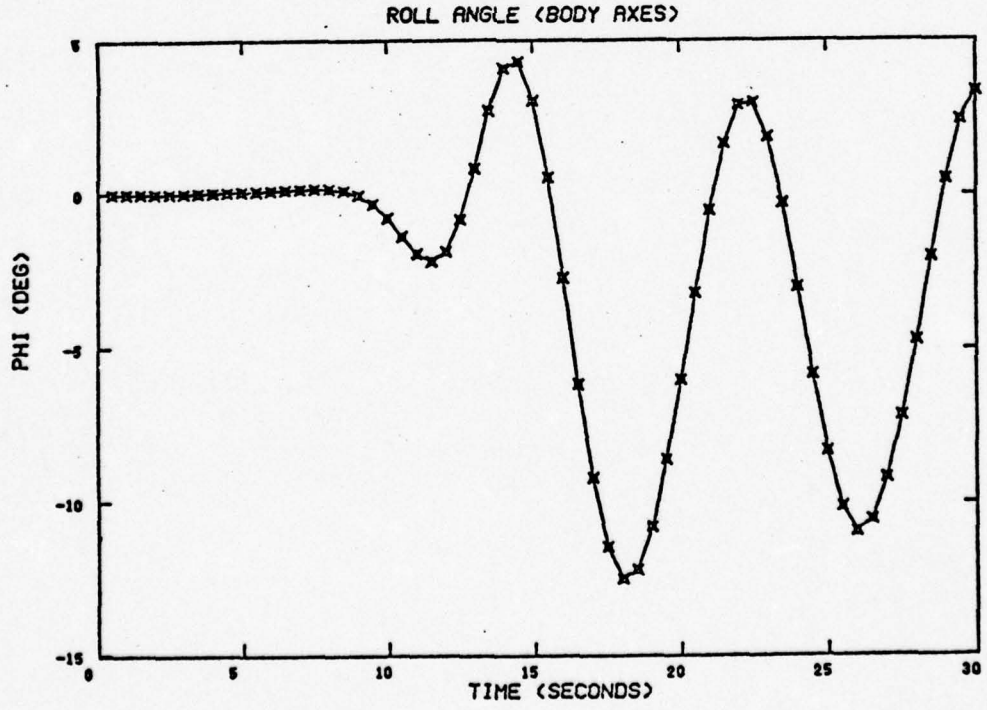
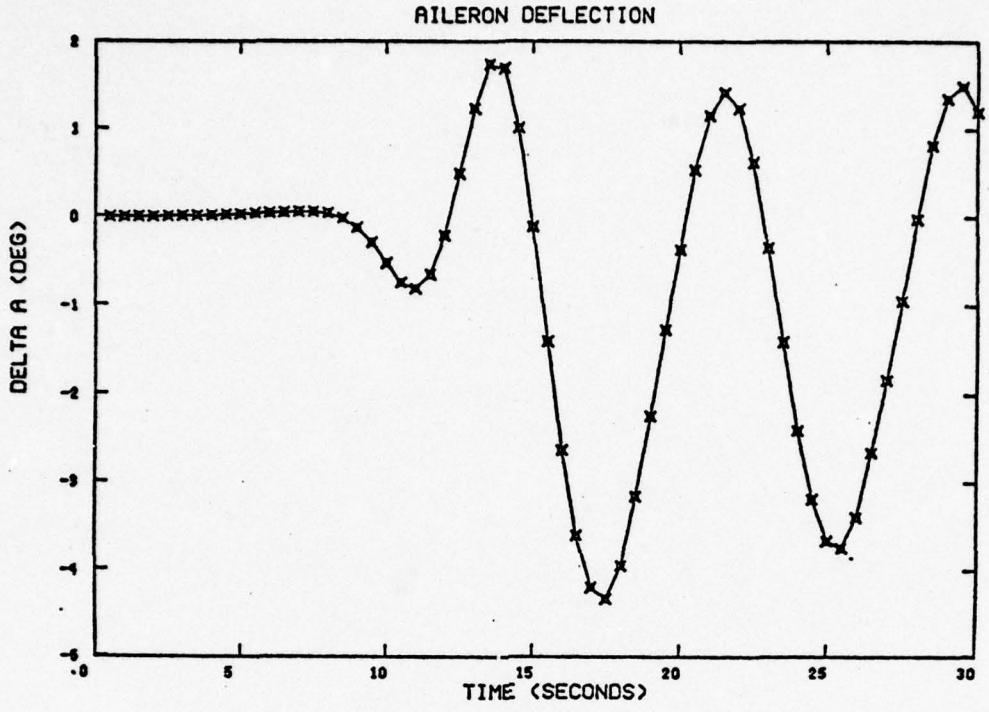


Figure 4.13a Simulated "1 g" Stall Leading to Convergent Wing Rock



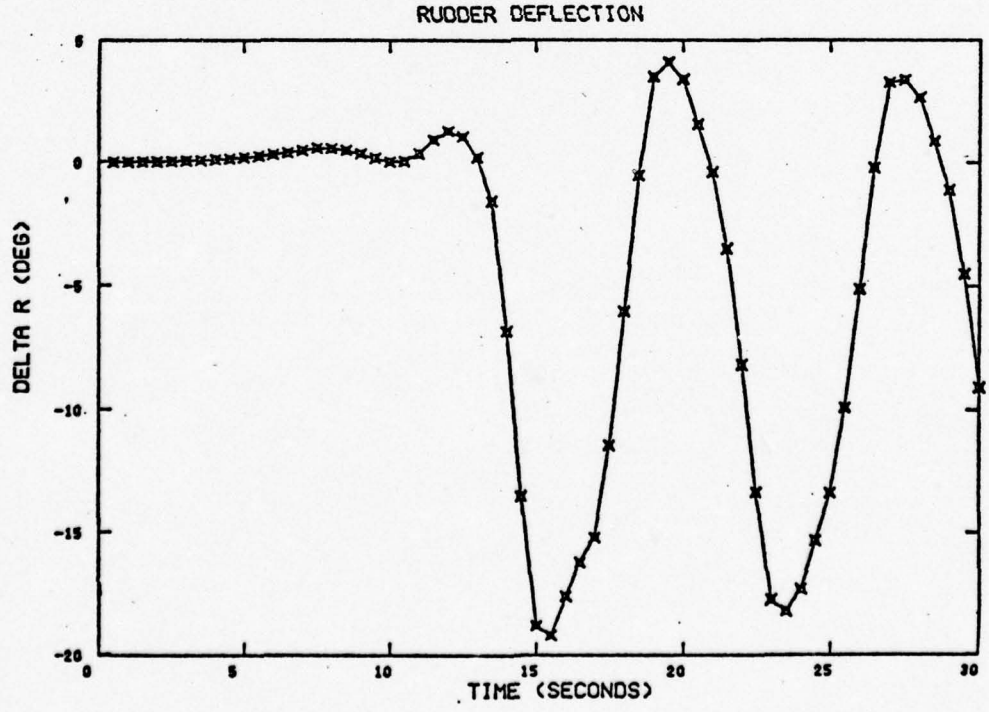
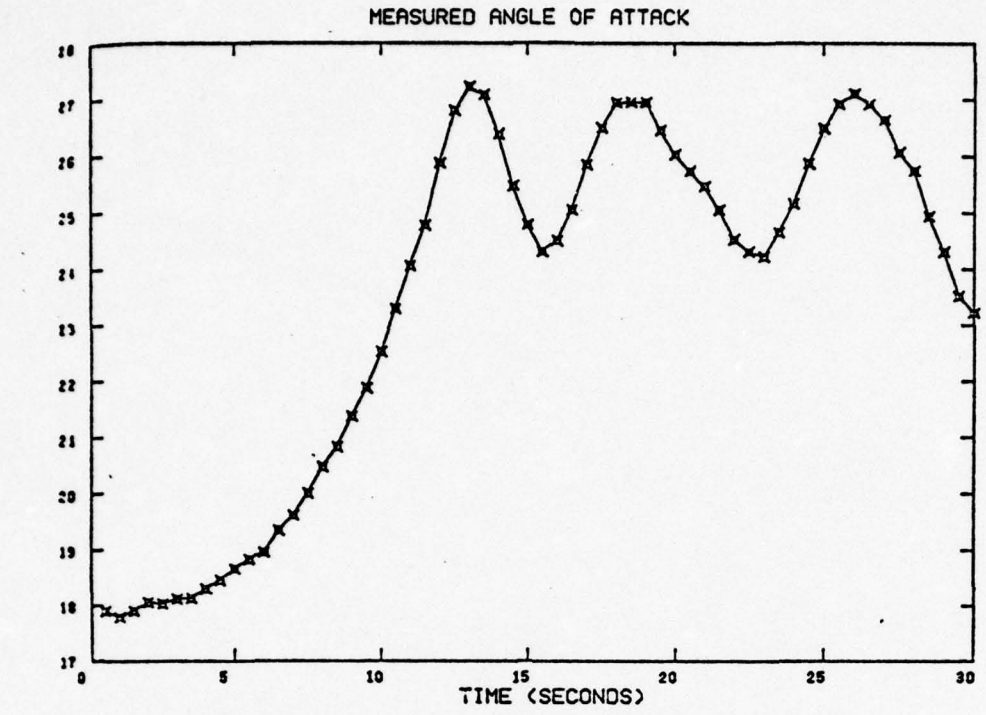


Figure 4.13b Simulated "1 g" Stall Leading to Convergent Wing Rock



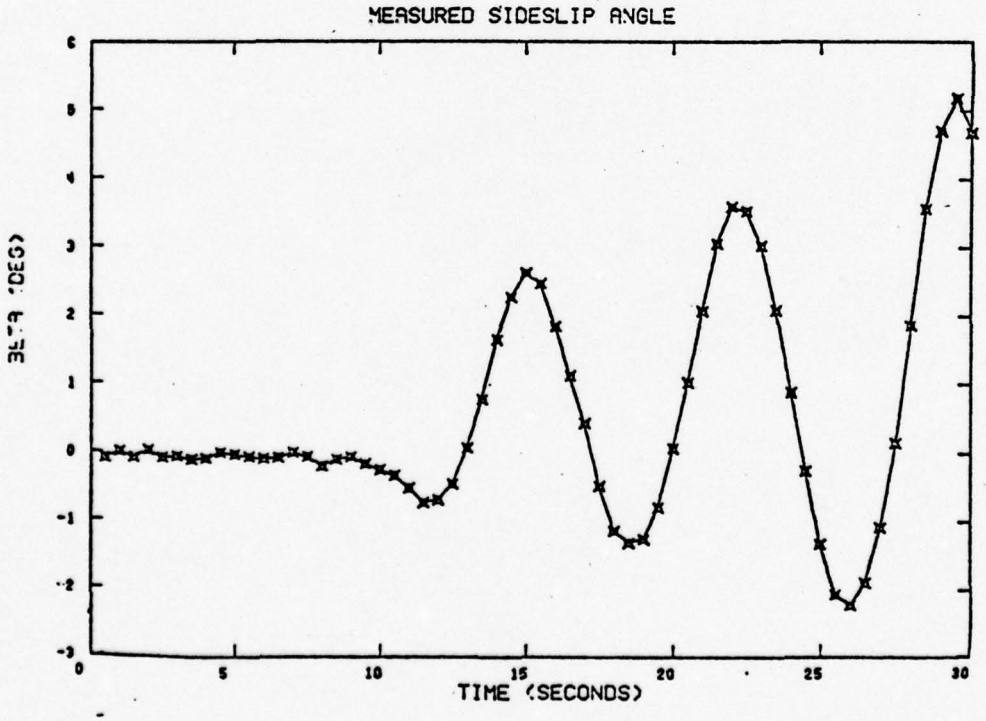
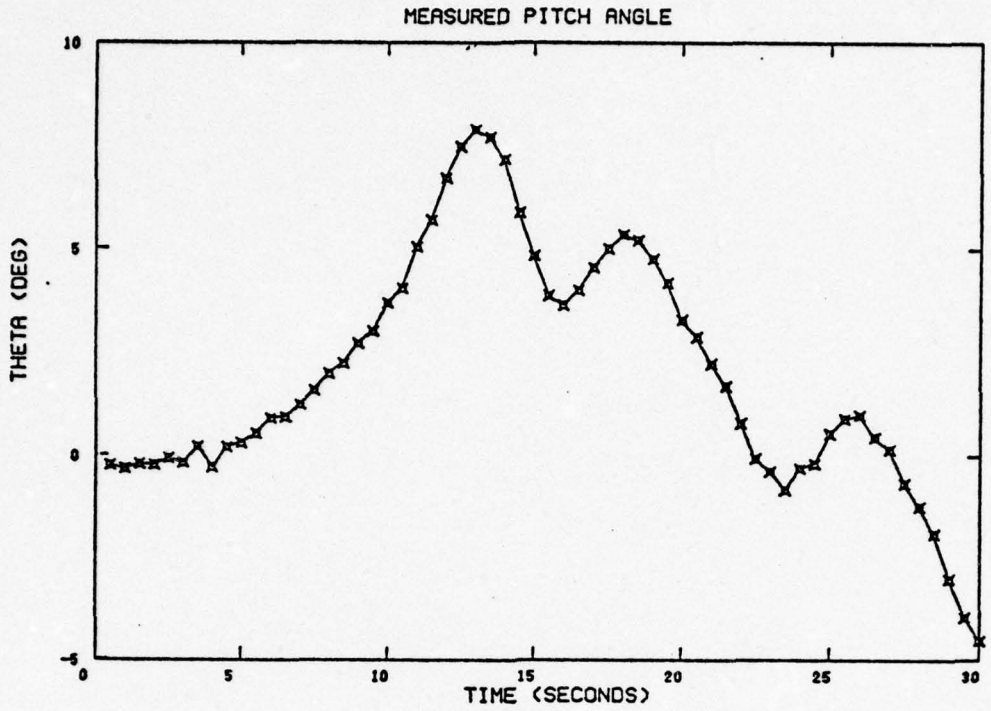


Figure 4.14a Simulation of Effect of Measurement Noise on Wing Rock and Departure Time Histories



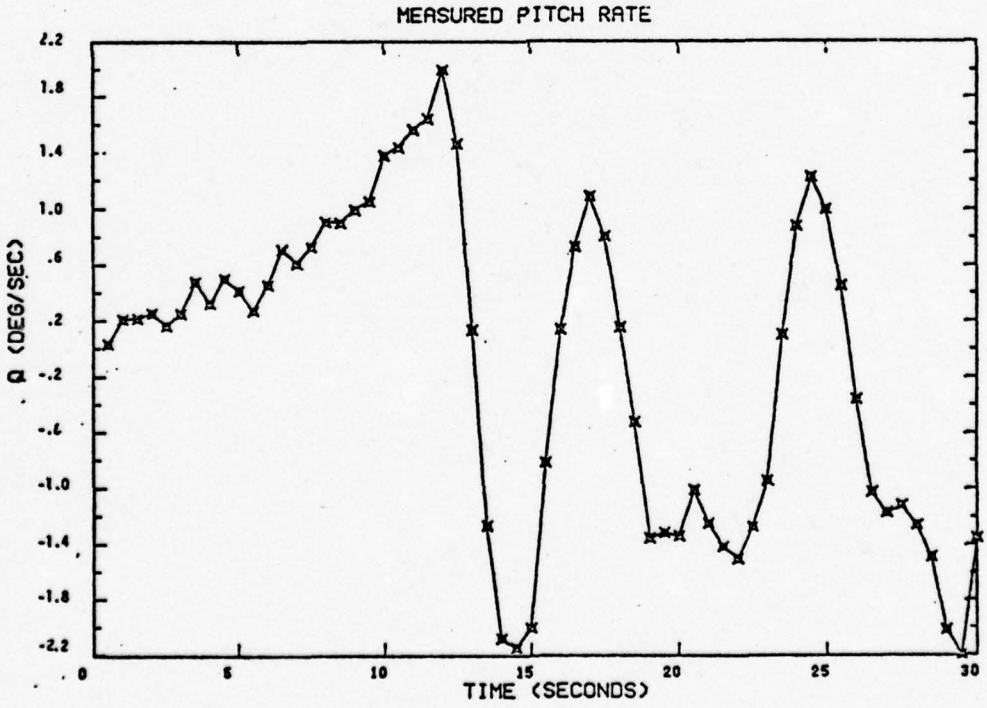


Figure 4.14b Simulation of Effect of Measurement Noise on Wing Rock and Departure Time Histories

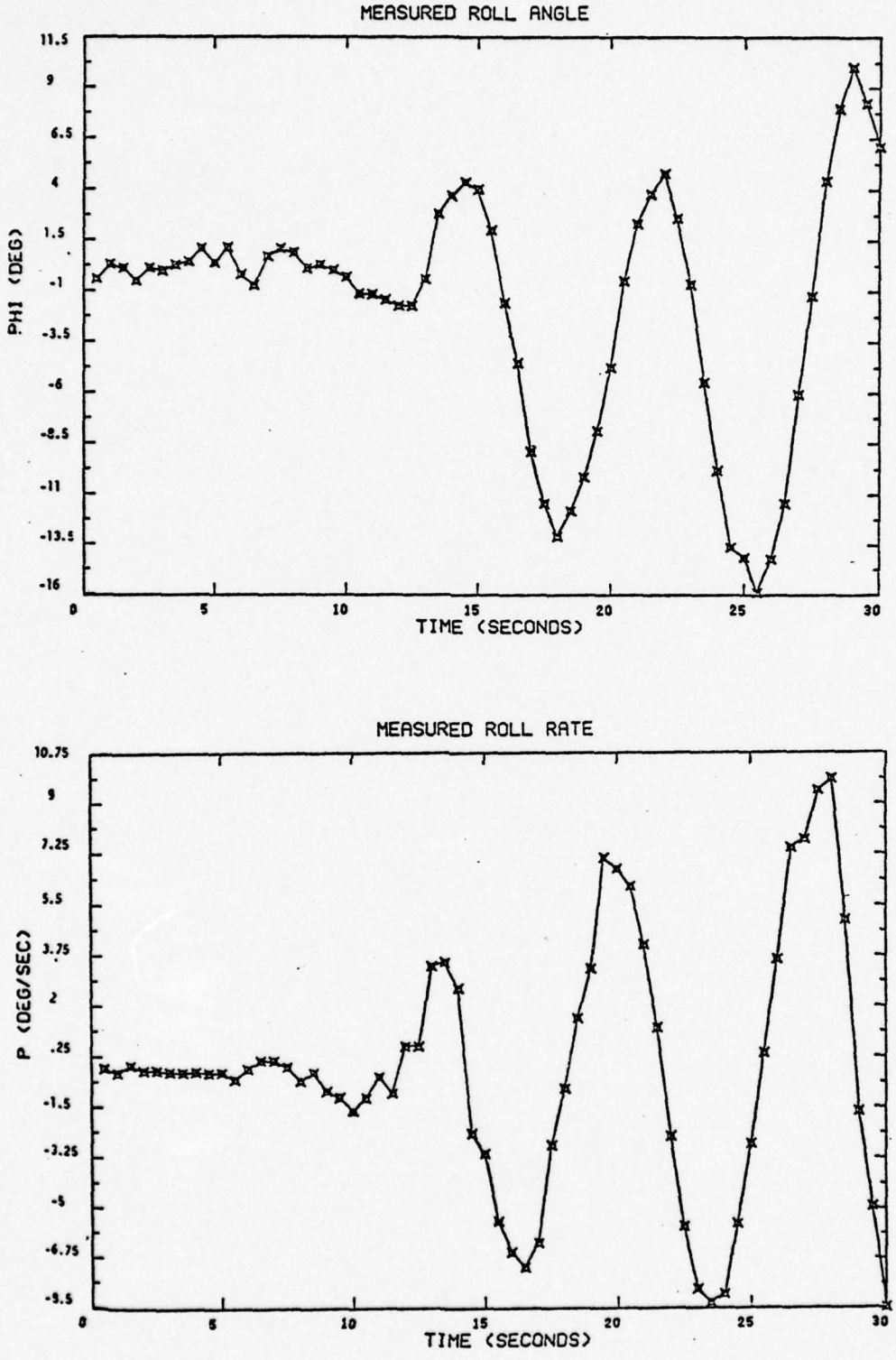


Figure 4.14c Simulation of Effect of Measurement Noise on Wing Rock and Departure Time Histories

The angle-of-attack error is very small over the entire time history. Similarly, the sideslip angle error is negligible. Pitch angle and roll angle errors are noticeable only for small departures from trim.

For this calculation, the only acceleration measurement is that of a vertical accelerometer at the pilot's seat. Such a measurement also shows the effect of pitch rate as expected.

These results are typical and similar effects of noisy measurements are noticeable in the flight traces. Effects of bias error, white noise disturbances, and cross coupling can be seen in computing many such histories, although it is noted that these runs are very time consuming.

4.4.7 Simulation of Random Disturbances

4.4.7.1 Buffet

Figure 4.7 is a time history of the wing rock/departure of Figures 4.5 and 4.6, with the simplified buffet simulation discussed in Section III.

These time histories are almost identical with those of Figure 4.6 which contained no simulated buffet effect. The differences in the runs are smoothed by the plotting technique, and are apparent with a point by point comparison of the respective time histories.

The principal effect of the simulated buffet on the response history is the introduction of a small time lag in the responses. Additionally, random excursions are introduced, principally in the vertical and longitudinal motions.

As expected, the simulated buffet has no significant effect on the stability of the response.

4.4.7.2 Random Angle of Attack

Figure 4.7 shows the effect of introducing a simplified random disturbance by letting angle of attack be subject to a white noise. Such a variation is typical of severe turbulence.

The traces of Figure 4.7 correspond to those of Figure 4.6. It is seen that the principal effect of the random angle-of-attack is in the longitudinal axis, particularly in the measured pilot seat acceleration. The important observation relevant to this calculation is that the basic character of the motion is preserved.

This method of simulating process noise is only one of several, which may be used, although such time histories are also very time consuming.

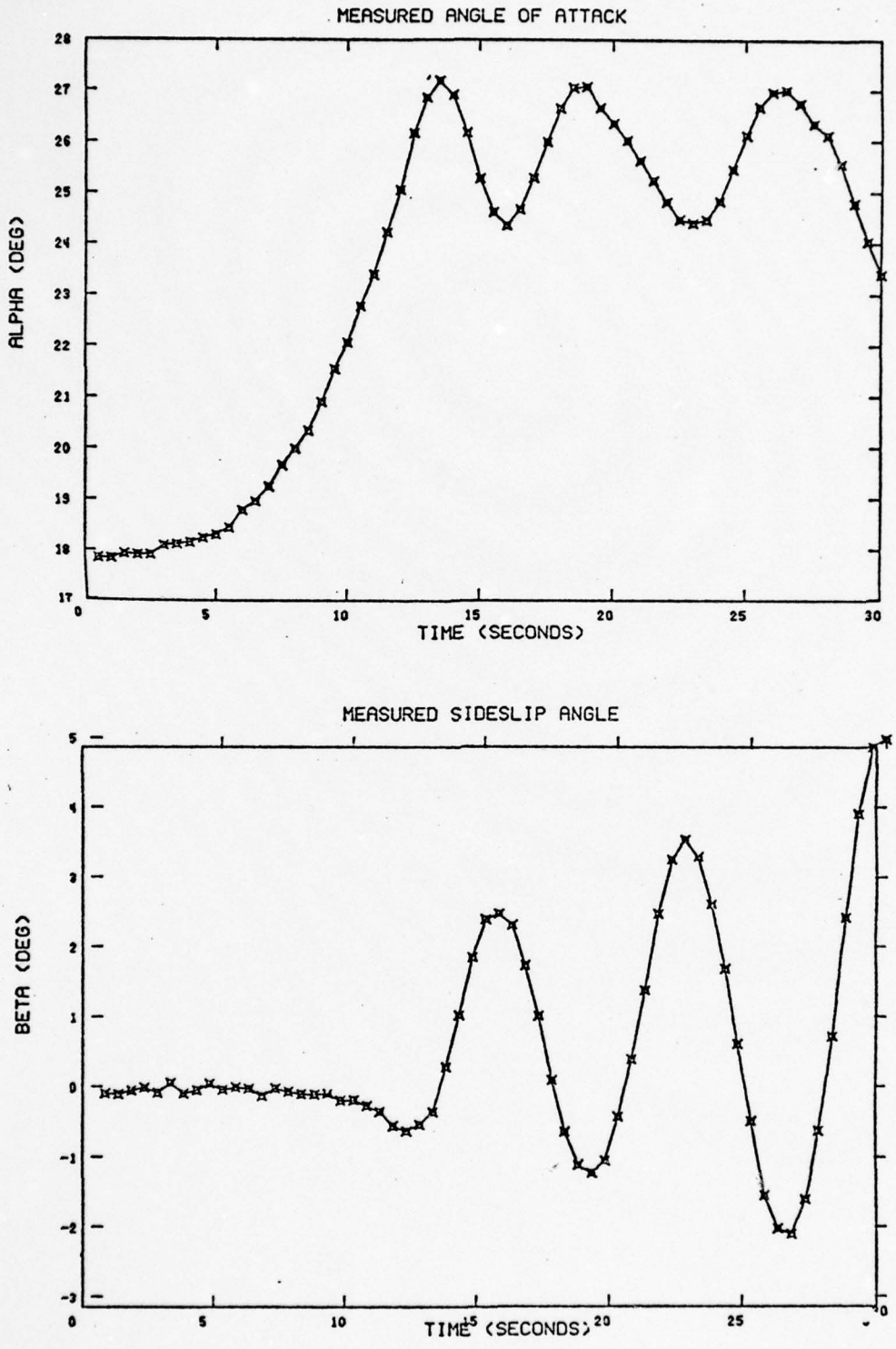


Figure 4.15a. Simulation of Effect of Buffet and Measurement Noise on Wing Rock & Departure Time Histories

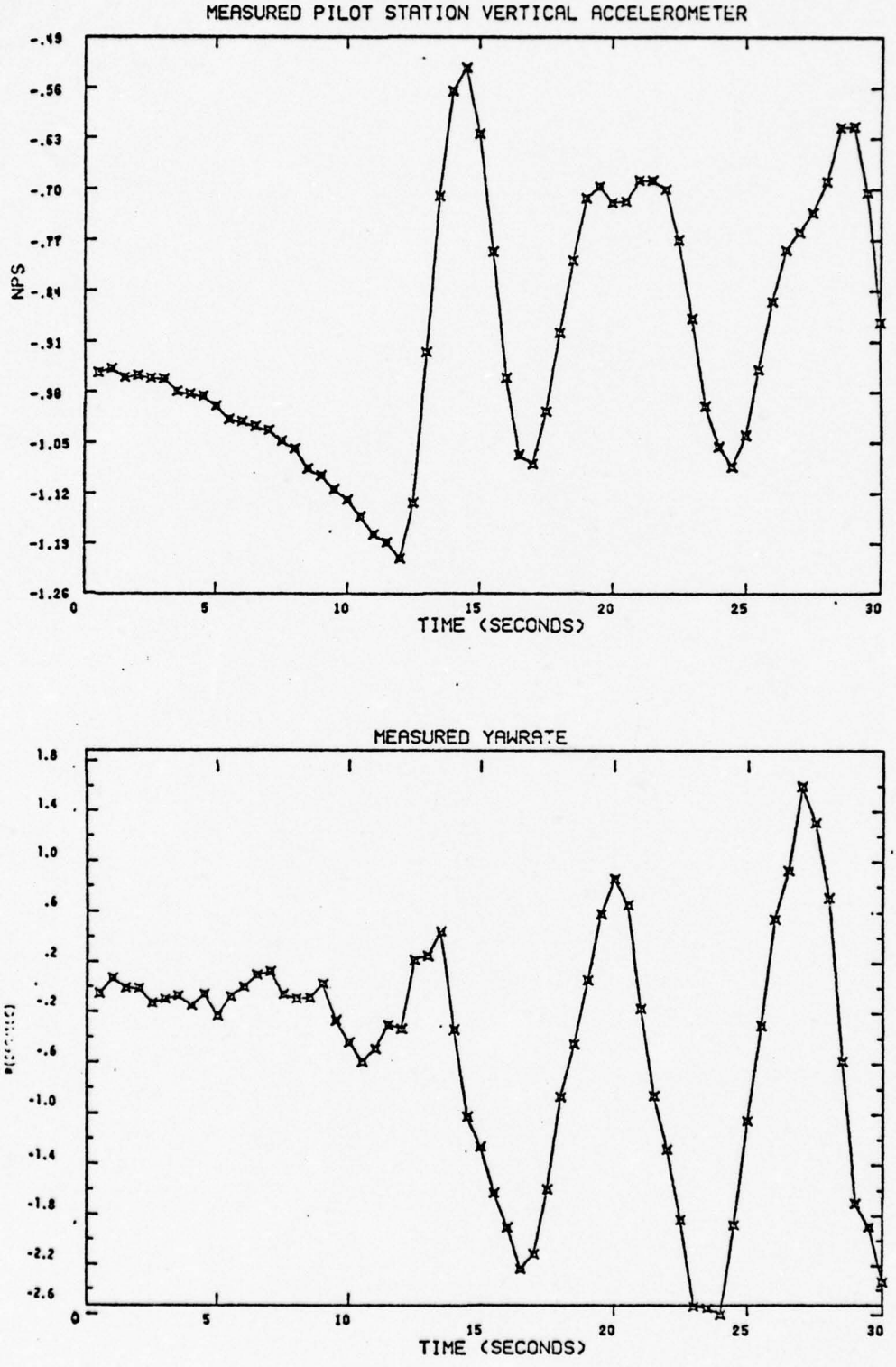
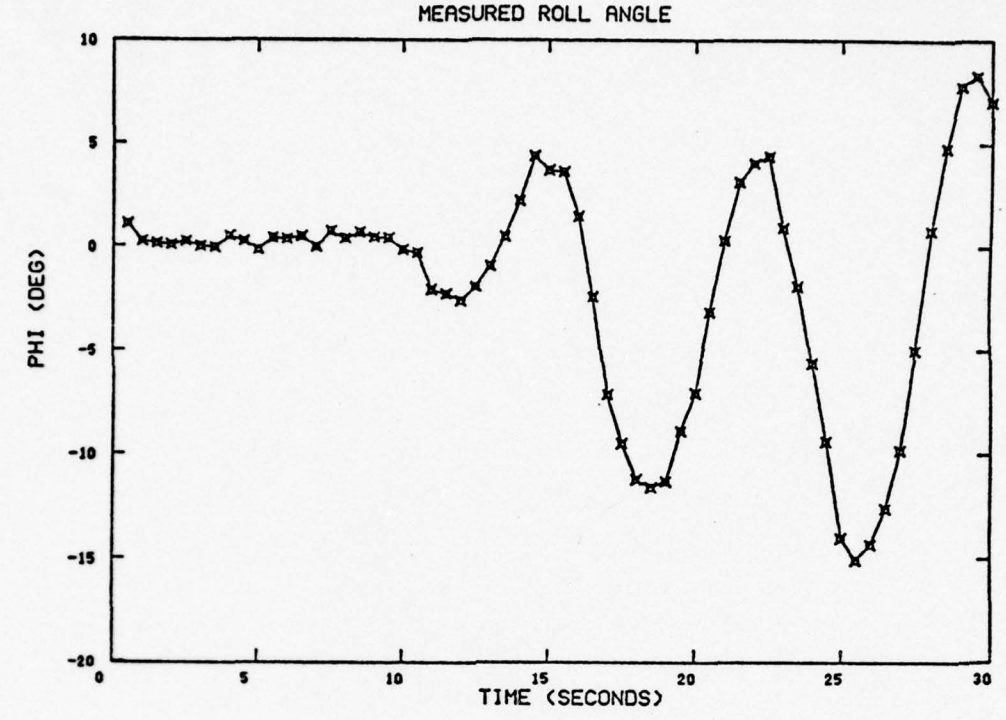


Figure 4.15b Simulation of Effect of Buffet and Measurement Noise on Wing Rock & Departure Time Histories



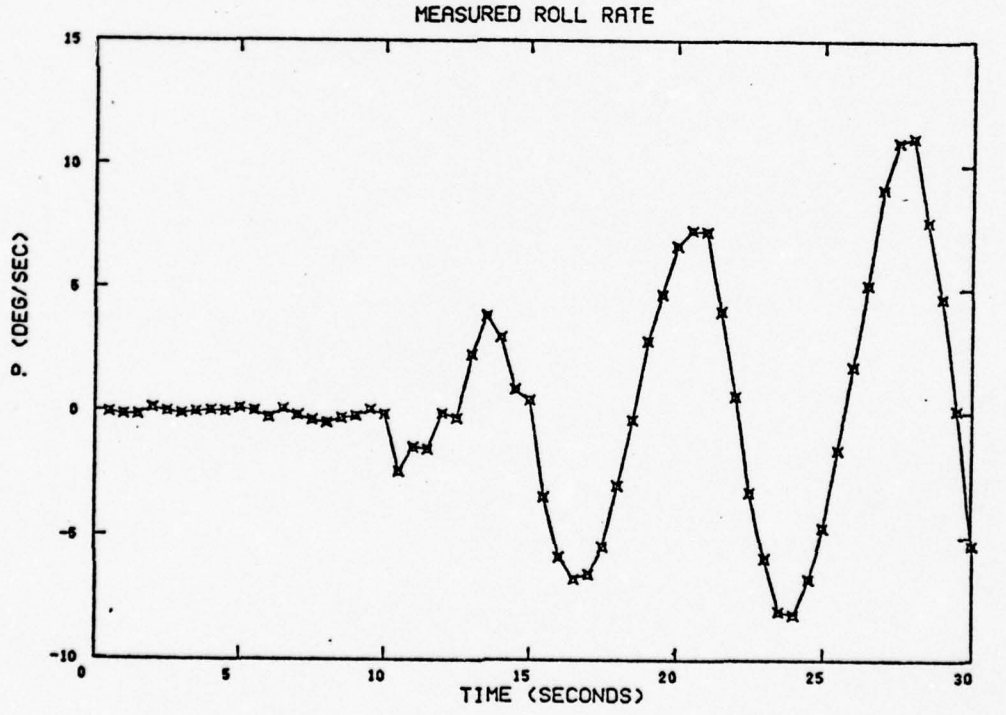
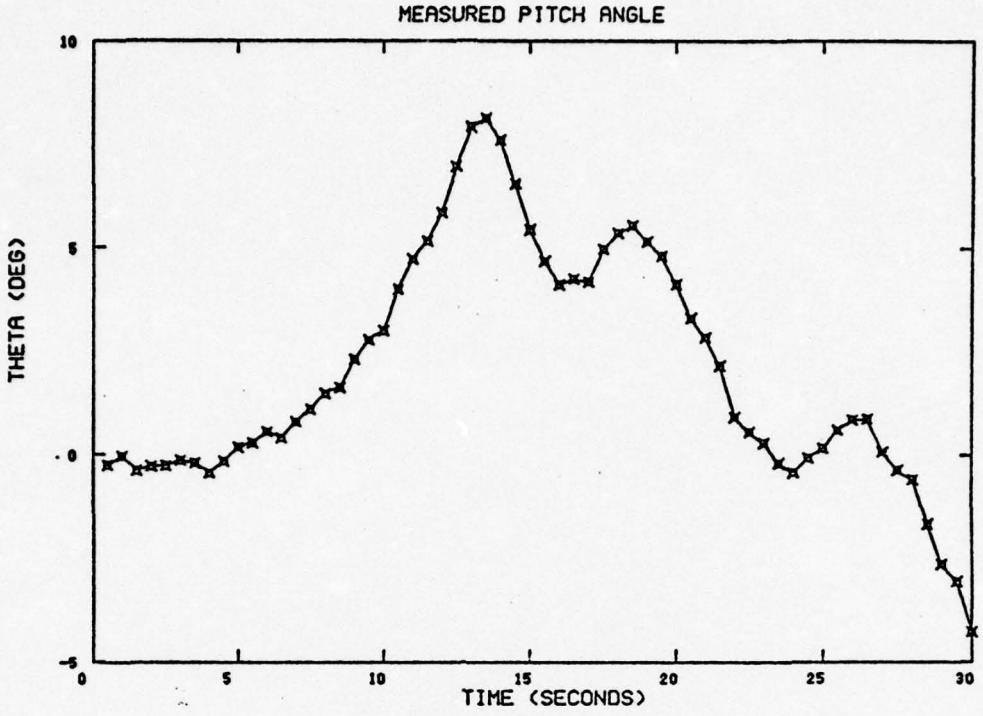


Figure 4.15c Simulation of Effect of Buffet and Measurement Noise on Wing Rock & Departure Time Histories



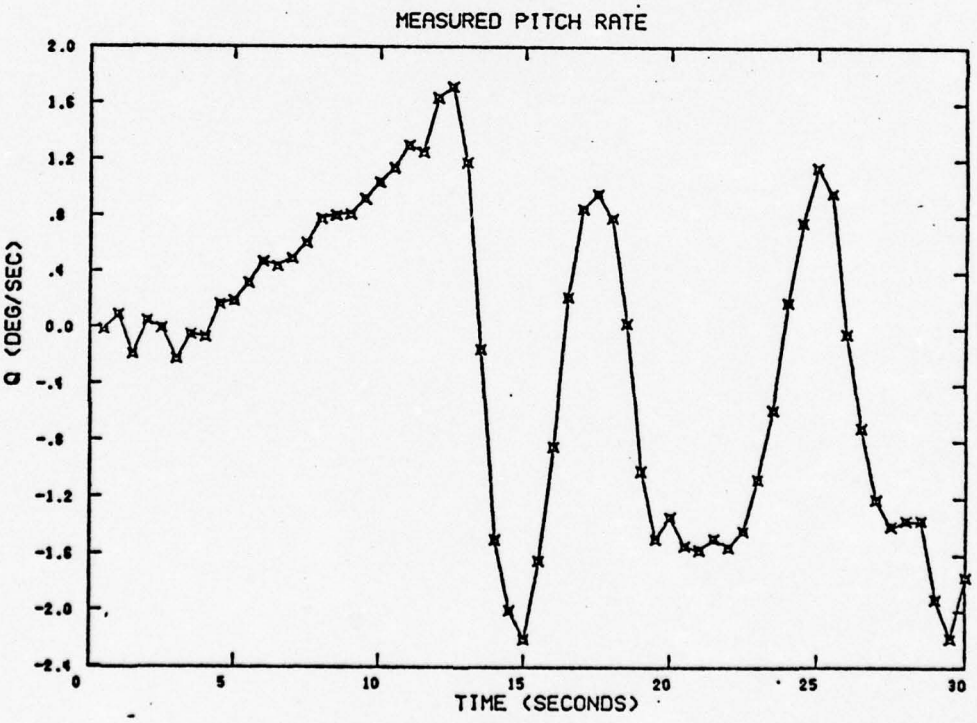
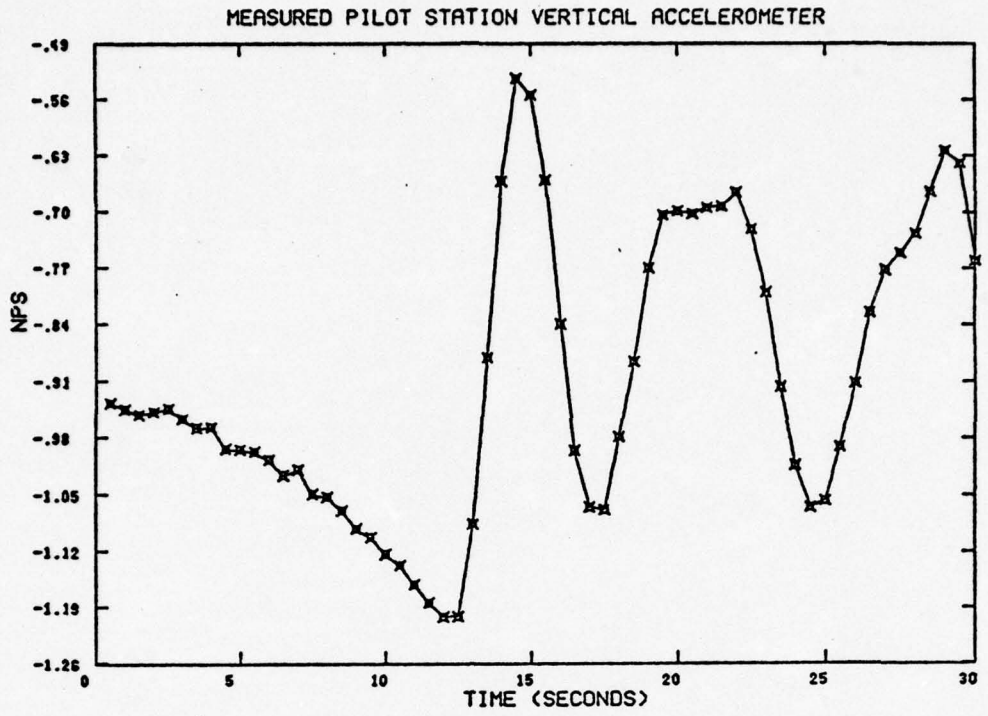


Figure 4.15d Simulation of Effect of Buffet and Measurement Noise on Wing Rock & Departure Time Histories



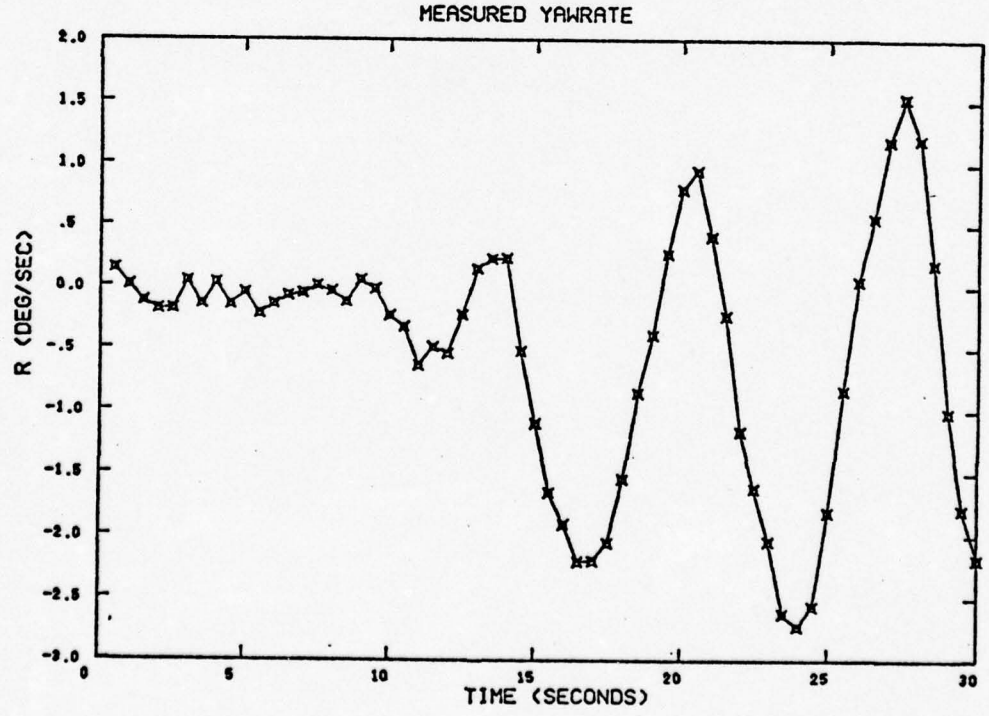
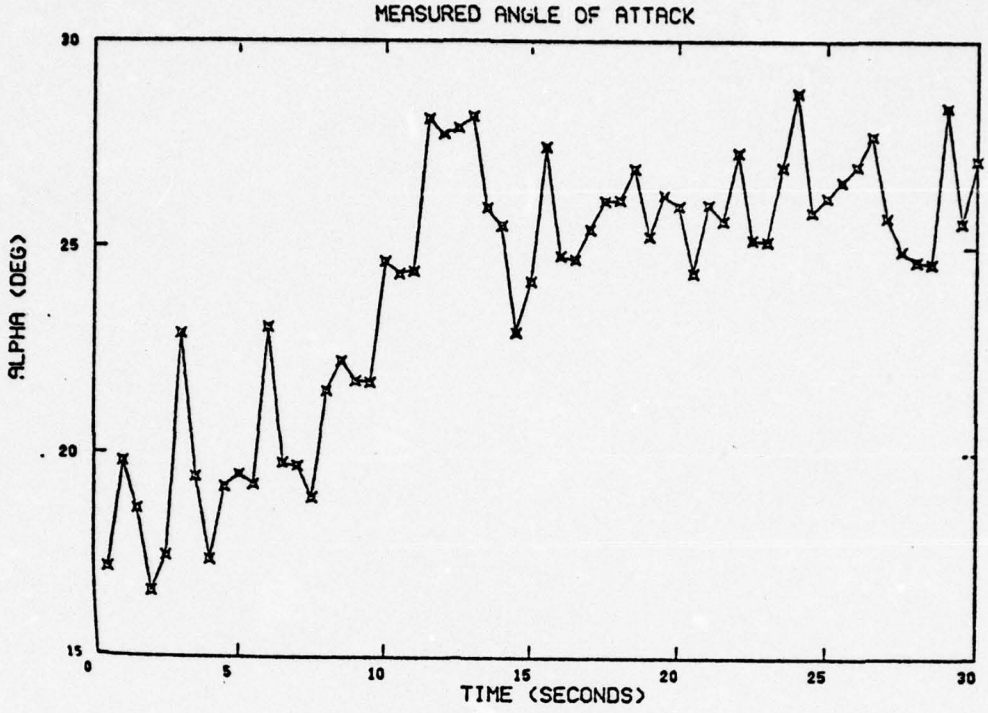


Figure 4.15e Simulation of Effect of Buffet and Measurement Noise on Wing Rock & Departure Time Histories



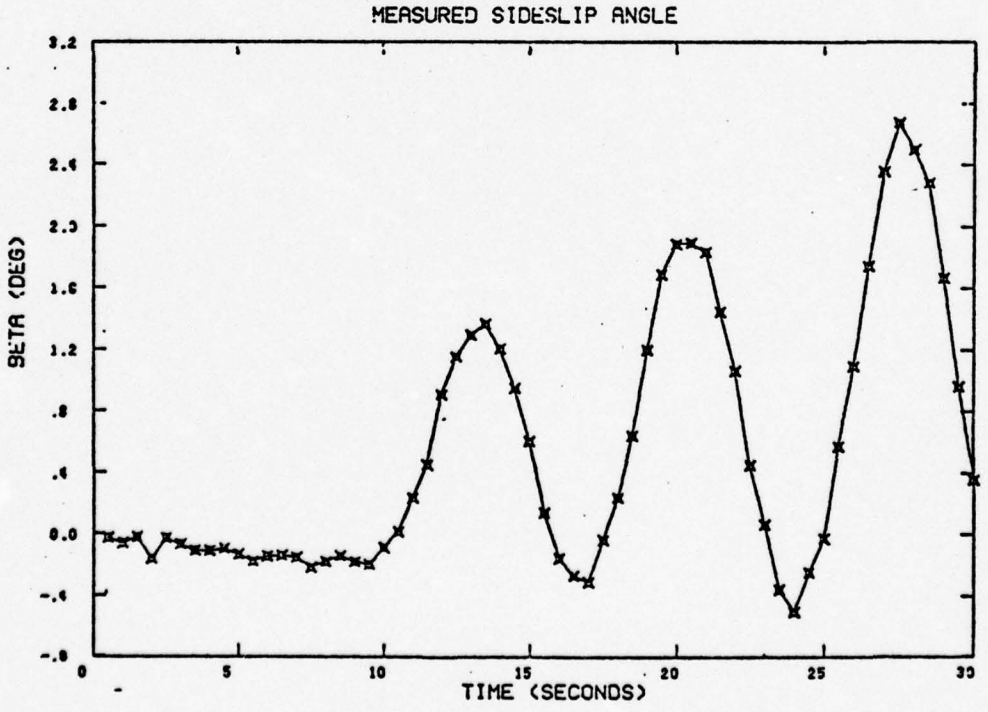
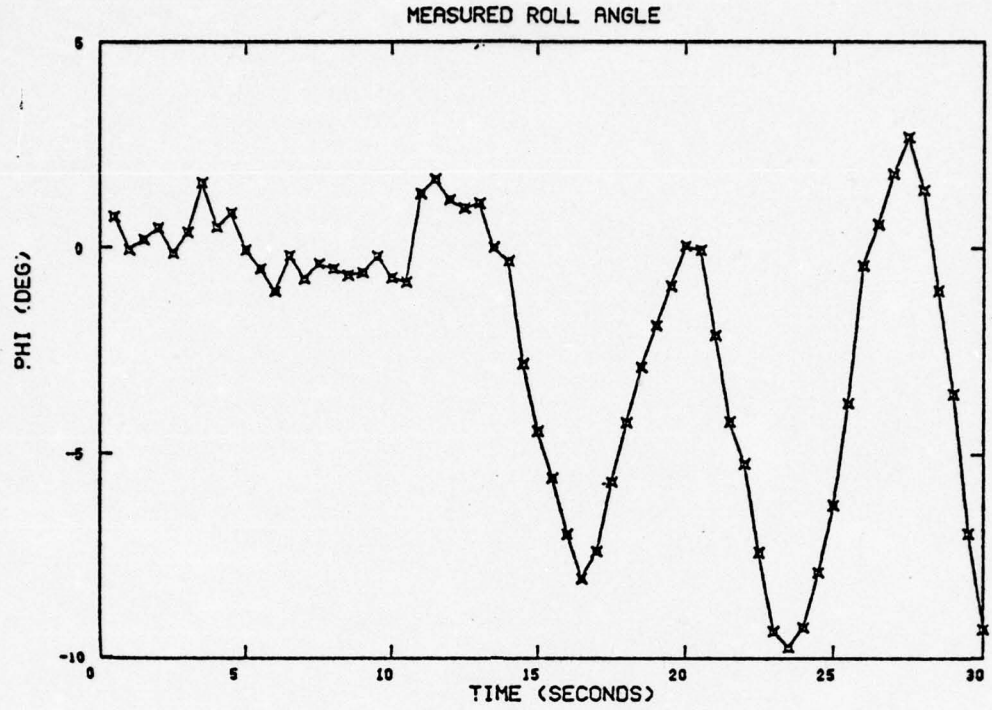


Figure 4.16a. Simulation of Effect of Severe Turbulence and Measurement Noise on Wing Rock and Departure Time Histories



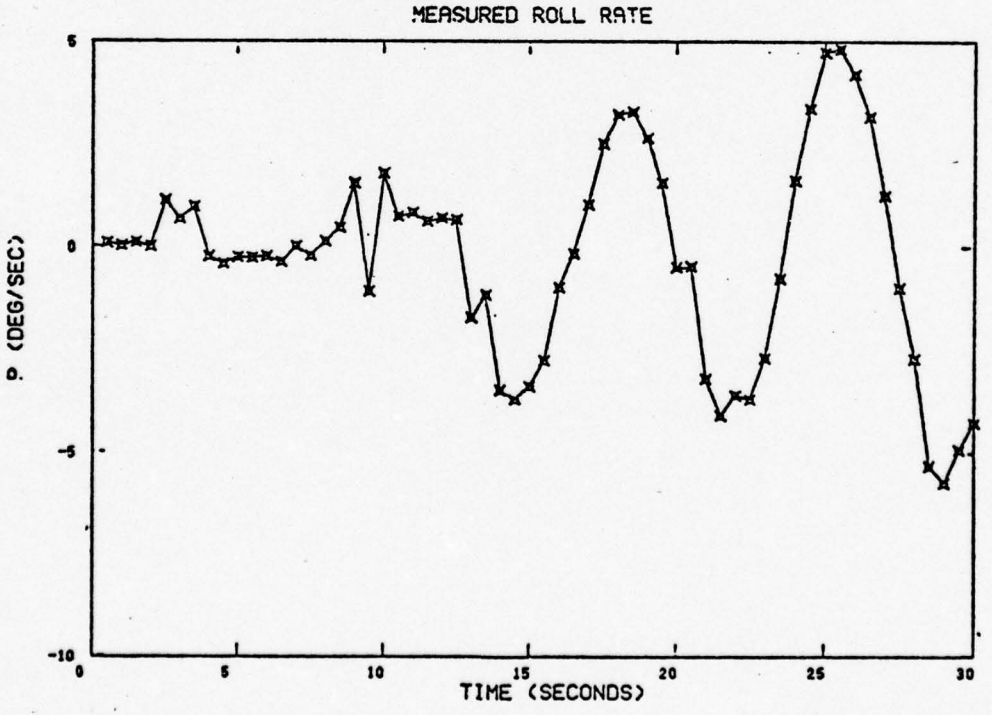
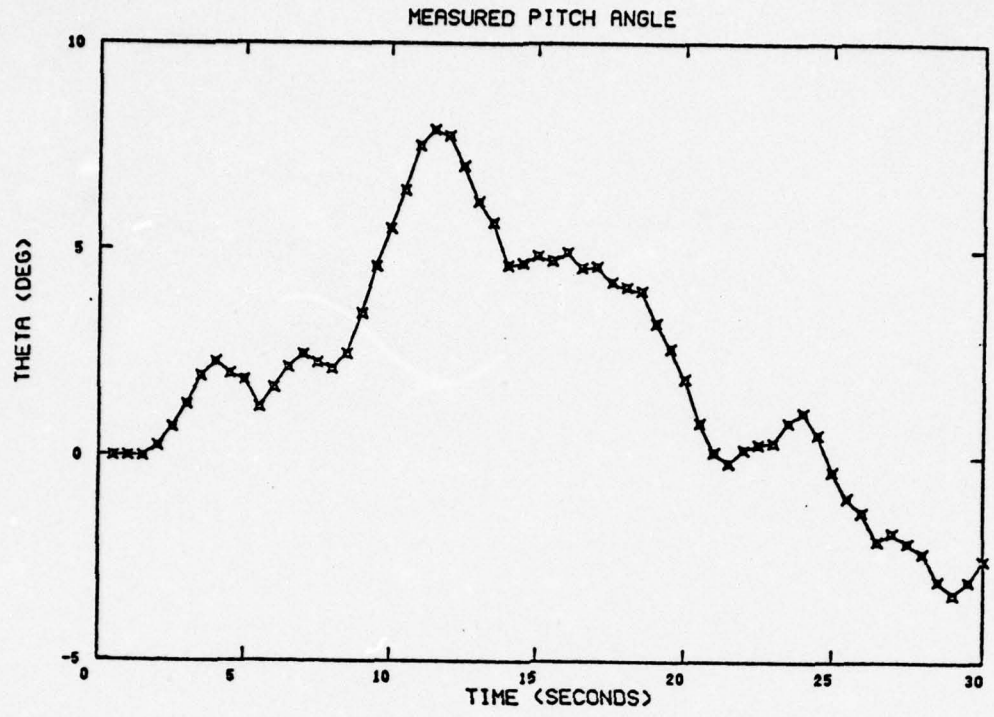


Figure 4.16b. Simulation of Effect of Severe Turbulence and Measurement Noise on Wing Rock and Departure Time Histories



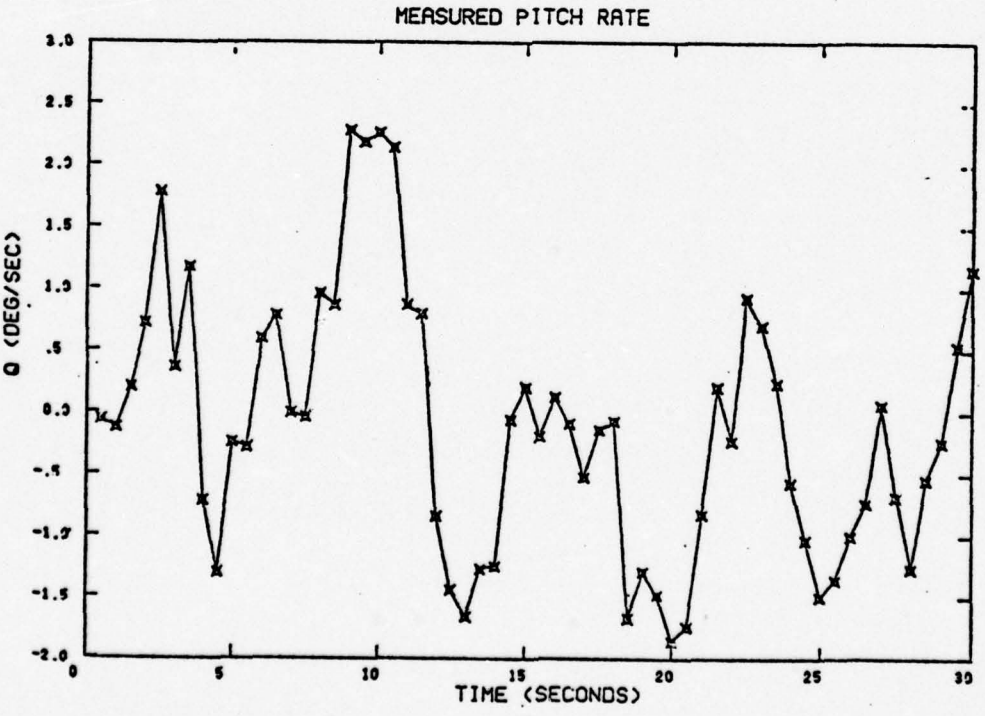
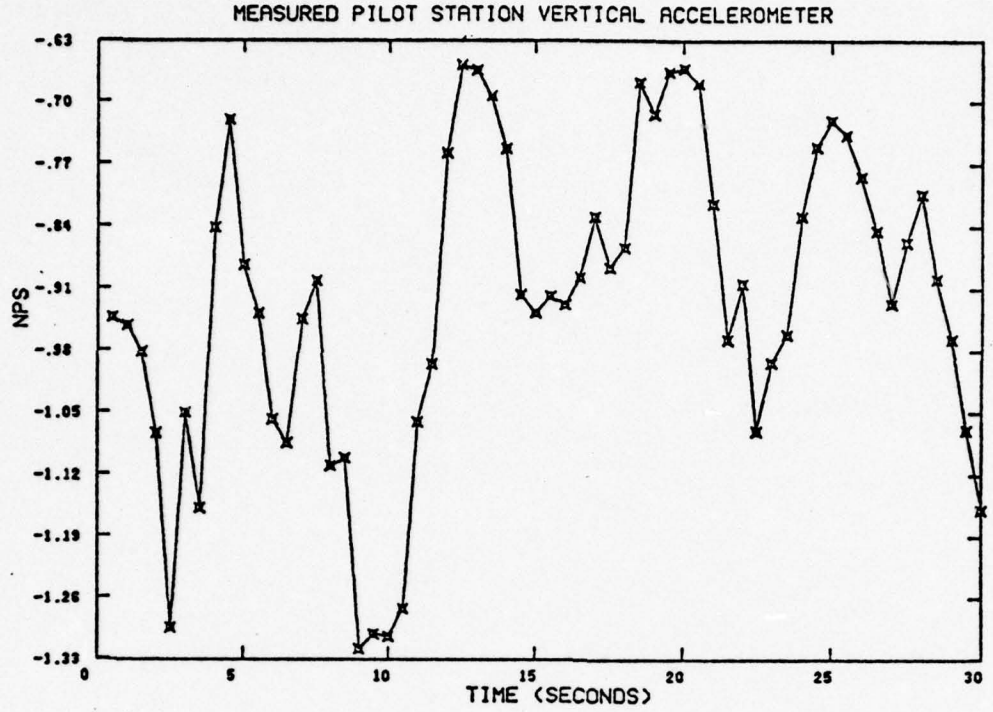


Figure 4.16c. Simulation of Effect of Severe Turbulence and Measurement Noise on Wing Rock and Departure Time Histories



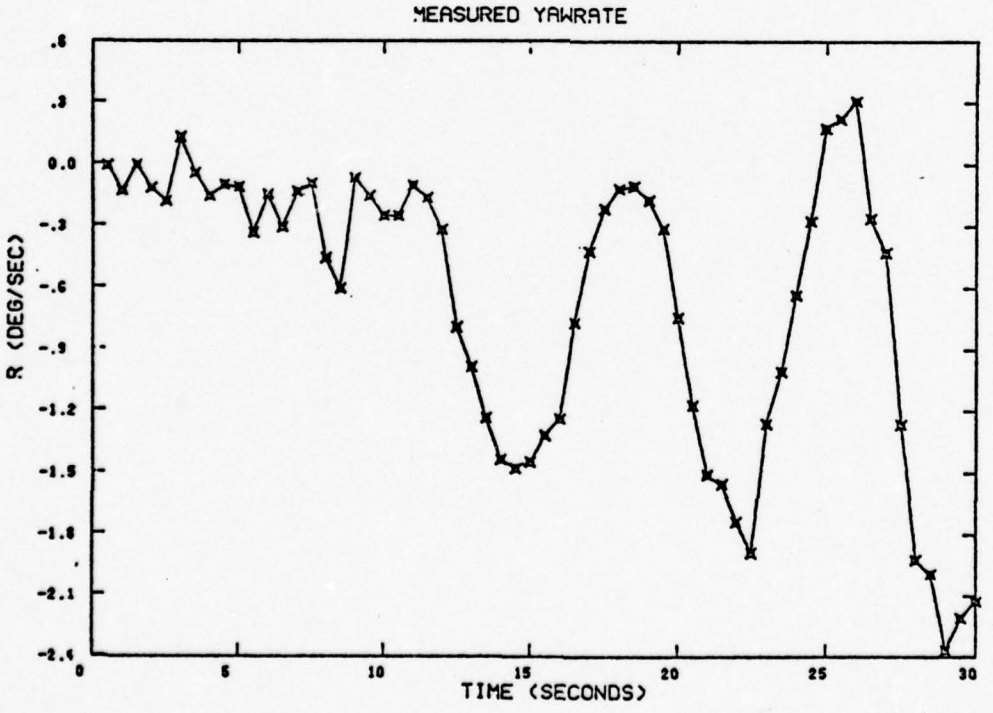


Figure 4.16d. Simulation of Effect of Severe Turbulence and Measurement Noise on Wing Rock and Departure Time Histories.

V

SUMMARY AND CONCLUSIONS

A review of high angle-of-attack aerodynamics has outlined the complicated flow interactions which occur in the stall/post-stall flight regime. This complicated aerodynamic environment causes nonlinear and unstable aircraft motions which may produce uncontrollable spins. "Pitch-up," "wing rock," and "yaw departure" are particular nonlinear motions which characterize such incipient spin conditions.

A significant amount of effort has been expended to predict and understand the stall/post-stall aerodynamic environment. Generally, the complexity of the problem and the lack of sufficiently powerful analytical techniques have tended to hinder such prediction and understanding. Qualitative explanations of the possible mechanisms for wing-rock, yaw departure, and spin indicate the importance of the wing lift and drag characteristics, the tail geometry, and the fuselage shape. Such a breakdown of the problem is useful for isolating elemental causes for the forces and moments. The phenomena are, however, a complicated superposition of the simpler mechanisms and more rigorous approaches must be used to analyze the actual situation.

One such analysis technique is the detailed wind tunnel measurement of forces and moments on a model of the aircraft. Related techniques are model drop tests, spin tunnel tests, and radio-controlled tunnel tests. It has been found that although such methods are effective for qualitative analysis of stall/post-stall aerodynamics, significant and consistent errors exist between wind tunnel predictions and actual flight test results.

A general six-degree-of-freedom simulation of the nonlinear equations of motion of a high performance fighter airplane, such as the F-4, has been developed. The aerodynamic model of this simulation presently consists of the static and dynamic forces and moment coefficients from subsonic (M = .2) F-4 tunnel tests. Although similar in structure to other such simulations, the scope of this program is wider than others which have been documented. The options available include the following:

(1) The direction cosine matrix is integrated directly. This procedure avoids singularities due to integrating the Euler equations through large pitch angles.

(2) A detailed simulation of the instrumentation system characteristic of flight tests is used. This option allows for the generation of calculated data more characteristic of actual recorded data.

(3) Turbulence and buffet characteristics may be simulated. This option also aids in calculating more realistic data.

(4) The ability to output not only all aircraft states, but also the time histories of the forces and moments for a specific calculation. This option aids in understanding mechanisms of stall/post-stall responses.

The simulation response has been compared with documented aircraft responses with satisfactory results which include:

(1) A qualitative correlation of low angle-of-attack longitudinal response to a stabilator doublet. Computed amplitudes for α were lower than that of the flight test noseboom measured angle-of-attack. The error is principally attributed to the nonexact reproduction of the flight test measured input by the program input. More importantly, however, the modes of response of α and normal acceleration were the same in the flight test and calculated case.

(2) Lateral-directional response to an aileron doublet was stable in the low angle-of-attack regime(SAS on). No similar inputs at a corresponding angle-of-attack were located, but the response was deemed good based on mode shapes and response times.

(3) A calculated high-angle-of-attack "1 g stall" correlated extremely well, although again not exactly with a documented occurrence of wing rock preceding yaw departure. This simulation was performed with an autopilot which was designed to approximate pilot response. All characteristics of the documented lateral-directional and longitudinal response were simulated.

One important aspect of this correlation is that no modification to the wind tunnel data was necessary. However, it is found that the response stability is strongly dependent on the reaction of the aileron and rudder controls to the aircraft motion.

The discrepancies between the simulation responses and actual aircraft responses arise from several sources, not the least of which is the simple fact that Mach numbers and Reynolds numbers of the data don't correspond to those of the flight test conditions. A recurring problem was also lack of knowledge of the flight test aircraft inertial mass properties and difficulty of reading flight data to determine the actual aircraft operating condition. Finally, the simulation used a linear autopilot to represent the apparently nonlinear pilot responses. Although the linear model did correlate well with recorded pilot responses over particular cycles, the pilot transfer function did change over other cycles which deteriorated overall correlation accuracy. The aircraft stability is very sensitive to pilot responses, as verified by both flight test and the simulation.

Flight tests have demonstrated that variations in aircraft configuration and geometry can affect the occurrence of wing rock and nose slice, as well as the amplitudes and stability of the responses. The reasons for the unpredictability of these occurrences and for the characteristics of high angle of attack in general, and for the quantitative discrepancies between flight test results and wind tunnel predictions are therefore still unknown.

The summary conclusions of this work are as follows:

(1) Qualitative prediction of stall/post-stall responses and stability may be calculated by simulations based on wind tunnel predictions of high angle-of-attack aerodynamics.

(2) The stability of high angle-of-attack responses may be significantly affected by control application from the pilot or autopilot.

(3) There are significant differences between the predictions using wind tunnel data and actual flight tests, the reasons for which are not quantitatively understood.

(4) These differences may be resolved to some extent by correcting the wind tunnel data until better correlation is obtained. Such empirical methods, however, obviously cannot provide the generality required for an accurate prediction methodology.

(5) Accurate flight testing procedures are important in order to achieve the goal of better modeling, understanding, and prediction of high angle-of-attack stability and control characteristics.

REFERENCES

CITED REFERENCES

1. "ad hoc Team Report on F-111 Stall/Post Stall/Spin Presentation Program" Aeronautical Systems Division, AFSC, USAF, 28 August 1970.

2. Anon, "Natops Flight Test Manual F-4F Aircraft," NAVAIR, 01-245FDD-1, 1 June 1971.

3. Kerr, T. H., "General Principals of Spinning," Agard Flight Test Manual, Vol. II, Chap. 8, 1958.

4. Weissman, R., Bowser, D. K., and Cord, T. J., "The Potential of Analytical Studies for the High Angle-of-Attack Flight Regime," ASD-AFFDL Stall/P Stall/Spin Symposium, Dec. 1971, pp. p-1/p-23.

5. Ellison, D. E. and Hoak, D. E., "Stability Derivative Estimation at Subsonic Speeds," International Congress on Subsonic Aerodynamics, Annals of the New York Academy of Sciences, Vol. 154, Art. 2, November 22, 1968, pp. 367-397.

6. Chambers, J. R. and Anglin, E.L., "Analysis of Lateral Directional Stability Characteristics of a Twin-Jet Fighter Airplane at High Angles of Attack," NASA TND-5361, August 1969.

7. Hancock, G. J., "Problems of Aircraft Behavior at High Angles of Attack," AGARDograph 139, April 1969.

8. Anglin, E. L., "Static Force Tests of a Model of a Twin-Jet Fighter Airplane for Angles of Attack from -10° to 110° and Sideslip Angles from -40 to +40°," NASA TND-6425, August 1971.

9. Shields, M. E., Shaw, A. W., Lauthan, J. D., "VAC Experiences in the Stall/Post Stall and Spin Flight Regimes," ASD Stall/Spin Symposium, Dec. 1971, pp. F-1/F-25.

10. Lang, J. D., "Aircraft Performance, Stability and Control," Course Notes, Aero 456, United States Air Force Academy, August 1971.

11. Young, John W. and Adams, W. M., "Analytic Prediction of Aircraft Spin Characteristics and Analysis of Spin Recovery," AIAA Paper 72-985, 2nd. Atmospheric Flight Dynamics Conference, Sept. 13, 1972.

12. Krings, J. E., and Weber, W. B., "McDonnell Aircraft Company's Experience and Viewpoint on the Stall/Post Stall Region of Flight," ASD Stall/Post-Stall/Spin Symposium, Dec. 1971, pp. E-1/E-25.

13. Titiriga, A., Jr. and Weyls, C. J., Jr., "Northrup Experience - Spin Characteristics for Fighter Type Aircraft," ASD Stall/Spin Symposium, Dec. 1971, pp. F-1/F-25.

14. McDonnell-Douglas Report MDC A0005, "Model F-4 Spin Evaluation Program," Vols. I and II, 15 Aug. 1969.

15. Abzug, M. J., "High Speed Stability and Control Problems," Agard Flight Test Manual, Vol. II, Chap. 9, 1959.

16. Stone, R. W. Jr., "Interpretation of Wind-Tunnel Data in Terms of Dynamic Behavior of Aircraft at High Angles-of-Attack," Wind Tunnel and Model Testing Session, Agard 19/D8, 1958.

17. McElroy, C. E. and Sharp, P. S., "Stall/Near Stall Investigation of the F-4E Aircraft," Air Force Flight Test Center, Edwards Air Force Base, FIC-SD-70-20, October 1970.

18. Etkin, E., Dynamics of Atmospheric Flight, John Wiley and Sons, (1971). (Also Dynamics of Flight, John Wiley (1959))

19. Grafton, S. B., and Libbey, C. E., "Dynamic Stability Derivatives of a Twin Jet Fighter for Angles of Attack from -10° to 110°," NASA TND-6091.

20. Hall, W. E., "Application of Lyapunov Theory to the Stability of Flapping Rotors at High Inflow Angles," Masters Thesis, SMU, 1965.

21. Kuhn, R. E., "Notes on Damping in Roll and Load Disturbances in Roll at High Angles of Attack and High Subsonic Speeds," NACA RML53G13a, Aug. 27, 1953.

22. Polhemus, E. C., and Sleenan, W. C., "The Rolling Moment Due to Sideslip of Swept Wings at Subsonic and Transonic Speeds," NASA TN D-209, 1960.

23. Letko, William, "A Low-Speed Experimental Study of the Directional Characteristics of a Sharp-Nosed Fuselage through a Large Angle-of-Attack Range at Zero Angle of Sideslip," NACA TN 2911, March, 1953.

24. Chambers, J. R., Anglin, E. L., Bowman, J. S., "Effects of a Pointed Nose on Spin Characteristics of a Fighter Airplane Model including Correlation with Theoretical Calculations," NASA TN D-5921, Sept. 1970.

25. Polhemus, E. C., and Spreeman, K. P., "Subsonic Wind-Tunnel Investigation of the Effect of Fuselage Afterbody on Directional Stability of Wing-Fuselage Combinations of High Angles of Attack," NACA TN 3896, Dec. 1956.

26. Clark, W. H., Peoples, J. R., Briggs, M., "Occurrence of Inhibition of Large Yawing Moments During High Incidence Flight of Slender Missile Configuration," AIAA Paper 72-968, 2nd. Atmospheric Flight Mechanics Conference, Sept. 11-13/1972.

27. Keith, L. A., Marrett, G. J., Richard, R. R., "F-4C Category II Follow-on Stability and Control Tests," FTC-TR-67-26, May 1968.

28. Ross, A. J., and Beecham, L. J., "An Approximate-Analysis of the Non-Linear Lateral Motion of a Slender Aircraft (HP115) at Low Speeds," R&M No. 3674 (British), May 1970.

29. Moore, F. L., Anglin, E. L., Adams, M. S., Deal, P. L., and Person, L. H. Jr., "Utilization of a Fixed-Base Simulator to Study the Stall and Spin Characteristics of Fighter Airplanes," NASA TND-6117, March 1971.

30. Wolowicz, C., "Considerations in the Determination of Stability and Control Derivatives and Dynamic Characteristics from Flight Data," Agard Report 549, Part I, 1966.

31. Gillis, C. L., Toll, T. A., "Stability and Control of High Speed Aircraft," High Speed Problems of Aircraft and Experimental Methods, Vol. VIII, Princeton U. Press, 1961.

32. Benine, et al, "Model F/RF-4B-C Aerodynamics Derivatives," McDonnell Douglas Report 9842, 10 Dec. 1971.

33. Private Communication, Capt. David Carlton, (Edwards Air Force Base), 7 July 1972.

34. Sorensen, J. A., "Analysis of Instrumentation Error Effects on the Identification Accuracy of Aircraft Parameters," NASA CR-112121, May 1972.

35. Blakelock, J. H., Automatic Control of Aircraft and Missiles, John Wiley and Sons, New York 1963.

36. Thelander, J. A., "Aircraft Motion Analysis," FDL-TDR-64-70, 1964.

37. Eney, J., "Buffet in Air Combat Maneuvering, Problem Definition," U.S. Naval Air Development Center, Report NADC-AM-7040, 23, September 1970.

38. Cohen, M., "Buffet Characteristics of the Model F-4 Airplane in the Transonic Flight Regime," AFFDL-TR-70-56, April 1970.

39. Hollingsworth, E. G., and Cohen, M., "Determination of F-4 Aircraft Transonic Buffet Characteristics," Journal of Aircraft, Vol. 8, No. 10, Oct. 1971, pp. 757-763.

40. Mayes, J. F., Lores, M. E., and Barnard, Hr. R., "Transonic Buffet Characteristics of a 60° Swept Wing with Design Variations," Journal of Aircraft, Vol. 8, No. 6, Nov.-Dec. 1970, pp. 524-530.

41. Damstrom, E. K., and Mayes, J. F., "Transonic Flight and Wind-Tunnel Buffet Onset Investigation of the F-8D Aircraft," Journal of Aircraft, Vol. 8, No. 4, April 1971, pp. 263-270.

42. Rutan, E. L., and Gentry J. R., "Category II Stability and Control Evaluation of the F-4C Aircraft," FTC-TR-69-14, April 1969.

43. Clexton, E. W., Sullivan, D. A., Dunn, J. L., "Evaluation of the Spin and Recovery Characteristics of the F-4B Airplane, Final Report," Naval Air Test Center FT-88R-67, 27 Dec. 1967.

44. Chambers, J. R., Private Communication, 8 July 1972.

45. Mehra, R. K., and Stepner, D. E., "Maximum Likelihood Identification and Optimal Input Design for Identifying Aircraft Stability and Control Derivatives," Final Report, NASA/LRC Contract NAS-1-10700, 30 June 1972.

UNCITED REFERENCES

Williams, John and Ross, Alice, "Some Airframe Problems at Low Speeds," International Congress on Subsonic Aerodynamics, Annals of the New York Academy of Sciences, Vol. 154, Art. 2, November 22, 1968, pp. 264-305.

Gilbert, W. P., and Libbey, C. E., "Investigation of an Automatic Spin-Prevention System for Fighter Airplanes," NASA TND-6670, March 1972.

Anderson, et al, "Model F-4 Longitudinal Flying Qualities," McDonnell Douglas Report 8528, 1 June 1971.

Nienmann, et al, "Model F-4 Lateral Directional Flying Qualities," McDonnell Douglas Report E583, 1 November 1970.

Ashley, H., "Some Considerations Relative to the Prediction of Unsteady Air Loads on Lifting Configuration," Journal of Aircraft, Oct. 1971, Vol. 10, pp. 747-756.

Angelucci, S. B., "A Multivortex Method for Axisymmetric Bodies at Angle-of-Attack," Journal of Aircraft, Vol. 8, No. 12, December 1971, pp. 959-966.

Boyden, R. P., "Effects of Leading - Edge Vortex Flow on the Roll Damping of Slender Wings," Journal of Aircraft, Vol. 8, No. 7, July 1971, pp. 543-547.

Peake, D. J., Rainbird, W. J., and Atraghji, H. K., "Three Dimensional Flow Separations on Aircraft and Missiles," Journal of Aircraft, Vol. 10, No. 5, May 1972, pp. 567-580.

Stanewsky, E., and Little, B. H., "Separation and Reattachment in Transonic Airfoil Flow," Journal of Aircraft, Vol. 8, No. 12, Dec. 1971, pp. 952-958.

Ericsson, L. E., and Reding, J. P., Unsteady Airfoil Stall, Review and Extension," Journal of Aircraft, Vol. 8, No. 8, Aug. 1971, pp. 609-616.

Seckel, E., Stability and Control of Airplanes and Helicopters, Academic Press, New York, 1964.

Weissman, Robert, "Development of Design Criteria for Predicting Susceptibility of Fighter-Type Aircraft," AIAA Paper No. 72-984 2nd. Atmospheric Flight Mechanics Conference, Sept. 13, 1972.

Pellikan, Ralph, (McDonnell-Douglas Aero Group), Private Communication 5 July 1972.

APPENDIX A

SIX-DEGREE-OF-FREEDOM EQUATIONS OF MOTION

The digital computer program for the six-degree-of-freedom equations of motion is diagrammed in Figure A.1. The dynamic equations are found in many advanced texts (see, for example, Etkin, Reference 18, and Thelander, Reference 36). The equations are general with the exception of the SAS and autopilot, which are peculiar to this F-4 representation.

A.1 PRELIMINARY CALCULATIONS

A.1.1 Orientation Initialization

A.1.1.1 Initial Inertial Angles

$\Theta = \alpha + \gamma$ (pitch)

$\Psi = \delta - \beta$ (yaw)

(Φ is inputed) (roll)

A.1.1.2 Direction Cosine Matrix Between Body and Inertial Frames

$$T^{B-I} = \begin{bmatrix} \cos\Theta\cos\Psi & \cos\Theta\sin\Psi & -\sin\Theta \\ \sin\Phi\sin\Theta\cos\Psi - \cos\Phi\sin\Psi & \sin\Phi\sin\Theta\sin\Psi + \cos\Phi\cos\Psi & \sin\Phi\cos\Theta \\ \cos\Phi\sin\Theta\cos\Psi + \sin\Phi\sin\Psi & \cos\Phi\sin\Theta\sin\Psi - \sin\Phi\cos\Psi & \cos\Phi\cos\Theta \end{bmatrix}$$

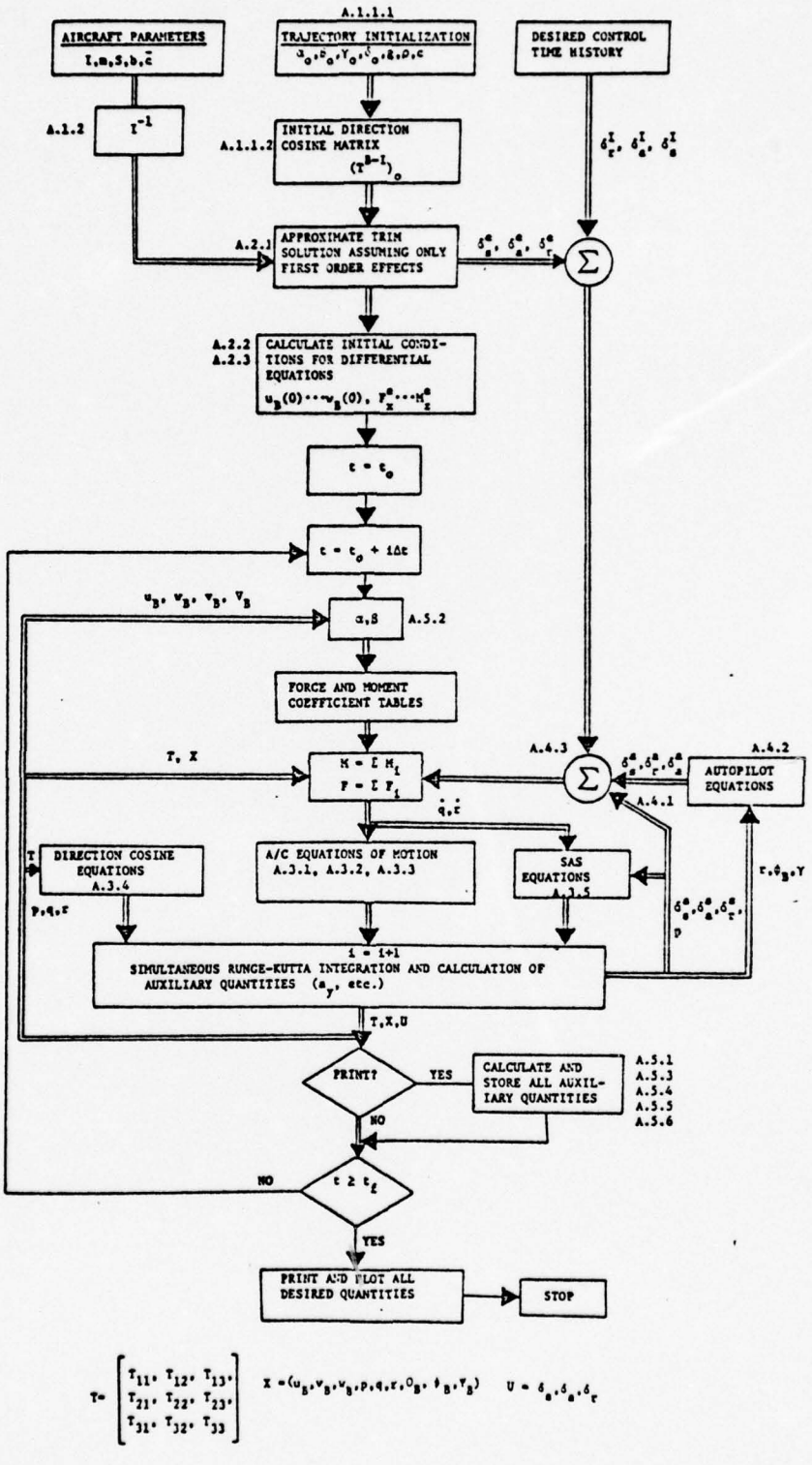


Figure A.1. Flow Chart of Six-Degree-of-Freedom Simulation

A.1.2 Inverse of Inertia Matrix

$$C = \begin{bmatrix} 1 & -I_{xy}/I_x & -I_{xz}/I_x \\ -I_{xy}/I_y & 1 & -I_{yz}/I_y \\ -I_{xz}/I_z & -I_{yz}/I_z & 1 \end{bmatrix}^{-1}$$

$$= \frac{1}{\Delta} \begin{bmatrix} 1 - I_{yz}^2/I_yI_z & (I_{xy} + I_{xz}I_{yz}/I_z)/I_x & (I_{xz} + I_{xy}I_{yz}/I_y)/I_x \\ (I_{xy} + I_{xz}I_{yz}/I_z)/I_y & 1 - I_{xz}^2/I_xI_z & (I_{yz} + I_{xy}I_{xz}/I_x)/I_y \\ (I_{xz} + I_{xy}I_{yz}/I_y)/I_z & (I_{yz} + I_{xy}I_{xz}/I_x)/I_z & 1 - I_{xy}^2/I_xI_y \end{bmatrix}$$

where

$$\Delta = 1 - \frac{I_{xy}^2}{I_xI_y} - \frac{I_{xz}^2}{I_xI_z} - \frac{I_{yz}^2}{I_yI_z} - \frac{2I_{xy}I_{xz}I_{yz}}{I_xI_yI_z}$$

A.2 TRIM CALCULATIONS

A.2.1 Approximate Solution for Trim Velocity and Controls

A.2.1.1 Initial Longitudinal Control for Trim

$$\begin{bmatrix} -h\cos\lambda & \bar{c}\,S\,C_m & \bar{c}S\,C_{m_{\delta s}} \\ \cos\lambda & S\,C_x & S\,C_{x_{\delta s}} \\ -\sin\lambda & S\,C_z & S\,C_{z_{\delta s}} \end{bmatrix} \begin{bmatrix} T \\ q_B \\ \xi \end{bmatrix} = \begin{bmatrix} 0 \\ -mg\,T_{1,3} \\ -mg\,T_{3,3} \end{bmatrix}$$

$$(\delta_s)_o = \frac{\xi}{q_B}$$

$$V = \sqrt{\frac{2q_B}{\rho}}$$

A.2.1.2 Initial Lateral Controls for Trim

$$\delta_{r_o} = \frac{C_n C_{\ell_{\delta a}} - C_\ell C_{n_{\delta a}}}{C_{\ell_{\delta r}} C_{n_{\delta a}} - C_{\ell_{\delta a}} C_{n_{\delta r}}}$$

$$\delta_{a_o} = \frac{C_\ell C_{n_{\delta r}} - C_n C_{\ell_{\delta r}}}{C_{\ell_{\delta r}} C_{n_{\delta a}} - C_{\ell_{\delta a}} C_{n_{\delta r}}}$$

A.2.2 Exact Engine Forces and Moments Required for Trim

A.2.2.1 Engine Forces

$$F_{x_o} = -\frac{q_B S}{m} (C_x + C_{x_{\delta_s}} \delta s_o) - g(T_{1,3})_o$$

$$F_{y_o} = -\frac{q_B S}{m} (C_y + C_{y_{\delta_r}} \delta r_o + C_{y_\delta} \delta a_o + C_{y_\delta} \delta s_o) - g(T_{2,3})_o$$

$$F_{z_o} = -\frac{q_B S}{m} (C_z + C_{z_{\delta_s}} \delta s_o) - g(T_{3,3})_o$$

A.2.2.2 Engine Moments

$$M_x = -\frac{q_B Sb}{I_x}\left(C_\ell + C_{\ell_{\delta_r}}\delta r_o + C_{\ell_{\delta_a}}\delta a_o + C_{\ell_{\delta_s}}\delta s_o\right)$$

$$M_y = -\frac{q_B S\bar{c}}{I_y}\left(C_m + C_{m_{\delta_s}}\delta s_o\right)$$

$$M_{z_o} = -\frac{q_B Sb}{I_z}\left(C_n + C_{n_{\delta_r}}\delta r + C_{n_{\delta_a}}\delta a + C_{n_{\delta_s}}\delta s\right)$$

A.2.3 Initial Conditions for Differential Equations

A.2.3.1 Initial Velocity Components Along Body Axes

$u = V \cos\alpha \cos\beta$

$v = V \sin\beta$

$w = V \sin\alpha \cos\beta$

(Initial Angular Velocities Along Body Axes Are Inputed)

A.3 EQUATIONS OF MOTION IN BODY AXES

A.3.1 Translation Equations

$$\begin{bmatrix} \dot{u} \\ \dot{v} \\ \dot{w} \end{bmatrix} = \begin{bmatrix} F_x^I + F_x^a + F_x^e + F_x^g \\ F_y^I + F_y^a + F_y^e + F_y^g \\ F_z^I + F_z^a + F_z^e + F_z^g \end{bmatrix}$$

where $$\begin{bmatrix} F_x^I \\ F_y^I \\ F_z^I \end{bmatrix} = \begin{bmatrix} vr - wq \\ wp - ur \\ uq - vp \end{bmatrix}$$

$$\begin{bmatrix} F_x^a \\ F_y^a \\ F_z^a \end{bmatrix} = \frac{q_B S}{m} \begin{bmatrix} C_x + C_{x_{\delta s}} \delta s + \bar{c} q \, C_{x_q} / 2V_B \\ C_y + C_{y_{\delta r}} \delta r + C_{y_{\delta a}} \delta a + C_{y_{\delta s}} \delta s + b(rC_{y_r} + p\, C_{y_p})/2V_B \\ C_z + C_{z_{\delta s}} \delta s + \bar{c} q \, C_{z_q} / 2V_B \end{bmatrix}$$

$$\begin{bmatrix} F_x^g \\ F_y^g \\ F_z^g \end{bmatrix} = g \begin{bmatrix} T_{1,3} \\ T_{2,3} \\ T_{3,3} \end{bmatrix}$$

A.3.2 Rotational Equations

$$\begin{bmatrix} \dot{p} \\ \dot{q} \\ \dot{r} \end{bmatrix} = C \begin{bmatrix} M_x^I + M_x^a + M_x^e \\ M_y^I + M_y^a + M_y^e \\ M_z^I + M_z^a + M_z^e \end{bmatrix}$$

where

$$\begin{bmatrix} M_x^I \\ M_y^I \\ M_z^I \end{bmatrix} = \begin{bmatrix} \frac{1}{I_x}\left\{p(qI_{xz}-rI_{xy}) + qr(I_y-I_z) + I_{yz}(q^2-r^2)\right\} \\ \frac{1}{I_y}\left\{q(rI_{xy}-pI_{yz}) + pr(I_z-I_x) + I_{xz}(r^2-p^2) - rI_E\Omega_E\right\} \\ \frac{1}{I_z}\left\{r(pI_{xy}-qI_{xz}) + pq(I_x-I_y) + I_{xy}(p^2-q^2) + qI_E\Omega_E\right\} \end{bmatrix}$$

$$\begin{bmatrix} M_x^a \\ M_y^a \\ M_z^a \end{bmatrix} = q_B S \begin{bmatrix} \frac{b}{I_x}\left\{C_\ell + C_{\ell_{\delta r}}\delta r + C_{\ell_{\delta a}}\delta a + C_{\ell_{\delta s}}\delta s + b(rC_{\ell_r} + pC_{\ell_p})/2V_B\right\} \\ \frac{\bar{c}}{I_y}\left\{C_m + C_{m_{\delta s}}\delta s + \bar{c}q\, C_{m_q}/2V_B\right\} \\ \frac{b}{I_z}\left\{C_n + C_{n_{\delta r}}\delta r + C_{n_{\delta a}}\delta a + C_{n_{\delta s}}\delta s + b(rC_{n_r} + pC_{n_p})/2V_B\right\} \end{bmatrix}$$

A.3.3 Roll, Pitch and Yaw Angles in Body-Axis System

$$\dot{\phi}_B = p$$

$$\dot{\theta}_B = q$$

$$\dot{\psi}_B = r$$

A.3.4 Rotation Matrix Between Body and Inertial Axis

$$\dot{T}_{1,2} = rT_{2,2} - qT_{3,2}$$

$$\dot{T}_{2,2} = pT_{3,2} - rT_{1,2}$$

$$\dot{T}_{3,2} = qT_{1,2} - pT_{2,2}$$

$$\dot{T}_{1,3} = rT_{2,3} - qT_{3,3}$$

$$\dot{T}_{2,3} = pT_{3,3} - rT_{1,3}$$

$$\dot{T}_{3,3} = qT_{1,3} - pT_{2,3}$$

A.3.5 Stability Augmentation System

$$\dot{\delta s}' = .15\dot{q} - \delta s' \qquad \text{pitch}$$

$$\dot{\delta r}_1' = 3\dot{r} - \frac{1}{2}\delta r_1' \qquad \text{yaw}$$

A.4 TOTAL CONTROLS CALCULATION

A.4.1 Stability Augmentation System

$$\delta r' = \delta r_1' + .0168 a_y g \qquad \text{if } |\delta r'| > 5^0, \text{ set } \delta r' = (\text{sgn } \delta r')5^\circ$$

$$\delta a' = .265p \qquad \text{if } |\delta a'| > 7^0.5, \text{ set } \delta a' = (\text{sgn } \delta a')7^0.5$$

$$\text{if } |\delta s'| > 0^0.5, \text{ set } \delta s' = (\text{sgn } \delta s')0^0.5$$

A.4.2 Autopilot

$$\delta_r^a = 7r + \phi_B$$

$$\delta_a^a = .3\phi_B$$

$$\delta_s^a = +\gamma$$

A.4.3 Total Controls

$$\delta r = \delta_r^e + \delta_r' + \delta_r^a + \delta_r^I \qquad |\delta r| \leq 30^0$$

$$\delta a = \delta_a^e + \delta_a' + \delta_a^a + \delta_a^I \qquad |\delta a| \leq 30^0$$

$$\delta_s = \delta_s^e + \delta_s' + \delta_s^a + \delta_s^I \qquad -21^\circ \leq \delta s \leq 9^\circ$$

where

δ_r^I, δ_a^I, δ_s^I are input controls

A.5 CALCULATION OF ADDITIONAL PARAMETERS OF MOTION

A.5.1 First Column of Rotation Matrix T

$$T_{1,1} = T_{2,2}\,T_{3,3} - T_{2,3}\,T_{3,2}$$

$$T_{2,1} = T_{3,2}\,T_{1,3} - T_{1,2}\,T_{3,3}$$

$$T_{3,1} = T_{1,2}\,T_{2,3} - T_{1,3}\,T_{2,2}$$

A.5.2 Instantaneous Angle-of-Attack and Sideslip Angle

$$\alpha = \tan^{-1}\frac{w}{u} \qquad \beta = \sin^{-1}\frac{v}{\sqrt{u^2 + v^2 + w^2}}$$

A.5.3 Roll, Pitch and Yaw Angles in Inertial System

$$\Phi = \tan^{-1}\frac{T_{2,3}}{T_{3,3}}$$

$$\Theta = -\sin^{-1} T_{1,3}$$

$$\Psi = \tan^{-1}\frac{T_{1,2}}{T_{1,1}}$$

A.5.4 Inertial Velocity Components

$$\begin{bmatrix} u_I \\ v_I \\ w_I \end{bmatrix} = T^T \begin{bmatrix} u \\ v \\ w \end{bmatrix}$$

A.5.5 Instantaneous Longitudinal and Lateral Flight Path Angles

$$\gamma = \tan^{-1}\left(\frac{w_I}{u_I}\right)$$

$$\delta = \tan^{-1}\left(\frac{v_I}{u_I}\right)$$

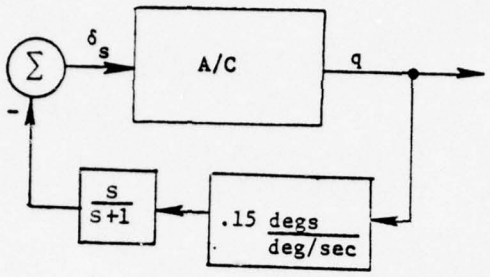
A.5.6 Body Axis Acceleration Components

$$a_x = \dot{u} - vr + wq - gT_{1,3}$$

$$a_y = \dot{v} - wp + ur - gT_{2,3}$$

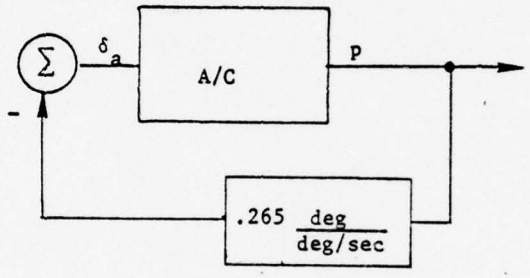
$$a_z = \dot{w} - uq - vp - gT_{3,3}$$

PITCH AXIS



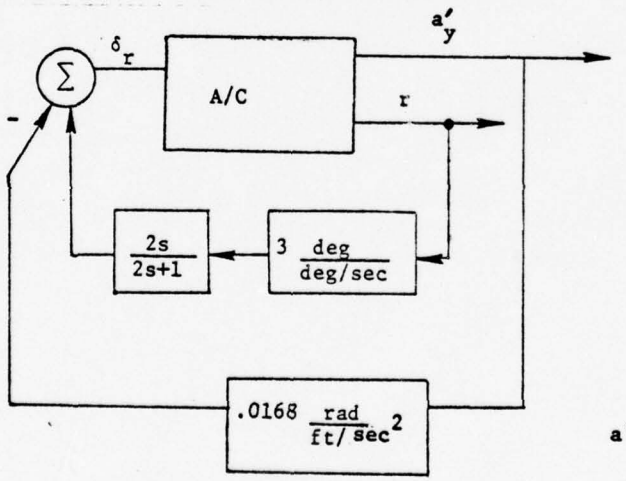
$[\delta'_s]_{max} = \pm \frac{1}{2}°$

ROLL AXIS



$[\delta'_a]_{max} = \pm 7.5°$

YAW AXIS



$[\delta'_r]_{max} = \pm 5°$

$a'_y = a_y + 9.9\dot{r} - .39\dot{p}$

Figure A.2. Block Diagram of Stability Augmentation System (SAS)

APPENDIX B

INSTRUMENTATION EQUATIONS

B.1 ATTITUDE GYROS

$$\theta_m = (1 + k_\theta)\,\theta + b_\theta + w_\theta$$

$$\phi_m = (1 + k_\phi)\,\phi + b_\phi + w_\phi$$

k_θ scale factor on pitch

b_θ bias on pitch

w_θ noise on pitch

B.2 RATE GYROS

B.2.1 Resolution

$$p_r = p + q\,\psi_p - r\,\theta_p$$

$$q_r = -p\,\psi_q + q - r\,\phi_q$$

$$r_r = p\,\theta_r - q\,\phi_r + r$$

where $\psi_p, \theta_p, \psi_q, \phi_q, \theta_r, \phi_r$ are random variables

B.2.2 Measurements

$$p_m = (1 + k_p)\,p_r + b_p + w_p$$

$$q_m = (1 + k_q)\,q_r + b_q + w_q$$

$$r_m = (1 + k_r)\,r_r + b_r + w_r$$

B.3 ANGULAR ACCELEROMETERS

B.3.1 Resolution

$$\dot{p}_r = \dot{p} + \dot{q}\,\psi_p - \dot{r}\,\theta_p$$

$$\dot{q}_r = -\dot{p}\,\psi_q + \dot{q} - \dot{r}\,\phi_q$$

$$\dot{r}_r = \dot{p}\,\theta_r - \dot{q}\,\phi_r + \dot{r}$$

B.3.2 Measurements

$$\dot{p}_m = (1 + k_{\dot{p}})\, p_r + b_{\dot{p}} + w_{\dot{p}}$$

$$\dot{q}_m = (1 + k_{\dot{q}})\, \dot{q}_r + b_{\dot{q}} + w_{\dot{q}}$$

$$\dot{r}_m = (1 + k_{\dot{r}})\, \dot{r}_r + b_{\dot{r}} + w_{\dot{r}}$$

B.4 VELOCITY

$$V_i^2 = (1 + k_v)\, V_B^2\, \sigma\, f_c(M) + b_v + w_v$$

where $\sigma = \rho/\rho_o$

$$f_c(M) = 1 + \frac{M^2}{4} + \frac{M^4}{40} + \ldots \qquad M = \text{Mach no.}$$

B.5 ANGLE-OF-ATTACK

B.5.1 Indicated

$$\alpha_i = (1 + k_\alpha)\, \tan^{-1} \frac{V_B \sin\alpha \cos\beta - q\,\ell_x + p\,\ell_y}{V_B \cos\alpha \cos\beta + q\ell_z - r\ell_y} + b_\alpha + w_\alpha$$

where ℓ_x, ℓ_y, ℓ_z are random variables

B.5.2 Corrected

$$\alpha_c = \alpha_i + \frac{\ell_x g}{V_i^2} (\bar{a}_n - \cos\phi_m \cos\theta_m) + \frac{q_m \hat{\ell}_x}{V_i} \cos\alpha_i$$

where $\bar{a}_n = -\hat{a}_{Z_{cg}}$

$\hat{\ell}_x$ is a constant

B.6 SIDESLIP ANGLE

B.6.1 Indicated

$$\beta_i = (1 + k_\beta)\, \tan^{-1} \frac{V_B \sin\beta + r\ell_x - p\,\ell_z}{V_B \cos\alpha \cos\beta + q\ell_z - r\ell_y} + b_\beta + w_\beta$$

B.6.2 Corrected

$$\beta_c = \beta_i |\cos \alpha_c| - \frac{r_m \hat{\ell}_x}{V_i} \cos \beta_i$$

B.7 LINEAR ACCELEROMETER

B.7.1 CG Acceleration

$$\ddot{x}_{cg} = \frac{\dot{u} - vr + wq}{g} - T_{1,3}$$

$$\ddot{y}_{cg} = \frac{\dot{v} - wp + ur}{g} - T_{2,3}$$

$$\ddot{z}_{cg} = \frac{\dot{w} - uq + vp}{g} - T_{3,3}$$

B.7.2 Accelerometer Triad

$$\ddot{x}_A = \ddot{x}_{cg} + \frac{\dot{q}z_{cg_A} - \dot{r}y_{cg_A} - (r^2+q^2)x_{cg_A} + rpz_{cg_A} + pqy_{cg_A}}{g}$$

$$\ddot{y}_L = \ddot{y}_{cg} + \frac{\dot{r}x_{cg_L} - \dot{p}z_{cg_L} - (r^2+p^2)y_{cg_L} + rqz_{cg_A} + pqx_{cg_A}}{g}$$

$$\ddot{z}_v = \ddot{z}_{cg} + \frac{\dot{p}y_{cg_v} - \dot{q}x_{cg_v} - (q^2+p^2)z_{cg_v} + prx_{cg_v} + qry_{cg_v}}{g}$$

where $x_{cg_A}, y_{cg_A}, \ldots, z_{cg_v}$ are random variables

B.7.3 Axial Accelerometer

$$n_x = \ddot{x}_A + \frac{\psi_A \ddot{y}_A - \theta_A \ddot{z}_v}{g}$$

$$n_{x_m} = (1 + k_{n_x}) n_x + b_{n_x} + w_{n_x}$$

$$\hat{a}_{x_{cg}} = n_{x_m} + \frac{\dot{r}_m \hat{y}_{cg_A} - \dot{q}_m \hat{z}_{cg_A}}{g}$$

where ψ_A, θ_A are random variables

$\hat{y}_{cg_A}, \hat{z}_{cg_A}$ are constants

B.7.4 Lateral Accelerometer

$$n_y = \ddot{y}_L + \frac{\phi_L \ddot{z}_v - \psi_L \ddot{x}_A}{g}$$

$$n_{y_m} = (1 + k_{n_y})\, n_y + b_{n_y} + w_{n_y}$$

$$\hat{a}_{y_{cg}} = n_{y_m} + \frac{\dot{p}_m \hat{z}_{cg_L} - \dot{r}_m \hat{x}_{cg_L}}{g}$$

where ϕ_L, ψ_L are random variables

$\hat{x}_{cg_L}$, $\hat{z}_{cg_L}$ are constants

B.7.5 Vertical Accelerometer

$$n_z = \ddot{z}_v + \frac{\theta_v \ddot{x}_A - \phi_v \ddot{y}_L}{g}$$

$$n_{z_m} = (1 + k_{n_z})\, n_z + b_{n_z} + w_{n_z}$$

$$\hat{a}_{z_{cg}} = n_{z_m} + \frac{\dot{q}_m \hat{x}_{cg_v} - \dot{p}_m \hat{y}_{cg_v}}{g}$$

where θ_v, ϕ_v are random variables

$\hat{x}_{cg_v}$, $\hat{y}_{cg_v}$ are constants

B.7.6 Pilot Station Vertical Accelerometer

$$\ddot{x}_{ps} = \ddot{x}_{cg} + \frac{\dot{q}z_{ps} - \dot{r}y_{ps} - (r^2+q^2)x_{ps} + rpz_{ps} + pqy_{ps}}{g}$$

$$\ddot{y}_{ps} = \ddot{y}_{cg} + \frac{\dot{r}x_{ps} - \dot{p}z_{ps} - (r^2+p^2)\, y_{ps} + rqz_{ps} + pqx_{ps}}{g}$$

$$\ddot{z}_{ps} = \ddot{z}_{cg} + \frac{\dot{p}y_{ps} - \dot{q}x_{ps} - (q^2+p^2)z_{ps} + prx_{ps} + qry_{ps}}{g}$$

$$n_{ps} = \ddot{z}_{ps} + \frac{\theta_v \ddot{x}_{ps} - \phi_v \ddot{y}_{ps}}{g}$$

$$n_{ps_m} = (1 + k_{n_z})\, n_{ps} + b_{n_z} + w_{n_z}$$

where x_{ps}, y_{ps}, z_{ps} are random variables

APPENDIX C

TYPICAL VARIATIONS OF FORCE AND MOMENT COEFFICIENTS

This appendix contains computer plots of the force and moment coefficients for qualitative evaluation of trends. This data is presented as computer output to provide simulation users with a ready reference of coefficient behavior. The plots are as follows

Figure	Plot
C.1	$C_x(\alpha)$ for $\beta = 0$
C.2	$C_z(\alpha)$ for $\beta = 0$
C.3	$C_m(\alpha)$ for $\beta = 0$
C.4	$C_{y_{\delta_r}}(\alpha)$ for $\beta = 0$
C.5	$C_{\ell_{\delta_s}}(\alpha)$ for $\beta = 0$
C.6	$C_{m_{\delta_s}}(\alpha)$ for $\beta = 0$
C.7	$C_{y_{\delta_s}}(\alpha)$ for $\beta = 0$
C.8	$C_{z_{\delta_s}}(\alpha)$ for $\beta = 0$
C.9	$C_{n_{\delta_a}}(\alpha)$ for $\beta = 0$
C.10	$C_{x_{\delta_s}}(\alpha)$ for $\beta = 0$
C.11	$C_{y_{\delta_a}}(\alpha)$ for $\beta = 0$
C.12	$C_{\ell_{\delta_a}}(\alpha)$ for $\beta = 0$
C.13	$C_{\ell_{\delta_r}}(\alpha)$ for $\beta = 0$
C.14	$C_{n_{\delta_r}}(\alpha)$ for $\beta = 0$

Figure	Plot
C.15	$C_{\ell_r}(\alpha)$
C.16	$C_{n_r}(\alpha)$
C.17	$C_{m_q}(\alpha)$
C.18	$C_{y_r}(\alpha)$
C.19	$C_{n_q}(\alpha)$
C.20	$C_{z_q}(\alpha)$
C.21	$C_{\ell_p}(\alpha)$
C.22	$C_{n_p}(\alpha)$
C.23	$C_{n_{\delta s}}(\alpha)$ for $\beta = 0$
C.24	$C_{y_p}(\alpha)$
C.25	$C_n(\beta)$ for $\alpha = 20$
C.26	$C_n(\beta)$ for $\alpha = 25$
C.27	$C_y(\beta)$ for $\alpha = 20$
C.28	$C_y(p)$ for $\alpha = 25$
C.29	$C_\ell(\beta)$ for $\alpha = 20$
C.30	$C_\ell(\beta)$ for $\alpha = 25$

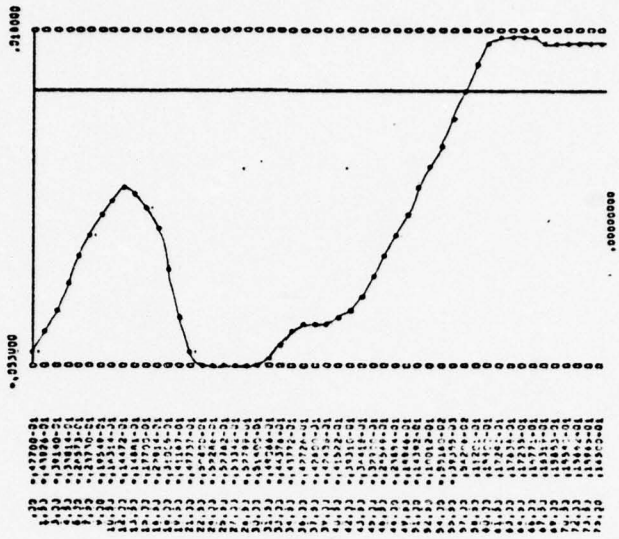


Figure C.1. $C_x(\alpha)$ for $\beta = 0$

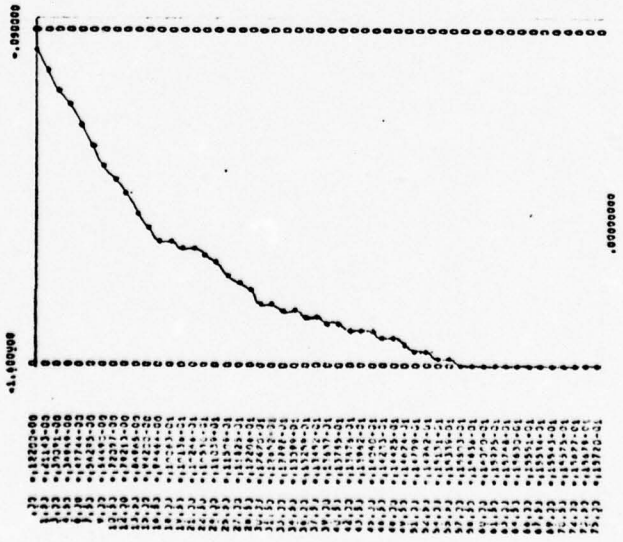


Figure C.2. $C_z(\alpha)$ for $\beta = 0$

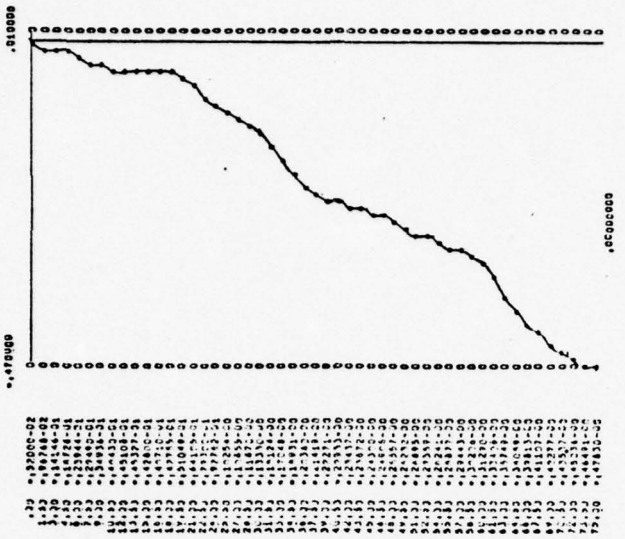


Figure C.3. $C_m(\alpha)$ for $\beta = 0$

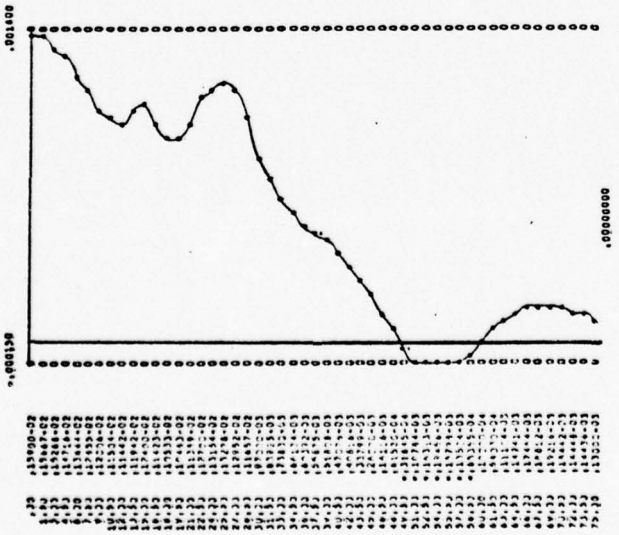


Figure C.4. $C_{y_{\delta_r}}(\alpha)$ for $\beta = 0$

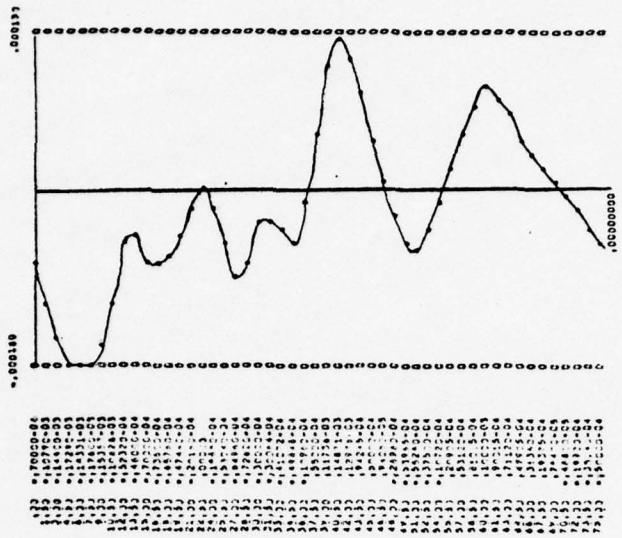


Figure C.5. $C_{\ell_{\delta_s}}(\alpha)$ for $\beta = 0$

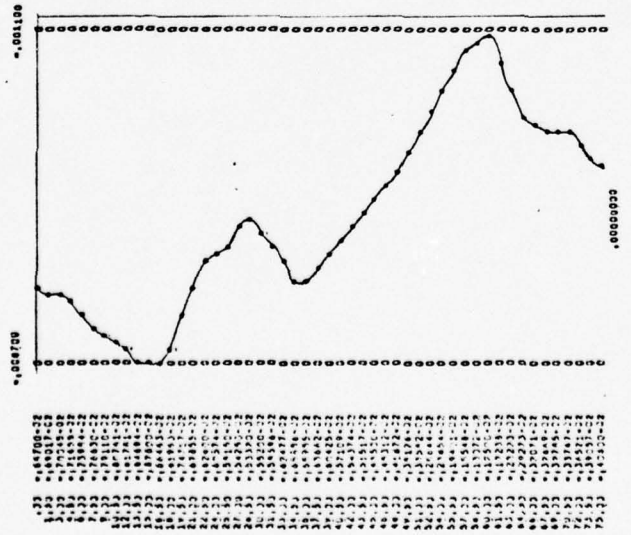


Figure C.6. $C_{m_{\delta_s}}(\alpha)$ for $\beta = 0$

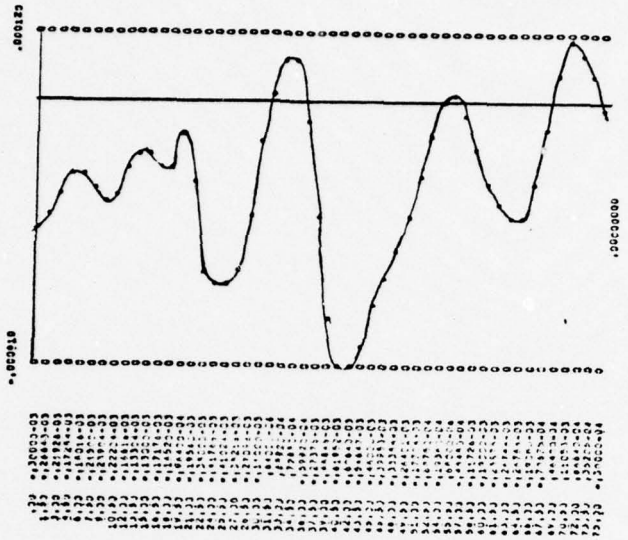


Figure C.7. $C_{y_{\delta_s}}(\alpha)$ for $\beta = 0$

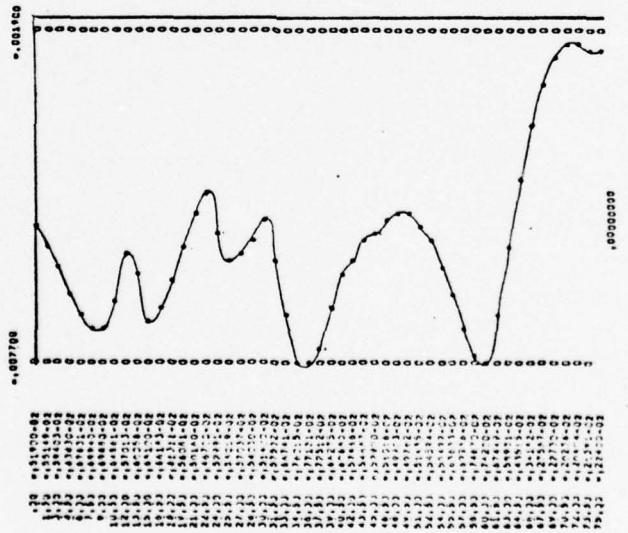


Figure C.8. $C_{z_{\delta_s}}(\alpha)$ for $\beta = 0$

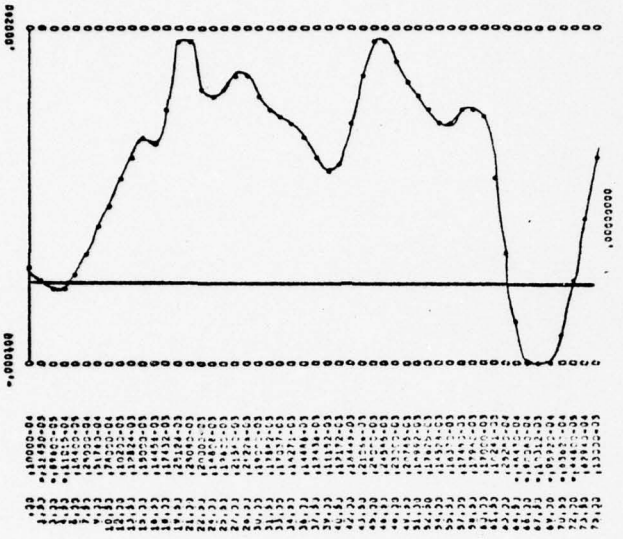


Figure C.9. $C_{n_{\delta_s}}(\alpha)$ for $\beta = 0$

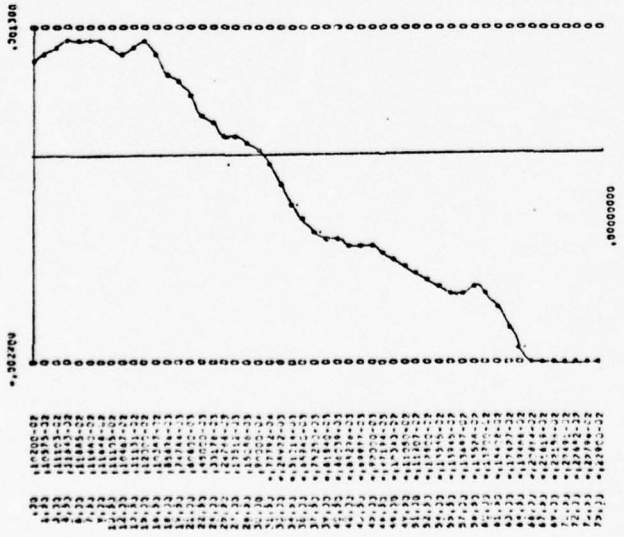


Figure C.10. $C_{x_{\delta_s}}(\alpha)$ for $\beta = 0$

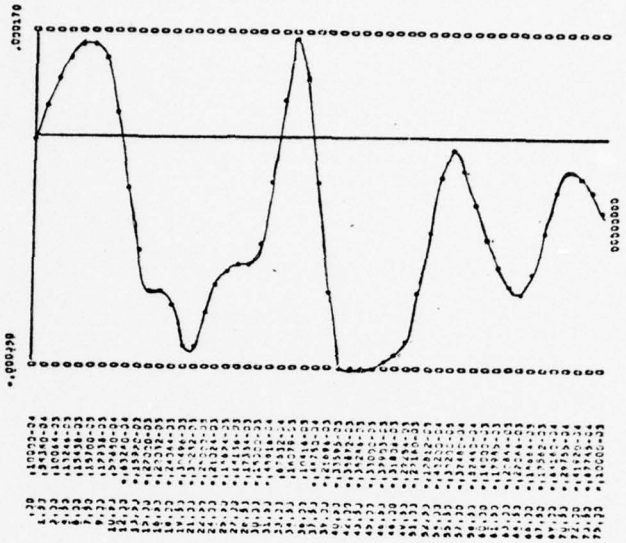


Figure C.11. $C_{y_{\delta_a}}$ (α) for $\beta = 0$

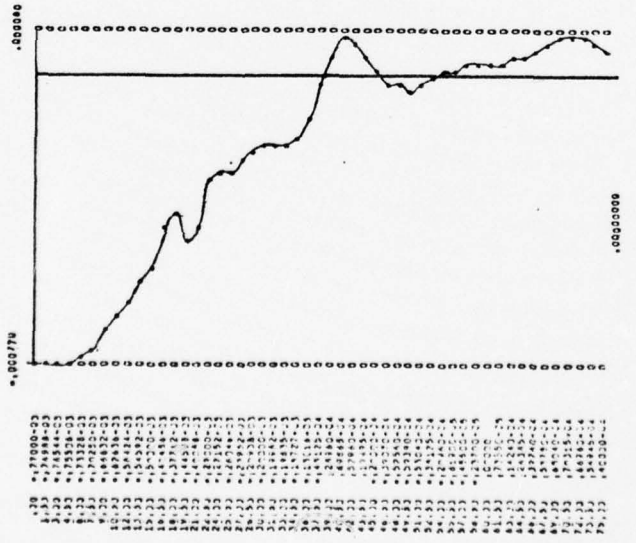


Figure C.12. $C_{\ell_{\delta_a}}$ (α) for $\beta = 0$

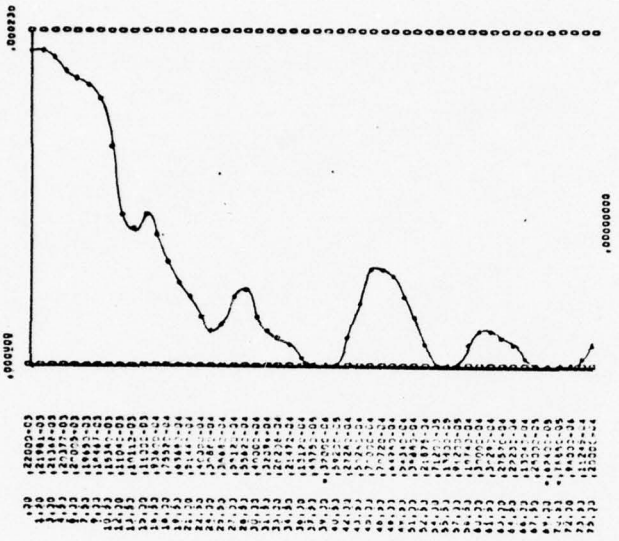


Figure C.13. $C_{\ell_{\delta_r}}(\alpha)$ for $\beta = 0$

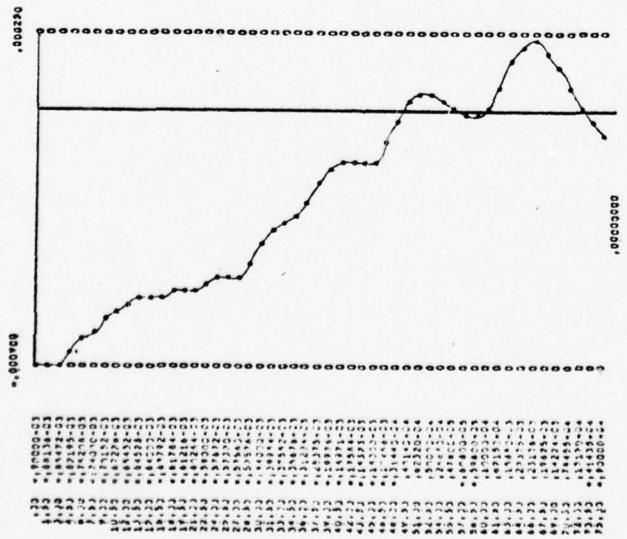


Figure C.14. $C_{n_{\delta_r}}(\alpha)$ for $\beta = 0$

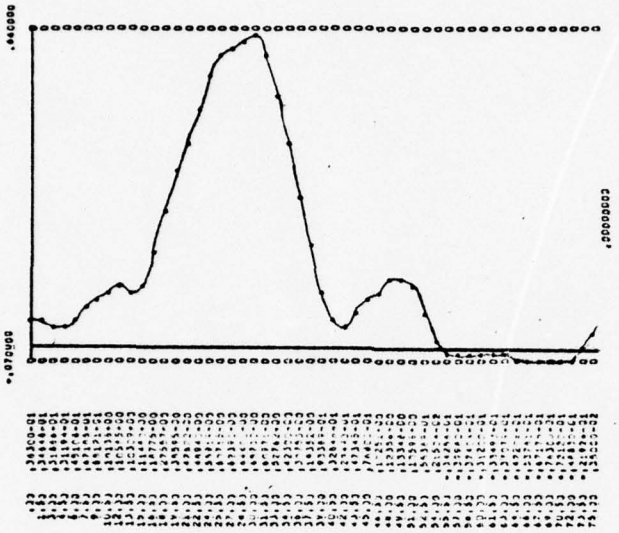


Figure C.15. $C_{\ell_r}(\alpha)$

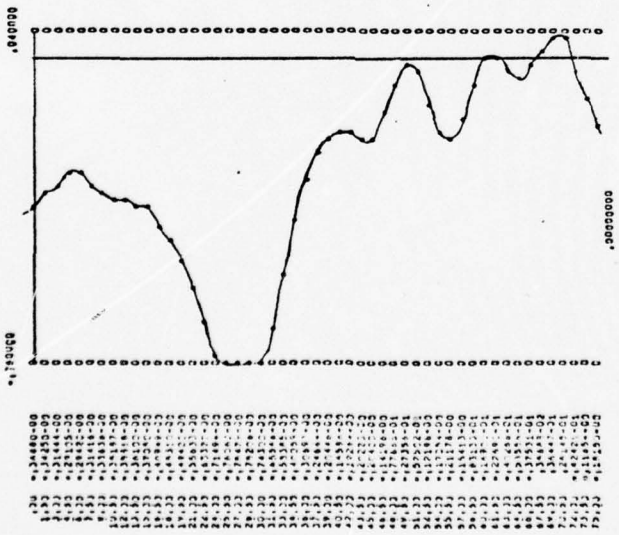


Figure C.16. $C_{n_r}(\alpha)$

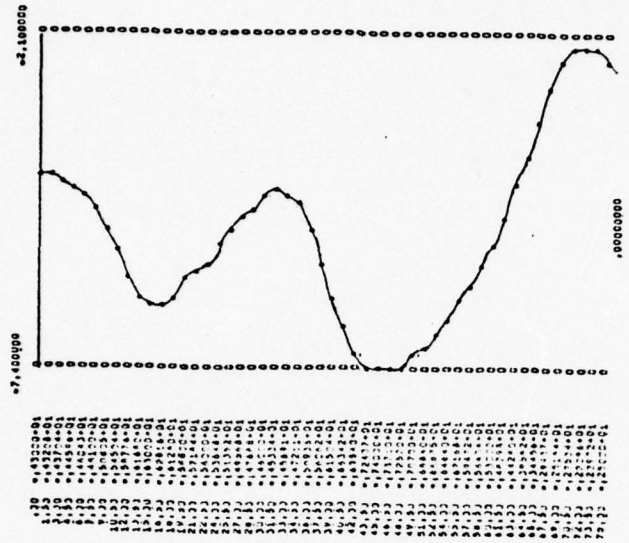


Figure C.17. $C_{m_q}(\alpha)$

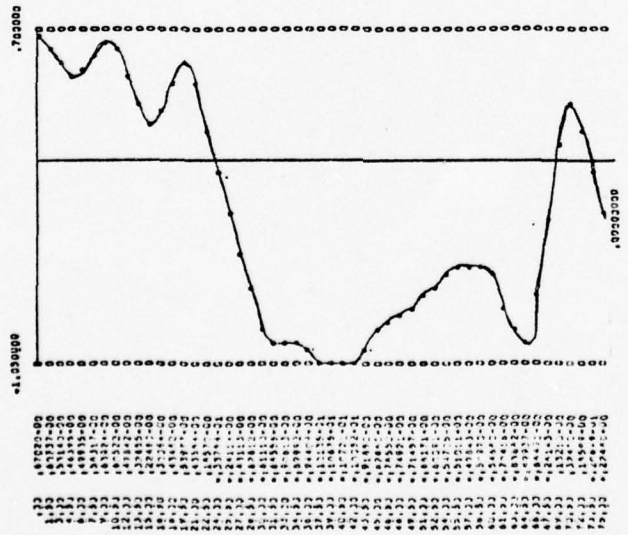


Figure C.18. $C_{y_r}(\alpha)$

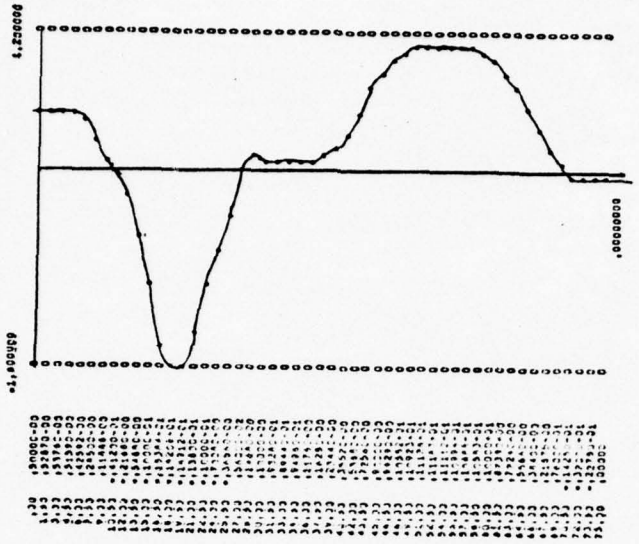


Figure C.19. $C_{n_q}(\alpha)$

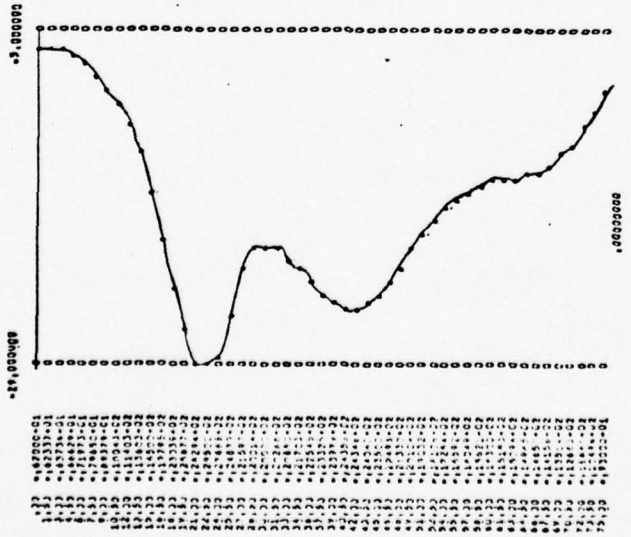


Figure C.20. $C_{z_q}(\alpha)$

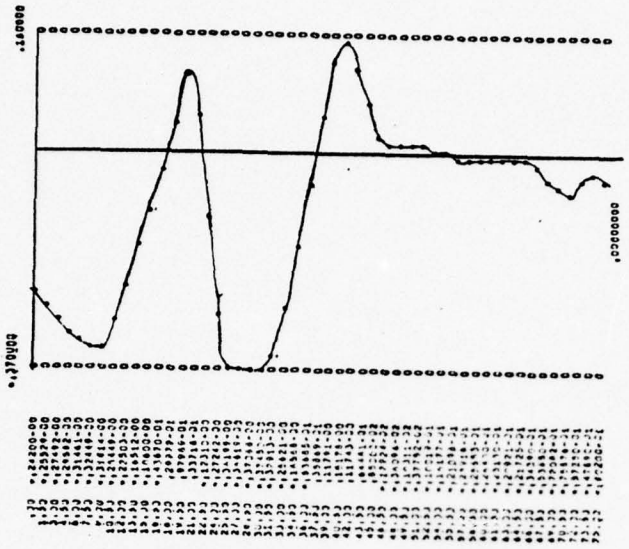


Figure C.21. $C_{\ell_p}(\alpha)$

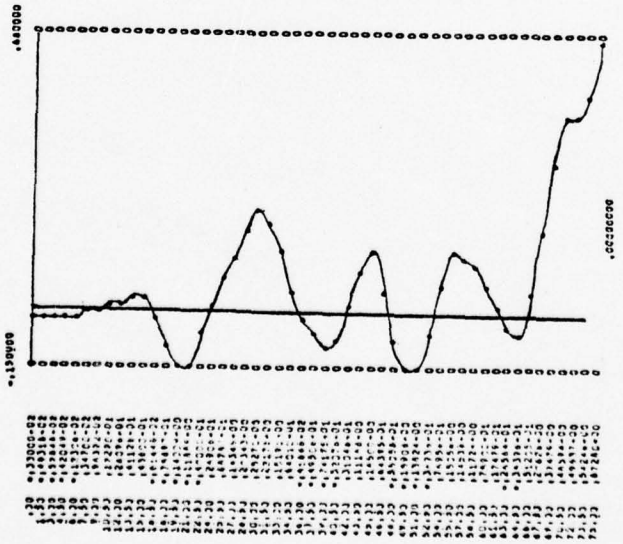


Figure C.22. $C_{n_p}(\alpha)$

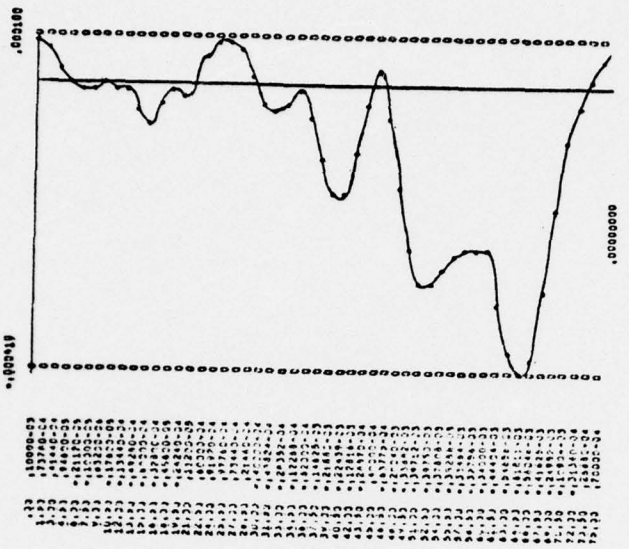


Figure C.23. $C_{n_{\delta_s}}(\alpha)$ for $\beta = 0$

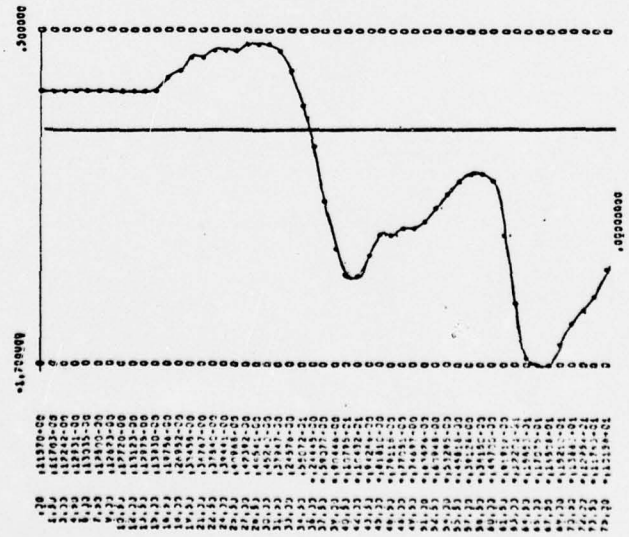


Figure C.24. $C_{y_p}(\alpha)$

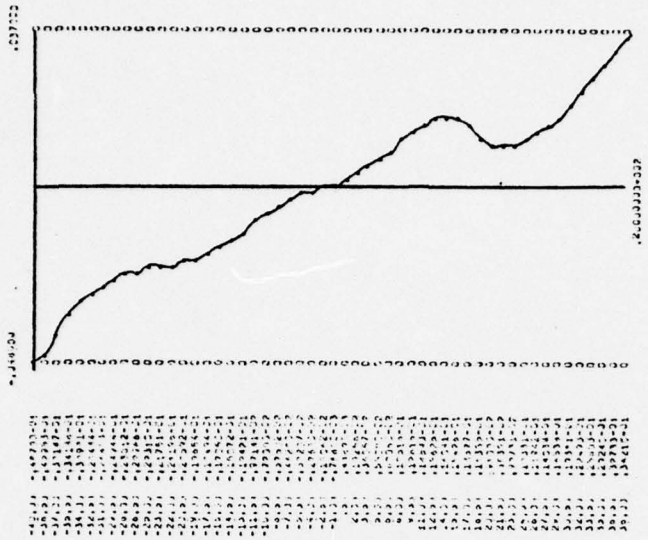


Figure C.25. $C_n(\beta)$ for $\alpha = 20$

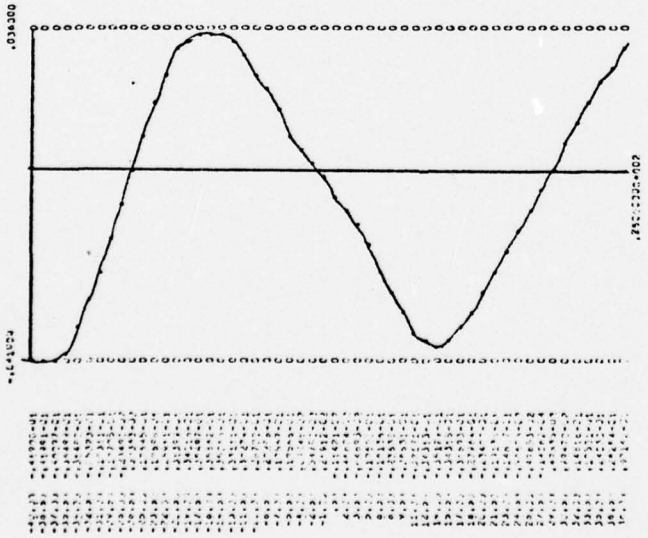


Figure C.26. $C_n(\beta)$ for $\alpha = 25$

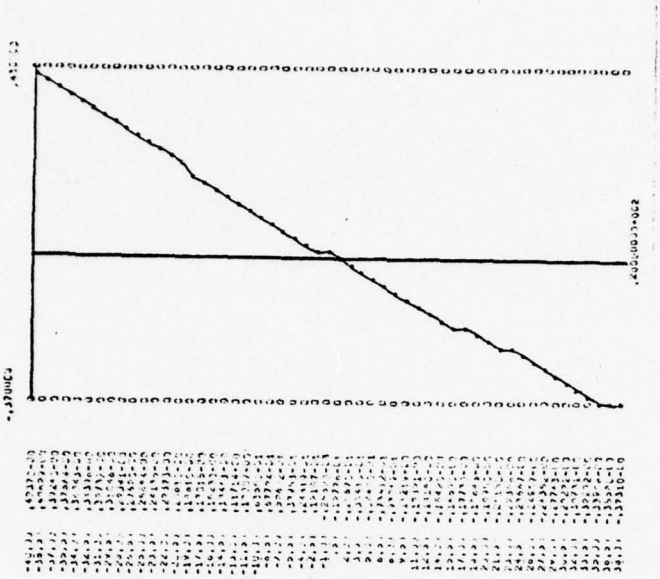


Figure C.27. $C_y(\beta)$ for $\alpha = 20$

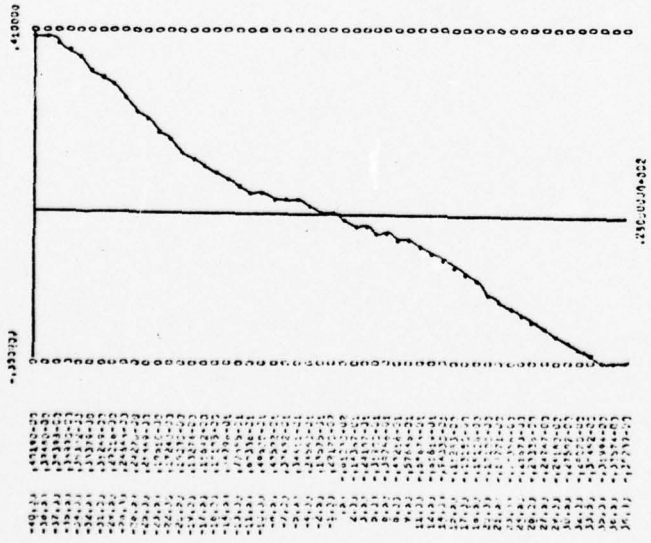


Figure C.28. $C_y(p)$ for $\alpha = 25$

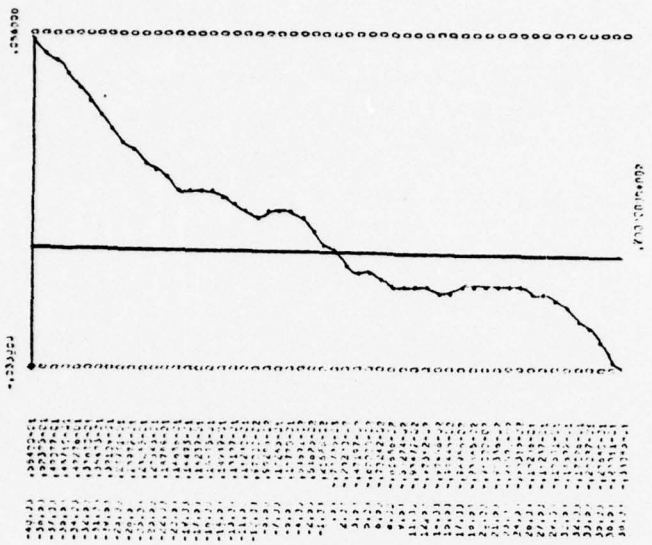


Figure C.29. $C_{\ell}(\beta)$ for $\alpha = 20$

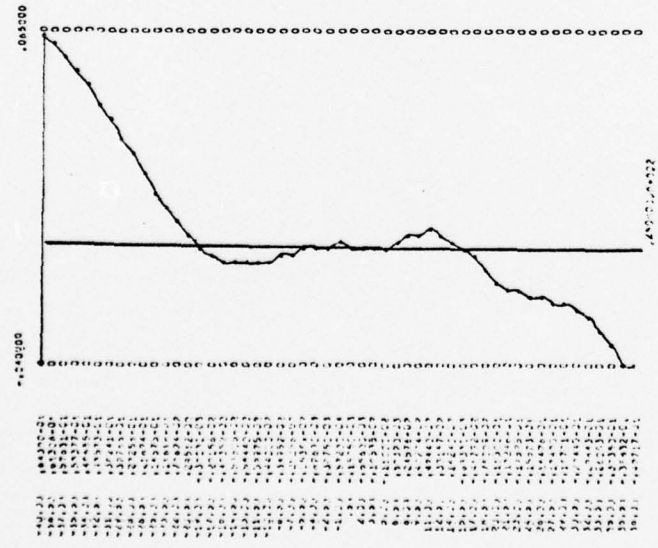


Figure C.30. $C_{\ell}(\beta)$ for $\alpha = 25$

APPENDIX D

REVIEW OF ACTUAL FLIGHT TRACES

OF THE F-4 AIRPLANE AT HIGH AOA

D.1 INTRODUCTION

The purpose of this appendix is to indicate how the actual flight traces might best be utilized in qualifying the response of the computer model simulation as satisfactorily accurate. These results are based on References 17 and 43.

D.2 SCOPE OF TRACES REVIEWED, CLEAN LOADINGS ONLY

D.2.1 Configurations

		AF (Ref 17)	Navy (Ref. 43)
	G(Glide)	0	7
	PA(power approach)	2	0
	CR(cruise)	18	0
mod	CR(cruise)	2	0
	CO(combat)	1	0
	D(Dive)	2	0
		25	7

D.2.2 Flight Conditions

No Departure (level)	4	0
Rolling Departure	8	0
Steep-smooth spin	1	0
Steep-mildly osc spin	12	5
Flat spin	0	2

D.2.3 Airspeed Entries

Transonic decelerations	2	1
Low speed	23	6

D.3 PRE-DEPARTURE WING ROCK CHARACTERISTICS

The following characteristics summarize the observed wing rock for high subsonic and transonic conditions.

Onset 21° - 23.6° or 22-24 units AOA

ϕ amplitude $\pm$ 20° - 30°

β amplitude $\pm$ 10° - 20°

Period 4 seconds at 140 KCAS
2 seconds at 280 KCAS

ϕ/β Phase Angle

Phase angle between ϕ and β is variable and no common factor for predicting phase angle could be found. Phase angles were found throughout the entire range $\pm$ 180°. Variable phase angle is probably due to changing nonlinearity of C_{l_β} and C_{n_β} with α. There is a possibility of phase angle dependency on angle of attack.

D.4 PRE-DEPARTURE PITCH ANGLE MOTION

All traces exhibit smooth pitch angle time histories with no apparent coupling between wing rock and pitch angle. Even transonic traces display very little pitch disturbances prior to departure AOA.

D.5 PILOT CONTROLLED PITCH RATES

Most entries into high AOA were performed in wind-up turns by pulling rapidly back on the stick resulting in only 1 to 3 seconds in the pre-departure wing rock range prior to a rolling departure or spin. Only traces 48 (PA Conf) and trace 154 (1/2 flaps) show extended time periods of pre-departure wing rock. Trace 48* shows 20 seconds and trace 154 shows 24 seconds of pre-departure wing rock.

D.6 CONTROL EFFECTIVENESS AND PILOT RESPONSE

D.6.1 Longitudinal Control and Pilot Response

Pre-departure wing rock does not adversely effect longitudinal control during a deceleration to a normal 1 "g" stall. Constant altitude can be rather easily maintained by simply pulling back to proper trim position during the deceleration, until departure AOA is reached and the pitch-down occurs. In the transonic flight regime, the higher buffet intensity and higher frequency wing rock causes somewhat more difficulty

* Trace number refers to page number of Reference 18.

in applying constant "g", but nothing severe until close to departure AOA. All pitch angle traces during pre-departure wing rock are smooth with high frequency stick motion amplitudes very small.

D.6.2 Lateral Control and Pilot Response

Lateral control is sufficient during a deceleration to a normal 1 "g" stall to maintain an "average" wings level and constant heading flight condition even with wing rock. Adverse yaw is sufficient at departure to determine direction of spin. Lateral control effectiveness is lost during a transonic stall entry at about 25 units AOA and adverse yaw results in significant yawing motion opposite to applied aileron. Departure generally is a snap roll in direction opposite to turn. Several traces (note 48 and 154) indicate pilot control of roll mode during wing rock to include primarily a negative gain on roll rate ($\delta a = + Cp$). Positive δa is right aileron down. Thus, a good lateral/directional autopilot during wing rock simulation is probably

$$\delta a = + C_1 p + C_2 r + C_3 \psi \ .$$

D.6.3 Directional Control and Pilot Response

Noticeable rudder motion occurred in many traces with no pilot rudder forces. Note traces 48, 50, and 78. It is difficult to determine how much yaw damper action may be affecting wing rock. However, the Navy report states that STAB AUG did not noticeably affect stall characteristics. Trace 52 definitely shows rudder motion out of phase with β while 1N shows rudder motion precisely in phase with β during wing rock. For simulation purposes, rudder motion could be a function only of STAB AUG and contain no pilot inputs.

D.7 BEST TRACES DISPLAYING PRE-DEPARTURE WING ROCK

			SAS		
			P	R	Y
Trace 48 (PA Conf)	1 "g"	120-110 KCAS	?	?	?
Trace 154 (1/2 flaps)	1 "g"	130- 50 KCAS	on	on	on
Trace 2N (G Conf)	2.5 "g"	300-200 KCAS	on	on	on

D.8 RECOMMENDED SIMULATION RUNS

D.8.1 Stick Fixed Response

a. Initial Conditions

$\alpha = 35°$ $\theta = 35°$ $\gamma = 0°$

$h = 30{,}000$ ft

$\phi = 0°$ $p = 0°/sec$

$\psi = 0°$ $r = 0°/sec$

$q = 0°/sec$

b. Trim

δs, δa, δr, V, and T for initial conditions

c. Control

δs, δa, and δr fixed at intial trim

d. STAB AUG on

D.8.2 Response with Lateral/Directional Autopilot

Same as Run A, but include Lat/Dir autopilot for δa control.

D.8.3 Response with Lat/Dir and Altitude Autopilot

Same as Run B, but include Altitude autopilot for δs control.

D.8.4 Deceleration Through Pre-Departure Wing Rock Range

Same as Run C, but begin at 25° AOA and reduce T to a constant setting slightly less than trim T, so that $\dot{V} \approx -1$ KCAS.

D.9 SIGNIFICANT PRE-DEPARTURE WING ROCK CHARACTERISTICS TO ACHIEVE IN IN SIMULATION

ϕ, β phasing.

ϕ, β amplitudes.

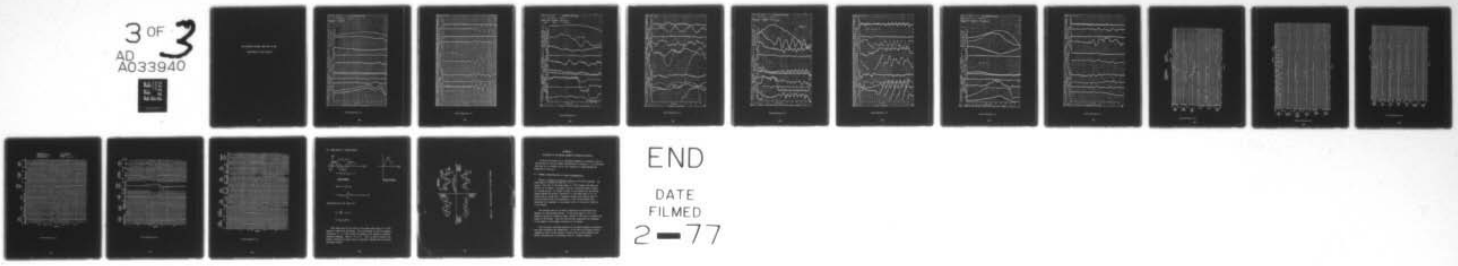
Appropriate period.

Smooth pitch angle motion.

Slight nose rise and pitch down at departure.

AD-A033 940 SYSTEMS CONTROL INC PALO ALTO CALIF F/G 1/2
IDENTIFICATION OF AIRCRAFT STABILITY DERIVATIVES FOR THE HIGH A--ETC(U)
1972 W E HALL N00014-72-C-0328
UNCLASSIFIED TR-1 NL

3 OF 3
AD A033940



END

DATE FILMED
2-77

THE FOLLOWING FIGURES WERE USED IN THE

DEVELOPMENT OF THE AUTOPILOT

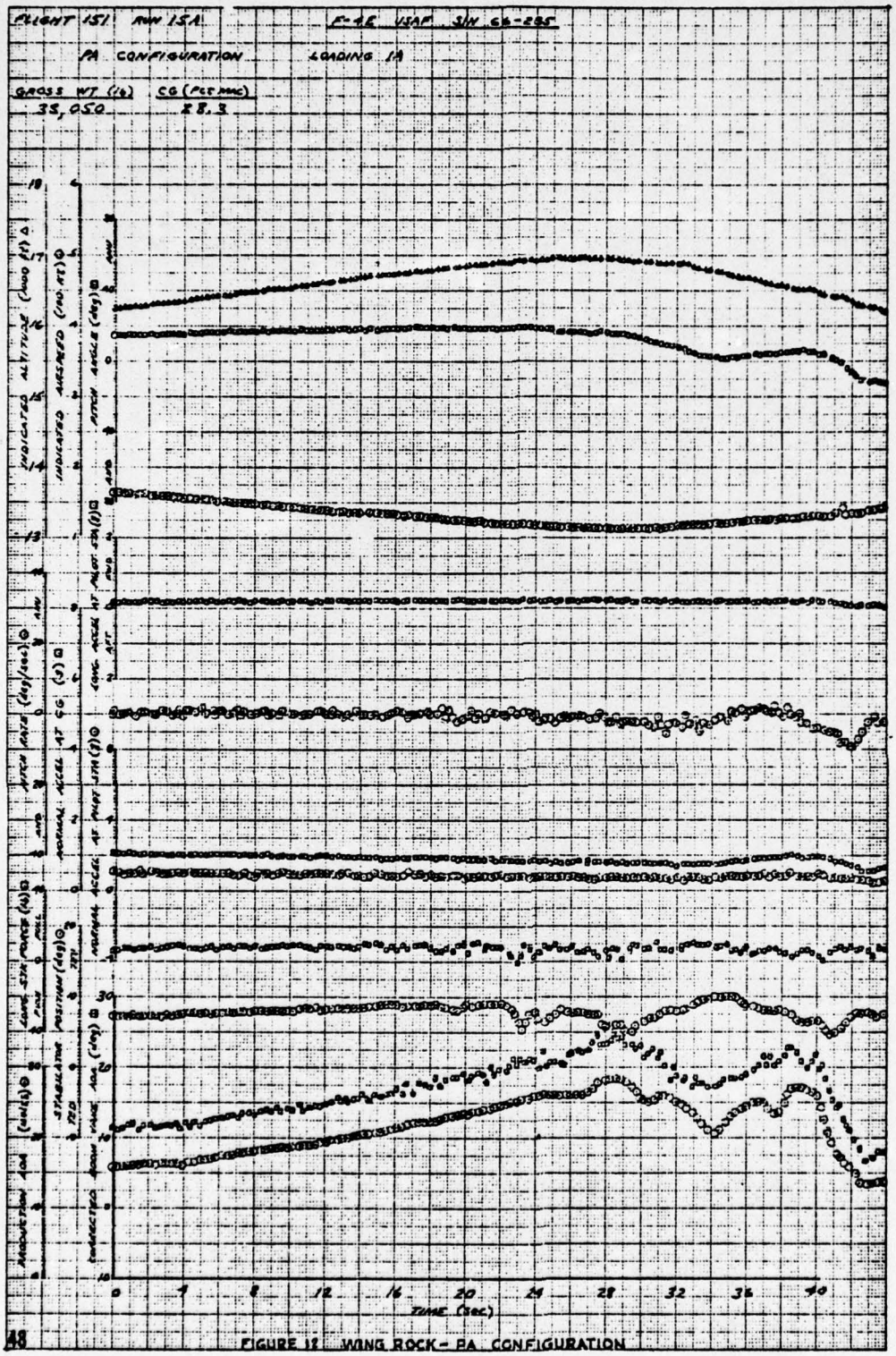


FIGURE 12 WING ROCK - PA CONFIGURATION

(from Reference 17)

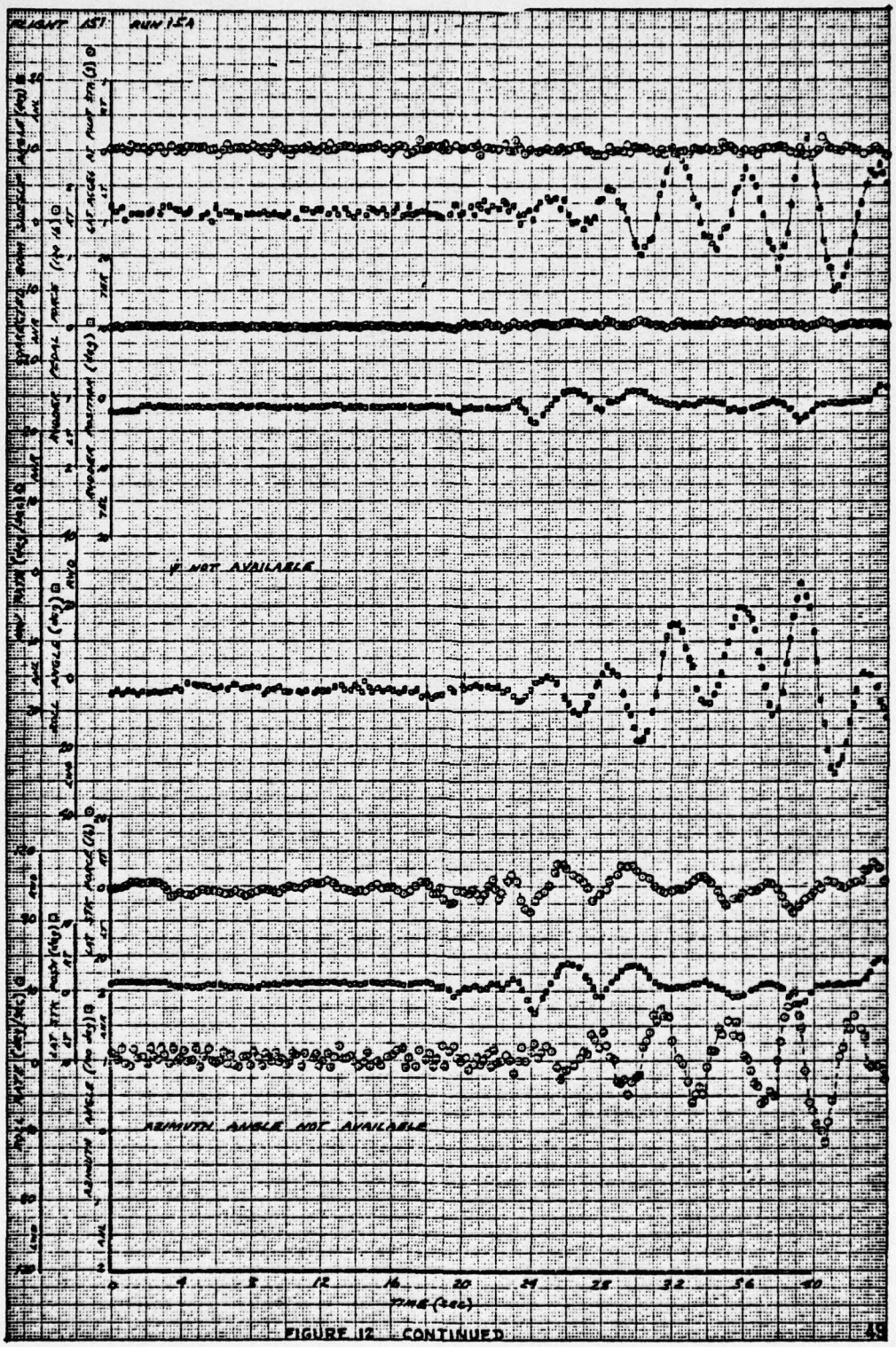


FIGURE 12 CONTINUED

(from Reference 17)

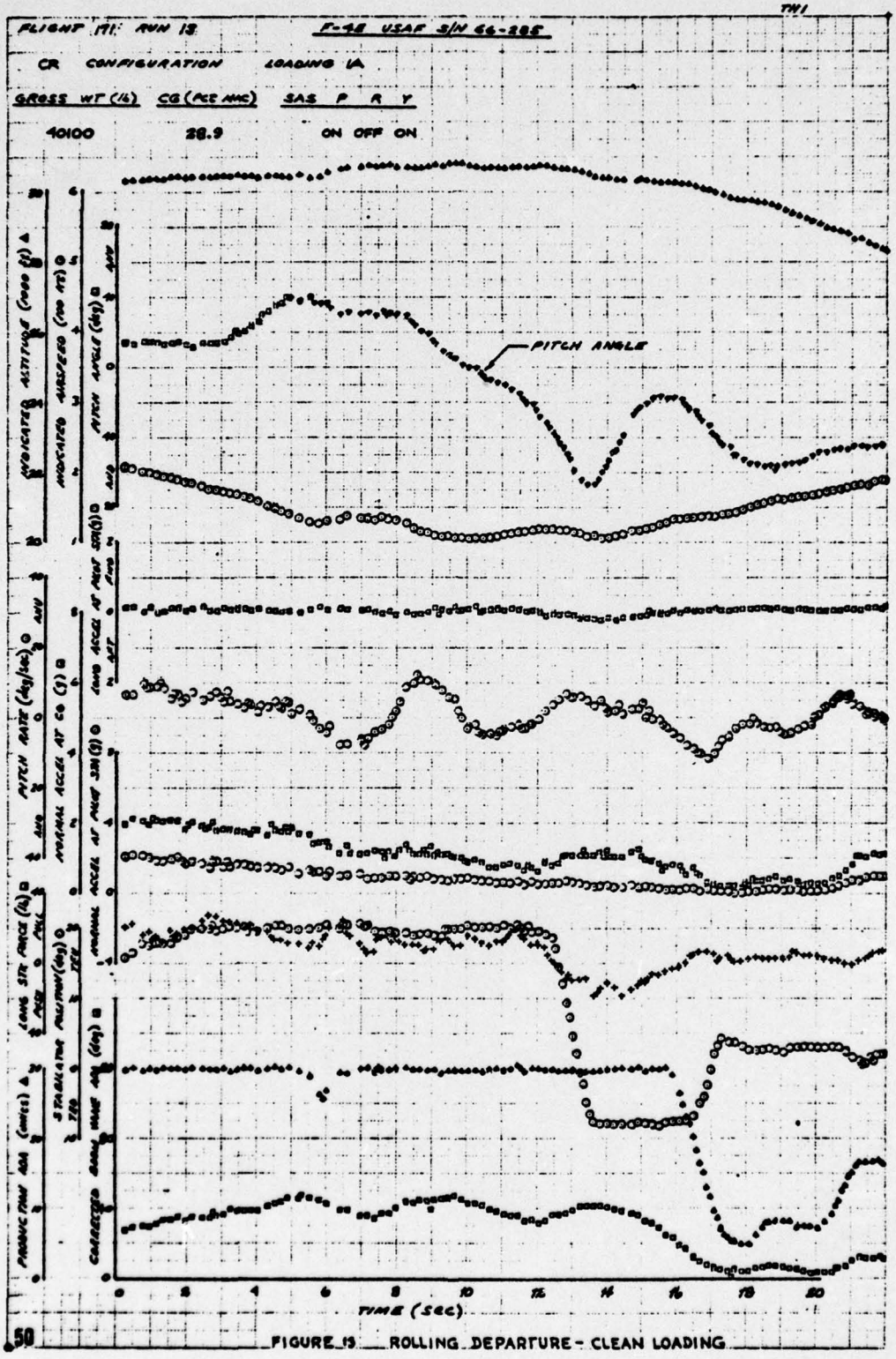


FIGURE 13 ROLLING DEPARTURE - CLEAN LOADING

(from Reference 17)

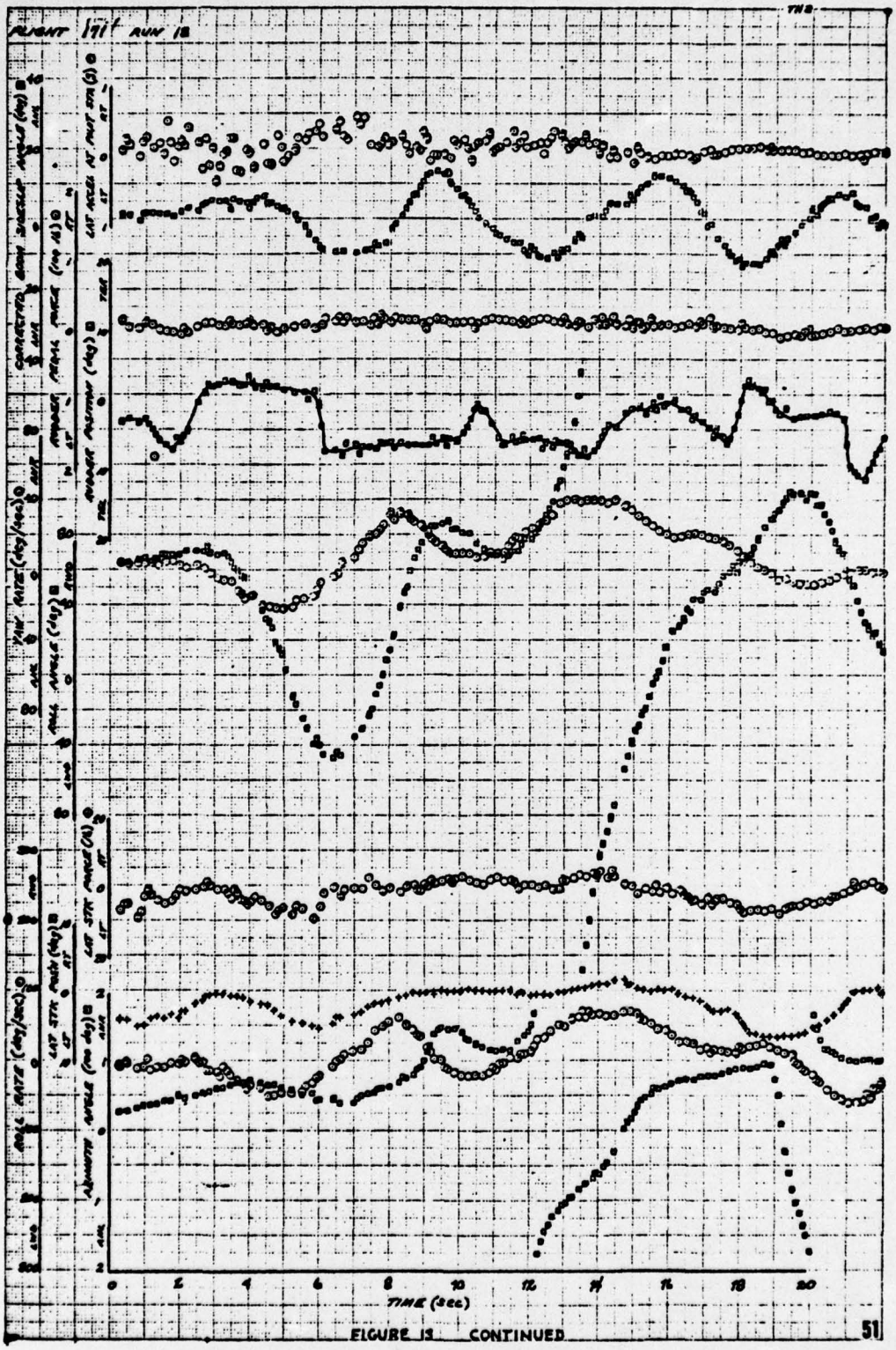


FIGURE 13 CONTINUED

51

(from Reference 17)

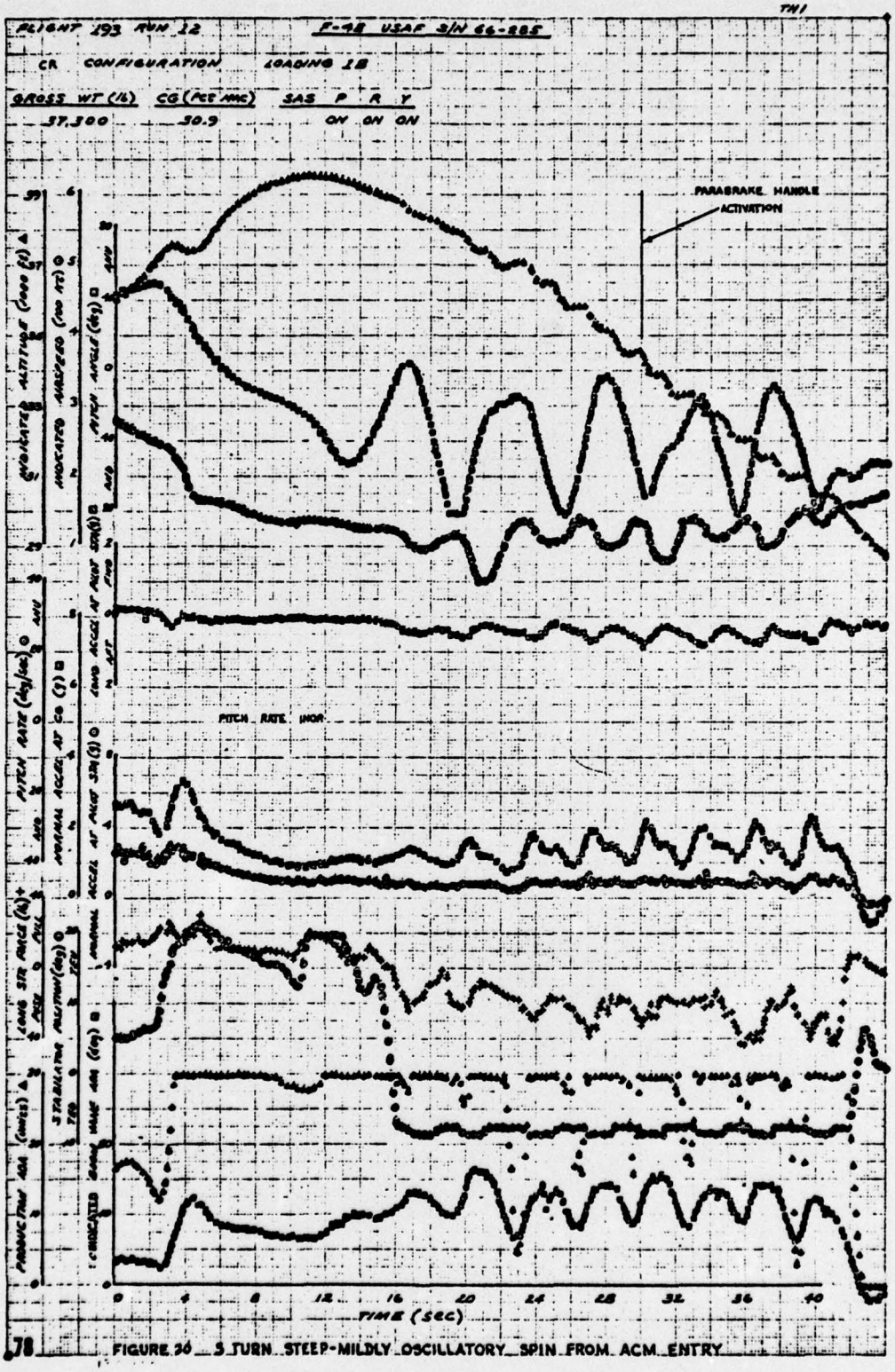


FIGURE 36 3 TURN STEEP-MILDLY OSCILLATORY SPIN FROM ACM ENTRY

(from Reference 17)

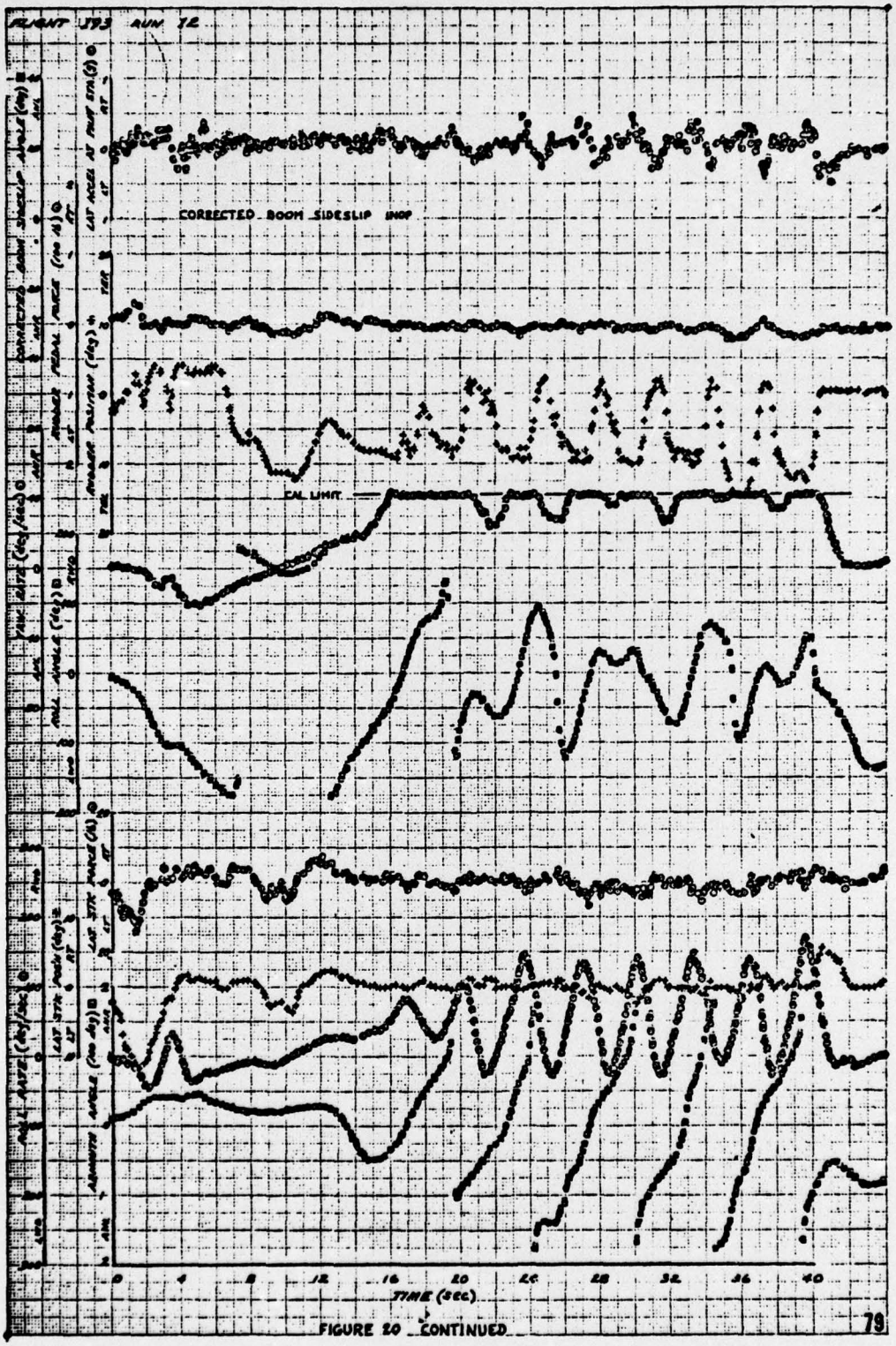
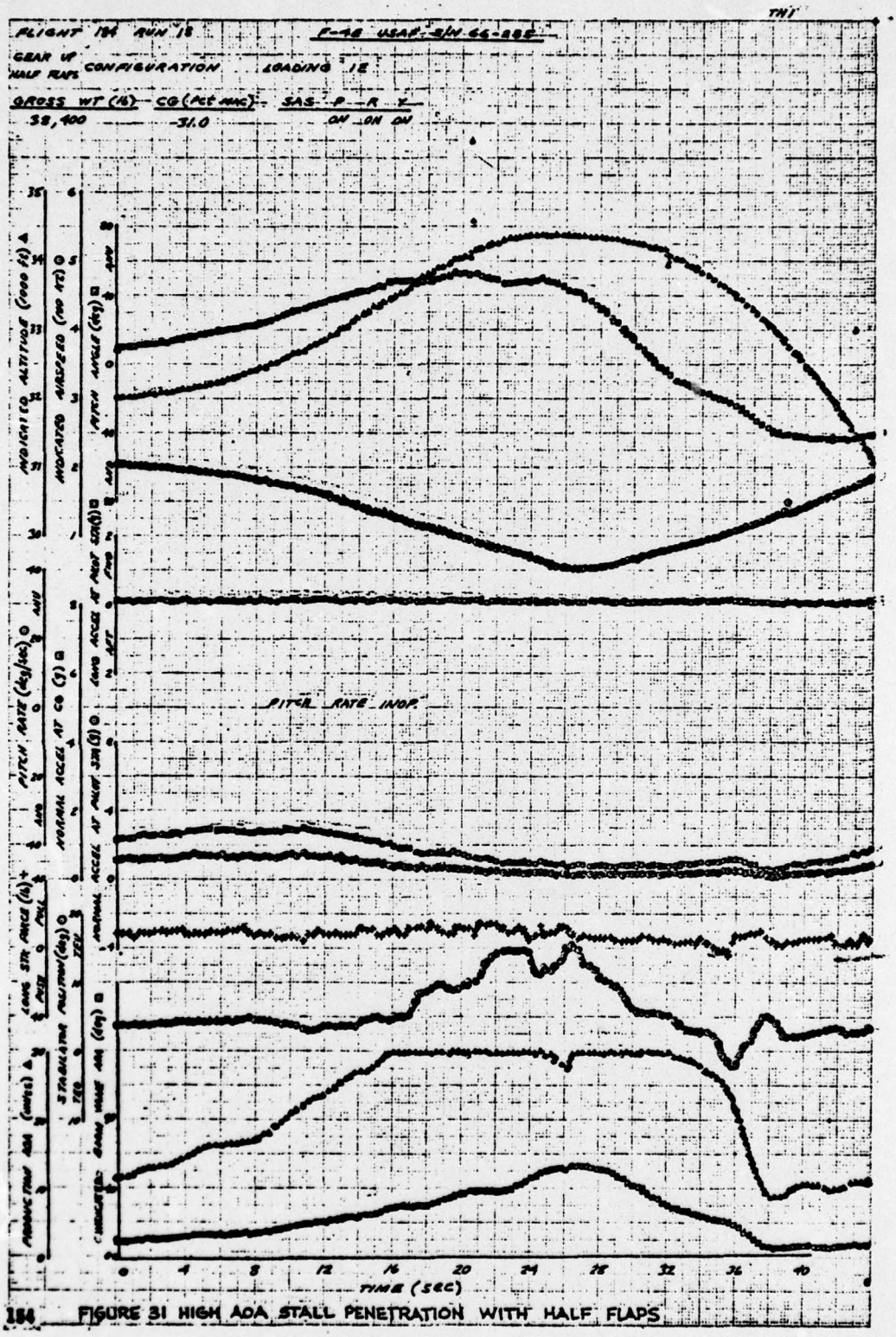


FIGURE 20 CONTINUED

79

(from Reference 17)



184 FIGURE 31 HIGH AOA STALL PENETRATION WITH HALF FLAPS

(from Reference 17)

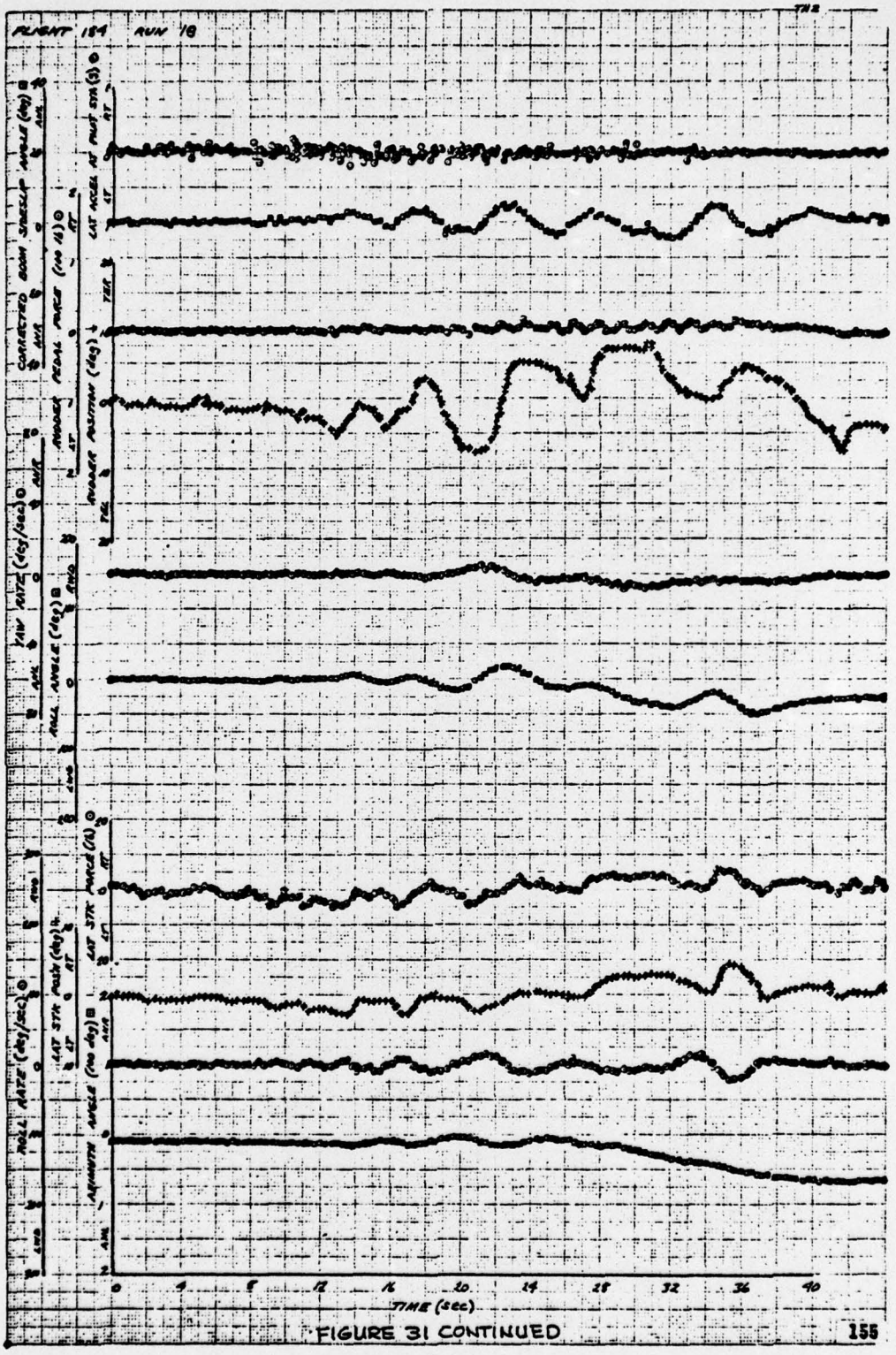
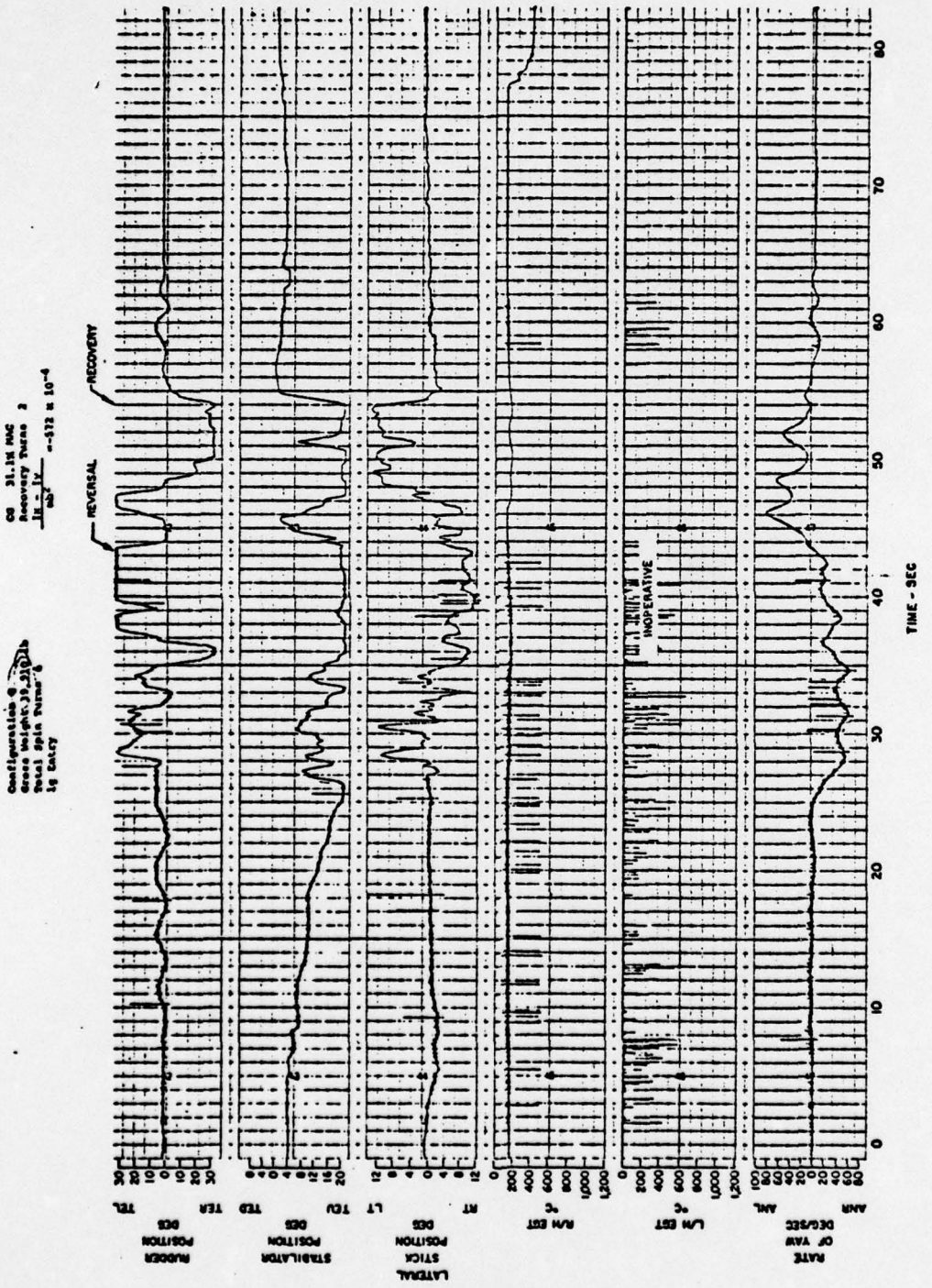
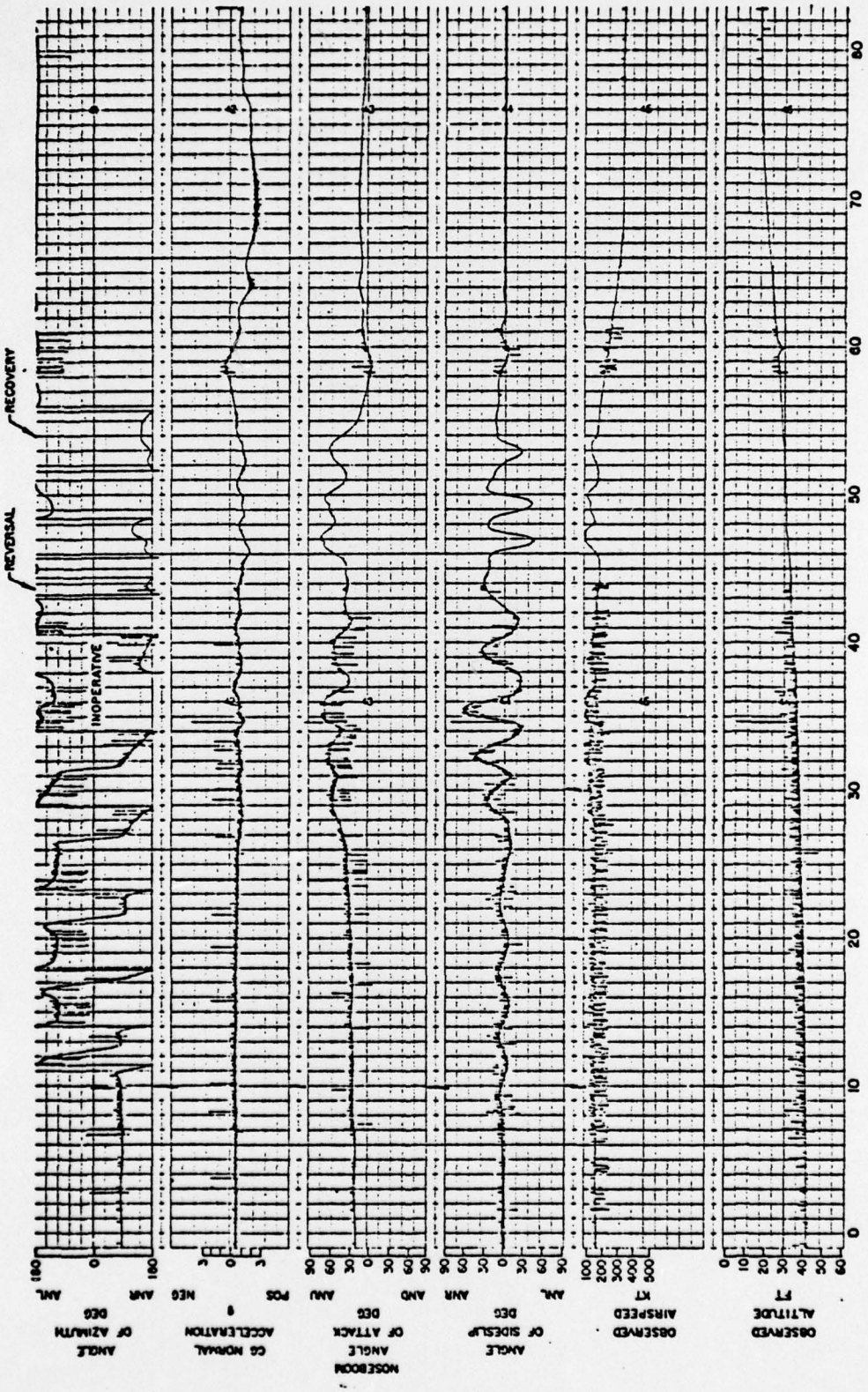


FIGURE 31 CONTINUED

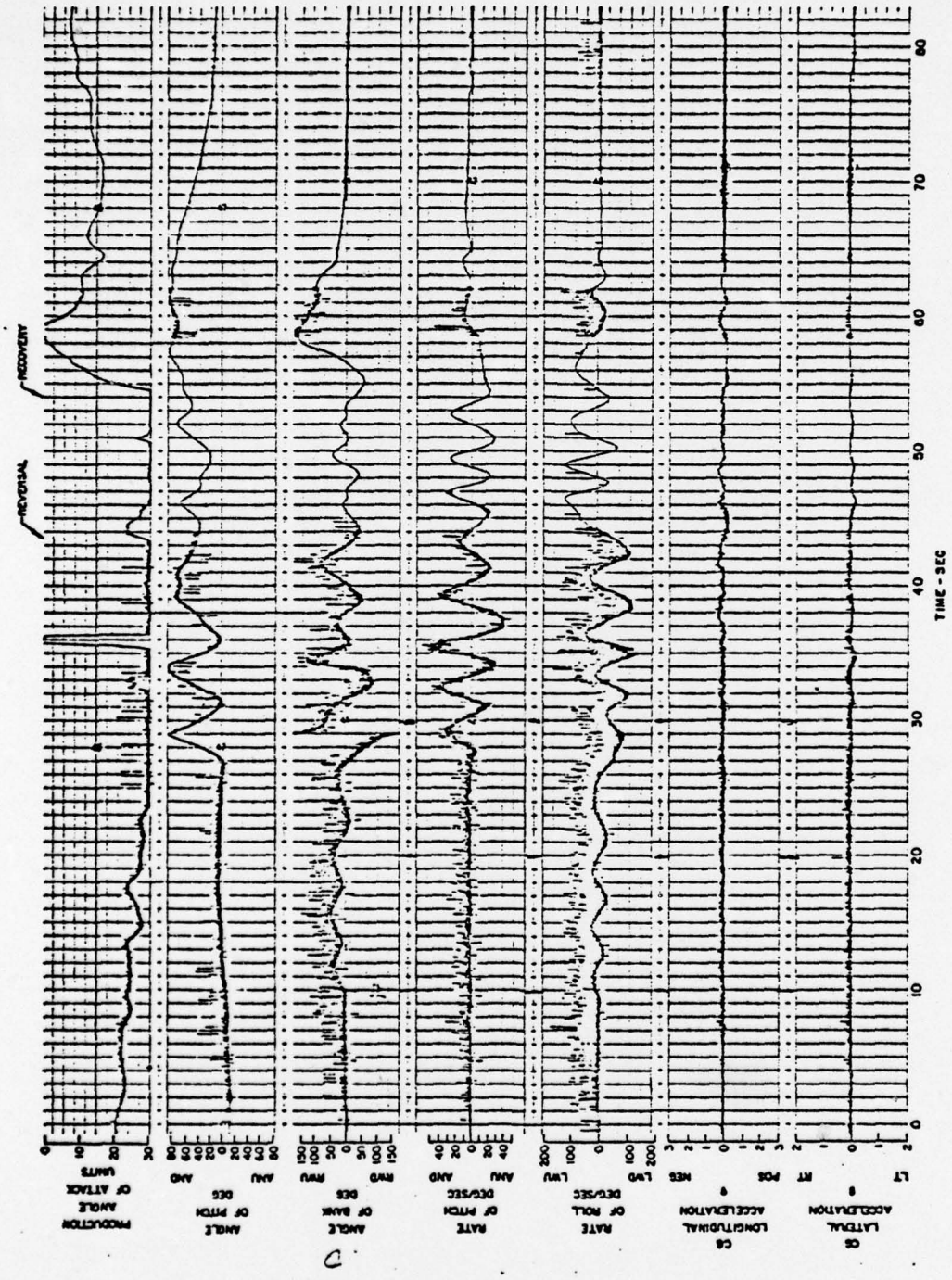
(from Reference 17)



(from Reference 43)

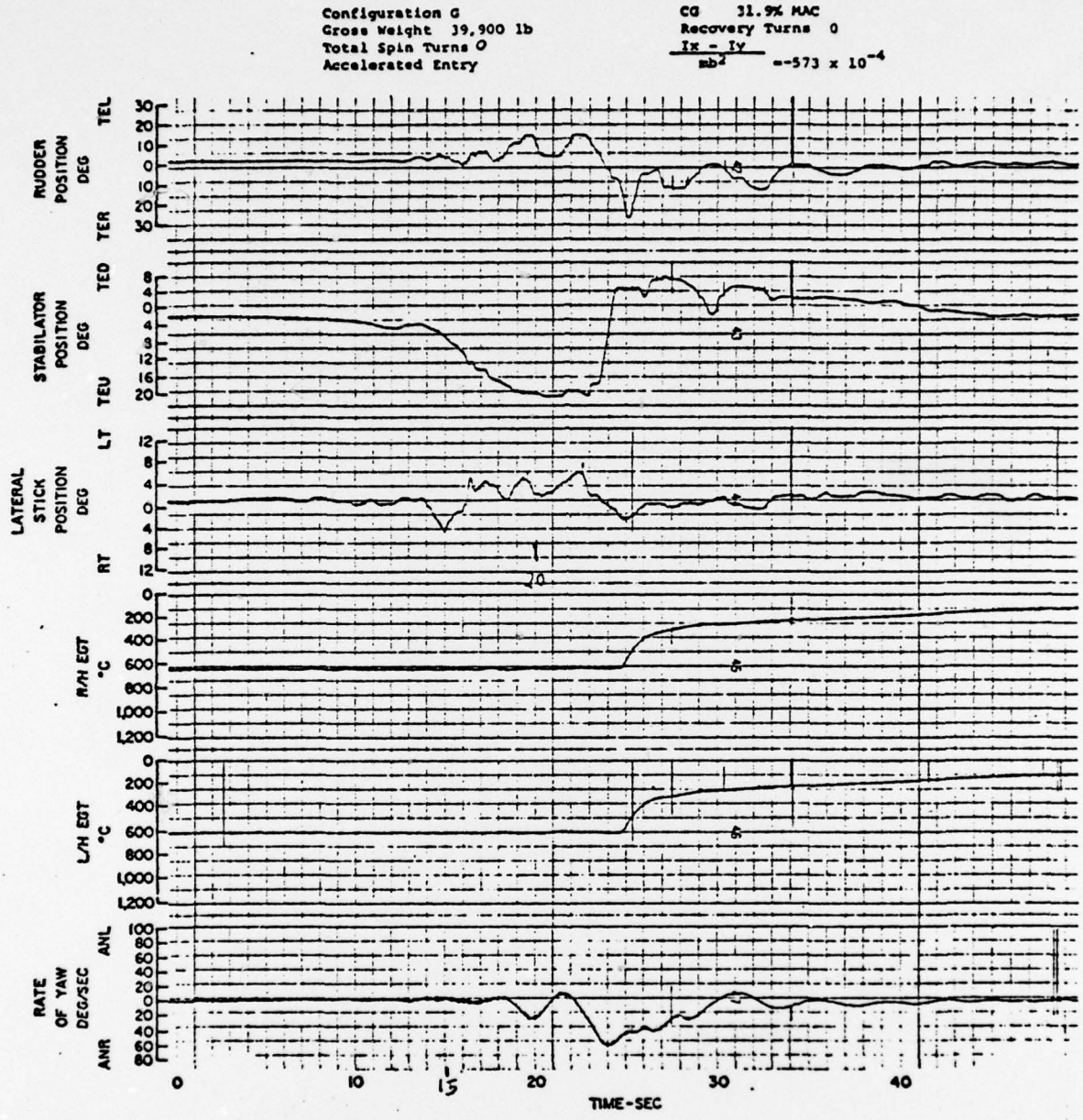


(from Reference 43)

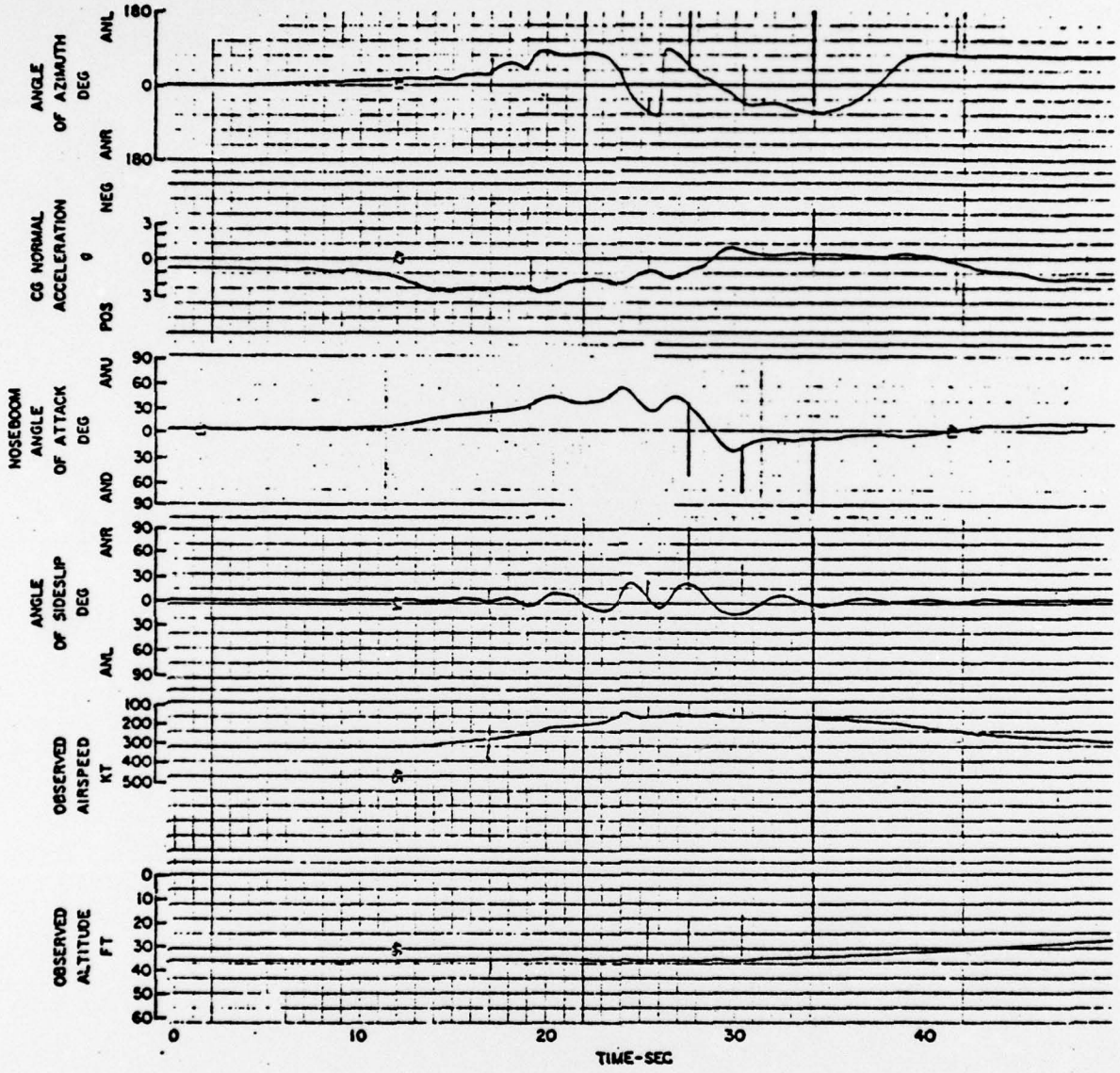


C

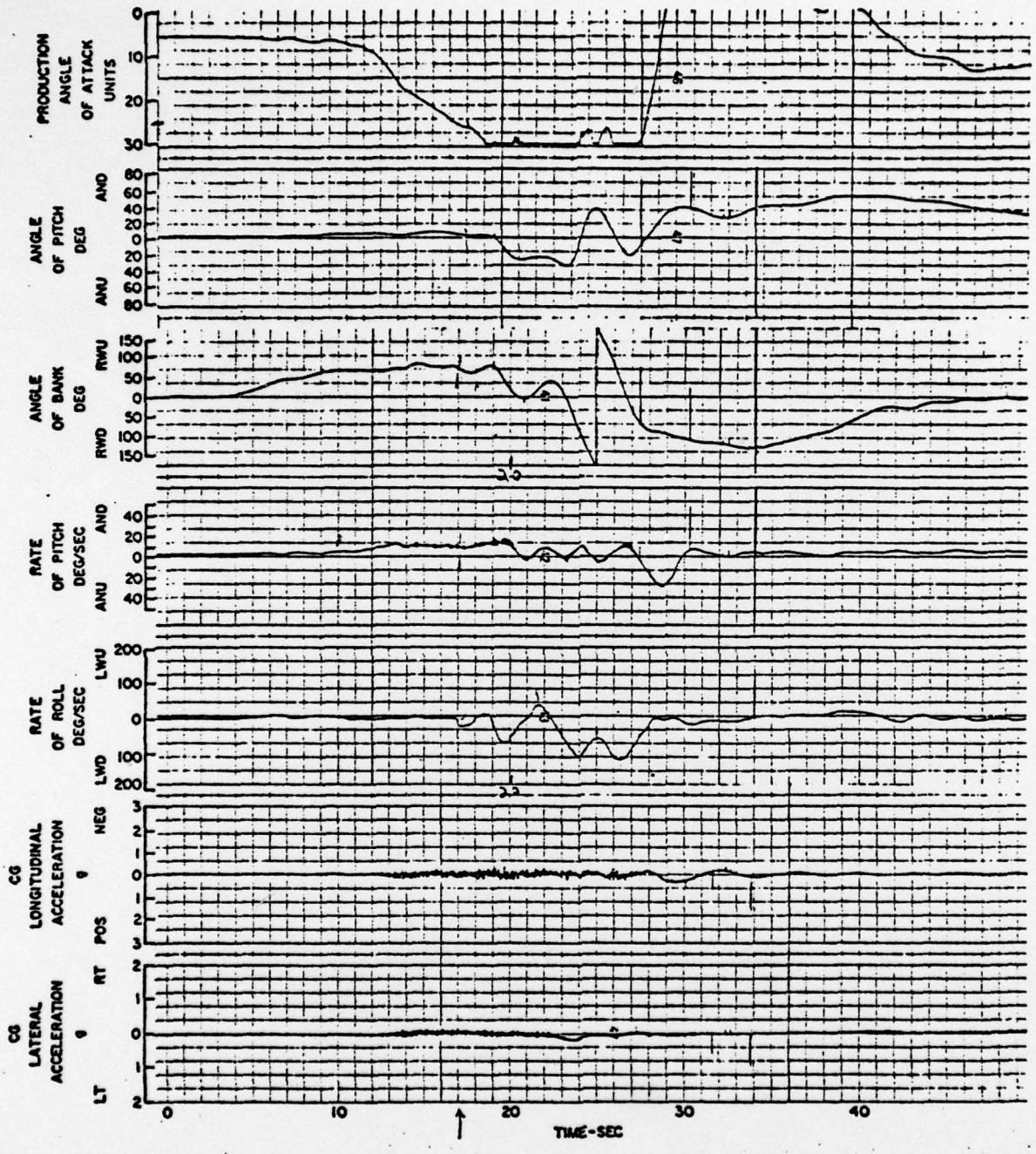
(from Reference 43)



(from Reference 43)

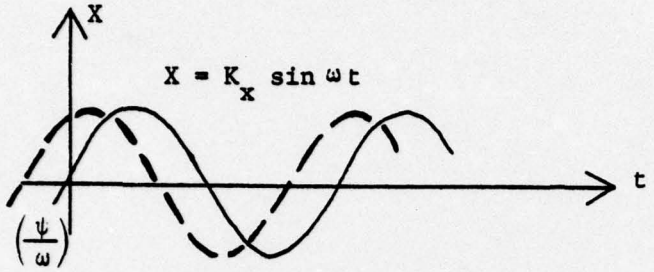


(from Reference 43)



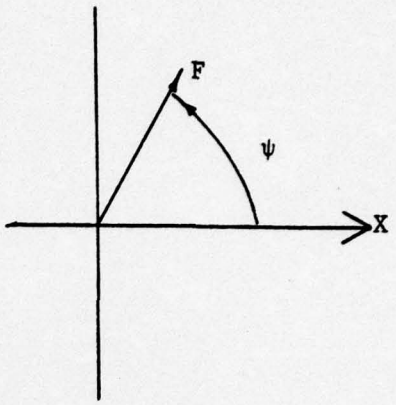
(from Reference 43)

E.2 WORK DONE BY A PHASOR VECTOR



$F = K_F \sin (\omega t + \psi)$

TIME DIAGRAM



PHASOR DIAGRAM

$$\text{Work} = W = \int F \, dx$$

$$W = K_F K_X \omega \int_{t_1}^{t_2} \sin (\omega t + \psi) \cos \omega t \, dt$$

Integrating over one cycle, let

$$t_2 = \frac{2\pi}{\omega} , \; t_1 = 0$$

$$W = K_F K_X \sin \psi$$

This shows that for any value of the phase angle from 0° to -180°, energy is taken from the system. This corresponds to positive damping. Conversely, $0° < \psi < 180°$ causes the energy of the system to increase (negative damping). When $\psi = 0°$ or $\psi = 180°$, no work is done on the system, although the former case is statically unstable and the latter, statically stable.

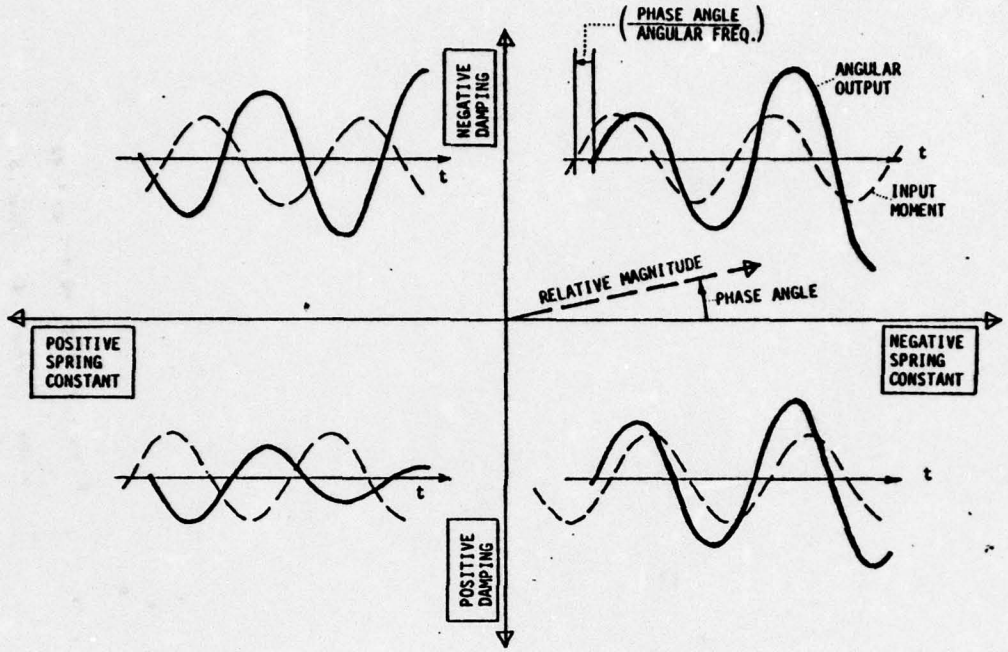


Figure E.1. Stability Regions of the Phasor Diagram

APPENDIX E

DISCUSSION OF THE PHASOR DIAGRAM IN STABILITY ANALYSIS

As shown in Section 4.3.5, the phasor diagram is a powerful tool in determining the various moment contributions to stability. It is believed that this is an original use of this technique in understanding the mechanism of wing rock.

E.1 GENERAL CHARACTERISTICS OF PHASOR REPRESENTATION

Figure E.1 shows the stability regions of the phasor diagram. The phase angle is defined as positive in the sense of the motion. Note that if the phase angle is ± 180° (moment and angle are exactly out of phase), the moment acts as a restoring moment, similar to a spring action. No energy is added to the system, but the spring always opposes the motion, Conversely, if the phase angle is 0°, an analogy may be formed with a "negative spring" which always seeks to drive the motion away from equilibrium. Thus the horizontal axis represents the component of the moment vector to the static stability of the system.

The vertical axis of the phasor diagram can be associated with damping in a second-order system. If the phase angle is -90°, the moment is acting as a dashpot, while a phase of +90° acts to increase the energy of the system. Thus the vertical axis represents the component of the moment to the dynamic stability of the system.

Only the lower left-hand quadrant of the phasor diagram is stabilizing, both statically and dynamically. If the sum of all moment vectors (summing is valid if the system is linear) lies in this quadrant, the motion resulting from a disturbance will be a damped sinusoid.